

# Co-ordination Chemistry of a Series of Bi- and Tripodal Ligands

## Thesis copyright declaration

to be signed by each user of this thesis

author KNIGHT, J.C.

title Co-ordination chemistry of a series of Bi- and Tripodal ligands.

year 2009

degree Ph.D.

accession no.

I undertake not to publish any portion of or use any information derived from, this thesis without the written consent of the Director. I further undertake to allow no one else to use this thesis while it is issued to me.

date	name and address in capitals	signature

A thesis submitted to the University of Wales in accordance with the requirements for the degree of Doctor of Philosophy in the Department of Chemistry, University of Wales

May 2009

UMI Number: U585266

All rights reserved

INFORMATION TO ALL USERS

The quality of this reproduction is dependent upon the quality of the copy submitted.

In the unlikely event that the author did not send a complete manuscript and there are missing pages, these will be noted. Also, if material had to be removed, a note will indicate the deletion.



UMI U585266

Published by ProQuest LLC 2013. Copyright in the Dissertation held by the Author.  
Microform Edition © ProQuest LLC.

All rights reserved. This work is protected against  
unauthorized copying under Title 17, United States Code.



ProQuest LLC  
789 East Eisenhower Parkway  
P.O. Box 1346  
Ann Arbor, MI 48106-1346

(

i-

# James Christopher Knight

A thesis submitted to the University of Wales in accordance with the requirements for the degree of Doctor of Philosophy in the Faculty of Science, Department of Chemistry, University of Wales, Cardiff.

May 2009

# Acknowledgements

---

*The work presented in the following pages has been contributed to in various forms by several people, and I am grateful to all those who have contributed their thoughts, efforts and time.*

*Firstly, I wish to thank Angelo and Pete for kindly offering me a PhD studentship and allowing me to start out on what I hope will be a lifetime spent in research. I feel very fortunate to have had such supportive supervisors who were always at hand with their advice and ideas. Thank you, Angelo, for always being so generous with your time and knowledge. Your passionate and ever-curious approach to science is one I hope to emulate throughout my career. Thank you, Pete, not only for your 'can do' attitude and positivity, but also for giving me my first skiing lesson and introducing me to the infamous Jagertea!*

*Over the last three years I have been privileged to work with many people who made life in lab 1.124 a genuine pleasure. I wish to thank, in no particular order, Mini, Glesni, Matt, Tom, Chris, Dan, Jo, Abdul and Saji, each of whom provided advice, support, and lots of great memories. I reserve a special mention for Fawaz Saad whom I respect and admire immensely. Thank you Fawaz for being a constant inspiration in the lab, your enthusiasm for the work was contagious and your sense of humour always kept my spirits high. I also wish to thank Neha Singh for her early work which prompted this research and for providing characterisation data for some of the compounds discussed herein.*

*This work could not have been completed without the assistance of various other talented people, in particular Rob Jenkins and Robin Hicks, who each provided technical assistance when it was desperately needed. I also wish to thank the numerous other technicians and staff who keep the department running smoothly, in particular, Gary, Dave, Jamie, Sham, Alun, John and Jobo.*

*I am eternally grateful to my family who have been a source of constant support throughout my studies. Thank you for always being there and helping me every step of the way.*

*Finally, I extend my heartfelt thanks to Ciara Hovey and Luke Woodyatt, who provided inspiration and encouragement at times when I needed them most. I could not wish for better friends than these and I am truly grateful. I hope I can repay the favour someday. This is for you, guys.*

*To see a World in a Grain of Sand  
And a Heaven in a Wild Flower,  
Hold Infinity in the palm of your hand  
And Eternity in an hour.*

*William Blake; Auguries of Innocence (ca. 1803)*

## Summary

A structural investigation into a series of transition metal complexes forms the basis of *Chapter 1*. Specifically, this work focuses on the co-ordination chemistry of two bipodal ligand frameworks,  $L^1$  and  $L^2$ . Each ligand contains a ketone moiety which, in the case of  $L^1$ , has been shown to undergo hemi-ketal formation upon complexation in some instances, yielding dinuclear complexes of the form  $[M_2\{(2\text{-bipy})_2\text{C}(\text{OMe})\text{O}^-\}_2][\text{ClO}_4]_2$  ( $M = \text{Fe}^{\text{II}}$  or  $\text{Zn}^{\text{II}}$ ).

*Chapters 2* and *3* take a detailed look at a series of transition metal complexes formed by the tripodal bipyridine-based ligand frameworks,  $L^3 - L^5$ . The tris-bipyridyl ligand,  $L^3$ , has been shown to enforce a predominantly trigonal prismatic co-ordination environment around a metal centre, even in cases where the metal has a strong stereoelectronic octahedral preference. For each ligand, the relationship between octahedral and trigonal prismatic character as the d-electron configuration of the metal centre is varied has been examined. Using the Cartesian coordinates obtained from crystallographic data sets, continuous shape mapping analysis (CShM) has been employed to assist in the quantification of the distortions away from these two ideal geometries.

*Chapters 4* and *5* report the protonation and stability constants for a series of potential MRI contrast agents which are based upon a tripodal ligand scaffold with a tris-pyridine core ( $L^6 - L^8$ ). This work examines how modifying the denticity of the ligands from four to six by changing the number of peripheral binding functions affects overall complex stability and the nature of species in solution.

*Chapter 6* investigates the efficacy of a series of gadolinium complexes as potential MRI contrast agents. This has been accomplished by measuring T1 relaxivities using a fast field-cycling (FFC) relaxometer.

## Contents

<i>Abbreviations</i> .....	v
----------------------------	---

## Chapter 1: Two Bipodal Ligand Frameworks: A Structural Exploration of Transition Metal Complexes *via* X-ray Diffraction Methods ..... 1

1.1	SCHEME FOR CHAPTER 1.....	2
1.2	INTRODUCTION .....	2
1.3	EXPERIMENTAL.....	16
1.3.1	<i>General</i> .....	16
1.3.2	<i>Preparations</i> .....	16
1.3.2.1	Bis(6-bromopyridin-2-yl)methanone, <i>L</i> <sup>1</sup> .....	16
1.3.2.2	Bis(2,2'-bipyrid-6'-yl)methanone, <i>L</i> <sup>1</sup> .....	17
1.3.2.3	Bis(2,2':6',2''-terpyrid-6''-yl)methanone, <i>L</i> <sup>2</sup> .....	17
1.3.2.4	General Procedure for the Synthesis of Metal Complexes .....	18
1.4	RESULTS AND DISCUSSION .....	21
1.4.1	<i>Ligand Synthesis</i> .....	21
1.4.2	<i>Synthesis of Complexes</i> .....	22
<i>Spectroscopic Properties of Complexes</i> .....	23	
1.4.3	<i>Vibrational Spectroscopy</i> .....	23
1.4.4	<sup>1</sup> H NMR of Zn and Cd Complexes.....	24
1.4.5	<i>Electronic Absorption Spectra</i> .....	25
1.4.6	<i>Electrochemical Studies</i> .....	30
1.4.7	<i>Crystallographic Studies</i> .....	35
1.4.7.1	Crystal Structure of [Mn <sup>II</sup> ( <i>L</i> <sup>1</sup> )(ClO <sub>4</sub> ) <sub>2</sub> ] (1.1).....	37
1.4.7.2	Crystal Structure of [Fe <sub>2</sub> ( <i>L</i> <sup>1</sup> -OCH <sub>3</sub> ) <sub>2</sub> ][ClO <sub>4</sub> ] <sub>2</sub> (1.2) .....	41
1.4.7.3	Crystal Structure of [Co <sup>II</sup> ( <i>L</i> <sup>1</sup> )(H <sub>2</sub> O) <sub>2</sub> ][ClO <sub>4</sub> ] <sub>2</sub> (1.3).....	44
1.4.7.4	Crystal Structure of [Ni <sup>II</sup> ( <i>L</i> <sup>1</sup> )(H <sub>2</sub> O) <sub>2</sub> ][ClO <sub>4</sub> ] <sub>2</sub> (1.4).....	48
1.4.7.5	Crystal Structure of [Cu <sup>II</sup> ( <i>L</i> <sup>1</sup> )(ClO <sub>4</sub> ) <sub>2</sub> ] (1.5).....	51
1.4.7.6	Crystal Structure of [Zn <sup>II</sup> ( <i>L</i> <sup>1</sup> )(H <sub>2</sub> O) <sub>2</sub> ][ClO <sub>4</sub> ] <sub>2</sub> (1.6).....	54
1.4.7.7	Crystal Structure of [Zn <sub>2</sub> ( <i>L</i> <sup>1</sup> -OCH <sub>3</sub> ) <sub>2</sub> ][ClO <sub>4</sub> ] <sub>2</sub> (1.7).....	57
1.4.7.8	Crystal Structure of [Cd <sup>II</sup> ( <i>L</i> <sup>1</sup> )(ClO <sub>4</sub> )(CH <sub>3</sub> CN)][ClO <sub>4</sub> ]-CH <sub>3</sub> CN (1.8).....	59
1.4.7.9	Crystal Structure of [Cu <sub>2</sub> ( <i>L</i> <sup>2</sup> )(CH <sub>3</sub> CN) <sub>4</sub> ][ClO <sub>4</sub> ] <sub>4</sub> ·2CH <sub>3</sub> CN (1.9).....	62
1.5	CONCLUSIONS.....	66
1.6	REFERENCES .....	67

## Chapter 2: A Bipyridine-based Tripodal Framework with a Strong Preference for Trigonal Prismatic Co-ordination Geometries ..... 75

2.1	SCHEME FOR CHAPTER 2.....	76
2.2	INTRODUCTION .....	76
<i>The Bailar Twist</i> .....	76	
<i>Trigonal Prismatic vs Octahedral Co-ordination Geometries</i> .....	77	
<i>Continuous Shape Mapping (CShM)</i> .....	80	
<i>A Review of Known Trigonal Prismatic Compounds</i> .....	82	
2.3	EXPERIMENTAL.....	89
2.3.1	<i>General</i> .....	89
2.3.2	<i>Preparations</i> .....	89
2.3.2.1	General Procedure for the synthesis of metal complexes .....	89
2.4	RESULTS AND DISCUSSION .....	92
2.4.1	<i>Ligand Synthesis</i> .....	92
2.4.2	<i>Synthesis of Complexes</i> .....	93
<i>Spectroscopic Properties of Complexes</i> .....	93	
2.4.3	<i>Vibrational Spectroscopy</i> .....	93

2.4.4	<i><sup>1</sup>H and <sup>13</sup>C NMR of Zn and Cd Complexes</i> .....	94
2.4.5	<i>Electronic Absorption Spectra</i> .....	96
2.4.6	<i>Electrochemical Studies</i> .....	103
2.4.7	<i>Crystallographic Studies</i> .....	110
2.4.7.1	Crystal Structure of [Mn <sup>II</sup> (L <sup>3</sup> )](ClO <sub>4</sub> ) <sub>2</sub> ·H <sub>2</sub> O (2.1).....	112
2.4.7.2	Crystal Structure of [Fe <sup>II</sup> (L <sup>3</sup> )](ClO <sub>4</sub> ) <sub>2</sub> (2.2).....	115
2.4.7.3	Crystal Structure of [Co <sup>II</sup> (L <sup>3</sup> )](ClO <sub>4</sub> ) <sub>2</sub> ·0.5CH <sub>3</sub> CN (2.3).....	117
2.4.7.4	Crystal Structure of [Ni <sup>II</sup> (L <sup>3</sup> )](ClO <sub>4</sub> ) <sub>2</sub> ·0.5CH <sub>3</sub> CN (2.4).....	119
2.4.7.5	Crystal Structure of [Cu <sup>II</sup> (L <sup>3</sup> )](ClO <sub>4</sub> ) <sub>2</sub> ·2CH <sub>3</sub> CN (2.5).....	121
2.4.7.6	Crystal Structure of [Zn <sup>II</sup> (L <sup>3</sup> )](ClO <sub>4</sub> ) <sub>2</sub> (2.6).....	124
2.4.7.7	Crystal Structure of [Cd <sup>II</sup> (L <sup>3</sup> )](ClO <sub>4</sub> ) <sub>2</sub> ·2CH <sub>3</sub> OH (2.7).....	126
2.5	CONCLUSIONS.....	128
	<i>Structural Overview and Continuous Shape Mapping</i> .....	128
2.6	REFERENCES.....	133

## Chapter 3: The Co-ordination and Electrochemical Behaviour of Two Analogous Tetra- and Pentadentate Tripodal Ligand Frameworks..... 137

3.1	SCHEME FOR CHAPTER 3.....	138
3.2	INTRODUCTION.....	138
	<i>Electrochemical Behaviour of Pyridine-Based Frameworks</i> .....	138
3.3	EXPERIMENTAL.....	145
3.3.1	<i>General</i> .....	145
3.3.2	<i>Preparations</i> .....	145
3.3.2.1	General Procedure for the synthesis of metal complexes.....	145
3.4	RESULTS AND DISCUSSION.....	150
3.4.1	<i>Ligand Synthesis</i> .....	150
3.4.2	<i>Synthesis of Complexes</i> .....	151
	<i>Spectroscopic Properties of Complexes</i> .....	151
3.4.3	<i>Vibrational Spectroscopy</i> .....	151
3.4.4	<i><sup>1</sup>H and <sup>13</sup>C NMR of Zn and Cd Complexes</i> .....	152
3.4.5	<i>Electronic Absorption Spectroscopy</i> .....	155
3.4.6	<i>Electrochemical Studies</i> .....	163
3.4.7	<i>Crystallographic Studies</i> .....	172
3.4.7.1	Crystal Structure of [Ni <sup>II</sup> (L <sup>4</sup> )(ClO <sub>4</sub> )(CH <sub>3</sub> CN)](ClO <sub>4</sub> ) (3.4).....	172
3.4.7.2	Crystal Structure of [Cu <sup>II</sup> (L <sup>4</sup> )(H <sub>2</sub> O)](ClO <sub>4</sub> ) <sub>2</sub> ·(CH <sub>3</sub> OH) (3.5).....	174
3.4.7.3	Crystal Structure of [Cd <sup>II</sup> (L <sup>4</sup> )(ClO <sub>4</sub> )(CH <sub>3</sub> CN)](ClO <sub>4</sub> ) (3.7).....	177
3.4.7.4	Crystal Structure of [Mn <sup>II</sup> (L <sup>5</sup> )(CH <sub>3</sub> CN)](ClO <sub>4</sub> ) <sub>2</sub> ·2(CH <sub>3</sub> CN) (3.8).....	180
3.4.7.5	Crystal Structure of [Fe <sup>II</sup> (L <sup>5</sup> )(CH <sub>3</sub> CN)](ClO <sub>4</sub> ) <sub>2</sub> ·(C <sub>4</sub> H <sub>10</sub> O) (3.9).....	182
3.4.7.6	Crystal Structure of [Co <sup>II</sup> (L <sup>5</sup> )(CH <sub>3</sub> CN)](ClO <sub>4</sub> ) <sub>2</sub> ·0.5(H <sub>2</sub> O) (3.10).....	185
3.4.7.7	Crystal Structure of [Ni <sup>II</sup> (L <sup>5</sup> )(Br)](ClO <sub>4</sub> ) (3.11).....	187
3.4.7.8	Crystal Structure of [Cd <sup>II</sup> (L <sup>5</sup> )(CH <sub>3</sub> CN)](ClO <sub>4</sub> ) <sub>2</sub> ·(CH <sub>3</sub> CN) (3.14).....	189
3.5	CONCLUSIONS.....	191
	<i>Structural Overview and Continuous Shape Mapping</i> .....	191
3.6	REFERENCES.....	194

## Chapter 4: Determination of Stability Constants for a Series of Pyridine-Carboxylate Based Tripodal Ligand Frameworks..... 199

4.1	INTRODUCTION.....	200
	<i>General Background and Aims</i> .....	200
	<i>Protonation and Stability Constants</i> .....	202
4.1.1	Historical Developments.....	202
4.1.2	Stability Constants – What are they?.....	203
4.1.3	Why Are Stability Constant's Useful?.....	205
4.1.4	The Chelate Effect.....	206



4.1.5	Hard-Soft Acid-Base Classification (HSAB).....	207
4.1.6	The Irving-Williams Order .....	207
4.1.7	Electrode Calibration Theory.....	208
4.1.8	Errors and their minimisation .....	210
4.2	EXPERIMENTAL.....	211
	<i>General</i> .....	211
	<i>Potentiometric Titrations</i> .....	213
4.3	RESULTS AND DISCUSSION .....	214
4.4	CONCLUSIONS.....	225
4.5	REFERENCES .....	226

## **Chapter 5: Determination of Stability Constants for a 2,2'-Bipyridine-Derivatised Tripodal Ligand Series..... 230**

5.1	INTRODUCTION .....	231
	<i>Solution Structure and Properties of 2,2'-Bipyridine:</i> .....	231
	5.1.1 Protonation Constants of 2,2'-Bipyridine and its Derivatives.....	232
	5.1.2 The Stability Constants for a Series of Tris 2,2'-Bipy Complexes .....	234
5.2	EXPERIMENTAL.....	235
5.3	RESULTS AND DISCUSSION .....	236
5.4	CONCLUSIONS.....	241
5.5	REFERENCES .....	242

## **Chapter 6: Novel Gd(III) Complexes as MRI Contrast Agents: Measuring Efficiency via Relaxometry ..... 245**

6.1	INTRODUCTION .....	246
	<i>Underlying Principles of Magnetic Resonance Imaging</i> <sup>5-8</sup> .....	246
	6.1.1 T <sub>1</sub> 'Longitudinal/Spin-Lattice' Relaxation .....	248
	6.1.2 T <sub>2</sub> 'Transverse/Spin-Spin' Relaxation .....	249
	<i>Fast Field-Cycling Relaxometry</i> <sup>9-11</sup> .....	250
	6.1.3 General Principles.....	251
	6.1.4 PPS: When B <sub>r</sub> << B <sub>0</sub> .....	251
	6.1.5 NPS: where B <sub>r</sub> → B <sub>d</sub> .....	252
	<i>Efficacy of T<sub>1</sub> Weighted Contrast agents:</i> .....	254
	<i>Using Luminescence Decay Lifetimes to Determine the Number of Inner Sphere Water Molecules</i> .....	256
6.2	EXPERIMENTAL.....	259
	6.2.1 <sup>1</sup> H NMRD acquisition:.....	259
	6.2.2 Luminescence.....	259
	6.2.3 Ligand Synthesis.....	260
	6.2.4 Sample Preparation .....	260
6.3	RESULTS AND CONCLUSIONS .....	260
	6.3.1 <i>Compound Gd-I: Overview</i> .....	260
	6.3.2 <i>Compounds Gd-II – Gd-VI: Overview</i> .....	266
	6.3.3 <i>Compound Gd-II</i> .....	268
	6.3.4 <i>Compound Gd-III</i> .....	268
	6.3.5 <i>Compound Gd-IV</i> .....	269
	6.3.6 <i>Compound Gd-V</i> .....	269
	6.3.7 <i>Compound Gd-VI</i> .....	270
6.4	REFERENCES .....	270

## **Appendix ..... 274**

## Abbreviations

Å	Angstrom
Ar	Aromatic
$\beta$	Equilibrium constant
bipy	2,2'-bipyridine
br	Broad
$^{13}\text{C}$	Carbon 13 isotope
$^{\circ}\text{C}$	Degrees centigrade
$\text{cm}^{-1}$	Reciprocal centimetres/wavenumber
$\text{CD}_3\text{CN}$	Deuterated acetonitrile
$\text{CDCl}_3$	Deuterated chloroform
$\delta$	NMR chemical shift
$\Delta$	Crystal field splitting
$\text{D}_2\text{O}$	Deuterated water
DCM	Dichloromethane
DMF	N,N-dimethylformamide
DMSO	Dimethylsulfoxide
d	Doublet
dd	Double doublet
$\epsilon$	Extinction coefficient
ESMS	Electrospray ionisation mass spectrometry
eq	Equivalent
eV	Electron volt
FAB	Fast atom bombardment
g	Grammes
h	Hour
$^1\text{H}$	Proton
HOMO	Highest occupied molecular orbital
HRMS	High resolution mass spectrometry
Hz	Hertz
IR	Infrared
J	Coupling constant
KBr	Potassium bromide
kJ	kilojoule
$\lambda$	Light wavelength
$\lambda_{\text{max}}$	Wavelength of the band at maximum absorption
L	Litre/ligand
LUMO	Lowest unoccupied molecular orbital
M	Metal/Molar concentration
m	Multiplet
Mr	Molecular weight
Me	Methyl
MeCN	Acetonitrile
mg	Milligram

MgSO <sub>4</sub>	Magnesium sulphate
MHz	Mega hertz
mL	Millilitre
mol	Mole
mmol	Millimole
MRI	Magnetic resonance imaging
MS	Mass spectrometry
<i>m/z</i>	Mass/charge ratio
nm	Nanometre (10 <sup>-9</sup> m)
NMR	Nuclear magnetic resonance
Nuc	Nucleophile
Ph	Phenyl
phen	1,10-phenanthroline
ppm	Parts per million
py	Pyridine
RT	Room temperature
s	Singlet
t	Triplet
T	Temperature/Tesla
terpy	2,2':6',2''-Terpyridine
θ	Angle
THF	Tetrahydrofuran
UV	Ultraviolet
Vis	Visible

# **Chapter 1: Two Bipodal Ligand Frameworks: A Structural Exploration of Transition Metal Complexes *via* X-ray Diffraction Methods**

*"The most beautiful experience we can have is the mysterious; it is the fundamental emotion which stands at the cradle of true art and science."*

*Albert Einstein*

## 1.1 Scheme for Chapter 1

A structural investigation into a series of transition metal complexes forms the basis of this chapter. Specifically, this work focuses on the co-ordination chemistry of two bipodal ligand frameworks,  $L^1$  and  $L^2$  (Fig. 1). Each ligand contains a ketone moiety which, in the case of  $L^1$ , has been shown to undergo hemi-ketal formation upon complexation in some instances, yielding dinuclear complexes of the form  $[M_2\{(2\text{-bipy})_2C(OMe)O^-\}_2][ClO_4]_2$  ( $M = Fe^{II}$  or  $Zn^{II}$ ).

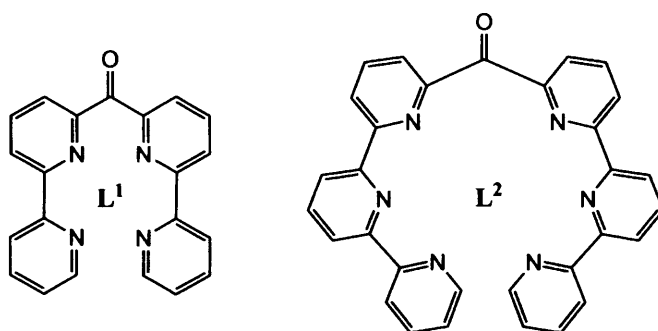


Figure 1: The ligands under investigation in this chapter.

## 1.2 Introduction

Investigations into the assembly of supramolecular arrays of metal ions have been carried out by a number of research groups, including Lehn,<sup>1-5</sup> Ward,<sup>6-8</sup> Constable,<sup>9-11</sup> Sauvage,<sup>12</sup> Bünzli<sup>13,14</sup> and Piguet.<sup>15-17</sup> Advances in this field have led to materials with beautiful and diverse molecular architectures which have shown promising catalytic,<sup>18-21</sup> electrochemical,<sup>19,22-23</sup> optical,<sup>24-29</sup> and magnetic<sup>24,30-32</sup> properties.

The use of N-heterocyclic donor groups has proven to be very successful in this area of chemistry and there has been a particular focus on pyridine-containing systems. The search for

novel metallo-supramolecular materials has also directed much attention towards ligands containing two non-equivalent metal binding units. For instance, the ligand dipyridylketone (dpk),  $(2\text{-py})_2\text{CO}$ , has been studied extensively<sup>33-58</sup> and has been shown to readily hydrate upon co-ordination to give  $(2\text{-py})_2\text{C}(\text{OH})_2$ ,  $(2\text{-py})_2\text{C}(\text{OR})(\text{OH})$ ,  $(2\text{-py})_2\text{C}(\text{OH})\text{O}^-$ ,  $(2\text{-py})_2\text{C}(\text{OR})\text{O}^-$ , and  $(2\text{-py})_2\text{CO}_2^{2-}$  (Fig. 2). These *gem*-diol and hemiketal species have yielded various polynuclear compounds, mainly due to the ability of the negatively charged  $\text{O}^-$  groups to bridge two or three metal ions, meaning the dianionic ligand may bridge upto five metal sites.

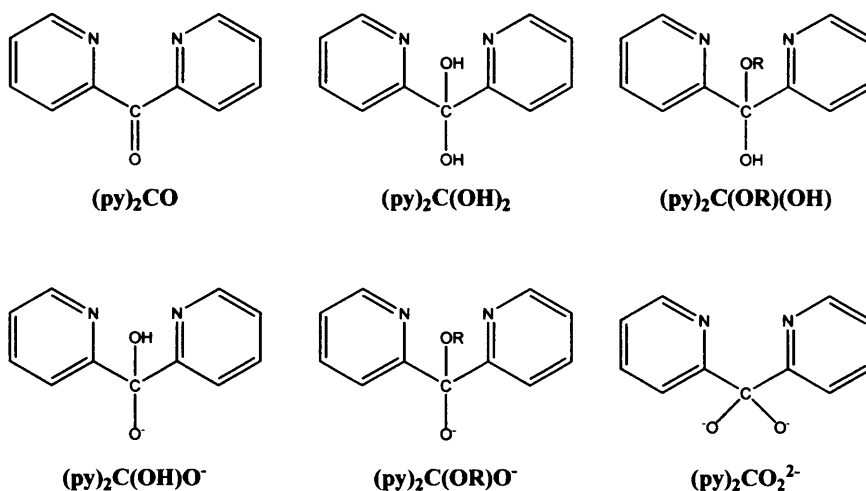


**Figure 2:** Water and alcohols can add to the carbonyl group of dpk generating a variety of ligands, the deprotonated forms are most interesting with respect to cluster chemistry.

The co-ordination behaviour of dpk was first investigated by Osborne and McWhinnie in 1967.<sup>33</sup> The complexes  $[\text{Cu}^{\text{II}}(\text{dpk})_2(\text{H}_2\text{O})_2](\text{ClO}_4)_2$  and  $[\text{Cu}^{\text{II}}(\text{dpk})_2(\text{ClO}_4)_2]$  were reported to exhibit *NO* and *NN* co-ordination modes respectively, *i.e.* co-ordination involved either one pyridyl nitrogen and the carbonyl oxygen (*NO*), or both pyridyl nitrogens (*NN*). However, Feller and Robson later concluded that both of these complexes, and indeed the majority of dpk complexes, involve co-ordination *via* both nitrogen donors.<sup>34-36</sup> Such a co-ordination mode is favourable as it allows  $\pi$ -back-bonding onto the pyridine rings and the electronegative carbonyl oxygen atom. Feller and Robson were also first to discuss the hydration behaviour of the ketone

and illustrated that dpk will readily hydrate in the presence of copper(II) sulphate in aqueous media, forming a *gem*-diol species.<sup>34</sup> Following co-ordination, the carbonyl carbon of dpk becomes more susceptible to nucleophilic attack and further experiments revealed similar hydration behaviour upon co-ordination to other transition metals.<sup>34-36</sup> This hydration behaviour is noteworthy as ketones do not readily hydrate in aqueous solutions unless they are flanked by very strong electron-withdrawing groups, *e.g.* Cl or F. It should be mentioned that metals in high oxidation states seem to facilitate this hydration behaviour,<sup>37-40</sup> while low oxidation state transition metals such as Au<sup>I</sup> have been shown to hinder it.<sup>41</sup> Furthermore, following UV experiments performed in both water and anhydrous diethyl ether it was concluded that ketone hydration does not occur to any significant extent in the absence of metal.<sup>35</sup>

The hydration behaviour associated with dpk is often attributed to the steric strain on the carbonyl carbon which is produced upon complexation. The carbonyl spacer group between the two pyridyl rings results in a large chelation angle, however in many instances<sup>42-44</sup> this angle becomes significantly smaller when the ligand is forced to partially fold in order for the nitrogen atoms to co-ordinate to a metal centre. Canty *et al.* studied the hydration behaviour of dpk and reported<sup>45</sup> the formation of the *gem*-diol moiety following reactions with Au<sup>III</sup>Me<sub>2</sub> and Ni<sup>II</sup> nitrate in water, leading to the species [AuMe<sub>2</sub>{(2-py)<sub>2</sub>C(OH)<sub>2</sub>}]NO<sub>3</sub> and [Ni{(2-py)<sub>2</sub>C(OH)<sub>2</sub>}<sub>2</sub>(NO<sub>3</sub>)<sub>2</sub>] $\cdot$ 0.5H<sub>2</sub>O respectively. It was proposed that in order to maintain typical M-N distances of *ca.* 2.0 Å, the initial co-ordination of the ketonic form of dpk requires either disruption of the planarity of the ketone with loss of carbonyl conjugation,<sup>46,47</sup> or retention of planarity but with poorer orbital overlap between the nitrogen lone pairs and the metal. Therefore, it was concluded that the hydration behaviour often observed in dpk is largely due to the desire of the carbonyl carbon to change from sp<sup>2</sup> to sp<sup>3</sup> hybridisation upon complexation, a phenomenon which was also found to be further facilitated by the formation of a six-membered

chelate ring with a stable boat conformation. The related ketones 2-pyridyl-*N*-methyl-2-imidazolylketone (pik) and di(*N*-methyl-2-imidazolyl)ketone (dik) (Fig. 3) were also investigated and did not result in hydrated species, forming instead  $[\text{AuMe}_2(\text{L})]\text{NO}_3$  ( $\text{L} = \text{pik}$  or  $\text{dik}$ ). Further reactions involving  $\text{CuSO}_4$  and  $\text{Ni}(\text{NO}_3)_2$  precursors also failed to hydrate these ketones. The absence of such hydration behaviour for both  $\text{dik}$  and  $\text{pik}$  was attributed to reduced angles within the imidazolyl rings, leading to a larger distance between the N-donor atoms and causing the N-M-N angles to approach  $90^\circ$ . This allows the ketone to maintain planarity while maximising N-donor orbital overlap with the metal.



**Figure 3:** The related ligands di(*N*-methyl-2-imidazolyl)ketone ( $\text{dik}$ ; left) and 2-pyridyl-*N*-methyl-2-imidazolylketone ( $\text{pik}$ ; right) do not undergo *gem*-diol formation

In contrast, Sienerth *et al.* examined a complex of  $\text{dpk}$  with platinum(IV) which is stable both in its anhydrous form,  $[\text{Pt}\{(2\text{-py})_2\text{CO}\}\text{Cl}_4]$ , and its hydrated form,  $[\text{Pt}\{(2\text{-py})_2\text{C}(\text{OH})\text{O}^-\}\text{Cl}_3]\cdot\text{H-PhenCl}$ , and proposed that the driving force for hydration in metal-bound  $\text{dpk}$  is instead due to a strongly electropositive carbonyl carbon.<sup>48</sup> This is caused by the electron-withdrawing nature of the pyridyl nitrogen atoms, an effect which is enhanced by their co-ordination to a Lewis acidic metal (Fig. 4). In this instance, the argument that the hydration behaviour is driven by steric strain was nullified as the crystal structure of the dehydrated ketonic form revealed a pyridine-carbonyl carbon-pyridine chelation angle of  $120.00^\circ$ , confirming the absence of any steric strain on the carbonyl carbon. In addition, it was also proposed that the aforementioned folding of the pyridines which is commonly seen in  $\text{dpk}$  metal complexes causes a loss of



planarity with the carbonyl group, therefore taking it out of conjugation with the  $\pi$ -system of the pyridyl rings. Consequently, the electron-deficient carbonyl carbon will not receive back-donation from the  $\pi$ -system of the pyridyl rings and will be even more susceptible to nucleophilic addition.

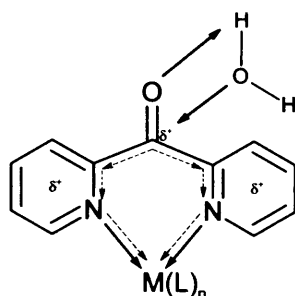


**Figure 4:** A schematic illustrating the inductive creation of a partial carbocation at the carbonyl carbon.

Natile *et al.* investigated this hydration behaviour following reactions with PdCl<sub>2</sub>, PtCl<sub>2</sub>, and HAuCl<sub>4</sub> precursors in both protic and aprotic solvents.<sup>46</sup> It was found that the palladium complexes prepared in protic solvents would exclusively give the condensation products [PdCl<sub>2</sub>(dpk·HX)] or [Pd(dpk·HX)<sub>2</sub>][ClO<sub>4</sub>]<sub>2</sub> (where X = OH or OR), depending on the metal to ligand ratio used. However, in aprotic solvents, no hydration occurred and the ketone was preserved. Similar behaviour was observed for the analogous platinum complexes, although the equilibrium describing the reversible uptake of a protic molecule seemingly favoured the ketone. This was evident as even in the presence of a large excess of water (50% v/v water:acetonitrile), both ketone and hydrate species were present at comparable concentrations. The Au<sup>III</sup> complexes heavily favoured the hydrated species which formed even in aprotic solvent where trace amounts of water in acetonitrile were sufficient to form condensation products. It was concluded that the stability of the hydrated species increases in a parallel with the electron-withdrawing capacity of the complexed metal ion, *i.e.* Pt<sup>II</sup> < Pd<sup>II</sup> < Au<sup>III</sup>. This supports the theory that the hydration of the ketone is driven largely by the electrophilicity of the carbonyl carbon. Further experiments

which monitored the progress of each reaction spectrophotometrically showed that hydration occurs after the formation of the ketonic complex in each case, including those carried out in pure protic solvents.

The neutral species  $(2\text{-py})_2\text{C}(\text{OH})_2$  and  $(2\text{-py})_2\text{C}(\text{OR})(\text{OH})$  typically act as tridentate chelates, forming mononuclear complexes *via* co-ordination of the two nitrogen atoms and an oxygen atom. These neutral ligands are not involved in cluster formation and typically form monomeric 1:1 and 1:2 metal to ligand complexes, however dinuclear and polymeric complexes have also been reported and are usually formed *via* bridging of the metal ions with anions such as chlorides or thiocyanates. For example, Cortés and Rojo *et al.*, while investigating the formation of infinite arrays, isolated two compounds with the general formula  $[\text{Cu}(\text{NCS})_2\{(2\text{-py})_2\text{C}(\text{OCH}_3)(\text{OH})\}]_n$ .<sup>49</sup> In both instances, the dpk had undergone metal-promoted solvolysis in methanol, generating the neutral alcoholated dpk-derivative,  $(2\text{-py})_2\text{C}(\text{OCH}_3)(\text{OH})$ . These compounds crystallised from the same mother liquor and yielded crystals with two distinct morphologies. X-ray analysis revealed one compound had formed a dimer in which two copper centres were bridged by two (*N,S*)-thiocyanate groups. The second compound contained infinite one-dimensional chains in which the copper centres were connected through single *end-to-end* thiocyanates bridges. In both instances, the hydrated dpk ligand exhibited a tridentate co-ordination mode in which both nitrogen atoms and the oxygen belonging to the  $-\text{O}-\text{CH}_3$  group were all bound to a single copper atom.

In contrast, the deprotonated forms of these ligands *i.e.*  $(2\text{-py})_2\text{C}(\text{OH})\text{O}^-$ ,  $(2\text{-py})_2\text{C}(\text{OR})\text{O}^-$  and  $(2\text{-py})_2\text{CO}_2^{2-}$  have been the focus of much interest with respect to cluster formation. The negatively charged oxygen from the deprotonated hydroxy groups has the ability to bridge two ( $\mu_2$ ) or three ( $\mu_3$ ) metal ions, and dianionic species can bridge as many as five metal sites. The ability of these ligands to form a large variety of co-ordination modes has resulted in the

Chapter 1: Two Bipodal Ligand Frameworks:  
A Structural Exploration *via* X-Ray Diffraction Methods

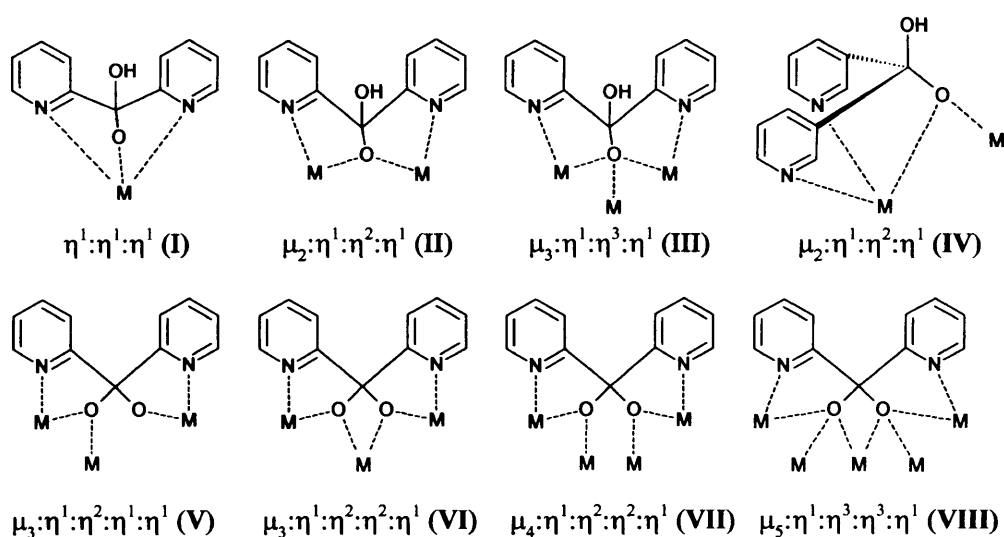


**Figure 5:** A selection of reported co-ordination modes for the mono- and di-anionic *gem*-diol forms of dpk.

isolation of clusters with nuclearities ranging from 4 to 14.<sup>50-52</sup> A recent example of such behaviour was reported by Padhi *et al.* who described the temperature dependant synthesis of a mononuclear complex and a neutral cubane cluster molecule.<sup>53</sup> The mononuclear complex,  $[\text{Co}\{(2\text{-py})_2\text{C}(\text{OH})\text{O}^-\}_2][\text{OAc}] \cdot 4\text{H}_2\text{O}$ , was shown to contain an  $\text{N}_4\text{O}_2$  octahedral co-ordination geometry around the cobalt(III) originating from two tridentate  $(2\text{-py})_2\text{C}(\text{OH})\text{O}^-$  species each exhibiting a  $\eta^1:\eta^1:\eta^1$  binding mode (Fig. 5; I). This compound was formed by simply stirring a methanolic solution of dpk and  $\text{Co}(\text{OAc})_2 \cdot 4\text{H}_2\text{O}$  for 1.5 h. However, heating the same reaction mixture to reflux for 2.5 h led to the formation of  $[\text{Co}_4\{(2\text{-py})_2\text{C}(\text{OH})\text{O}^-\}_4][\text{OAc}]_4$ , a tetranuclear cluster molecule with a cubane core. X-ray analysis of this compound revealed this core contained  $\text{Co}^{\text{II}}$  and oxygen atoms located at alternate vertices. The monoanionic *gem*-diol species in this instance was shown to function as a  $\mu_3:\eta^1:\eta^3:\eta^1$  ligand (Fig. 5; III) in which the deprotonated alkoxo oxygen bridged three cobalt centres. The co-ordination sphere of each  $\text{Co}^{\text{II}}$  cation also contained two pyridyl nitrogen atoms located on different ligands and a monodentate acetate anion, resulting in an  $\text{N}_2\text{O}_4$  chromophore with a distorted octahedral geometry. Further

examples of tetranuclear cubane-like cluster compounds resulting from the hydrated *gem*-diol form of dpk have been provided by other groups<sup>54,55</sup> who commonly report a similar  $M_4O_4$  core.

The dianionic doubly deprotonated *gem*-diol species,  $(2\text{-py})_2\text{CO}_2^{2-}$ , is also very useful in the synthesis of polynuclear clusters and exhibits a range of binding modes. For example, a zinc co-ordination polymer derived from  $(2\text{-py})_2\text{CO}_2^{2-}$  and acetate has been reported<sup>56</sup> containing repeating hexameric units,  $[\text{Zn}_6\{(2\text{-py})_2\text{C}(\text{O})_2^{2-}\}_2(\text{MeCO}_2^-)_8]$ . The cluster units were shown to contain two  $(2\text{-py})_2\text{CO}_2^{2-}$  dianions exhibiting a  $\mu_4:\eta^1:\eta^2:\eta^2:\eta^1$  binding mode (Fig. 5; VII) in which each deprotonated alkoxo oxygen bridged two zinc centres. Each cluster unit also contained six *syn,syn*- $\mu_2:\eta^1:\eta^1$   $\text{MeCO}_2^-$  ions and two *syn,anti*- $\mu_2:\eta^1:\eta^1$   $\text{MeCO}_2^-$  ions as ligands. Remarkably, treatment of this three-dimensional polymeric compound with terminal donor solvent molecules led to polymer cleavage and the formation of discrete hexanuclear zinc clusters,  $[\text{Zn}_6\{(2\text{-py})_2\text{CO}_2^{2-}\}_2(\text{MeCO}_2^-)_8(\text{H}_2\text{O})_2]$ , which retained a very similar formulation and structural arrangement compared to the constituent polymeric units. These discrete clusters also contained two  $\mu_4:\eta^1:\eta^2:\eta^2:\eta^1$   $(2\text{-py})_2\text{CO}_2^{2-}$  dianions and, in this instance, two terminal water ligands, two asymmetrically co-ordinating  $\text{MeCO}_2^-$  ions, four *syn,syn*- $\mu_2:\eta^1:\eta^1$   $\text{MeCO}_2^-$  ions, and two  $\mu_2:\eta^1:\eta^2$  acetate ions.

This doubly deprotonated *gem*-diol form of dpk can be observed bridging five metal sites in the nonanuclear cluster compound  $[\text{Co}_9\{(2\text{-py})\text{CO}_2^{2-}\}_4(\text{O}_2\text{CMe})_8(\text{OH})_2]\cdot 14.6\text{H}_2\text{O}$ .<sup>57</sup> Each of the four  $(2\text{-py})\text{CO}_2^{2-}$  species in this instance adopts a  $\mu_5:\eta^1:\eta^3:\eta^3:\eta^1$  binding mode in which each deprotonated oxygen bridges three  $\text{Co}^{\text{II}}$  centres (Fig. 5; VIII). The central cobalt site of this nonanuclear arrangement is situated at the shared apex of two square pyramids, a geometry which could also be described as a square prism in which an additional cobalt atom occupies an interstitial position. Each cobalt...cobalt edge of the bases is bridged by one of the eight *syn,syn*- $\mu_2:\eta^1:\eta^1$ - $\text{MeCO}_2^-$  groups, one of the two  $\mu_4\text{-OH}^-$  groups and a single oxygen atom originating

from a (2-py)CO<sub>2</sub><sup>2-</sup> ligand. This compound was synthesised after mixing Co(O<sub>2</sub>CMe)<sub>2</sub>·4H<sub>2</sub>O and dpk in acetonitrile at a 2:1 ratio. However, conducting this experiment using an equimolar ratio led instead to the formation of [Co<sub>4</sub>{(2-py)C(OH)O<sup>-</sup>}<sub>4</sub>(O<sub>2</sub>CMe)<sub>4</sub>]·H<sub>2</sub>O, a tetranuclear cubane complex in which the *gem*-diol form of dpk is only mono-deprotonated and adopts a μ<sub>3</sub>:η<sup>1</sup>:η<sup>3</sup>:η<sup>1</sup> co-ordination mode (Fig. 5; III). The alternate non-metallic vertices of this cubane core are occupied by the deprotonated oxygen atoms of the (2-py)C(OH)O<sup>-</sup> species. The co-ordination sphere of each cobalt cation is completed by a monodentate acetate ion, resulting in a N<sub>2</sub>O<sub>4</sub> co-ordination environment which is best described as distorted octahedral.

The ligating flexibility of dipyridyl-diolate chelates has also been illustrated in another high nuclearity molecule containing an alkoxide-bridged Mn<sup>II/III</sup><sub>26</sub> cluster.<sup>58</sup> The compound [Mn<sub>26</sub>O<sub>16</sub>(OMe)<sub>12</sub>{(2-py)<sub>2</sub>CO<sub>2</sub><sup>2-</sup>}<sub>12</sub>(MeOH)<sub>6</sub>](OH)<sub>6</sub> was formed *via* the reaction of Mn(ClO<sub>4</sub>)<sub>2</sub>·6H<sub>2</sub>O, dpk, NaOMe and NEt<sub>3</sub> in MeOH/MeCN. The core of this cluster molecule has been shown to contain an internal Mn<sup>III</sup><sub>16</sub> cage of adjacent Mn<sub>4</sub> tetrahedra which is surrounded by an outer Mn<sup>II</sup><sub>4</sub>Mn<sup>III</sup><sub>6</sub> shell. The outer shell is supported by the alkoxide groups of twelve μ<sub>3</sub>:η<sup>1</sup>:η<sup>2</sup>:η<sup>1</sup>:η<sup>1</sup> (2-py)<sub>2</sub>CO<sub>2</sub><sup>2-</sup> dianions (Fig. 5; V). This compound demonstrates the usefulness of deprotonated dpk hydrates in the synthesis of polynuclear clusters in the absence of carboxylate ligands as seen in the previous two examples.

Apart from dpk·HX (where X = OH, OR), crystal structures of transition metal complexes with metal-hemiacetal or hemiketal co-ordination are quite uncommon. Recently, Erxleben<sup>59</sup> investigated the copper complexes of 4-bromo-2-[(2-diethylaminoethyl)ethylaminomethyl]-6-formylphenol and reported ligand binding in both the aldehyde and hemiacetal forms (Fig. 6). In weakly acidic aqueous solutions, complexes of the form [Cu(H<sub>2</sub>L)<sub>2</sub>X<sub>2</sub>]<sub>2</sub> (X = NO<sub>3</sub><sup>-</sup> or ClO<sub>4</sub><sup>-</sup>) were generated in which co-ordination occurred *via*

the phenolate and aldehyde oxygen atoms, while in alkaline solutions complexes of the form  $[\text{CuL}_2]$  were synthesised. However, in methanolic solutions the carbonyl underwent nucleophilic attack from the solvent, resulting in the formation of a hemiacetal which was subsequently deprotonated upon co-ordination to the copper, forming  $[\text{Cu}(\text{L}')_2] \cdot 2\text{CH}_3\text{OH}$ .

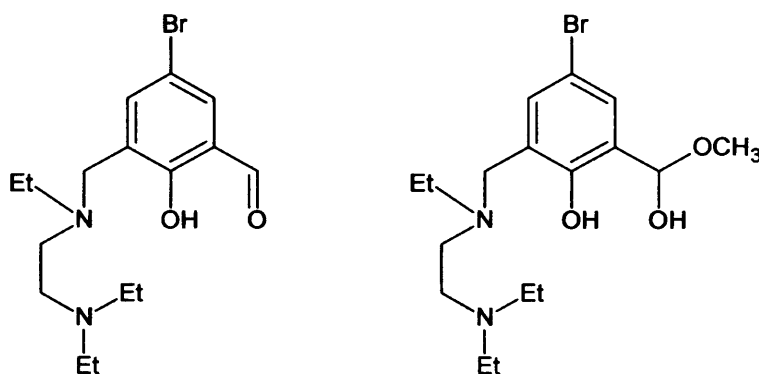


**Figure 6:** The ligand 4-bromo-2-[(2-diethylaminoethyl)ethylaminomethyl]-6-formylphenol in its aldehyde form, HL (left), and its hemiacetal form, H<sub>2</sub>L' (right).

Another example is provided in the  $\text{Fe}^{\text{III}}$  complexes of 2,6-pyridinediylbis(2-pyridinyl)methanone (Fig. 7), synthesised by Chen and co-workers.<sup>60</sup> Heating a methanolic solution of this ligand in the presence of  $\text{FeCl}_3$  resulted in metal-promoted solvolysis at both carbonyl positions and the formation of a trinuclear  $\text{Fe}^{\text{III}}$  complex incorporating two *cis*-related deprotonated di-hemiketals, each bridging two iron centres. However, as observed in many of these examples, the course of this reaction was heavily solvent-dependant and an alternative reaction involving the diffusion of THF into a mixed solvent of MeOH and  $\text{CH}_3\text{CN}$  led instead to a solvated mononuclear complex. In this instance, the ligand underwent nucleophilic addition with methanol at only one carbonyl position while the other carbonyl remained intact. This formed a hemiketal in which the hydroxyl group co-ordinated to a single  $\text{Fe}^{\text{III}}$  centre upon deprotonation. Likewise, repeating the reaction in a mixed solvent of  $\text{CH}_3\text{CN}$  and water led to a

similar mononuclear complex in which the ligand formed a monoanionic *gem*-diol at one carbonyl position rather than a hemiketal.

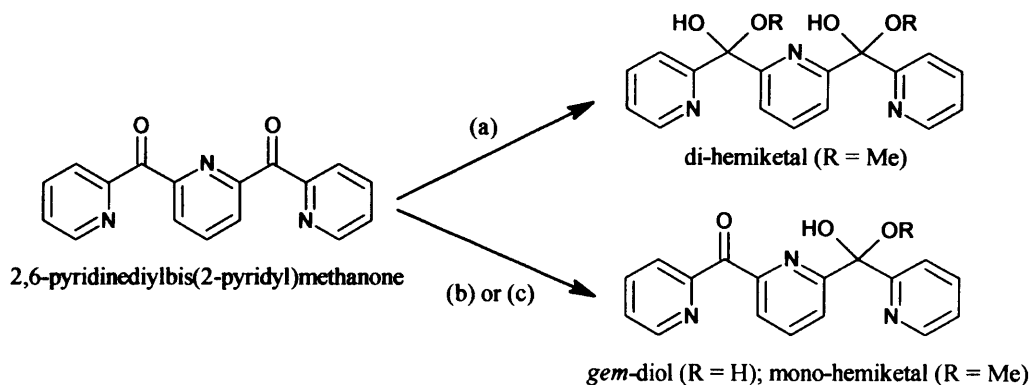


**Figure 7:** The hydrolysis and solvolysis of 2,6-pyridinediylbis(2-pyridyl)methanone in the presence of  $\text{FeCl}_3$ . The course of the reaction is heavily solvent-dependant; (a) hot MeOH, (b) diffusion of THF into a mixed  $\text{H}_2\text{O}/\text{CH}_3\text{CN}$  solution, or (c) diffusion of THF into a mixed  $\text{CH}_3\text{CN}/\text{MeOH}$  solution.

Further examples have also been provided by Perlepes and co-workers who reported a series of pentanuclear  $\text{Cu}^{\text{II}}$  complexes with dianionic bis(hemiacetals) resulting from metal-mediated alcoholysis of 2,2'-pyridil.<sup>61</sup> The co-ordination mode of the dianionic ligand was shown to be  $\mu_3:\eta^1:\eta^2:\eta^1:\eta^2:\eta^1:\eta^1$  and each deprotonated hydroxy oxygen atom can be observed bridging two metal centres (Fig. 8).

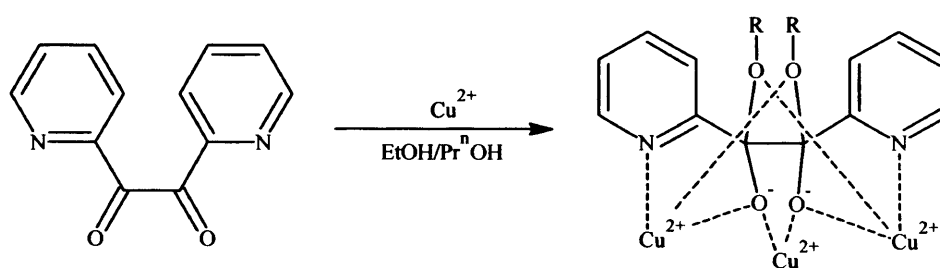


**Figure 8:** Co-ordination mode of the dianionic bis-(hemiacetal) form of 2,2'-pyridil following copper-mediated alcoholysis.

These compounds were formed *via* reaction of 2,2'-pyridil with  $[\text{Cu}_2(\text{O}_2\text{CMe})_4(\text{H}_2\text{O})_2]$  or  $\text{Cu}(\text{O}_2\text{CPh})\cdot\text{EtOH}$  in the presence of either EtOH or  $\text{Pr}^n\text{OH}$  and have the general formula  $[\text{Cu}_5(\text{OH})_2\{(2\text{-py})\text{C}(\text{O})\text{C}(\text{OR})\text{C}(\text{O})\text{C}(\text{OR})(2\text{-py})\}_2(\text{O}_2\text{CR}')_4(\text{ROH})_2]$  ( $\text{R} = \text{EtOH}, \text{Pr}^n\text{OH}$ ;  $\text{R}' = \text{O}_2\text{CMe}$  or  $\text{O}_2\text{CPh}$ ). Each of these pentanuclear copper complexes exhibited a rectangular

assembly of four copper atoms, in which the fifth copper occupied a central position. In addition to the bis-(hemiacetal) ligand, these discrete clusters were also held together with two  $\mu_3$ -OH<sup>-</sup> ions, two  $\mu_2$ : $\eta^1$ : $\eta^1$ -RCO<sub>2</sub><sup>-</sup> ions, two monodentate RCO<sub>2</sub><sup>-</sup> ions, and a terminal ROH molecule. These examples serve to illustrate the co-ordinative flexibility of hemiacetals and the structural diversity of the polynuclear complexes they form.

The bipyridyl analogue of dpk, bis(2,2'-bipyrid-6'-yl)methanone (Fig. 1; L<sup>1</sup>), has been shown by electrospray (ES) mass spectrometry experiments to yield polynuclear copper complexes.<sup>62</sup> It was demonstrated that mixing equimolar amounts of L<sup>1</sup> and Cu(CF<sub>3</sub>SO<sub>3</sub>) in anhydrous solvents generates a mixture of high molecular weight co-ordination polymers with the general formula [L<sup>1</sup>Cu(CF<sub>3</sub>SO<sub>3</sub>)<sub>2</sub>]<sub>n</sub>. The largest clearly identifiable oligomer contained 47 units. These polymers exhibited high kinetic stability in a variety of anhydrous solvents which was demonstrated by comparing mass spectra taken 5 min after sample preparation with those taken after 40 days. However, the addition of 5% water led to the progressive disappearance of the higher molecular weight oligomers and after 24 h only a single peak remained in the ES mass spectrum corresponding to the monomer complex. This indicated that these self-assembled polymeric complexes were created in solution and were not artefacts caused by the ES process. Attempts at isolating individual oligomers *via* column chromatography and HPLC yielded only the monomer, indicating that these components exist at equilibrium in solution.

The analogous phenanthroline-based ligand, di(1,10-phenanthrolin-2-yl)-methanone, forms 1:1 complexes with metals such as Ru<sup>II</sup> and Pd<sup>II</sup>, although the use of suitable metal precursors, [Ru<sup>II</sup>(bipy)<sub>2</sub>Cl<sub>2</sub>], has been shown to yield binuclear species (Fig. 9).<sup>63</sup> The diphen ketone ligand may exist in one of three planar conformations; the *syn,syn*, *anti,anti*, or *syn,anti* conformation. Complexation with the precursor Pd(CH<sub>3</sub>CN)<sub>4</sub>(BF<sub>4</sub>)<sub>2</sub> led to an *anti,anti* arrangement in which the diphen ketone acts as a planar tetradentate with the four nitrogen atoms



assuming a square planar arrangement around the metal. An identical ligand conformation is also seen following the reaction with  $\text{Ru}(\text{DMSO})_4\text{Cl}_2$  in the presence of  $\text{AgBF}_4$ . In this instance two 4-substituted pyridines (4-R-Py; where  $\text{R} = \text{CH}_3, \text{NMe}_2, \text{or CF}_3$ ) were also used as axial ligands. The binuclear species which results from the  $\text{Ru}(\text{bipy})_2\text{Cl}_2$  precursor causes the diphen ketone to adopt a *syn,syn* conformation in which each 1,10-phenanthroline group co-ordinates to a separate  $\text{Ru}^{\text{II}}$  centre.

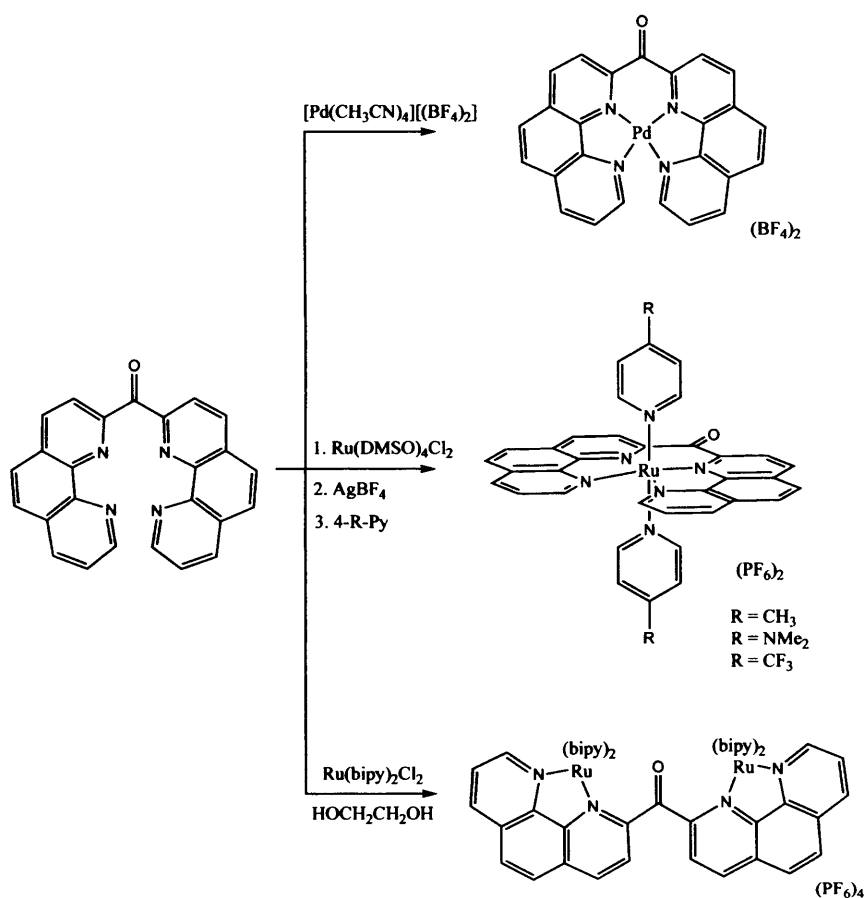


**Figure 9:** The ligand di(1,10-phenanthrolin-2-yl)methanone complexes as a planar tetradentate with  $\text{Pd}^{\text{II}}$  and with  $\text{Ru}^{\text{II}}$  and two 4-substituted pyridines (4-R-Py) (*anti,anti* conformation). With  $\text{Ru}(\text{bipy})_2\text{Cl}_2$ , a dinuclear complex is formed with the diphen ketone (*syn,syn* conformation).

The presence of two bipy units on each ruthenium means only bidentate co-ordination is possible, therefore in this instance the diphen ketone ligand functions as a bis-bidentate producing two stereogenic metal centres. The resulting complex consequently exists as a mixture

Chapter 1: Two Bipodal Ligand Frameworks:  
A Structural Exploration *via* X-Ray Diffraction Methods

of meso- and  $\Delta\Delta$ ,  $\Lambda\Lambda$ -forms. Interestingly, the hydration behaviour observed in the dipyridylketone has not previously been reported in the aforementioned bipyridyl or phenanthroline analogues.

In view of these findings it is of interest to determine if the co-ordinative properties of dpk may be extended to the bipyridine and terpyridine analogues. Therefore, the work in this chapter aims to investigate the co-ordinative properties of both the bipyridine and terpyridine species,  $L^1$  and  $L^2$  (Fig. 1; p. 1).

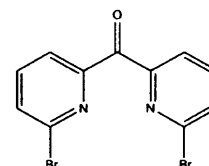
## 1.3 Experimental

### 1.3.1 General

NMR spectra were measured on a Bruker AM-400 or Bruker Av-500 Plus FT-NMR spectrometer. For infrared spectra, each compound was pressed into a disk with an excess of dried KBr and measured on a Jasco FT-IR spectrophotometer. Electrospray (ES) and high-resolution (HR) mass spectra were measured on a Waters LCT Premier XE (oa-TOF) mass spectrometer. UV-VIS absorption spectra were run in HPLC grade acetonitrile (Fisher) and measured on a Jasco V-570 spectrophotometer from 200 to 1,100 nm (optical path length 1.0 cm). Elemental analyses were carried out by the Warwick Analytical Service, University of Warwick.

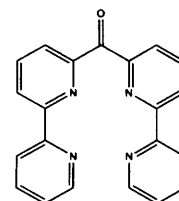
### 1.3.2 Preparations

#### 1.3.2.1 Bis(6-bromopyridin-2-yl)methanone, **1a**



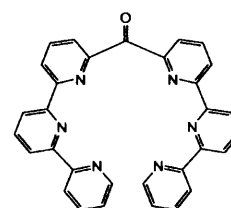
2,6-dibromopyridine (10 g, 42 mmol) was dissolved in dry diethyl ether (*ca.* 150 mL), and the resulting solution was cooled to  $-78^{\circ}\text{C}$  under  $\text{N}_{2(\text{g})}$ . A solution of *n*-butyllithium in hexanes (1.1 equivalent, 34.6 mL, 46.2 mmol of a 1.6 M solution in hexanes) was added dropwise to the cooled solution. After a period of 5 min, a solution of diethyl carbonate (2.54 mL, 21 mmol in 20 mL of dry diethyl ether) was slowly transferred *via* cannula to the solution of the lithiate. After stirring for 2 h at  $-78^{\circ}\text{C}$ , the reaction was allowed to warm to  $0^{\circ}\text{C}$ , then quenched with 10% HCl until acidic. The resulting mixture was basified with 10% aqueous  $\text{K}_2\text{CO}_3$  and the crude product partitioned between  $\text{CHCl}_3$  and water. The aqueous layer was washed twice with  $\text{CHCl}_3$ , the organic layers were then combined and dried with anhydrous  $\text{MgSO}_4$ . The resulting brown

solution was evaporated under reduced pressure. A white solid product was obtained by recrystallisation from hot methanol. (3.33 g, 67%).  $^1\text{H}$  NMR (400 MHz;  $\text{CDCl}_3$ ):  $\delta$  8.09 (d, 2H,  $J$  8.0 Hz), 7.76 (t, 2H,  $J$  8.0 Hz), 7.70 (d, 2H,  $J$  8.0 Hz);  $^{13}\text{C}$  NMR (100 MHz;  $\text{CDCl}_3$ )  $\delta$  188.8, 154.1, 141.3, 138.9, 131.0, 123.7; FAB-MS:  $m/z$  (%) 341 (100)  $[\text{M} + \text{H}]^+$ .



### 1.3.2.2 Bis(2,2'-bipyrid-6'-yl)methanone, $\text{L}^1$

Toluene (20 mL) was added to a mixture of 2-tributylstannylpyridine (2.15 g, 5.48 mmol), **1a** (0.50 g, 1.46 mmol), and tetrakis(triphenylphosphane)palladium ( $\text{Pd}(\text{PPh}_3)_4$ ) (0.34 g, 0.29 mmol) and the resulting mixture was stirred at  $110^\circ\text{C}$  under nitrogen for 24 h. The toluene was then evaporated under reduced pressure and the residue was chromatographed on silica gel eluting with acetone/hexane (2:5). The resulting pale yellow solid was washed twice with hexane to afford a white solid (0.37 g, 75%).  $^1\text{H}$  NMR (400 MHz;  $\text{CDCl}_3$ ):  $\delta$  8.61 - 8.51 (m, 4H), 8.29 (d, 2H,  $J$  7.9 Hz), 8.10 (d, 2H,  $J$  6.8 Hz), 8.0 (t, 2H,  $J$  7.8 Hz), 7.65 (t, 2H,  $J$  7.7 Hz), 7.24 - 7.16 (m, 2H);  $^{13}\text{C}$  NMR (100 MHz;  $\text{CDCl}_3$ ):  $\delta$  189.8, 154.5, 152.7, 148.1 (2C), 140.5, 137.6, 125.1, 123.9, 123.1, 120.5; IR  $\text{KBr}/\text{cm}^{-1}$ :  $\nu$  = 1686s, 1581s, 1430m, 1320s, 1258m, 1097m, 992s, 752m, 667m; FAB-MS:  $m/z$  (%) 339.1 (100)  $[\text{M} + \text{H}]^+$ .



### 1.3.2.3 Bis(2,2':6',2''-terpyrid-6''-yl)methanone, $\text{L}^2$

Toluene (20 mL) was added to a mixture of **1a** (0.25 g, 0.731 mmol), 6-(tributylstannyl)-2,2'-bipyridine (0.65g, 1.46 mmol), and tetrakis(triphenylphosphane)palladium ( $\text{Pd}(\text{PPh}_3)_4$ ) (0.34 g, 0.29 mmol) and the resulting mixture was stirred at  $110^\circ\text{C}$  under nitrogen for 24 h. The reaction mixture was then cooled to room temperature and the solution was filtered. The crude solid was washed with  $\text{Et}_2\text{O}$  ( $3 \times 10$  mL) and dried *in vacuo* to give the pure product as a pale yellow solid (0.23 g, 64%).  $^1\text{H}$  NMR (400 MHz;  $\text{CDCl}_3$ ):  $\delta$  8.80 (d, 2H,  $J$  7.7 Hz), 8.65 (d, 2H,  $J$  8.0), 8.55 (t,

2H,  $J$  7.7 Hz), 8.40 (d, 2H,  $J$  7.4 Hz), 8.30 (d, 2H,  $J$  7.7 Hz), 8.15 (d, 2H,  $J$  7.9 Hz), 8.05 (d, 2H,  $J$  7.9 Hz), 7.80 (t, 2H,  $J$  7.9 Hz), 7.75 – 7.66 (m, 2H), 7.25 – 7.18 (m, 2H);  $^{13}\text{C}$  NMR (100 MHz;  $\text{CDCl}_3$ ):  $\delta$  194.0 ( $-\text{C}=\text{O}$ ), 156.0, 155.5, 154.0, 153.0, 149.1, 138.0, 137.0, 136.3, 132.9, 128.3, 125.5, 123.5, 123.9, 121.0, 120.4; HRMS (ES):  $m/z$  (%) 492.1689 (100) ( $[\text{M}]^+$ ;  $\text{C}_{31}\text{H}_{20}\text{N}_6\text{O}$  requires 492.1699).

#### 1.3.2.4 General Procedure for the Synthesis of Metal Complexes

The ligand (1 equivalent, typically 0.1 mmol) was dissolved in the minimum amount (typically 3 mL) of acetonitrile in the case of **1.1**, **1.3**, **1.4**, **1.5**, **1.6**, **1.8** and **1.9** and methanol in the case of **1.2** and **1.7**. The solutions were warmed to *ca.* 60°C to ensure that the ligand fully dissolved. To this stirring solution, the metal perchlorate salt (1 equivalent) dissolved in water (typically ~2 mL) was added dropwise. A precipitate was collected and dried in air. Recrystallisation of the compounds typically involved the diffusion of diethyl ether into acetonitrile or methanolic solutions which were filtered through Celite.

**WARNING:** Perchlorate salts of metal complexes are potentially explosive. Care should be taken while handling such complexes.

$[\text{Mn}^{\text{II}}(\text{L}^1)(\text{ClO}_4)_2]$  (**1.1**): Colourless crystals (58% yield). Found: C, 42.73; H, 2.45; N, 9.54%.  $\text{MnC}_{21}\text{H}_{14}\text{N}_4\text{O}(\text{ClO}_4)_2$  requires C, 42.59; H, 2.38; N, 9.46%; ESMS  $m/z$  (%): 428.10 (100)  $[\text{Mn}(\text{L}^1) + 2\text{H}_2\text{O}]^+$ ; IR (KBr pellet,  $\text{cm}^{-1}$ ): 3072(m), 1686(s), 1581(s), 1431(s), 1098(m), 757(s), 634(m); UV/Vis [ $\lambda_{\text{max}}$ , nm ( $\epsilon_{\text{M}}$ ,  $\text{M}^{-1}\text{cm}^{-1}$ )] in  $\text{CH}_3\text{CN}$ : 229(28,720), 289(20,200), 309(6,140).

Chapter 1: Two Bipodal Ligand Frameworks:  
A Structural Exploration *via* X-Ray Diffraction Methods

**[Fe<sup>II</sup>(L<sup>1</sup>·OCH<sub>3</sub>)<sub>2</sub>][ClO<sub>4</sub>]<sub>2</sub> (1.2):** Orange crystals (32% yield). Found: C, 49.98; H, 3.20; N, 10.29%. Fe<sub>2</sub>C<sub>44</sub>H<sub>34</sub>N<sub>8</sub>O<sub>4</sub>(ClO<sub>4</sub>)<sub>2</sub> requires C, 50.36; H, 3.27; N, 10.68%; HRMS (ES) *m/z* (%): 949.0878 (35) ([Fe<sub>2</sub>(C<sub>44</sub>H<sub>34</sub>N<sub>8</sub>O<sub>4</sub>) + ClO<sub>4</sub>]<sup>+</sup>; Fe<sub>2</sub>C<sub>44</sub>H<sub>34</sub>N<sub>8</sub>O<sub>8</sub>Cl requires 949.0887); IR (KBr pellet, cm<sup>-1</sup>): 3096(s), 1596(m), 1447(m), 1084(s), 764(m), 623(s); UV/Vis [ $\lambda_{\text{max}}$ , nm ( $\epsilon_{\text{M}}$ , M<sup>-1</sup>cm<sup>-1</sup>)] in CH<sub>3</sub>CN: 239(25,500), 295(22,250), 328(4,100), 507(10.1), 562(7.3).

**[Co<sup>II</sup>(L<sup>1</sup>)(H<sub>2</sub>O)<sub>2</sub>][ClO<sub>4</sub>]<sub>2</sub> (1.3):** Orange crystals (55% yield). Found: C, 40.10; H, 2.86; N, 8.79%. CoC<sub>21</sub>H<sub>14</sub>N<sub>4</sub>O(ClO<sub>4</sub>)<sub>2</sub>·2H<sub>2</sub>O requires C, 39.89; H, 2.87; N, 8.86%; ESMS *m/z* (%): 397.09 (50) [Co(L<sup>1</sup>)]<sup>+</sup>; IR (KBr pellet, cm<sup>-1</sup>): 3427(br), 3085(m), 1682(s), 1604(s), 1448(s), 1104(s), 767(s), 618(s); UV/Vis [ $\lambda_{\text{max}}$ , nm ( $\epsilon_{\text{M}}$ , M<sup>-1</sup>cm<sup>-1</sup>)] in CH<sub>3</sub>CN: 235(26,200), 286(22,000), 319(5,800), 485(820), 555(82.9), 960(9.1).

**[Ni<sup>II</sup>(L<sup>1</sup>)(H<sub>2</sub>O)<sub>2</sub>][ClO<sub>4</sub>]<sub>2</sub> (1.4):** Purple crystals (69% yield). Found: C, 40.05; H, 2.98; N, 8.98%. NiC<sub>21</sub>H<sub>14</sub>N<sub>4</sub>O(ClO<sub>4</sub>)<sub>2</sub>·2H<sub>2</sub>O requires C, 39.91; H, 2.87; N, 8.87%; HRMS (ES) *m/z* (%): 495.0004 (100) ([Ni(L<sup>1</sup>) + ClO<sub>4</sub>]<sup>+</sup>; NiC<sub>21</sub>H<sub>14</sub>ClN<sub>4</sub>O<sub>5</sub> requires 495.0006); IR (KBr pellet, cm<sup>-1</sup>): 3383(br), 3088(s), 1681(s), 1604(s), 1449(s), 1101(s), 762(s), 621(s); UV/Vis [ $\lambda_{\text{max}}$ , nm ( $\epsilon_{\text{M}}$ , M<sup>-1</sup>cm<sup>-1</sup>)] in CH<sub>3</sub>CN: 235(25,700), 285(22,250), 320(8,100), 416(36.0), 497(21.9), 748(5.5), 822(17.8), 1054(9.4).

**[Cu<sup>II</sup>(L<sup>1</sup>)(ClO<sub>4</sub>)<sub>2</sub>] (1.5):** Blue crystals (52% yield). Found: C, 42.13; H, 2.51; N, 9.57%. CuC<sub>21</sub>H<sub>14</sub>N<sub>4</sub>O(ClO<sub>4</sub>)<sub>2</sub> requires C, 41.98; H, 2.35; N, 9.33%; ESMS *m/z* (%): 401 (100) [Cu(L<sup>1</sup>) + H]<sup>+</sup>; IR (KBr pellet, cm<sup>-1</sup>): 3080(m), 1686(s), 1605(s), 1450(s), 1099(s), 767(m), 623(s); UV/Vis [ $\lambda_{\text{max}}$ , nm ( $\epsilon_{\text{M}}$ , M<sup>-1</sup>cm<sup>-1</sup>)] in CH<sub>3</sub>CN: 234(27,050), 294(20,400), 314(3,800), 602(50), 684(22), 748(8).

Chapter 1: Two Bipodal Ligand Frameworks:  
A Structural Exploration *via* X-Ray Diffraction Methods

**[Zn<sup>II</sup>(L<sup>1</sup>)(H<sub>2</sub>O)<sub>2</sub>][ClO<sub>4</sub>]<sub>2</sub> (1.6):** Colourless crystals (39% yield). Found: C, 39.83; H, 2.87; N, 8.90%. ZnC<sub>21</sub>H<sub>14</sub>N<sub>4</sub>O(ClO<sub>4</sub>)<sub>2</sub>·2H<sub>2</sub>O requires C, 39.49; H, 2.84; N, 8.77%; HRMS (ES) *m/z* (%): 421.0642 (60) ([Zn(L<sup>1</sup>) + H<sub>2</sub>O + H]<sup>+</sup>; ZnC<sub>21</sub>H<sub>17</sub>N<sub>4</sub>O<sub>2</sub> requires 421.0643); <sup>1</sup>H NMR (500MHz; CD<sub>3</sub>CN): δ 9.03 (d, 2H, *J* 4.6 Hz), 8.78 (d, 2H, *J* 7.9 Hz), 8.64-8.48 (m, 6H), 8.39 (t, 2H, *J* 7.8 Hz), 7.93 (t, 2H, *J* 5.2 Hz); <sup>13</sup>C NMR (125 MHz; CD<sub>3</sub>CN): δ 158.2, 152.5, 149.1, 148.3, 148.1, 143.1, 142.4, 128.9, 127.8, 126.5, 124.1; IR (KBr pellet, cm<sup>-1</sup>): 3398(br), 3082(m), 1682(s), 1603(s), 1448(m), 1087(s), 764(m), 628(s).

**[Zn<sup>II</sup><sub>2</sub>(L<sup>1</sup>·OCH<sub>3</sub>)<sub>2</sub>][ClO<sub>4</sub>]<sub>2</sub> (1.7):** Colourless crystals (48% yield). Found: C, 49.53; H, 3.29; N, 10.57%. Zn<sub>2</sub>C<sub>44</sub>H<sub>34</sub>N<sub>8</sub>O<sub>4</sub>(ClO<sub>4</sub>)<sub>2</sub> requires C, 49.46; H, 3.21; N, 10.49%; ESMS *m/z* (%): 968.17 (100) [M + ClO<sub>4</sub>]<sup>+</sup>; <sup>1</sup>H NMR (500 MHz; d<sub>6</sub>-DMSO): δ 8.55 (d, 2H, *J* 4.6 Hz), 8.51 (m, 8H), 7.96 (t, 4H), 7.66 (t, 4H), 7.45 (d, 4H), 7.12 (t, 4H), 3.24 (s, 6H, -OCH<sub>3</sub>); IR (KBr pellet, cm<sup>-1</sup>): 3073(m), 1590(s), 1449(m), 1095(s), 761(m), 619(s).

**[Cd<sup>II</sup>(L<sup>1</sup>)(ClO<sub>4</sub>)(CH<sub>3</sub>CN)][ClO<sub>4</sub>]·CH<sub>3</sub>CN (1.8):** Colourless crystals (34% yield). Found: C, 41.12; H, 2.80; N, 11.63%. CdC<sub>21</sub>H<sub>14</sub>N<sub>4</sub>O(ClO<sub>4</sub>)<sub>2</sub>·2CH<sub>3</sub>CN requires C, 41.03; H, 2.75; N, 11.48%; ESMS *m/z* (%): 451.03 (100) [M + H]<sup>+</sup>; <sup>1</sup>H NMR (500 MHz; CD<sub>3</sub>CN): δ 8.70 (d, 2H, *J* 7.9 Hz), 8.51 (d, 2H, *J* 7.9 Hz), 8.45 (d, 2H, *J* 8.0 Hz), 8.24 (t, 2H, *J* 7.0 Hz), 8.22 (t, 2H, *J* 7.1 Hz), 8.11 (d, 2H, *J* 7.4 Hz), 7.76 (t, 2H, *J* 7.0 Hz); <sup>13</sup>C NMR (125 MHz; CD<sub>3</sub>CN): δ 191.4, 173.1, 151.5, 150.9, 150.6, 139.8, 139.6, 127.5, 126.4, 126.0, 123.3; IR (KBr pellet, cm<sup>-1</sup>): 3093(m), 1681(s), 1602(s), 1449(s), 1108(s), 768(s), 620(s).

$[\text{Cu}_2^{\text{II}}(\text{L}^2)(\text{CH}_3\text{CN})_4][\text{ClO}_4]_4 \cdot 2\text{CH}_3\text{CN}$  (**1.9**): Blue crystals (51% yield). Found: C, 39.83; H, 2.74; N, 11.98%.  $\text{Cu}_2\text{C}_{31}\text{H}_{20}\text{N}_6\text{O}(\text{ClO}_4)_4 \cdot 4\text{CH}_3\text{CN}$  requires C, 39.64; H, 2.73; N, 11.85%; ESMS  $m/z$  (%): 659.05 (100)  $[\text{Cu}_2(\text{L}^2) + \text{CH}_3\text{CN}]^+$ ; IR (KBr pellet,  $\text{cm}^{-1}$ ): 3437(br), 1713(s), 1603(s), 1580(m), 1098(br), 765(m), 624(s).

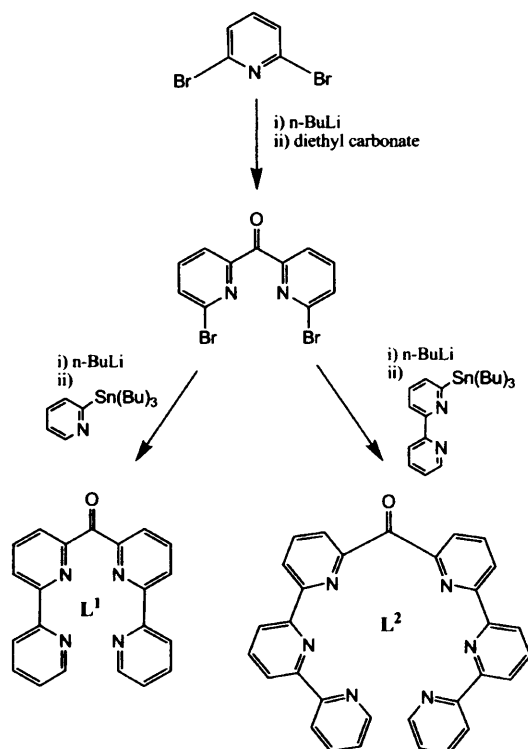
## 1.4 Results and Discussion

### 1.4.1 Ligand Synthesis

The precursor compounds 2-tributylstannylpyridine and 6-tributylstannyl-2,2'-bipyridine were synthesised as described by Leize *et al.*<sup>62</sup> and Lehn *et al.*<sup>64</sup> respectively. Bis(2,2'-bipyrid-6-yl)ketone,  $\text{L}^1$ , was prepared in reasonable yield by following the method described by Leize *et al.*<sup>62</sup> which has been summarised in Scheme 1.1. This synthesis involved the stannylation of 2-bromopyridine in THF with one equivalent of *n*-BuLi and tributylstannyl chloride to give a pale yellow oil of 2-tributylstannylpyridine upon removal of the solvent. The precursor compound bis(2,6-dibromopyridyl)ketone, **1a**, was prepared from 2,6-dibromopyridine by monolithiation and reaction with diethyl carbonate. The cross coupling reaction performed in toluene between 2-tributylstannylpyridine and **1a** in the presence of  $\text{Pd}(\text{PPh}_3)_4$  catalyst yielded a dark residue which was purified by column chromatography on silica gel with acetone/hexane (2:5) to yield  $\text{L}^1$  (75%).



## Chapter 1: Two Bipodal Ligand Frameworks: A Structural Exploration *via* X-Ray Diffraction Methods



**Scheme 1.1:** Synthetic route to L<sup>1</sup> and L<sup>2</sup>.

### 1.4.2 Synthesis of Complexes

Compounds **1.2**, **1.4**, **1.5** and **1.7** have been reported by Dr. Neha Singh,<sup>65</sup> but were re-made in an attempt to obtain higher quality crystallographic data sets. These have been discussed here in detail for the first time. Compound **1.9** was kindly provided by Dr. Ravi Prabakaran. The synthetic procedures and characterisation data, including those of the parent ligand, have been included for reference.

The ligand was dissolved in the minimum amount (typically 3 mL) of warm acetonitrile in the case of **1.1**, **1.3**, **1.4**, **1.5**, **1.6**, **1.8** and **1.9** or warm methanol in the case of **1.2** and **1.7**. In each case, the dropwise addition of an aqueous solution containing the relevant metal perchlorate salt instantly yielded a precipitate. These compounds were recrystallised *via* the diffusion of diethyl ether into acetonitrile or methanolic solutions resulting in crystals suitable for single-

crystal X-ray diffraction. The yields from these reactions were moderate (32-69%) and this crystalline material was then subsequently used for all spectroscopic measurements.

## Spectroscopic Properties of Complexes

### 1.4.3 Vibrational Spectroscopy

The IR spectra of the hemi-ketal complexes **1.2** and **1.7** confirms the absence of any carbonyl groups. The shift of pyridine ring vibration which typically occurred at *ca.* 1,600 cm<sup>-1</sup> and 1,450 cm<sup>-1</sup> indicates co-ordination from the pyridine ring nitrogens, a feature which is confirmed for all complexes by X-ray diffraction studies. The  $\pi(\text{C-H})$  vibrational frequency of complexes **1.1-1.9**, attributed to the rocking vibrations of the pyridyl C-H bonds is shifted to higher field by *ca.* 5-16 cm<sup>-1</sup> compared to the parent ligand, further suggesting pyridyl co-ordination. The IR spectra of complexes **1.3**, **1.4** and **1.6** show that a broad band around 3,300 – 3,500 cm<sup>-1</sup> can be attributed to co-ordinated water molecules present in the complexes. A very strong and broad band near 1,100 cm<sup>-1</sup> and a strong sharp vibration near 630 cm<sup>-1</sup> is observed for all complexes due to the presence of ionic perchlorate.<sup>66,67</sup>

**Table 1:** IR Stretching Frequencies of Complexes of L<sup>1</sup> and L<sup>2</sup>

Compound	$\nu(\text{C=O})$	Other characteristic vibrations/cm <sup>-1</sup>				
		aromatic $\nu(\text{C-H})$	$\nu(\text{O-H})$	$\nu(\text{C=N})$ and $\nu(\text{C=C})$	$\pi(\text{C-H})$	$\nu(\text{Cl-O})$
L <sup>1</sup>	1685(s)	3072(m)	-	1581(s), 1431(s)	752(s)	-
L <sup>2</sup>	1683(s)	2956(m)	-	1579(s)	755(s)	-
<b>1.1</b>	1686(s)	3072(m)	-	1581(s), 1431(s)	757(s)	1098(m), 634(m)
<b>1.2</b>	-	3096(s)	-	1596(m), 1447(m)	764(m)	1084(s), 623(s)
<b>1.3</b>	1682(s)	3085(m)	3427(br)	1604(s), 1448(s)	767(s)	1104(s), 618(s)
<b>1.4</b>	1681(s)	3088(s)	3383(br)	1604(s), 1449(s)	762(s)	1101(s), 621(s)
<b>1.5</b>	1686(s)	3080(m)	-	1605(s), 1450(s)	767(m)	1099(s), 623(s)
<b>1.6</b>	1682(s)	3082(m)	3398(br)	1603(s), 1448(m)	764(m)	1087(s), 628(s)
<b>1.7</b>	-	3073(m)	-	1590(s), 1449(m)	761(m)	1095(s), 619(s)
<b>1.8</b>	1681(s)	3093(m)	-	1602(s), 1449(s)	768(s)	1108(s), 620(s)
<b>1.9</b>	1713(s)	-	3437(br)	1603(s), 1580(m)	765(m)	1098(br), 624(s)

<sup>a</sup> IR spectra measured as KBr discs.

#### 1.4.4 $^1\text{H}$ NMR of Zn and Cd Complexes

Inspection of the  $^1\text{H}$ -NMR spectrum of the mononuclear  $\text{Zn}^{\text{II}}$  complex (**1.6**) (Fig. 10), reveals that the aromatic signals particularly *ortho*- and *para*- to the pyridyl-N donors have experienced a significant downfield shift compared to the parent ligand. This effect is most likely caused by a negative inductive effect upon co-ordination to the strongly Lewis acidic  $\text{Zn}^{\text{II}}$  cation. The multiplet observed in the region 8.48 – 8.64 ppm consists of two doublets and a triplet. In this region the ratio of chemical shift separation in Hz between each set of signals and the coupling constant for each multiplicity pattern is less than 10 ( $\Delta\delta\nu/J < 10$ ) and consequently second order effects are clearly visible.

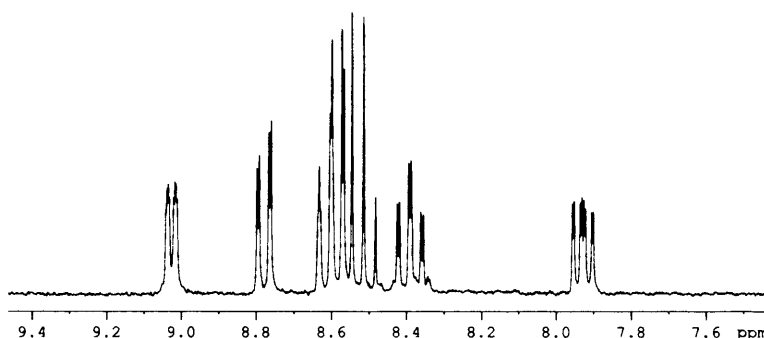


Figure 10:  $^1\text{H}$  NMR of  $\text{L}^1\text{-Zn}$  (**1.6**) in  $\text{CD}_3\text{CN}$ .

Conversely, the  $^1\text{H}$  NMR spectrum of the dinuclear zinc complex (**1.7**) reveals slightly upfield proton resonances on comparison to  $\text{L}^1$ . This may be due to a difference in the binding modes of the bipyridyl groups (*cf.* Section 1.4.7.7; p. 57), enhancing the interaction between the diamagnetic ring current and the paired metal d-electrons. This would have the effect of increasing the proton shielding and inducing an upfield shift. A strong singlet at 3.24 ppm is attributable to the  $-\text{O}-\text{CH}_3$  protons, which is a direct consequence of the hemiketal formation.

The  $^1\text{H-NMR}$  spectrum of the mononuclear cadmium complex, **1.8**, much like the analogous zinc complex is also shifted downfield significantly compared to the free ligand, however this effect is not as prominent as in the zinc species, due to the poorer Lewis acidity of  $\text{Cd}^{\text{II}}$ . The spectrum (Fig. 11) reveals a multiplet, in this case consisting of two overlapping triplet signals exhibiting second order effects. On comparison to **1.6**, the ordering of signals is slightly different and all four doublet signals are clearly observed this is most likely due to differences in the co-ordination modes. Data from single crystal X-ray diffraction studies indicates that for **1.6**, the zinc lies equidistant between the two symmetrically related bipy arms at the centre of an octahedral environment while the larger  $\text{Cd}^{\text{II}}$  occupies a position at the centre of a trigonal prismatic geometry being co-ordinated in a ‘side-on’ fashion by the four bipy-N donors (*cf.* Section 1.4.7.8; p. 59).

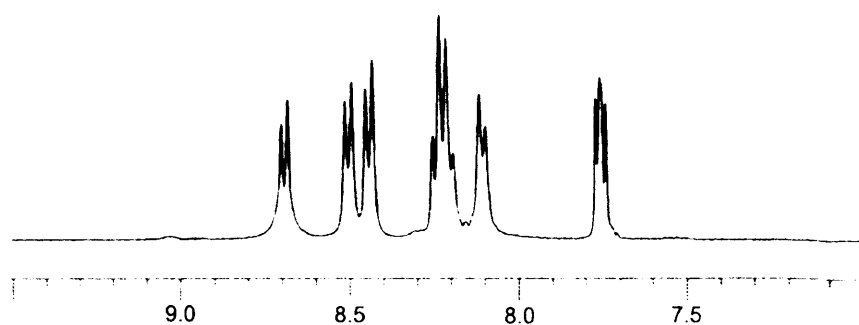


Figure 11:  $^1\text{H NMR}$  of  $\text{L}^1\text{-Cd}$  (**1.8**) in  $\text{CD}_3\text{CN}$ .

### 1.4.5 Electronic Absorption Spectra

The electronic spectra of complexes **1.1**, **1.2**, **1.3**, **1.4** and **1.5** have been measured and the data are presented in Table 2. The electronic absorption spectra for all complexes of  $\text{L}^1$  possess two strong peaks between 229 nm and 295 nm characteristic of intra-ligand bipyridine  $\pi\text{-}\pi^*$  transitions. The manganese complex, **1.1**, did not reveal any indication of a d-d transition even in highly concentrated solutions. The molar extinction coefficients for the spin-forbidden d-d

transitions of an octahedral  $\text{Mn}^{\text{II}}$  complex are typically in the range  $10^{-2}$  -  $10^{-1} \text{ dm}^3\text{mol}^{-1}\text{cm}^{-1}$ . The identification of the d-d bands of a  $\text{Mn}^{\text{II}}$  complex is usually not possible as even the weak tail of UV organic absorptions tailing into the visible region can obscure them.

**Table 2:** Electronic spectral assignments for complexes **1.1** – **1.5**

Compound	$\pi$ - $\pi^*$ transitions / $\lambda$ (nm)	MLCT / $\lambda$ (nm)	d-d transitions / $\lambda$ (nm)	$\Delta$ ( $\text{cm}^{-1}$ ) <sup>b</sup>	$B'$ ( $\text{cm}^{-1}$ ) <sup>b</sup>	$\beta$
1.1	229(28,720), 289(20,200)	309(6,140)	-	-	-	-
1.2	239(25,500), 295(22,250)	328(4,100)	507(10.1), 562(7.3)	-	-	-
1.3	235(26,200), 286(22,000)	319(5,800), 485(820)	555(82.9), 960(9.1)	11,458	575.8	0.59
1.4	235(25,700), 285(22,250)	320(8,100)	416(36.0), 497(21.9), 748(5.5), 822(17.8), 1054(9.4)	-	-	-
1.5	234(27,050), 294(20,400)	314(3,800)	602(50), 684(22), 748(8)	-	-	-

<sup>a</sup>performed in  $\text{CH}_3\text{CN}$  solution at room temperature; Numbers in parentheses indicate molar absorption coefficients  $\epsilon$  ( $\text{M}^{-1}\text{cm}^{-1}$ ). <sup>b</sup>values calculated by assuming an octahedral geometry.

The intense colours observed in  $\text{Fe}^{\text{II}}$  complexes with diimines such as bipyridine<sup>68-70</sup> and bipyrazine<sup>71</sup> have been thoroughly studied and are known to be caused by  $\text{Fe}^{\text{II}}$  to diimine metal to ligand charge transfer (MLCT). Bipyridine has a low-lying  $\pi^*$  orbital of symmetry  $B_2$  and two further  $\pi^*$  orbitals of symmetry  $A_2$  and  $B_2$  both lying at higher energy.<sup>72</sup> Therefore, the absorption at 328 nm in the electronic spectrum of **1.2** is attributed to a  $d \rightarrow \pi^*(B_2)$  (bipy) MLCT. The visible-near infrared region of the  $\text{Fe}^{\text{II}}$  compound reveals two prominent bands at  $17,790 \text{ cm}^{-1}$  and  $19,720 \text{ cm}^{-1}$  (Fig. 12). In the case of a high-spin octahedral co-ordination geometry, there is only one spin-allowed d-electron transition ( $(t_{2g})^4(e_g)^2 \rightarrow (t_{2g})^3(e_g)^3$ , *i.e.*  ${}^5E_g \leftarrow {}^5T_{2g}$ ). However, the presence of two bands could be attributable to the splitting of the  ${}^5E_g$  state resulting from the  $D_{4h}$  symmetry of this system. It is also worth noting that even in a system with perfect  $O_h$  symmetry this transition would lead to an asymmetrically filled  $e_g$  subset of orbitals which would subsequently undergo a Jahn-Teller distortion in order to remove the degeneracy. The resulting splitting into  ${}^5A_1 + {}^5B_1$  in  $D_{4h}$  means two bands are frequently observed in complexes of this type. The related  $D_{4h}$  compound,  $\text{Fe}^{\text{II}}(\text{Py})_4\text{Cl}_2$  has absorption bands at  $8,720 \text{ cm}^{-1}$  and  $10,520 \text{ cm}^{-1}$

<sup>1</sup>,<sup>73,74</sup> which are clearly present at much lower energies than the bands observed for **1.2**. An alternative scenario is that of a low-spin octahedral co-ordination geometry. Again, two transitions (<sup>1</sup>T<sub>1g</sub>←<sup>1</sup>A<sub>1g</sub> and <sup>1</sup>T<sub>2g</sub>←<sup>1</sup>A<sub>1g</sub>) are typically seen, however they appear at much higher energies on comparison to similar high-spin complexes. The low-spin complex, c-Fe<sup>II</sup>Cl<sub>2</sub>(ArNC)<sub>4</sub> reveals absorption bands at 17,400 cm<sup>-1</sup> and *ca.* 22,900 cm<sup>-1</sup> which correspond to the two aforementioned spin-allowed transitions.<sup>75</sup> In low-spin complexes such as this, a third transition attributable to the spin-forbidden triplet states <sup>3</sup>T<sub>1</sub> and <sup>3</sup>T<sub>2</sub> is occasionally reported but is often obscured by a charge transfer band. While attempts to acquire the <sup>1</sup>H NMR spectrum of this compound were unsuccessful, which suggests a high-spin paramagnetic d-electron configuration rather than the low-spin diamagnetic state, the electronic absorption pattern is evidently more characteristic of a low-spin complex.

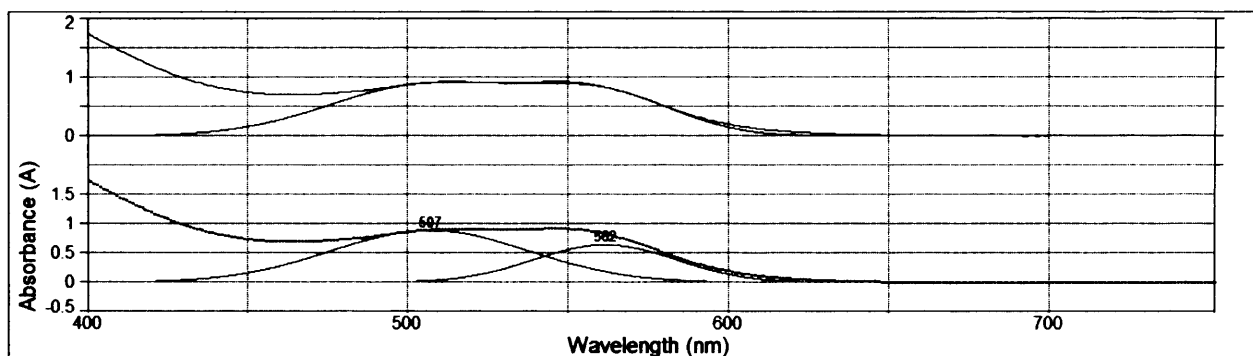


**Figure 12:** Deconvolution of the electronic spectrum of the Fe<sup>II</sup> compound, **1.2**. The lower graph contains a trace revealing the individual component peaks, while the upper graph has a trace which reflects the sum curve of these peaks. Both the upper and lower graphs also contain a trace of the raw input data.

The cobalt compound, **1.3**, contains three bands in the visible region. In the solid state, the geometry surrounding the Co<sup>II</sup> centre is a slightly distorted octahedron with D<sub>4h</sub> symmetry, with two solvent molecules occupying axial positions (*cf.* Section 1.4.7.3; p. 44). Octahedral Co<sup>II</sup> complexes are known to prefer high-spin configurations, while a low-spin configuration is only achievable in the presence of a sufficiently strong ligand field ( $\Delta_o \geq 15,000 \text{ cm}^{-1}$ ) which is

## Chapter 1: Two Bipodal Ligand Frameworks: A Structural Exploration *via* X-Ray Diffraction Methods

required to obtain a  ${}^2E$  ground state, originating from the  ${}^2G$  state of the free ion.<sup>76,77</sup> Assuming a high-spin configuration, the two lowest energy bands ( $10,420\text{ cm}^{-1}$  and  $18,020\text{ cm}^{-1}$ ) can be attributed to the d-d transitions  $\nu_1 = {}^4T_{2g}(F) \leftarrow {}^4T_{1g}(F)$  and  $\nu_2 = {}^4T_{1g}(P) \leftarrow {}^4T_{1g}(F)$  respectively. In this instance, the value  $\nu_2/\nu_1 = 1.73$  lies within the range generally reported for high-spin  $\text{Co}^{\text{II}}$  octahedral complexes. The third spin-allowed transition,  $\nu_3$  *i.e.*  ${}^4A_{2g}(F) \leftarrow {}^4T_{1g}(F)$ , was not observed in the absorbance spectrum but is predicted to appear at  $21,880\text{ cm}^{-1}$  and is most likely obscured by the strong MLCT band. From the positions of the bands  $\nu_1$  and  $\nu_2$ ,  $\Delta$  and the Racah  $B$  parameters were estimated as  $\Delta = 11,458\text{ cm}^{-1}$  and  $B = 575.8\text{ cm}^{-1}$ . The nephelauxetic ratio,  $\beta = 0.593$  (assuming free ion  $[\text{Co}^{\text{II}}]$ ;  $B = 971\text{ cm}^{-1}$ ), indicates a significant degree of covalency as expected due to the co-ordination sphere becoming enriched by N-donors. Again, two characteristic metal to ligand charge transfer bands, involving low-lying bipy-based  $\pi^*$  orbitals, are observed ( $20,620\text{ cm}^{-1}$  and  $31,350\text{ cm}^{-1}$ ). An example of a high-spin  $\text{Co}^{\text{II}}$  octahedral complex,  $[\text{Co}(\text{py})_6]^{2+}$ , reveals a similar absorption pattern to that observed for 1.3 with bands at  $9,800\text{ cm}^{-1}$  and  $20,400\text{ cm}^{-1}$ .<sup>78</sup>

The nickel compound, 1.4, contains an  $\text{N}_4\text{O}_2$  chromophore surrounding the  $\text{Ni}^{\text{II}}$  centre and exhibits pseudo- $D_{4h}$  symmetry in the solid state (*cf.* Section 1.4.7.4; p. 48). High-spin  $\text{Ni}^{\text{II}}$  complexes with  $D_{4h}$  symmetry have six spin-allowed transitions from the orbital singlet ( ${}^3B_{1g}$ ) to the terms  ${}^3E_g(F)$ ,  ${}^3B_{2g}(F)$ ,  ${}^3A_{2g}(F)$ ,  ${}^3E_g(F)$ ,  ${}^3A_{2g}(P)$ , and  ${}^3E_g(P)$ , in order from lowest to highest energy respectively. The first five of these transitions were located *via* computational analysis of the spectrum using the software PeakFit version 4.12 (SeaSolve Software, Richmond, CA, USA) which applies a Gaussian response function with a Fourier deconvolution algorithm. These were located at  $9,490$ ,  $12,165$ ,  $13,370$ ,  $20,120$  and  $24,040\text{ cm}^{-1}$ , with the sixth absorption peak most likely obscured by an intense MLCT band at  $31,250\text{ cm}^{-1}$ . These values are close to those reported for similar  $\text{Ni}^{\text{II}}$  complexes with  $D_{4h}$  symmetry. For example, the high-spin compound

$[\text{Ni}^{\text{II}}(\text{py})_4(\text{H}_2\text{O})_2]^{2+}$  also contains an  $\text{N}_4\text{O}_2$  chromophore and exhibits five spin-allowed transitions at 9,750, 11,780, 15,760, 17,390 and 28,000  $\text{cm}^{-1}$ .<sup>79</sup> The sixth band in this example has also not been reported.

The copper compound, **1.5**, features an  $\text{N}_4\text{O}_2$  chromophore surrounding the  $\text{Cu}^{\text{II}}$  centre and exhibits pseudo- $\text{D}_{4\text{h}}$  symmetry in the solid state (*cf.* Section 1.4.7.5; p. 51). The electronic spectra contains a very broad asymmetric peak in the visible region (Fig. 13) which is very common for Jahn-Teller distorted  $\text{Cu}^{\text{II}}$  complexes. For all ions with a  $d^9$  configuration, the lowest electron configuration is  $t_{2g}^6 e_g^3$  leading to a  $^2\text{D}$  ground state, and in an octahedral environment this ground state will split into a  $^2\text{E}_g$  term and a  $^2\text{T}_{2g}$  term. Due to the asymmetric filling of the anti-bonding  $e_g$  subset of orbitals a tetragonal distortion arises in an attempt to remove the orbital degeneracy. Consequently, the  $^2\text{E}_g$  term splits into  $^2\text{B}_{1g}$  and  $^2\text{A}_{1g}$ , while the  $^2\text{T}_{2g}$  term splits into  $^2\text{B}_{2g}$  and  $^2\text{E}_g$  (Fig. 14). Upon deconvolution of the spectrum, the broad visible band envelope is seen to be composed of three smaller peaks (13,370, 14,620, and 16,610  $\text{cm}^{-1}$ ) which are attributable to the transitions  $\nu_1 = ^2\text{A}_{1g} \leftarrow ^2\text{B}_{1g}$ ,  $\nu_2 = ^2\text{B}_{2g} \leftarrow ^2\text{B}_{1g}$ , and  $\nu_3 = ^2\text{E}_g \leftarrow ^2\text{B}_{1g}$  in order of increasing energy. These transitions are tentatively labelled as  $(d_z^2 \rightarrow d_{x-y}^2)$ ,  $(d_{xy} \rightarrow d_{x^2-y^2})$  and  $(d_{xz}, d_{yz} \rightarrow d_{x^2-y^2})$  respectively.

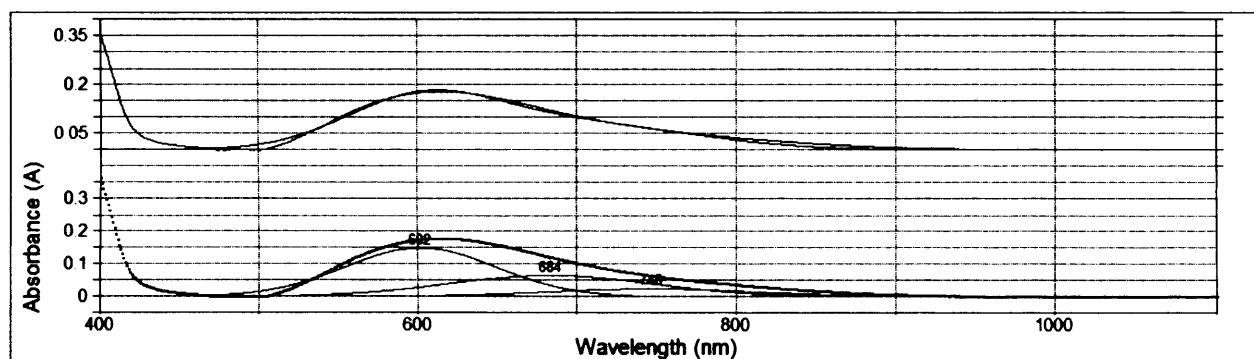
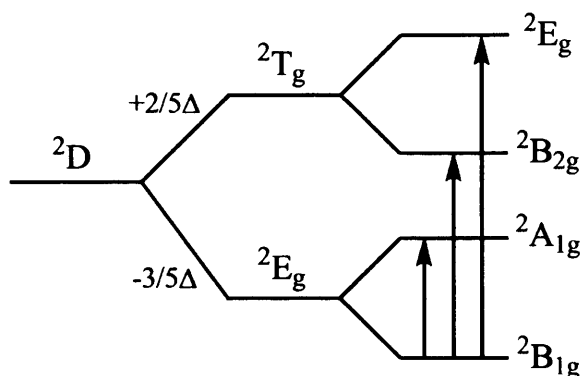


Figure 13: Deconvolution of the electronic spectrum of  $\text{Cu}^{\text{II}}$  compound, **1.5**.





**Figure 14:** A splitting diagram revealing how the Jahn-Teller effect causes the  ${}^2T_g$  and  ${}^2E_g$  term symbols to split, leading to three separate transitions for the  $d^9$  ion.

#### 1.4.6 Electrochemical Studies

The cyclic voltammetry experiments were carried out with an AUTOLAB PGSTAT12 potentiostat in conjunction with General Purpose Electrochemical System software (GPES version 4.7 for Windows) in a specially designed three-electrode glass cell with a Teflon-coated cell cap. A Bioanalytical platinum working electrode (model no. MF2013) with a 1.6 mm disk was used for all experiments. The counter electrode was a platinum wire and the reference electrode a non-aqueous Ag/AgNO<sub>3</sub> electrode. To regain electrochemical sensitivity and reproducibility the working electrode was polished, with 600 grid emery paper, to a mirror surface and then ultrasonicated. Prior to each experiment, the electrode was washed with high performance liquid chromatography (HPLC) grade CH<sub>3</sub>CN and dried in air for about 15 min. A 0.1 M [Bu<sub>4</sub>N][PF<sub>6</sub>] solution in CH<sub>3</sub>CN was used as supporting electrolyte. In all cases, ferrocene was used as an internal reference. Solutions were degassed with nitrogen and a nitrogen atmosphere was maintained over the solution during the experiment.

Chapter 1: Two Bipodal Ligand Frameworks:  
A Structural Exploration *via* X-Ray Diffraction Methods

**Table 3:** Electrochemical parameters for the redox processes exhibited by complexes **1.1**, **1.2**, **1.3**, **1.4** and **1.5** in acetonitrile solution (supporting electrolyte: [Bu<sub>4</sub>N][PF<sub>6</sub>] (0.1 mol dm<sup>-3</sup>); T = 20 °C). Measured at 0.1 Vs<sup>-1</sup>.

Compound	$E_p/V$ ( $\Delta E$ , mV) <sup>a,b</sup>
<b>1.1</b>	-1.027, -1.742, -1.893
<b>1.2</b>	+1.038 (61), -1.027, -2.123, -2.262
<b>1.3</b>	+0.222, -0.695, -1.349, -1.691, -1.843
<b>1.4</b>	-0.886 (80.5), -0.968, -1.522, -1.893, -2.391
<b>1.5</b>	+0.720, -0.358 (101), -1.153, -1.818

<sup>a</sup>The potentials at which reversible processes occur are calculated as the average of the oxidative and reductive peak potentials ( $E_p^{ox} + E_p^{red}$ )/2. <sup>b</sup>For irreversible processes, the anodic or cathodic peak potentials are given. Potentials are given in volts *versus* Ferrocenium/Ferrocene.

The cyclic voltammogram of the manganese compound, **1.1**, reveals an irreversible reduction at a cathodic potential of -1.027 V referenced against ferrocenium/ferrocene (Fc<sup>+</sup>/Fc).<sup>\*</sup> This feature could be attributable to the reduction of the metal centre, thus forming a Mn<sup>I</sup> species. The related compounds [Mn<sup>II</sup>(bipy)<sub>3</sub>]<sup>2+</sup> and [Mn<sup>II</sup>(Ph<sub>2</sub>bipy)<sub>3</sub>]<sup>2+</sup> both undergo metal-based reductions in similar conditions at potentials of -1.314 and -1.228 V (*vs* Ag<sup>+</sup>/Ag) respectively.<sup>80</sup> The redox couples in these examples are fully reversible which conflicts with the irreversible wave process observed in **1.1**, however the aforementioned examples were performed in the presence of excess ligand which can have the effect of inhibiting ligand dissociation and facilitating metal-based electrochemical reversibility. It is also possible that this wave could be attributable to the one-electron reduction of the C=O. For example, Tong *et al.* studied a polynuclear Cu<sup>II</sup> complex containing the similar carbonyl-containing ligand, dpk, and reported a quasi-reversible ligand-based reduction at -1.05 V (*vs* Ag<sup>+</sup>/Ag).<sup>82</sup> Similarly, Bakir and McKenzie studied a Re(I) complex containing dpk which exhibited a reduction at *ca.* -1 V (*vs* Ag<sup>+</sup>/Ag), although in this instance the wave was highly reversible.<sup>83-84</sup> There are two further reductions in the voltammogram of **1.1** which take place at -1.742 V and -1.893 V. These are most likely

<sup>\*</sup> To assist in the comparison of compounds **1.1** – **1.5** to several of the literature compounds mentioned in the discussion, the Fc<sup>+</sup>/Fc couple is 0.40 V *vs* SCE (electrolyte: [Bu<sub>4</sub>N][PF<sub>6</sub>]) and 0.445 V *vs* Ag/AgCl. A useful review by Connelly and Geiger<sup>81</sup> includes a compilation of formal potentials for the Fc<sup>+</sup>/Fc couple *vs* various reference electrodes in selected electrolytes.

associated with the addition of an electron into the low lying unoccupied  $\pi^*$  orbital on each of the bipyridine units.

The voltammogram of the  $\text{Fe}^{\text{II}}$  compound, **1.2**, shows a reversible process attributable to the  $\text{Fe}^{\text{II/III}}$  redox couple. The reversible formal reduction potential ( $E_f^\circ$  - calculated as the average of the oxidative and reductive peak potentials) for the  $\text{Fe}^{\text{II/III}}$  half-cell reaction is located at +1.038 V (*vs*  $\text{Fc}^+/\text{Fc}$ ). The linear relationship between the peak current and the square root of the scan rate (50 – 1000  $\text{mVs}^{-1}$ ) indicates an ideal diffusion controlled response which abides by the Randles-Sevcik equation for a reversible process (Eq. 1).<sup>85-86</sup>

$$i_{p,c} = -2.69 \times 10^5 n^{3/2} A D_0^{1/2} [O]_{\infty} v^{1/2} \quad (1)$$

where  $n$  is the number of transferred electrons,  $A$  is the area of the electrode,  $D_0$  is the diffusion coefficient,  $[O]$  is the analyte concentration, and  $v$  is the scan rate.

The voltammogram also contains a prominent irreversible reduction process in the cathodic region at -1.027 V, which is at the same potential as the irreversible reduction shown in compound **1.1**. It is again reasonable to assume this could be caused by the one-electron reduction of the carbonyl. There are two further reduction processes at -2.123 and -2.262 V which are attributed to bipyridine-based reductions.

The  $\text{Co}^{\text{II}}$  compound, **1.3**, reveals a wave process at +0.241 V which is most likely attributable to the  $\text{Co}^{\text{II/III}}$  redox couple, however it is not well defined. The  $[\text{Co}^{\text{II}}(\text{bipy})_3]^{2+}$  complex exhibits a reversible  $\text{Co}^{\text{II/III}}$  redox couple at +0.2 V (*vs* SCE;  $\text{NEt}_4\text{ClO}_4$  electrolyte in acetonitrile).<sup>87</sup> A wave process at -1.349 V with a peak to peak separation of 101 mV (scan rate: 200  $\text{mVs}^{-1}$ ) is most likely caused by the  $\text{Co}^{\text{III}}$  redox couple. A plot of the square root of the scan rate *versus* the anodic peak height is non-linear and indicates irreversibility. This may be an

indication of ligand dissociation upon reduction to the  $\text{Co}^{\text{I}}$  species. Ligand loss from the similar monocationic species,  $[\text{Co}(\text{bipy})_3]^+$ , has been shown to be facile.<sup>87</sup> There are also two irreversible reductions at -0.695 V and -1.843 V which are likely to be associated with ligand-based processes.

The voltammogram of  $\text{Ni}^{\text{II}}$  compound, **1.4** (Fig. 15), shows a reversible process corresponding to the  $\text{Ni}^{\text{II/III}}$  redox couple located at a formal reduction potential of -0.886 V vs  $\text{Fc}^+/\text{Fc}$ . The peak current was found to be linearly dependant on the square root of the scan rate, as expected for a diffusion-controlled process, while the the ratio  $i_{\text{pa}}/i_{\text{pc}}$  for these peaks is 0.97 confirming that the redox couple is reversible over the scan rate range. This couple is immediately preceded by an oxidation process at -0.968 V (Fig. 15; orange overlay) which is destroyed by the product of an irreversible reduction at -1.522 V and is greatly diminished in the second sweep (Fig. 15; blue overlay). There are two further processes within the scan window; a quasi-reversible reduction at a formal reduction potential of -1.893 V, and an irreversible reduction process at -2.391 V both likely to be associated with the tetradentate ligand.

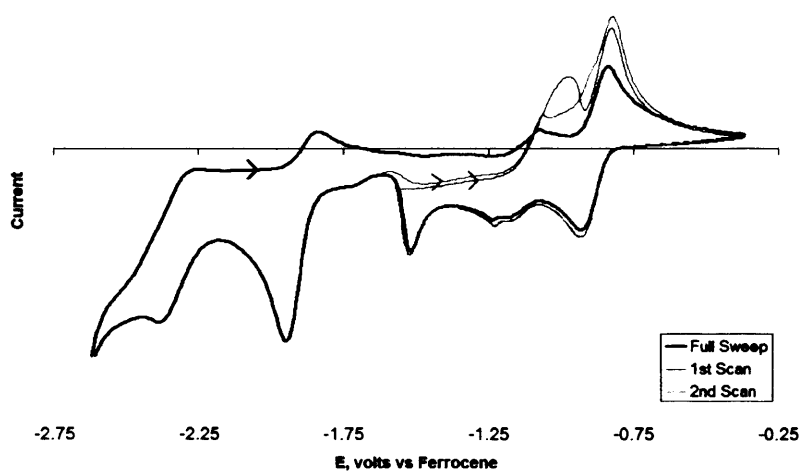


**Figure 15:** Cyclic voltammogram of compound **1.4**. The oxidation process at -0.968 V (orange overlay) is destroyed by an irreversible reduction at -1.522V and is diminished in the second scan (blue overlay).

The voltammogram of Cu<sup>II</sup> compound, **1.5** (Fig. 16), reveals a reversible Cu<sup>III</sup> redox couple centred at -0.358 V. As observed in the voltammogram of **1.4**, this redox couple is in close proximity to an irreversible oxidation process (-0.579 V). In this instance, however, this oxidation appears to be generated by the product of an irreversible reduction process at cathodic potential of -1.153 V. Increasing the scan rate to 300 mVs<sup>-1</sup> also caused the oxidation wave to shift to a more negative potential by *ca.* 0.1 V (Fig 16; blue overlay), this behaviour is typically associated with an irreversible process. Again, this is most likely attributable to a one-electron reduction of the C=O and bypassing this reduction process (Fig. 16; orange overlay) terminates the subsequent oxidation completely. A further irreversible oxidation occurring at +0.720 V also diminishes completely when this reduction is bypassed. A bipy-based redox couple at -1.818 V, with a peak-to-peak separation of 121 mV is also observed corresponding to the addition, and subsequent removal, of an electron from the low lying unoccupied  $\pi^*$  orbital.

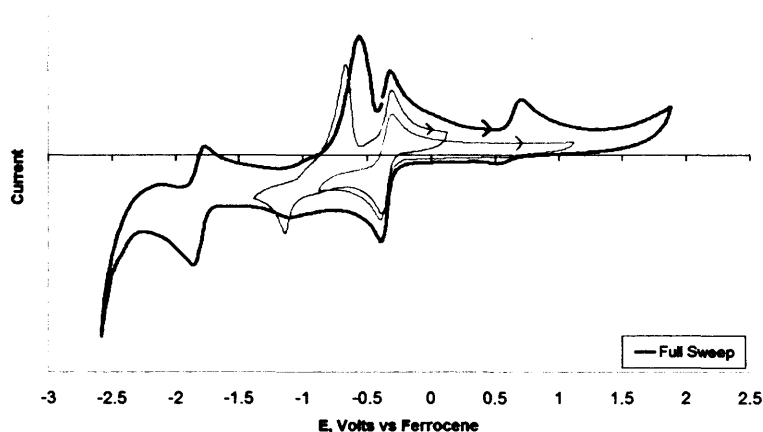


**Figure 16:** Cyclic voltammogram of **1.5**. An irreversible reduction at -1.153 V appears to generate irreversible oxidation processes at -0.579 V and +0.720 V. By-passing this reduction (orange overlay) eliminates both of these oxidations.

### 1.4.7 Crystallographic Studies

All single crystal X-ray data was collected at 150 K on a Bruker/Nonius Kappa CCD diffractometer using graphite monochromated Mo-K $\alpha$  radiation ( $\lambda = 0.71073 \text{ \AA}$ ), equipped with an Oxford Cryostream cooling apparatus. Crystal parameters and details of the data collection, solution and refinement are presented in Table 4. The data was corrected for Lorentz and polarisation effects and for absorption using SORTAV.<sup>88</sup> Structure solution was achieved by direct methods (Sir-92 program system<sup>89</sup>) and refined by full-matrix least-squares on F<sup>2</sup> (SHELXL-97<sup>90</sup>) with all non-hydrogen atoms assigned anisotropic displacement parameters. Hydrogen atoms attached to carbon atoms were placed in idealised positions and allowed to ride on the relevant carbon atom. In the final cycles of refinement, a weighting scheme that gave a relatively flat analysis of variance was introduced and refinement continued until convergence was reached. Molecular structures in the figures were drawn with ORTEP 3.0 for Windows (version 1.08).<sup>91</sup>

**Table 4: Crystal Structure Data for 1.1 – 1.9**

Complex	Chemical formula	Mr. g mol	Crystal system	Space group	T(K)	a, Å	b, Å	c, Å	$\alpha$ , deg	$\beta$ , deg	$\gamma$ , deg	V, Å <sup>3</sup>	Z	D <sub>c</sub> , Mg/m <sup>3</sup>	$\mu$ (Mo K $\alpha$ ), mm <sup>-1</sup>	Observed Reflections	Unique Reflections	R <sub>int</sub>	R <sub>1</sub> [I>2 $\sigma$ (I)]	wR <sub>2</sub> (all data)
1.1	C <sub>21</sub> H <sub>14</sub> Cl <sub>2</sub> MnN <sub>4</sub> O <sub>9</sub>	592.2	Monoclinic	P12/c	150(2)	12.4434(4)	12.9901(4)	14.1014(5)	90	104.5880(10)	90	2205.88(13)	4	1.783	0.906	4982	16314	0.0706	0.0455	0.1196
1.2	C <sub>44</sub> H <sub>34</sub> Cl <sub>2</sub> Fe <sub>2</sub> N <sub>6</sub> O <sub>12</sub>	1049.39	Orthorhombic	P c 21 b	150(2)	10.9746(2)	15.6196(3)	24.5741(5)	90	90	90	4212.46	4	1.655	0.894	7923	30798	0.0749	0.0566	0.1431
1.3	CoC <sub>21</sub> H <sub>14</sub> C <sub>12</sub> N <sub>4</sub> O <sub>11</sub>	628.19	Orthorhombic	Pbca	150(2)	11.3538(3)	15.1853(5)	29.0604(8)	90	90	90	5010.3(3)	8	1.666	0.966	5707	20942	0.1389	0.0844	0.2828
1.4	C <sub>21</sub> H <sub>18</sub> C <sub>12</sub> N <sub>4</sub> NiO <sub>11</sub>	632	Orthorhombic	Pccn	150(2)	9.802(2)	12.453(3)	19.760(4)	90	90	90	2412.1(8)	4	1.74	1.097	2755	10140	0.0909	0.0465	0.1059
1.5	C <sub>21</sub> H <sub>14</sub> Cl <sub>2</sub> CuN <sub>4</sub> O <sub>9</sub>	600.8	Triclinic	P-1	150(2)	9.4710(3)	9.9530(3)	12.4610(5)	71.2520(10)	80.9860(10)	78.4190(10)	1084.28(6)	2	1.84	1.32	4419	15393	0.0859	0.0487	0.1115
1.6	C <sub>21</sub> H <sub>18</sub> Cl <sub>2</sub> ZnN <sub>4</sub> O <sub>11</sub>	638.66	Orthorhombic	Pccn	150(2)	9.8506(3)	12.4696(4)	19.7856(6)	90	90	90	2430.33(13)	4	1.7545	1.301	2758	8971	0.0473	0.0394	0.0956
1.7	C <sub>48</sub> H <sub>44</sub> Cl <sub>2</sub> N <sub>6</sub> O <sub>14</sub> Zn <sub>2</sub>	1158.59	Monoclinic	P 21/n	100(2)	9.515(2)	15.661(3)	15.612(3)	90	103.87(3)	90	2258.6(8)	4	1.704	1.263	4291	17542	0.0204	0.0461	0.1176
1.8	C <sub>23</sub> H <sub>20</sub> CdCl <sub>2</sub> N <sub>6</sub> O <sub>9</sub>	731.77	Monoclinic	P21/n	150(2)	7.29700(10)	15.3263(3)	25.3479(5)	90	91.6780(10)	90	2833.59(9)	4	1.715	1.023	6451	23459	0.074	0.054	0.1525
1.9	C <sub>43</sub> H <sub>34</sub> Cl <sub>4</sub> Cu <sub>2</sub> N <sub>12</sub> O <sub>17</sub>	1263.75	Monoclinic	C 2/c	150(2)	21.3400(5)	14.0040(4)	18.3680(5)	90	106.575(1)	90	5261.1(2)	4	1.595	1.093	5341	17045	0.044	0.0568	0.1389

### 1.4.7.1 Crystal Structure of $[\text{Mn}^{\text{II}}(\text{L}^1)(\text{ClO}_4)_2]$ (1.1)

The manganese compound crystallises in the monoclinic space group  $P2_1/c$  with four molecules in the unit cell. The  $\text{Mn}^{\text{II}}$  ion lies at the centre of a slightly distorted octahedral co-ordination geometry and is surrounded by two types of donor atom. There are four pyridyl N-donors (N1, N2, N3 and N4) originating from the bipyridine-based ligand which all occupy equatorial positions within the octahedron, and two oxygen donors (O2 and O6) in axial positions located on two perchlorate counterions within the asymmetric unit (Fig. 17).

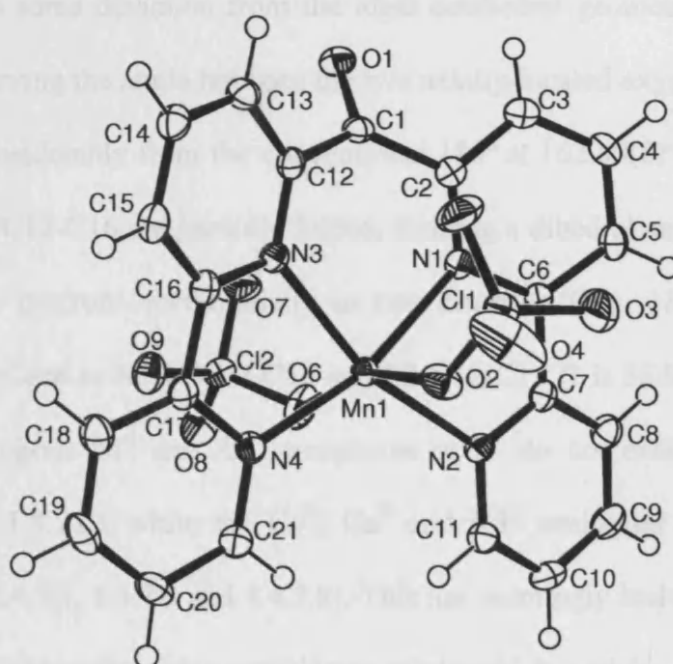


**Figure 17:** Perspective view of the asymmetric unit of **1.1** showing the atom numbering. Displacement ellipsoids are shown at the 50% probability level. H atoms are represented by circles of arbitrary size.

The N-donors located on each of the pyridines which are adjacent to the linking ketone group (N1/C2-C6 and N3/C12-C16) display significantly longer co-ordinative bonds (2.222(2) Å and 2.216(2) Å) to the manganese compared to the pyridine N-donors on the more distant adjoining pyridines (2.190(2) Å and 2.175(2) Å). The latter pair of these bond lengths are slightly shorter on comparison to the  $\text{Mn}^{\text{II}}\text{-N}(\text{bipy})$  bond lengths of structurally similar



complexes. For example, the related compound, aqua-bis(2,2'-bipyridine)-(perchlorato)-manganese(II) perchlorate synthesised by Ruiz-Perez *et al.*<sup>92</sup> comprises of a Mn<sup>II</sup> ion being co-ordinated by four pyridyl N-donors which range between 2.222(5) Å and 2.228(5) Å. The angle between the lines defined as C3-C6 and C7-C10 on one bipyridine group is 3.77(7)°, indicating a small amount of strain on C6-C7. The equivalent line angle on the other bipy unit is again small at 4.92(8)°.

The axially located oxygen donor atoms lie at slightly longer distances (2.2568(19) Å and 2.246(2) Å). There is some deviation from the ideal octahedral geometry, this is most clearly distinguished by observing the angle between the two axially-located oxygen atoms O(2)-Mn(1)-O(6) which varies considerably from the conventional 180° at 162.50(8)°. This is not surprising as N1/C2-C6 and N3/C12-C16 are partially folded, forming a dihedral angle of 33.31(12)°. This causes the ketone to protrude preferentially in one direction (Fig. 18). The dihedral angle between the planes defined as N1-N3-C2-C12 and C2-C12-C1-O1 is 35.81(16)°. It is interesting to note that the analogous Ni<sup>II</sup> and Zn<sup>II</sup> complexes of L<sup>1</sup> do not exhibit this behaviour (*cf.* Sections 1.4.7.4 and 1.4.7.6), while the Co<sup>II</sup>, Cu<sup>II</sup> and Cd<sup>II</sup> analogues do, albeit to differing extents (*cf.* Sections 1.4.7.3, 1.4.7.5 and 1.4.7.8). This has seemingly had a direct affect upon the co-ordination angle of the approaching perchlorate anions which explains why the angle between the two axial donors is significantly less obtuse than expected.

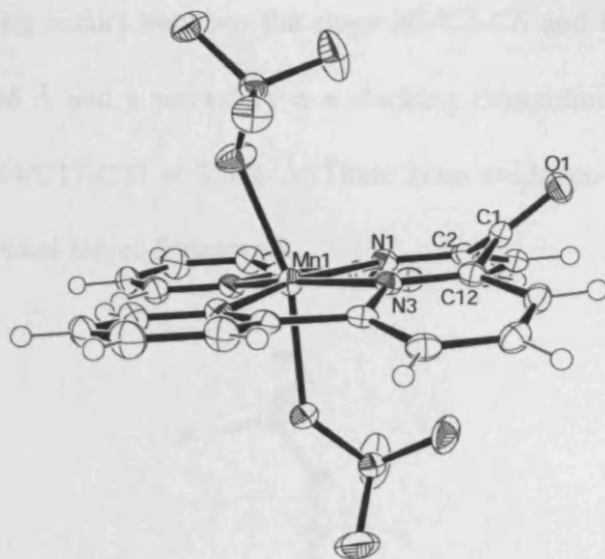


**Fig 18:** A view showing how the ketone group protrudes outwards in one direction. The dihedral angle between the planes defined as N1-N3-C2-C12 and C2-C12-C1-O1 is 35.81(16)°.

Whilst the furthest two pyridine rings from the ketone group lie virtually on the same plane forming a dihedral angle between both ring systems of 4.76(13)°, the closest two pyridine rings are tilted in opposing directions with a dihedral angle of 33.31(12)°. It is also worth noting the dihedral angles between each pair of pyridines belonging to the same bipyridyl unit (20.15(13)° and 17.69(13)°; Fig. 19) as this highlights the extent of the deviation away from planarity for this particular ligand which is quite surprising on comparison to other first row transition metal complexes. This may reflect the larger covalent radius of Mn<sup>II</sup> compared to later transition metals.

There are several examples of crystallographically characterised co-ordination spheres involving two bipyridine groups around a manganese centre. A search of the Cambridge Structural Database (CSD)<sup>93</sup> using Conquest<sup>94</sup> results in 92 hits for such criteria (Date: 09/2008). However, **1.1** presents a novel situation where the two bipyridine groups are co-planar occupying equatorial positions. The molecular packing (Fig. 20) is supported by intermolecular  $\pi$ - $\pi$  stacking between overlapping bipyridyl groups which are arranged into chains which run parallel

to the b-axis. The stacking occurs between the rings N1/C2-C6 and N2/C7-C11 at a centroid-centroid distance of 3.556 Å and a secondary  $\pi$ - $\pi$  stacking interaction also occurs between the rings N3/C12-C16 and N4/C17-C21 at 3.626 Å. There is no evidence of any hydrogen bonding interactions within the crystal lattice framework.

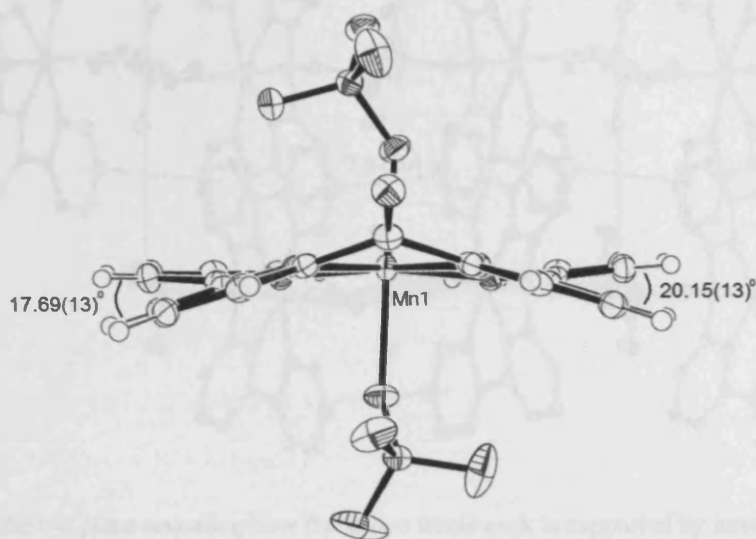


**Figure 19:** An alternative view of compound **1.1**, illustrating the twist (dihedral angles) between the pyridyl units of each bipyridine group.

**Table 5:** Significant Bond lengths (Å) and Angles (°) for  $[\text{Mn}^{\text{II}}(\text{L}^1)(\text{ClO}_4)_2]$

C(2)-C(1)-C(12)	123.9(2)	C(2)-C(1)-O(1)	117.8(2)
C(12)-C(1)-O(1)	118.0(2)		
Mn(1)-N(1)	2.216(2)	Mn(1)-N(2)	2.190(2)
Mn(1)-N(3)	2.222(2)	Mn(1)-N(4)	2.174(2)
Mn(1)-O(2)	2.2568(19)	Mn(1)-O(6)	2.246(2)
N(4)-Mn(1)-N(2)	119.24(9)	N(4)-Mn(1)-N(1)	163.34(8)
N(2)-Mn(1)-N(1)	76.58(8)	N(4)-Mn(1)-N(3)	76.10(8)
N(2)-Mn(1)-N(3)	163.42(8)	N(1)-Mn(1)-N(3)	87.63(8)
N(4)-Mn(1)-O(6)	88.93(8)	N(2)-Mn(1)-O(6)	82.55(7)
N(1)-Mn(1)-O(6)	98.93(8)	N(3)-Mn(1)-O(6)	105.21(7)
N(4)-Mn(1)-O(2)	83.65(7)	N(2)-Mn(1)-O(2)	87.28(7)
N(1)-Mn(1)-O(2)	92.47(7)	N(3)-Mn(1)-O(2)	88.40(7)
O(6)-Mn(1)-O(2)	162.50(8)		

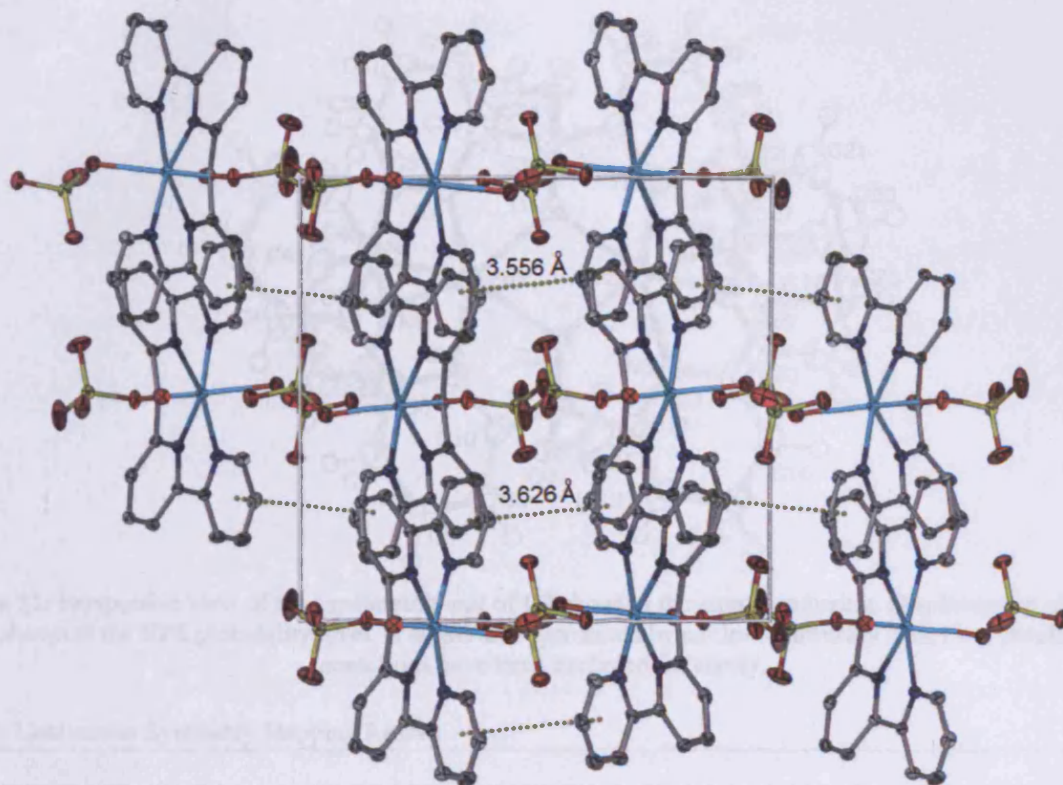


**Figure 20:** A view of the b-c plane revealing how the lattice framework is supported by intermolecular  $\pi$ - $\pi$  stacking interactions (dotted lines). Hydrogen atoms are omitted for clarity.

#### 1.4.7.2 Crystal Structure of $[\text{Fe}_2(\text{L}^1\text{-OCH}_3)_2][\text{ClO}_4]_2$ (1.2)

The compound crystallises in the orthorhombic space group  $\text{Pc}2_1\text{b}$  with eight molecules in the unit cell. The dinuclear complex exhibits a diamond core in which two divalent iron cations are bridged by the negatively charged oxygen from the deprotonated hydroxy groups. The coordination sphere of each  $\text{Fe}^{\text{II}}$  cation is completed four pyridyl nitrogen donors belonging to two bipyridyl units which reside on separate ligands. Symmetry mapping calculations\* indicate that both of these  $\text{Fe}^{\text{II}}$  cations are situated at the centre of predominantly octahedral geometries, albeit those which are significantly distorted (Fig. 21; Table 6).

\* Symmetry mapping is discussed in greater detail in Section 2.2

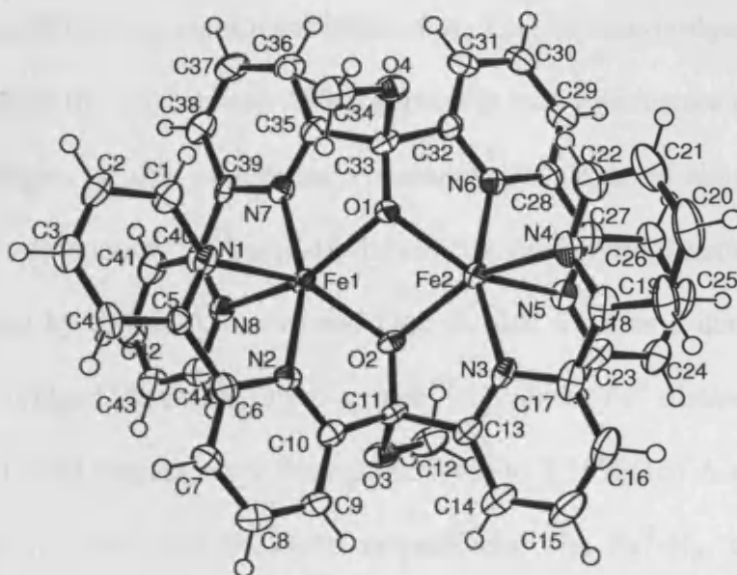


**Figure 21:** Perspective view of the asymmetric unit of **1.2** showing the atom numbering. Displacement ellipsoids are shown at the 50% probability level. H atoms are represented by circles of arbitrary size. Four perchlorate counterions have been excluded for clarity.

**Table 6:** Continuous Symmetry Mapping Results

	HP	PPY	OC	TP	JPPY
<b>Fe1</b>	28.39936	14.44253	6.57888	8.50791	17.90031
<b>Fe2</b>	27.72722	13.24791	7.38089	7.87865	16.62363

HP: Hexagon ( $D_{6h}$ ), PPY: Pentagonal pyramid ( $C_{5v}$ ), OC: Octahedron ( $O_h$ ), TP: Trigonal Pyramidal ( $D_{3h}$ ), JPPY: Johnson's pentagonal pyramid J2 ( $C_{5v}$ ).

The N-donors located on the pyridyl groups closest to the hemiketal moieties (N2, N3, N6 and N7) display significantly shorter co-ordinative bond lengths ( $Fe^{II}-N_{av} = 2.093 \text{ \AA}$ ) compared to the N-donors (N1, N4, N5 and N8) located on the furthest lying pyridyl groups ( $Fe^{II}-N_{av} = 2.233 \text{ \AA}$ ). This is most likely caused by the  $sp^3$  hybridisation of carbon atoms C11 and C33 which restrains the immediately adjacent pyridyl rings, preventing them from adopting more protracted distances. The bridging oxygen atoms, O1 and O2, lie equidistant between each  $Fe^{II}$  ion and reveal co-ordinative bond lengths ranging from 2.078(3)  $\text{\AA}$  to 2.087(3)  $\text{\AA}$ . The Fe1-O1-Fe2 and Fe1-O2-Fe2 bond angles are 98.51(13) $^\circ$  and 98.72(13) $^\circ$  respectively, while the O1-Fe1-O2 and O1-Fe2-O2 angles are 81.37(13) $^\circ$  and 81.38(12) $^\circ$ . The  $Fe^{II}\cdots Fe^{II}$  distance is

3.1594(10) Å which indicates no significant interaction. This oxygen-bridged dinuclear moiety is not rare and a search of the CSD reveals 693 compounds with this feature (Date: 12/2008). The bond lengths and angles of this moiety are comparable to those of similar compounds. For instance, the compound bis( $\mu_2$ -Hydroxo)-bis(tris(2-pyridylmethyl)amine)-di-iron(II) diperchlorate reported by Rybak-Akimova and Que Jr. also features a diamond core in which two Fe<sup>II</sup> centres are bridged via two hydroxo groups.<sup>95</sup> The Fe<sup>II</sup>...Fe<sup>II</sup> distance in this example is 3.087 Å. The Fe<sup>II</sup>-O bond lengths range from 2.0059(15) to 2.1595(16) Å and the angles Fe-O-Fe and O-Fe-O are 95.57(6)° and 84.43(6)° respectively. The Fe<sup>II</sup>-N<sub>py</sub> bond lengths in this example range from 2.191(2) to 2.235(2) Å which also agrees well with the pyridyl groups lying furthest from the hemiketal moieties in compound **1.2**, however as expected they are significantly longer than the pyridyl groups lying adjacent to the hemiketal moieties.

The molecular packing is arranged into parallel regions of complexes which are interspaced with perchlorate counterions which occupy the empty space between the rows which run parallel to the b-axis of the unit cell (Fig. 22).

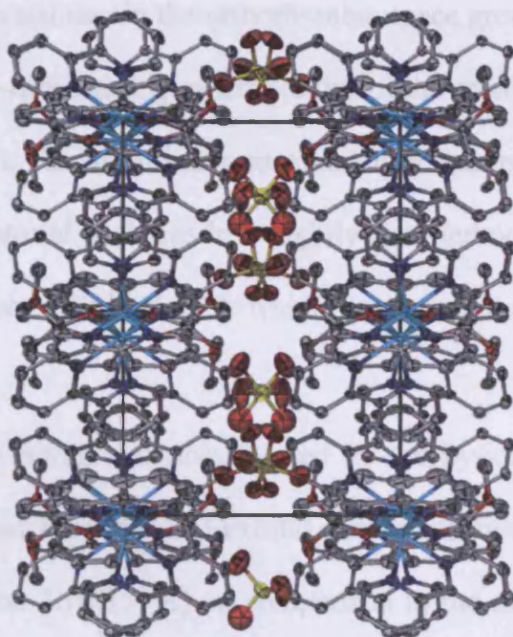


**Figure 22:** A view of the a-b plane, showing how the perchlorate counterions are sandwiched between rows of complexes which run parallel to the b-axis. Hydrogen atoms are omitted for clarity.

Chapter 1: Two Bipodal Ligand Frameworks:  
A Structural Exploration *via* X-Ray Diffraction Methods

**Table 7:** Significant Bond lengths (Å) and Angles (°) for  $[\text{Fe}_2(\text{L}^1\cdot\text{OCH}_3)_2][\text{ClO}_4]_2$

Fe(1)-Fe(2)	3.087		
Fe(1)-O(1)	2.082(3)	Fe(1)-O(2)	2.085(3)
Fe(2)-O(1)	2.087(3)	Fe(2)-O(2)	2.078(3)
Fe(1)-N(1)	2.243(5)	Fe(1)-N(2)	2.090(4)
Fe(2)-N(3)	2.082(4)	Fe(2)-N(4)	2.202(4)
Fe(2)-N(5)	2.269(5)	Fe(2)-N(6)	2.098(4)
Fe(1)-N(7)	2.100(4)	Fe(1)-N(8)	2.216(4)
N(3)-Fe(2)-N(4)	74.40(16)	O(1)-Fe(2)-N(4)	104.51(16)
O(1)-Fe(1)-O(2)	81.35(13)	O(1)-Fe(1)-N(2)	119.26(15)
O(2)-Fe(1)-N(2)	76.28(15)	O(1)-Fe(1)-N(7)	76.01(14)
N(2)-Fe(1)-N(7)	161.00(17)	O(2)-Fe(1)-N(7)	119.39(17)
O(1)-Fe(1)-N(8)	148.26(16)	O(2)-Fe(1)-N(8)	103.52(15)
N(2)-Fe(1)-N(8)	92.12(16)	N(7)-Fe(1)-N(8)	74.40(15)
O(1)-Fe(1)-N(1)	106.63(15)	O(2)-Fe(1)-N(1)	149.42(15)
N(2)-Fe(1)-N(1)	74.14(16)	N(7)-Fe(1)-N(1)	91.14(17)
N(8)-Fe(1)-N(1)	85.23(17)	O(2)-Fe(2)-N(3)	76.02(15)
O(2)-Fe(2)-O(1)	81.38(12)	N(3)-Fe(2)-O(1)	124.01(16)
O(2)-Fe(2)-N(6)	121.23(15)	N(3)-Fe(2)-N(6)	157.23(16)
O(1)-Fe(2)-N(6)	76.04(15)	O(2)-Fe(2)-N(4)	147.54(17)
N(6)-Fe(2)-N(4)	90.94(17)	O(2)-Fe(2)-N(5)	106.71(15)
N(3)-Fe(2)-N(5)	87.55(17)	O(1)-Fe(2)-N(5)	148.33(16)
N(6)-Fe(2)-N(5)	73.69(16)	N(4)-Fe(2)-N(5)	85.15(17)

#### 1.4.7.3 Crystal Structure of $[\text{Co}^{\text{II}}(\text{L}^1)(\text{H}_2\text{O})_2][\text{ClO}_4]_2$ (1.3)

The cobalt complex, **1.3**, crystallises in the orthorhombic space group *Pbca* with eight molecules in the unit cell. A similar co-ordination geometry to that of the analogous  $\text{Mn}^{\text{II}}$ ,  $\text{Ni}^{\text{II}}$ ,  $\text{Cu}^{\text{II}}$  and  $\text{Zn}^{\text{II}}$  complexes of  $\text{L}^1$  is observed. The metal ion is surrounded by four pyridyl N-donors (N1, N2, N3 and N4) which occupy equatorial positions in a slightly distorted octahedral geometry. The axial sites contain oxygen donors (O2 and O3) which are located on two co-ordinating water molecules (Fig. 23).

In this instance, the nitrogen donors located on the pyridines which lie closest to the ketone group (N1/C2-C6 and N3/C12-C16) exhibit almost identical co-ordinative bond lengths to the cobalt (2.097(5) Å and 2.107(5) Å) on comparison to the nitrogen donors located on the more distant adjoining pyridines (2.130(5) Å and 2.122(6) Å).

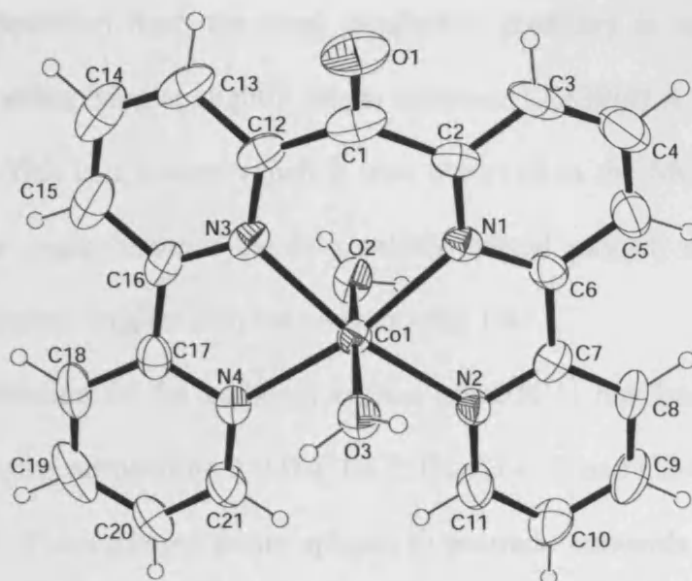


**Figure 23:** Perspective view of the asymmetric unit of **1.3** showing the atom numbering. Displacement ellipsoids are shown at the 30% probability level. H atoms are represented by circles of arbitrary size. Two perchlorate counterions have been excluded for clarity.

It is worth noting that the analogous Ni<sup>II</sup> and Cu<sup>II</sup> complexes of L<sup>1</sup> exhibit co-ordination environments in which the nitrogen donors located closest to the ketone group display significantly shorter co-ordinative bond lengths on comparison to the more distal nitrogen donors. In contrast, the Mn<sup>II</sup>, Zn<sup>II</sup> and Cd<sup>II</sup> complexes all display the shortest bonds from the pyridyl N-donors lying furthest from the ketone group.

The co-ordinative bond lengths observed in compound **1.3** are significantly longer compared to those of related Co<sup>II</sup> complexes which contain sterically unrestricted bipyridyl N-donors. For example, the compound bis(2,2'-bipyridine)-(nitrate)-cobalt(II) synthesised by Atencio *et al.* features (pyridyl)-N-Co<sup>II</sup> bond lengths ranging from 1.925(5) to 1.938(6) Å.<sup>96</sup> There are 155 similar examples of crystallographically characterised co-ordination spheres involving two bipyridine groups co-ordinating to a cobalt centre within the CSD (Date: 09/2008). However, compound **1.3** presents a novel situation in which two bipyridine groups are co-planar, occupying equatorial positions.



## Chapter 1: Two Bipodal Ligand Frameworks: A Structural Exploration *via* X-Ray Diffraction Methods

A significant deviation from the ideal octahedral geometry is caused by the axially located oxygen donor atoms lying at slightly longer distances (2.139(4) Å and 2.102(4) Å) than the pyridyl N-donors. This is a feature which is also observed in the Mn<sup>II</sup>, Ni<sup>II</sup>, Cu<sup>II</sup> and Zn<sup>II</sup> complexes of L<sup>1</sup>. The angle between the two axially-located oxygen atoms O2-Co1-O3 is 172.36(19)° which is slightly smaller than the conventional 180°.

The sp<sup>2</sup> hybridisation of the carbonyl carbon atom (C1) has been confirmed by the examining the three angles surrounding it (O1-C1-C2, O1-C1-C12 and C2-C1-C12), the average of which is 119.97(7)°. This carbonyl group appears to protrude outwards preferentially in one direction, *i.e.* the dihedral angle between the planes N1-N3-C2-C12 and C2-C12-C1-O1 is 20.4(4)°. This is a feature which has also been observed in the analogous Mn<sup>II</sup>, Cu<sup>II</sup> and Cd<sup>II</sup> complexes and is a direct result of the complex partially folding. The pyridyl rings closest to the carbonyl group (N1/C2-C6 and N3/C12-C16) are more acutely folded than the more distant pyridyl rings (N2/C7-C11 and N4/C17-C21), forming dihedral angles of 23.8(4)° and 15.2(4)° respectively. The line angle between C3-C6 and C7-C10 is 9.2(2)° and the line angle between C13-C16 and C17-C20 is 6.5(3)°. These values suggest a degree of strain on the bipyridine units.

The molecular packing (Fig. 24) is supported by hydrogen bonding interactions between the perchlorate counterions and the co-ordinating water molecules. (Table 9; Fig. 24). There are no  $\pi$ - $\pi$  stacking interactions observed in the molecular packing.

**Table 8:** Significant Bond lengths (Å) and Angles (°) for  $[\text{Co}^{\text{II}}(\text{L}^1)(\text{H}_2\text{O})_2][\text{ClO}_4]_2$

C(2)-C(1)-C(12)	127.4(6)	C(2)-C(1)-O(1)	116.2(8)
C(12)-C(1)-O(1)	116.3(8)		
Co(1)-N(1)	2.097(5)	Co(1)-N(2)	2.130(5)
Co(1)-N(3)	2.107(5)	Co(1)-N(4)	2.122(6)
Co(1)-O(2)	2.139(4)	Co(1)-O(3)	2.102(4)
N(1)-Co(1)-O(3)	94.38(19)	N(1)-Co(1)-N(3)	91.7(2)
O(3)-Co(1)-N(3)	97.64(18)	N(1)-Co(1)-N(4)	168.9(2)
O(3)-Co(1)-N(4)	90.9(2)	N(3)-Co(1)-N(4)	78.0(2)
N(1)-Co(1)-N(2)	78.3(2)	O(3)-Co(1)-N(2)	88.86(19)
N(3)-Co(1)-N(2)	168.5(2)	N(4)-Co(1)-N(2)	111.6(2)
N(1)-Co(1)-O(2)	90.05(19)	O(3)-Co(1)-O(2)	172.36(19)

**Table 9:** H-bonding geometry (Å, °) for 1.3

D-H...A	d(D-H)	d(H...A)	d(D...A)	<(DHA)
O(2)-H(2A)...O(10)#1	0.86	2.23	2.875(15)	132
O(2)-H(2B)...O(9)	0.86	2.09	2.856(15)	149
O(3)-H(3A)...O(5)#2	0.86	2.27	2.963(9)	138
O(3)-H(3B)...O(4)	0.86	2.17	2.738(8)	124

Symmetry transformations used to generate equivalent atoms:

#1  $\frac{1}{2}+x, \frac{1}{2}-y, -z$ . #2  $\frac{1}{2}+x, y, \frac{1}{2}-z$ .

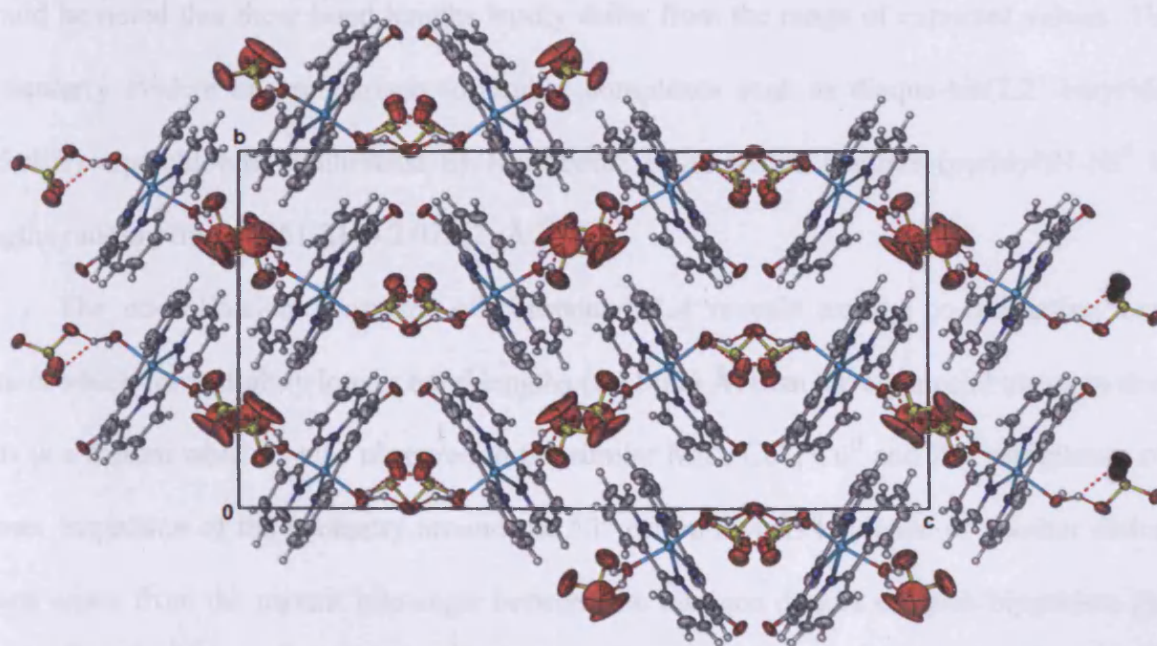


**Figure 24:** A view of the bc plane showing the intermolecular H-bonding interactions supporting the lattice framework.

#### 1.4.7.4 Crystal Structure of $[\text{Ni}^{\text{II}}(\text{L}^1)(\text{H}_2\text{O})_2][\text{ClO}_4]_2$ (1.4)

The nickel compound **1.4** crystallises in the orthorhombic Pccn space group with four independent molecules in the unit cell. The slightly distorted octahedral co-ordination environment is similar to the analogous  $\text{Mn}^{\text{II}}$ ,  $\text{Co}^{\text{II}}$ ,  $\text{Cu}^{\text{II}}$  and  $\text{Zn}^{\text{II}}$  complexes of  $\text{L}^1$ . The  $\text{Ni}^{\text{II}}$  cation is co-ordinated by four equatorial pyridyl N-donors and two axial oxygen donors (O1 and O1A) which in this instance are located on co-ordinating water molecules (Fig. 25). The asymmetric unit contains only half of the complex, the other half is generated *via* the symmetry operator  $[1/2-x, 3/2-y, z]$ .

The  $\text{Ni}^{\text{II}}$ -N bond lengths range from 2.042(2) Å to 2.064(2) Å. This complex resembles the analogous  $\text{Cu}^{\text{II}}$  complex in which the shortest co-ordinative bonds originate from the two pyridines which lie closest to the linking ketone group (N1/C2-C6). Whilst there is a noticeable difference between the co-ordinative bond lengths of the two pyridines on each bipyridyl arm, it should be noted that these bond lengths hardly differ from the range of expected values. This is particularly evident on comparison to similar complexes such as diaqua-bis(2,2'-bipyridine)-nickel(II) diperchlorate synthesised by Ruiz-Perez *et al.* which features (pyridyl)N- $\text{Ni}^{\text{II}}$  bond lengths ranging from 2.061(2) to 2.075(2) Å.<sup>97</sup>

The co-ordination geometry of compound **1.4** reveals axially co-ordinating oxygen donors which form slightly longer bond lengths (2.111(2) Å) than the equatorial nitrogen donors. This is a feature which is also observed in the similar  $\text{Mn}^{\text{II}}$ ,  $\text{Co}^{\text{II}}$ ,  $\text{Cu}^{\text{II}}$  and  $\text{Zn}^{\text{II}}$  complexes of  $\text{L}^1$ . Closer inspection of the geometry around the  $\text{Ni}^{\text{II}}$  cation reveals evidence of another distortion which arises from the narrow bite angle between the nitrogen donors on each bipyridine group. This is evident in the most extreme case N(1)-Ni(1)-N(2) (80.51(9)°). Furthermore, the angle between the two axial groups varies slightly from the conventional 180° at a modestly less obtuse 175.47(10)°.

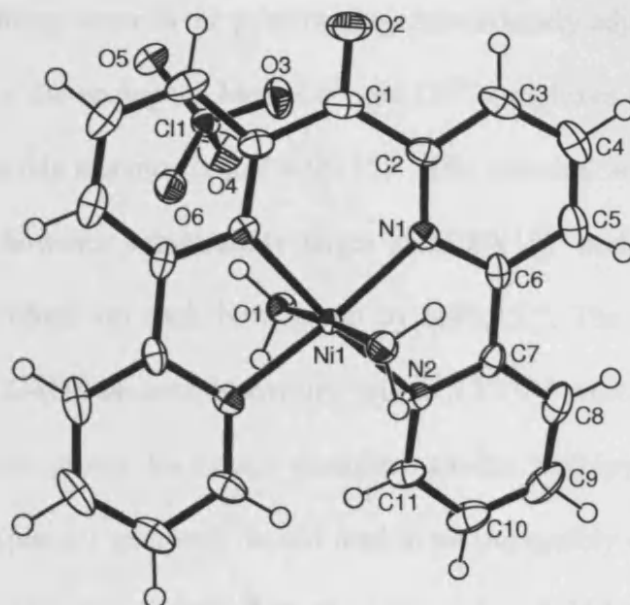


**Figure 25:** Perspective view of the asymmetric unit of **1.4**, expanded to complete the Ni co-ordination, showing the atom numbering. Displacement ellipsoids are shown at the 50% probability level. H atoms are represented by circles of arbitrary size. [Symmetry code: (i)  $1/2-x, 3/2-y, z$ .]

**Table 10:** Significant Bond lengths (Å) and Angles (°) for  $[\text{Ni}^{\text{II}}(\text{L}^1)(\text{H}_2\text{O})_2][\text{ClO}_4]_2$

C(2)-C(1)-C(2)#1	126.4(3)	C(2)-C(1)-O(2)	116.81(17)
Ni(1)-N(1)	2.042(2)	Ni(1)-N(1)#1	2.042(2)
Ni(1)-N(2)#1	2.064(2)	Ni(1)-N(2)	2.064(2)
Ni(1)-O(1)#1	2.111(2)	Ni(1)-O(1)	2.111(2)
N(1)-Ni(1)-N(1)#1	92.97(13)	N(1)-Ni(1)-N(2)#1	170.37(9)
N(1)#1-Ni(1)-N(2)#	180.51(9)	N(1)-Ni(1)-N(2)	80.51(9)
N(1)#1-Ni(1)-N(2)	170.37(9)	N(2)#1-Ni(1)-N(2)	106.81(13)
N(1)-Ni(1)-O(1)#1	88.05(8)	N(1)#1-Ni(1)-O(1)#1	95.07(8)
N(2)#1-Ni(1)-O(1)#1	85.50(9)	N(2)-Ni(1)-O(1)#1	91.80(9)
N(1)-Ni(1)-O(1)	95.07(8)	N(1)#1-Ni(1)-O(1)	88.05(8)
N(2)#1-Ni(1)-O(1)	91.80(9)	N(2)-Ni(1)-O(1)	85.50(9)
O(1)#1-Ni(1)-O(1)	175.47(10)		

Symmetry transformations used to generate equivalent atoms:

#1  $-x+1/2, -y+3/2, z$

The ketone in this instance clearly lies along the same plane as the two bipyridines, the dihedral angle between the planes defined by  $\text{N1-N1}'\text{-C2-C2}'$  and  $\text{C2-C2}'\text{-C1-O2}$  is just  $2.16(15)^\circ$ . Interestingly, this is statistically identical to the corresponding angle in the  $\text{Zn}^{\text{II}}$  complex, **1.6**, which is  $2.24(14)^\circ$ . Another similarity between these complexes is that there is a

far smaller degree of folding between the pyridine rings immediately adjacent to the ketone group (N1/C2-C6) compared to the analogous Mn<sup>II</sup>, Co<sup>II</sup> and Cu<sup>II</sup> complexes of L<sup>1</sup>. The dihedral angle between these planes in this instance is just 8.95(15)°. The dihedral angle between the furthest lying pyridine rings is however substantially larger at 21.89(15)° and this disparity leads to a twisting of the two pyridines on each bipy group by 6.86(15)°. The angle between the lines defined as C3-C6 and C7-C10 on each bipyridine unit is 9.23(9)° which also indicates a degree of strain on the bipyridine group. McKenzie examined similar bis(bipyridyl) metal compounds and stated that a *trans* (planar) geometry would lead to an impossibly close approach of the  $\alpha$ -hydrogen atoms on the opposing ligands.<sup>98</sup> Such compounds would have to distort in order to relieve this steric strain and it is very likely this which causes the ligand distortions observed in this compound.

The molecular packing (Fig. 26) is arranged with chains of complexes running parallel to the b-axis. These chains are connected *via* hydrogen bonding involving both sets of protons on each axially located water molecule (Table 10). The hydrogen bonding (Table 11) occurs between the oxygen atoms O4 and O6 belonging to the same perchlorate counterion and the protons of the axial water molecules H1A and H1B which are located on a complex above and below the counterion respectively. The lattice is also supported by intermolecular  $\pi$ - $\pi$  stacking interactions between N1/C2-C6 and N2/C7-C11 (centroid-centroid distance = 3.934 Å), the latter of which is located on a symmetry generated complex (symmetry code: 1 - x, 2 - y, - z).

**Table 11:** H-bonding geometry (Å, °) for 1.4

<i>D</i> -H... <i>A</i>	<i>D</i> -H	H... <i>A</i>	<i>D</i> ... <i>A</i>	<i>D</i> -H... <i>A</i>
O(1)-H(1)...O(6)	0.95	1.82	2.767(3)	171
O(1)-H(2)...O(4)#1	0.95	1.99	2.929(3)	169

Symmetry Code: #1 = -x, 2-y, -z

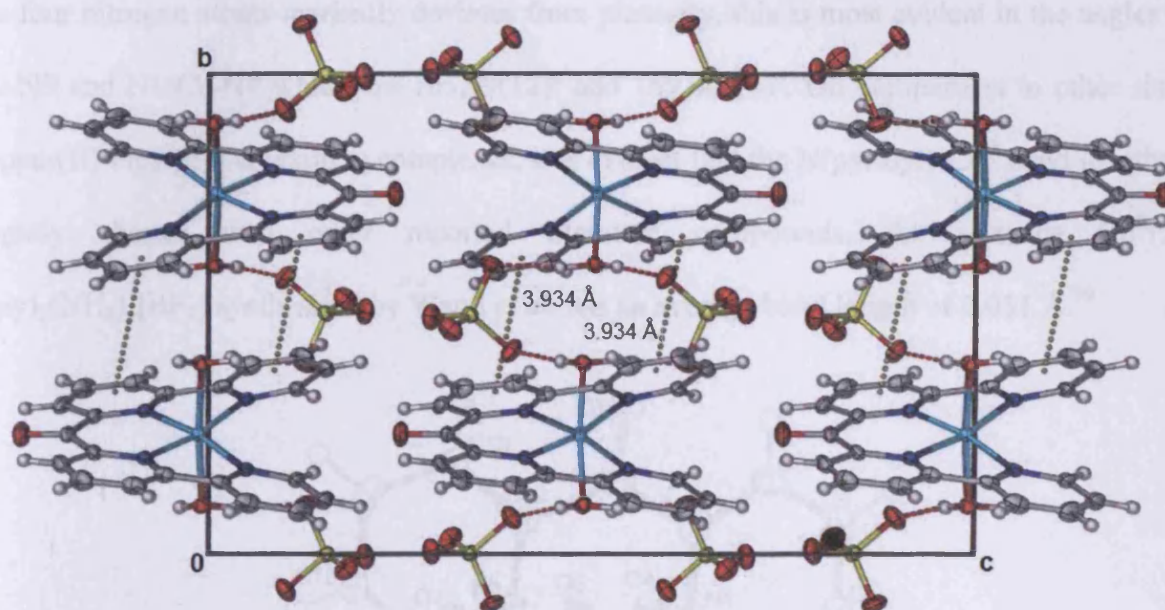


**Figure 26:** A view of the b-c plane revealing rows of complexes running parallel to the b-axis which are supported *via* intermolecular  $\pi$ - $\pi$  stacking interactions (gold dotted lines) and H-bond interactions (red dotted lines) with perchlorate counterions.

#### 1.4.7.5 Crystal Structure of $[\text{Cu}^{\text{II}}(\text{L}^1)(\text{ClO}_4)_2]$ (1.5)

The copper compound **1.5** crystallises in the triclinic space group P-1 with two complexes in the unit cell. The co-ordination sphere is comparable to that of the analogous  $\text{Mn}^{\text{II}}$ ,  $\text{Co}^{\text{II}}$ ,  $\text{Ni}^{\text{II}}$  and  $\text{Zn}^{\text{II}}$  complexes of  $\text{L}^1$ . The metal ion is surrounded by four pyridyl N-donors which all occupy equatorial position within a slightly distorted octahedral geometry. The axial sites are occupied by the oxygen donors O2 and O3 which in this instance arise from two co-ordinating perchlorate molecules (Fig. 27).

Again, as observed in the analogous  $\text{Ni}^{\text{II}}$  complex, the pyridyl N-donors located closest to the ketone group (N1/C2-C6 and N3/C12-C16) exhibit shorter co-ordinative bonds to the copper (1.964(3) Å and 1.971(3) Å) compared to the nitrogen donors located on the more distant adjoining pyridines (1.987(3) Å and 1.995(3) Å). The two axial oxygen donors have considerably longer bond lengths of 2.552(3) Å and 2.703(3) Å and are indicative of a Jahn-Teller tetragonal distortion which is typical of  $d^9$  metal complexes. The square face defined by

the four nitrogen atoms markedly deviates from planarity, this is most evident in the angles N2-Cu-N3 and N1-Cu-N4 which are 165.99(12)° and 169.00(11)°. On comparison to other similar copper(II) bipyridyl-containing complexes, it is evident that the N(pyridyl)-Cu<sup>II</sup> bond lengths are slightly shorter than other reported literature compounds, for instance Cu<sup>II</sup>(2,2'-bipy)<sub>2</sub>(NH<sub>3</sub>)[BF<sub>4</sub>] synthesised by Wang *et al.* has an average bond length of 2.031 Å.<sup>99</sup>

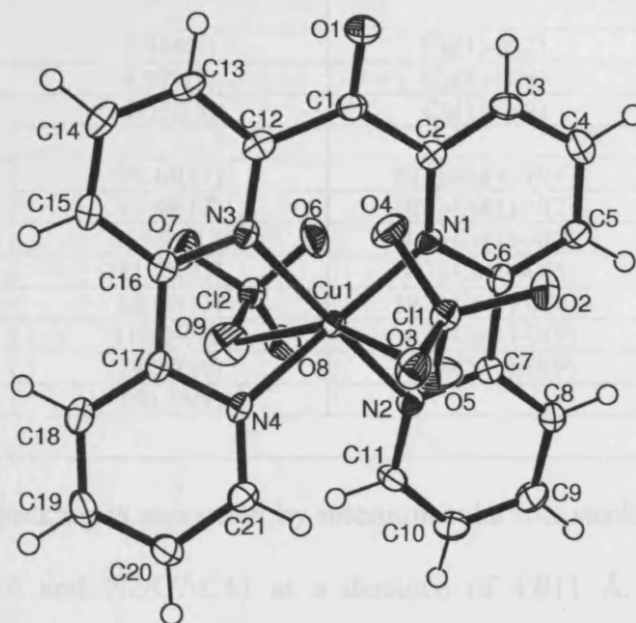


**Figure 27:** Perspective view of the asymmetric unit of **1.5** showing the atom numbering. Displacement ellipsoids are shown at the 50% probability level. H atoms are represented by circles of arbitrary size.

As observed in the analogous Mn<sup>II</sup>, Co<sup>II</sup> and Cd<sup>II</sup> complexes, the carbonyl group appears to protrude outwards from the complex, albeit to a much lesser extent. The dihedral angle between the planes defined as N1-N3-C2-C12 and C2-C12-C1-O1 is 13.4(2)°. Unlike the aforementioned complexes however, the copper complex does not exhibit folding but rather adopts a twisted configuration (Fig. 28). The pyridines which are adjacent to the ketone group (N1/C2-C6 and N3/C12-C16) lie almost on the same plane, forming a dihedral angle of 11.33(18)°. However, the furthest lying pyridine rings (N2/C7-C11 and N4/C17-C21) form a much larger dihedral angle of 27.79(18)°. The twist angles between the two pyridines on each

bipyridine unit are  $10.40(19)^\circ$  and  $7.57(18)^\circ$ , while the line angle between C3-C6 and C7-C10 is  $11.73(12)^\circ$  and the line angle between C13-C16 and C17-C21 is  $13.82(12)^\circ$ . These values indicate a much greater strain on the bipyridine units compared to the other complexes of  $L^1$ .

**Table 12:** Significant Bond lengths (Å) and Angles ( $^\circ$ ) for  $[Cu^{II}(L^1)(ClO_4)_2]$

C(2)-C(1)-C(12)	125.1(3)	C(2)-C(1)-O(1)	117.5(3)
C(12)-C(1)-O(1)	117.5(3)		
Cu(1)-N(1)	1.964(3)	Cu(1)-N(2)	1.995(3)
Cu(1)-N(3)	1.971(3)	Cu(1)-N(4)	1.987(3)
Cu(1)-O(5)	2.552(3)	Cu(1)-O(9)	2.703(3)
N(1)-Cu(1)-N(3)	95.14(12)	N(1)-Cu(1)-N(4)	169.00(11)
N(3)-Cu(1)-N(4)	82.46(12)	N(1)-Cu(1)-N(2)	82.48(12)
N(3)-Cu(1)-N(2)	165.99(12)	N(4)-Cu(1)-N(2)	102.38(12)
N(1)-Cu(1)-O(5)	81.78(11)	N(3)-Cu(1)-O(5)	110.56(10)
N(4)-Cu(1)-O(5)	88.99(11)	N(2)-Cu(1)-O(5)	82.86(10)
N(1)-Cu(1)-O(9)	116.14(10)	N(3)-Cu(1)-O(9)	83.53(10)
N(4)-Cu(1)-O(9)	74.38(10)	N(2)-Cu(1)-O(9)	85.14(10)
O(5)-Cu(1)-O(9)	156.88(9)		

The molecular packing is supported by intermolecular  $\pi$ - $\pi$  stacking interactions between ring systems N1/C2-C6 and N2/C7-C11 at a distance of 4.011 Å. There are no classical hydrogen bonds supporting the lattice framework.

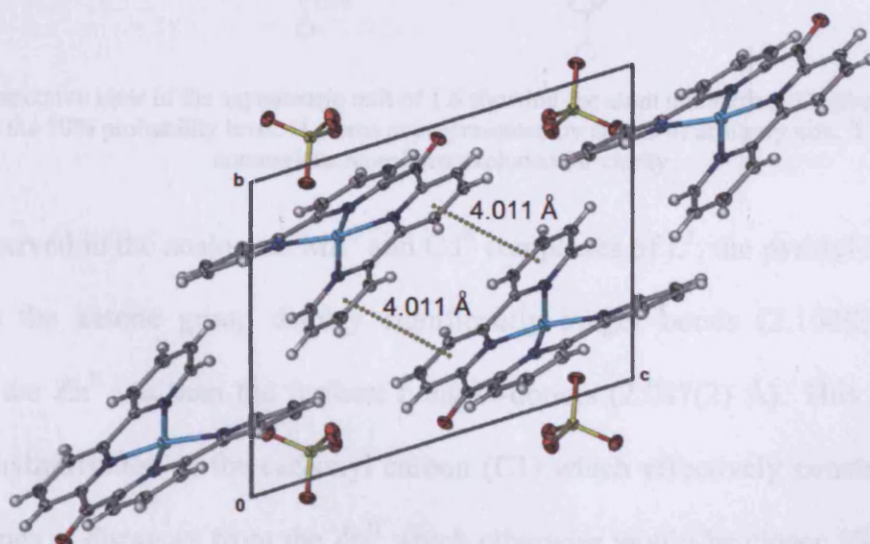


**Figure 28:** The molecular packing of **1.5**, viewed here along the *bc* plane, is supported by intermolecular  $\pi$ - $\pi$  stacking interactions (gold dotted lines). Two perchlorates have been omitted from the unit cell so the  $\pi$ - $\pi$  stacking can be clearly seen.



#### 1.4.7.6 Crystal Structure of $[\text{Zn}^{\text{II}}(\text{L}^1)(\text{H}_2\text{O})_2][\text{ClO}_4]_2$ (1.6)

This compound crystallises in the orthorhombic space group  $Pccn$  with four complexes in the unit cell. Half of the complex lies within the asymmetric unit, the other half is generated *via* the symmetry operator  $[3/2-x, 1/2-y, z]$ . The  $\text{Zn}^{\text{II}}$  cation lies at the centre of a slightly distorted octahedral geometry and reveals a similar co-ordination environment to the analogous  $\text{Mn}^{\text{II}}$ ,  $\text{Co}^{\text{II}}$ ,  $\text{Ni}^{\text{II}}$  and  $\text{Cu}^{\text{II}}$  complexes of  $\text{L}^1$ . There are four equatorial nitrogen donors (N1, N2) which are located on the bipyridyl groups, and two oxygen donors (O2 and O2') which are positioned on two axially located water molecules (Fig. 29).

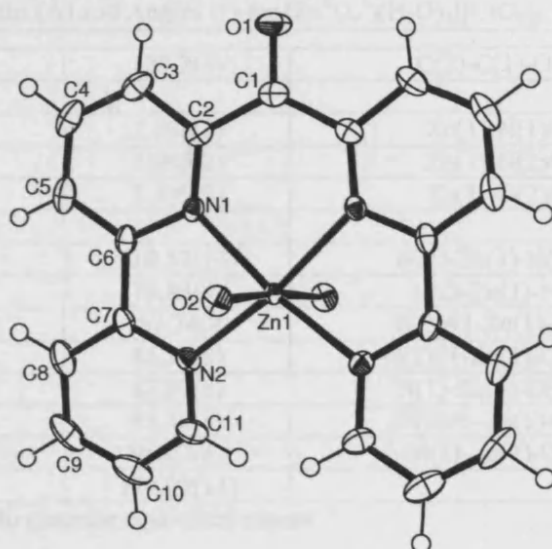


**Figure 29:** Perspective view of the asymmetric unit of **1.6** showing the atom numbering. Displacement ellipsoids are shown at the 50% probability level. H atoms are represented by circles of arbitrary size. Two perchlorate counterions have been excluded for clarity.

As observed in the analogous  $\text{Mn}^{\text{II}}$  and  $\text{Cd}^{\text{II}}$  complexes of  $\text{L}^1$ , the pyridyl N-donors which lie closest to the ketone group display significantly longer bonds (2.108(2) Å) upon coordination to the  $\text{Zn}^{\text{II}}$  ion than the furthest lying N-donors (2.087(2) Å). This possibly results from the  $\text{sp}^2$  hybridisation of the carbonyl carbon (C1) which effectively constrains the closest two pyridyl rings at distances from the  $\text{Zn}^{\text{II}}$  which otherwise would be closer. The furthest lying pyridyl rings without such immediate restriction are free to adopt positions closer to the  $\text{Zn}^{\text{II}}$

cation. These bond distances are significantly shorter than might be expected when compared to the similar compound synthesised by Seik Weng Ng *et al.*<sup>100</sup> which contains two bipyridyl groups occupying all four equatorial positions within an octahedral environment, the (pyridyl)N-Zn<sup>II</sup> bond lengths in this example range between 2.151(4) Å and 2.276(4) Å. It is worth noting that this style of co-ordination in which the two bipy-units are co-planar in mononuclear complexes is very rare. A survey of the CSD (Date: 09/2008) reveals that this feature is only present in 2 out of 115 examples of (bipy)<sub>2</sub>ZnL<sub>x</sub> (where there are no restrictions on the identity of L).

**Table 13:** Significant Bond lengths (Å) and Angles (°) for [Zn<sup>II</sup>(L<sup>1</sup>)(H<sub>2</sub>O)<sub>2</sub>][ClO<sub>4</sub>]<sub>2</sub>

C(2)-C(1)-C(2)#1	127.2(3)	C(2)-C(1)-O(2)	116.39(17)
Zn(1)-N(1)	2.108(2)	Zn(1)-N(1)#1	
Zn(1)-N(2)	2.088(2)	Zn(1)-N(2)#1	2.108(2)
Zn(1)-O(2)	2.199(2)	Zn(1)-O(2)#1	2.088(2)
			2.199(2)
N(2)-Zn(1)-N(2)#1	110.57(13)	N(2)-Zn(1)-N(1)#1	
N(2)#1-Zn(1)-N(1)#1	79.83(9)	N(2)-Zn(1)-N(1)	167.74(9)
N(2)#1-Zn(1)-N(1)	167.74(9)	N(1)#1-Zn(1)-N(1)	79.83(9)
N(2)-Zn(1)-O(2)#1	85.73(8)	N(2)#1-Zn(1)-O(2)#1	90.68(13)
N(1)#1-Zn(1)-O(2)#1	87.57(8)	N(1)-Zn(1)-O(2)#1	91.36(8)
N(2)-Zn(1)-O(2)	91.36(8)	N(2)#1-Zn(1)-O(2)	96.02(8)
N(1)#1-Zn(1)-O(2)	96.02(8)	N(1)-Zn(1)-O(2)	85.73(8)
O(2)#1-Zn(1)-O(2)	174.90(11)		87.57(8)

Symmetry transformations used to generate equivalent atoms:

#1 -x+3/2,-y+1/2,z

Further distortions from the ideal octahedral co-ordination environment arise from the O-donors which lie at significantly longer distances (2.1938(18) Å) from the Zn<sup>II</sup> compared to the equatorial nitrogen donors. This feature has been shown to be common to all the mononuclear complexes of L<sup>1</sup> with the exception of the cadmium compound, **1.8**, which has a trigonal prismatic co-ordination geometry. An example of a water molecule co-ordinating to a Zn<sup>II</sup> cation in the presence of two co-ordinating bipy units was presented by Ye *et al.* in the complex [Zn<sup>II</sup>(bipy)<sub>2</sub>(H<sub>2</sub>O)(CF<sub>3</sub>CO<sub>2</sub>)] [ClO<sub>4</sub>], the bond length in this instance was very similar (2.148(2)

Å).<sup>101</sup> The angle between the axially located oxygen donor atoms varies from the expected 180° at a modestly less obtuse 174.95(10)°. Again, this is comparable to the analogous complexes of L<sup>1</sup> in this series. Finally, the bond angles comprising the square face deviate away from the ideal 90° due to the narrow bite angles of the bipy groups (79.81(8)°).

This complex does not appear to be folded and the ketone group remains in the plane of the complex. The dihedral angle defined by the planes N1-N3-C2-C12 and C2-C12-C1-O1 is just 2.24(14)°, confirming the ketone group does not protrude outwards as observed in the Mn<sup>II</sup>, Co<sup>II</sup>, Cu<sup>II</sup> and Cd<sup>II</sup> complexes. The dihedral angle between the pyridine rings closest to the ketone group is just 9.73(12)°, while the equivalent angle between the furthest lying pyridines is 20.94(13)°. This large difference causes each bipyridine group to twist and a dihedral angle of 5.97(12)° is created between the two pyridines. The line angle between C3-C6 and C7-C10 is 8.11(9)° which also indicates an amount of strain on the bipyridine group. This is reminiscent of the Ni<sup>II</sup> complex, **1.4**, which exhibits a similar ligand conformation. Again, this distortion away from an ideal *trans* configuration has the effect of relieving steric strain caused by the impossibly close approach of the  $\alpha$ -hydrogens on the opposing bipy groups.

The molecular packing (Fig. 30) is supported by a network of intermolecular hydrogen bonding (Table 14). Furthermore, intermolecular  $\pi$ - $\pi$  stacking interactions also support the lattice framework. Specifically, this occurs between the ring system N1/C2-C6 and N2/C7-C11 which is located on an adjacent complex generated by the symmetry operator 1-x, 1-y, -z.

**Table 14:** H-bonding geometry (Å, °) for **1.6**

D-H...A	d(D-H)	d(H...A)	d(D...A)	<(DHA)
O(2)-H(2A)...O(3)#1	0.95	2.57	3.175(3)	122
O(2)-H(2A)...O(6)#1	0.95	1.99	2.927(3)	170
O(2)-H(2B)...O(3)	0.92	1.85	2.770(3)	174

Symmetry transformations used to generate equivalent atoms:

#1 = 1-x, -y, -z

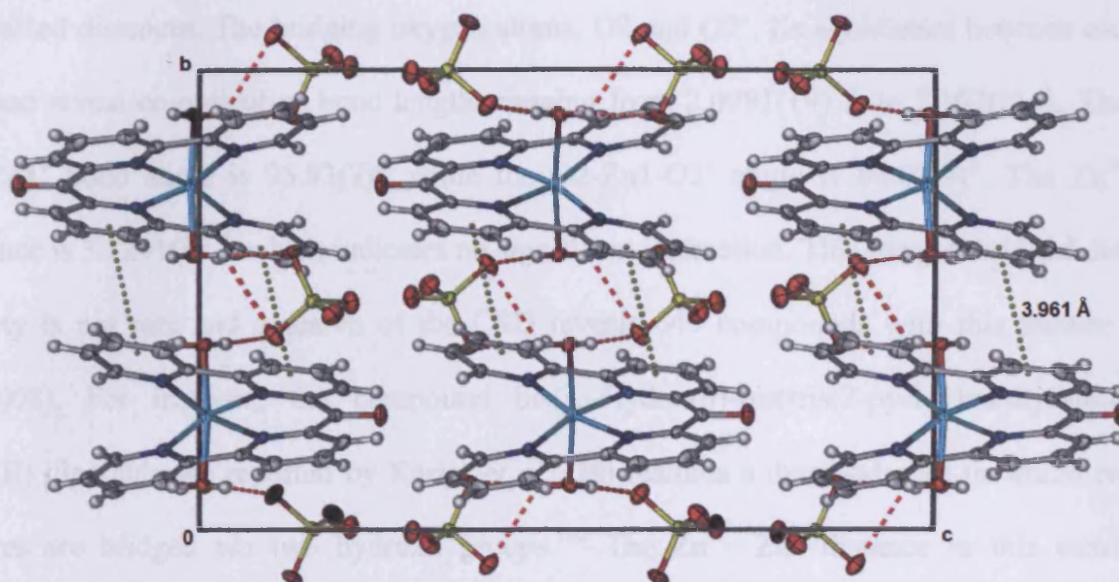


**Figure 30:** A view of the molecular packing showing the bc plane. The intermolecular  $\pi$ - $\pi$  stacking interactions are shown as gold dotted lines. The H-bonds are shown as red dashed lines.

#### 1.4.7.7 Crystal Structure of $[\text{Zn}_2(\text{L}^1\text{-OCH}_3)_2][\text{ClO}_4]_2$ (1.7)

This compound crystallises in the monoclinic space group  $P2_1/n$  and contains four complexes within the unit cell. Only half of the dinuclear complex resides within the asymmetric unit, the other half is generated *via* the symmetry operator  $[-x, -y, 1-z]$ . The dinuclear complex exhibits a diamond core in which two divalent zinc cations are bridged by the negatively charged oxygen from the deprotonated hydroxy groups. Both the structural arrangement and co-ordination mode of the hemiketal ligand which is formed are essentially identical to the analogous iron complex, 1.2. Symmetry mapping calculations indicate that both of these  $\text{Zn}^{\text{II}}$  cations are situated at the centre of significantly distorted octahedral geometries (Fig. 31; Table 15).

The N-donors located on the pyridyl groups closest to the hemiketal moieties (N2, N4) display significantly shorter co-ordinative bond lengths ( $\text{Zn}^{\text{II}}\text{-N}_{\text{av}} = 2.060(2) \text{ \AA}$ ) compared to the N-donors (N1 and N3) located on the furthest lying pyridyl groups ( $\text{Zn}^{\text{II}}\text{-N}_{\text{av}} = 2.268(2) \text{ \AA}$ ). Again, as in 1.2, this is probably due to the  $sp^3$  hybridisation of carbon atoms C11 and C11' restraining the immediately adjacent pyridyl rings and preventing them from adopting more

protracted distances. The bridging oxygen atoms, O2 and O2', lie equidistant between each Zn<sup>II</sup> ion and reveal co-ordinative bond lengths ranging from 2.0991(19) Å to 2.107(2) Å. The Zn1-O2-Zn1' bond angle is 95.93(7)°, while the O2-Zn1-O2' angle is 84.07(7)°. The Zn<sup>II</sup>...Zn<sup>II</sup> distance is 3.1241(8) Å which indicates no significant interaction. This oxygen-bridged dinuclear moiety is not rare and a search of the CSD reveals 649 compounds with this feature (Date: 12/2008). For instance, the compound bis( $\mu_2$ -Hydroxo)-bis(tris(2-pyridylmethyl)amine)-dizinc(II) diperchlorate reported by Karlin *et al.* also features a diamond core in which two Zn<sup>II</sup> centres are bridged *via* two hydroxo groups.<sup>102</sup> The Zn<sup>II</sup>...Zn<sup>II</sup> distance in this example is significantly shorter at 2.992 Å indicating a stronger interaction between the zinc centres. The Zn<sup>II</sup>-O bond lengths are also shorter, ranging from 1.962(1) to 2.048(5) Å, while the Zn-O-Zn' angle is statistically identical at 96.5(2)°. The Zn<sup>II</sup>-N<sub>py</sub> bond lengths in this example range from 2.179(7) to 2.200(8) Å which are slightly shorter than the pyridyl groups lying furthest from the hemiketal moieties in compound **1.7**, however they are still significantly longer than the pyridyl groups lying adjacent to the hemiketal moieties.

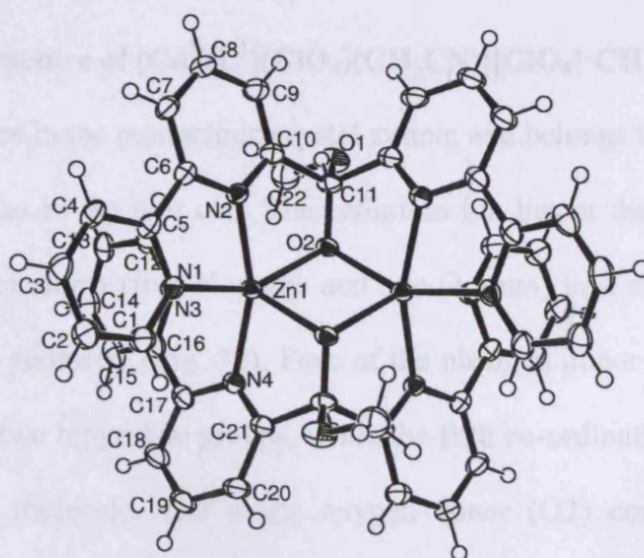


**Figure 31:** Perspective view of the asymmetric unit of **1.7** showing the atom numbering. Displacement ellipsoids are shown at the 50% probability level. H atoms are represented by circles of arbitrary size.

**Table 15:** Continuous Symmetry Mapping Results

Compound	HP	PPY	OC	TP	JPPY
1.7	30.15343	16.04622	5.27427	8.41014	19.77419

HP: Hexagon ( $D_{6h}$ ), PPY: Pentagonal pyramid ( $C_{5v}$ ), OC: Octahedron ( $O_h$ ), TP: Trigonal Pyramidal ( $D_{3h}$ ), JPPY: Johnson's pentagonal pyramid J2 ( $C_{5v}$ ).

**Table 16:** Significant Bond lengths (Å) and Angles ( $^\circ$ ) for  $[Zn_2(L^1-OCH_3)_2][ClO_4]_2$

Zn(1)-Zn(1)#1	2.992		
Zn(1)-N(1)	2.248(2)	Zn(1)-N(2)	2.055(2)
Zn(1)-N(3)	2.287(2)	Zn(1)-N(4)	2.064(2)
Zn(1)-O(2)	2.0991(19)	Zn(1)-O(2)#1	2.107(2)
N(2)-Zn(1)-N(4)	161.87(9)	N(2)-Zn(1)-O(2)	77.68(8)
N(4)-Zn(1)-O(2)	116.64(8)	N(2)-Zn(1)-O(2)#1	115.63(8)
N(4)-Zn(1)-O(2)#1	78.50(8)	O(2)-Zn(1)-O(2)#1	84.07(8)
N(2)-Zn(1)-N(1)	75.08(9)	N(4)-Zn(1)-N(1)	92.26(9)
O(2)-Zn(1)-N(1)	150.73(8)	O(2)#1-Zn(1)-N(1)	98.16(8)
N(2)-Zn(1)-N(3)	91.88(9)	N(4)-Zn(1)-N(3)	74.43(9)
O(2)-Zn(1)-N(3)	103.62(8)	O(2)#1-Zn(1)-N(3)	152.48(8)
N(1)-Zn(1)-N(3)	87.86(9)	N(2)-Zn(1)-Zn(1)#1	98.53(7)
N(4)-Zn(1)-Zn(1)#1	99.60(7)	O(2)-Zn(1)-Zn(1)#1	42.13(5)
O(2)#1-Zn(1)-Zn(1)#1	41.94(5)	N(1)-Zn(1)-Zn(1)#1	132.99(7)
N(3)-Zn(1)-Zn(1)#1	139.14(6)		

Symmetry transformations used to generate equivalent atoms:

#1 -x,-y,-z+1

#### 1.4.7.8 Crystal Structure of $[Cd^{II}(L^1)(ClO_4)(CH_3CN)][ClO_4] \cdot CH_3CN$ (1.8)

This complex crystallises in the monoclinic crystal system and belongs to the  $P2_1/n$  space group. There are four molecules in the unit cell. The cadmium ion lies at the centre of the molecule surrounded by six donor atoms (five N atoms and one O atom) in a slightly distorted trigonal prismatic co-ordination geometry (Fig. 32). Four of the nitrogen donor atoms (N1, N2, N3 and N4) originate from the two bipyridine groups, while the fifth co-ordinating N-atom (N5) is from an acetonitrile solvent molecule. The single oxygen donor (O2) comes from a perchlorate counterion situated in the lattice framework. These donor groups are the basis of two triangles

(A: [N1, O2, N3] and B: [N2, N5, N4]) which lie in approximately parallel planes (dihedral angle =  $9.52(19)^\circ$ ).

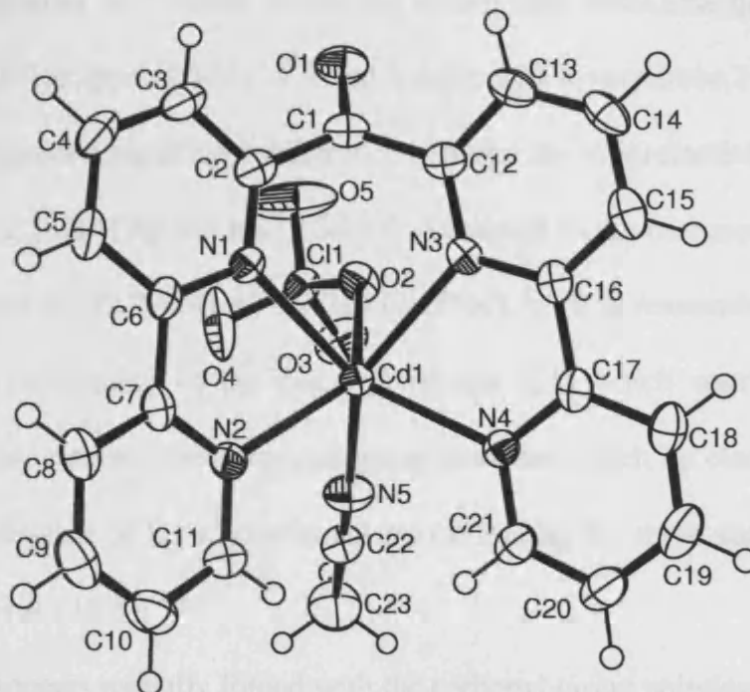


**Figure 32:** Perspective view of the asymmetric unit of **1.8** showing the atom numbering. Displacement ellipsoids are shown at the 50% probability level. H atoms are represented by circles of arbitrary size.

The torsion angles  $A'-C_n-C_n'-B'$  ( $C_n, C_n'$  = centroids of the triangles;  $A', B'$  = near eclipsed pair of donor atoms) of  $4.2^\circ$ ,  $-6.6^\circ$  and  $-9.4^\circ$  (averaging at  $-3.93^\circ$ ) are reasonably close to the twist angle of a conventional TP geometry ( $\varphi = 0^\circ$ ). This reflects the significant distortion from an octahedral geometry where the twist angle is in theory  $60^\circ$ . There is an inter-triangular separation ( $h$ ) between the centroids of  $2.812 \text{ \AA}$ . The mean  $s/h$  ratio (where  $s$  is the average length of each of the sides of each face of the trigonal prism) is 1.14 indicating a slight compression relative to an ideal trigonal prism with square faces ( $s = h, s/h = 1.00$ ).

There are several examples of crystallographically characterised co-ordination spheres involving two bipyridine groups around a cadmium centre. A search of the CSD results in 54 hits for such criteria (Date: 12/2008). The bond lengths between the bipyridyl N-donors and the

## Chapter 1: Two Bipodal Ligand Frameworks: A Structural Exploration *via* X-Ray Diffraction Methods

central Cd<sup>II</sup> cation lie within the expected ranges on comparison to similar complexes, particularly the compound Aqua-bis(2,2'-bipyridine)-(perchlorate-O)-cadmium(II) perchlorate synthesised by Ranjbar *et al.*<sup>103</sup> which comprises of two bipy-units arranged around a cadmium centre. This example has (pyridyl)-N-Cd<sup>II</sup> bond lengths which vary from 2.316(5) Å to 2.359(6) Å. Compound **1.8** shows a significant difference between the co-ordinative bond lengths of the bipy N-donors N1 (2.338(4) Å) and N3 (2.344(4) Å) closest to the carbonyl group and the more distant bipy N-donors N2 (2.294(4) Å) and N4 (2.286(4) Å). It is reasonable to assume this is a result of the sp<sup>2</sup> hybridisation of the carbonyl carbon (C1) which restricts the immediately adjacent pyridines and prevent them from adopting positions which lie closer to the central Cd<sup>II</sup> ion. The sp<sup>2</sup> hybridisation of C1 is confirmed by examining the three surrounding around the plane which average at 119.67(5)°.

The ligand appears partially folded with the carbonyl group pointing preferentially in one direction. The two pyridyl units which are immediately linked to the carbonyl group tilt in opposing directions and form a dihedral angle of 49.60° and the two furthest lying pyridyl units also tilt in a similar manner however with a slightly less acute dihedral angle of 58.64°. The two pyridyl units comprising each of the bipyridyl arms deviate slightly away from planarity. The dihedral angles between the pyridyl rings N1/C3-C6 and N2/C7-C11, and N3/C12-C16 and N4/C17-C21 are 10.11° and 1.94° respectively.

The molecular packing is supported by intermolecular  $\pi$ - $\pi$  stacking interactions which form infinite chains running parallel to the b axis (Fig. 33). The packing is supported by non-classical hydrogen bonds which link each symmetry generated complex along each chain. There is one solvent molecule of acetonitrile in the asymmetric unit which is not involved in any intermolecular interactions.



**Table 17:** Significant Bond lengths (Å) and Angles (°) for  $[\text{Cd}^{\text{II}}(\text{L}^1)(\text{ClO}_4)(\text{CH}_3\text{CN})][\text{ClO}_4]\cdot\text{CH}_3\text{CN}$

C(2)-C(1)-C(12)	120.8(4)	C(2)-C(1)-O(1)	119.4(5)
C(12)-C(1)-O(1)	118.8(5)		
Cd(1)-N(1)	2.338(4)	Cd(1)-N(2)	2.294(4)
Cd(1)-N(3)	2.344(4)	Cd(1)-N(4)	2.286(4)
Cd(1)-N(5)	2.352(4)	Cd(1)-O(2)	2.406(3)
N(4)-Cd(1)-N(2)	110.33(14)	N(4)-Cd(1)-N(1)	138.08(13)
N(2)-Cd(1)-N(1)	71.39(13)	N(4)-Cd(1)-N(3)	71.53(13)
N(2)-Cd(1)-N(3)	136.52(13)	N(1)-Cd(1)-N(3)	79.81(13)
N(4)-Cd(1)-N(5)	86.06(15)	N(2)-Cd(1)-N(5)	85.65(15)
N(1)-Cd(1)-N(5)	134.73(14)	N(3)-Cd(1)-N(5)	136.65(14)
N(4)-Cd(1)-O(2)	116.31(13)	N(2)-Cd(1)-O(2)	130.37(13)
N(1)-Cd(1)-O(2)	84.54(12)	N(3)-Cd(1)-O(2)	76.34(12)
N(5)-Cd(1)-O(2)	81.60(14)		

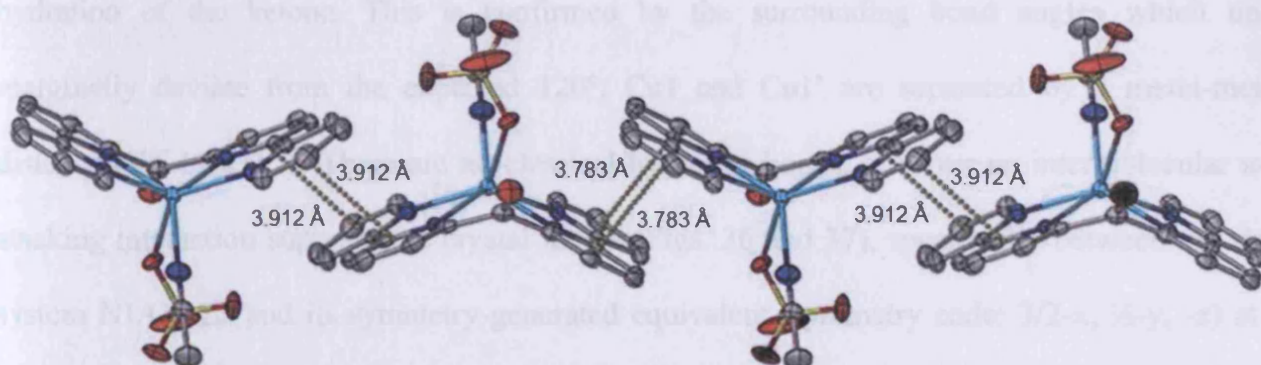


**Figure 33:** The lattice framework of compound **1.8** is composed of infinite chains running parallel to the *b*-axis, supported by  $\pi$ - $\pi$  stacking interactions (gold dotted lines). Hydrogen atoms have been omitted for clarity.

#### 1.4.7.9 Crystal Structure of $[\text{Cu}_2(\text{L}^2)(\text{CH}_3\text{CN})_4][\text{ClO}_4]_4\cdot 2\text{CH}_3\text{CN}$ (**1.9**)

The compound crystallises in the monoclinic space group  $C2/c$  with four complexes within the unit cell. The complexation results in a binuclear 1:2 ligand to metal complex, with each metal at the centre of a five co-ordinate geometry which is best described as a highly distorted trigonal bipyramid (Fig. 35). Only half of the complex resides within the asymmetric unit, the other half is generated *via* the symmetry operator  $[-x, y, \frac{1}{2} - z]$ . Each  $\text{Cu}^{\text{II}}$  cation is co-ordinated by three terpyridine N-donors, with each arm of the bipodal ligand co-ordinating to different copper

## Chapter 1: Two Bipodal Ligand Frameworks: A Structural Exploration *via* X-Ray Diffraction Methods

centres. The two co-ordinating acetonitrile molecules occupy positions on the trigonal face. The bond lengths between the terpyridine N-donors and the Cu<sup>II</sup> ion range between 1.926(3) Å and 2.132(3) Å. These values are consistent with similar terpyridine-containing copper(II) complexes, for instance the compound bis(2,2':6',2''-terpyridine)-copper(II) diperchlorate monohydrate synthesised by Valdes-Martinez *et al.* reveals bond lengths ranging from 1.994(7) to 2.210(5) Å.<sup>104</sup> The shortest bond lengths in this example involve the terpy N-donors originating from the central pyridine unit on each terpyridine, this is also observed for compound 1.9.

The carbonyl carbon, C16, is clearly sp<sup>2</sup> hybridised, indicating the absence of any hydration of the ketone. This is confirmed by the surrounding bond angles which only marginally deviate from the expected 120°. Cu1 and Cu1' are separated by a metal-metal distance of 6.196(3) Å. There are no classical hydrogen bonds, however an intermolecular  $\pi$ - $\pi$  stacking interaction supports the crystal lattice (Figs. 36 and 37), specifically between the ring system N1/C1-C5 and its symmetry-generated equivalent (symmetry code: 3/2-x, 1/2-y, -z) at a centroid-centroid distance of 3.819(3) Å.

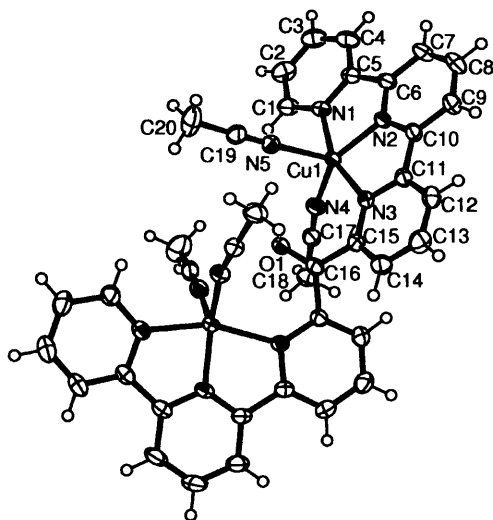


**Figure 34:** Perspective view of the asymmetric unit of 1.9 showing the atom numbering. Displacement ellipsoids are shown at the 50% probability level. H atoms are represented by circles of arbitrary size.

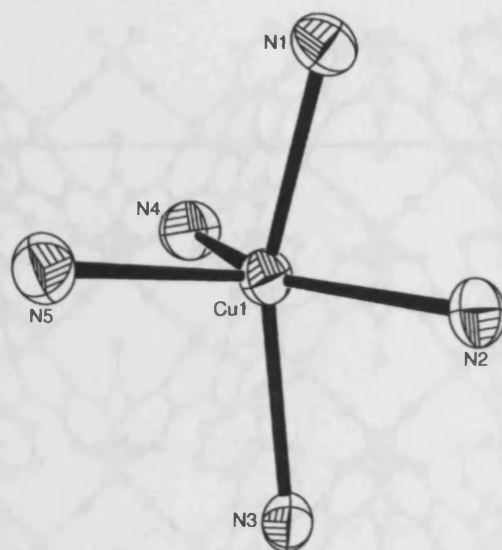


**Figure 35:** A view of the core geometry of **1.9** showing the atom numbering. The co-ordination geometry is best described as a highly distorted trigonal bipyramid. Displacement ellipsoids are shown at the 50% probability level.

**Table 18:** Significant Bond lengths (Å) and Angles (°) for  $[\text{Cu}_2(\text{L}^2)(\text{CH}_3\text{CN})_4][\text{ClO}_4]_4 \cdot 2\text{CH}_3\text{CN}$

Cu(1)-Cu(1)#1	6.196(3)		
C(15)-C(16)-C(15)#1	116.1(3)	C(15)-C(16)-O(1)	121.96(14)
Cu(1)-N(1)	2.023(3)	Cu(1)-N(2)	1.926(3)
Cu(1)-N(3)	2.102(3)	Cu(1)-N(4)	1.996(3)
Cu(1)-N(5)	2.132(3)		
N(2)-Cu(1)-N(4)	141.58(14)	N(2)-Cu(1)-N(1)	80.42(13)
N(4)-Cu(1)-N(1)	94.44(13)	N(2)-Cu(1)-N(3)	79.54(12)
N(4)-Cu(1)-N(3)	100.11(12)	N(1)-Cu(1)-N(3)	159.88(12)
N(2)-Cu(1)-N(5)	113.26(13)	N(4)-Cu(1)-N(5)	104.85(14)
N(1)-Cu(1)-N(5)	91.13(13)	N(3)-Cu(1)-N(5)	98.42(12)

Symmetry transformations used to generate equivalent atoms:

#1  $-x+2, y, -z+1/2$

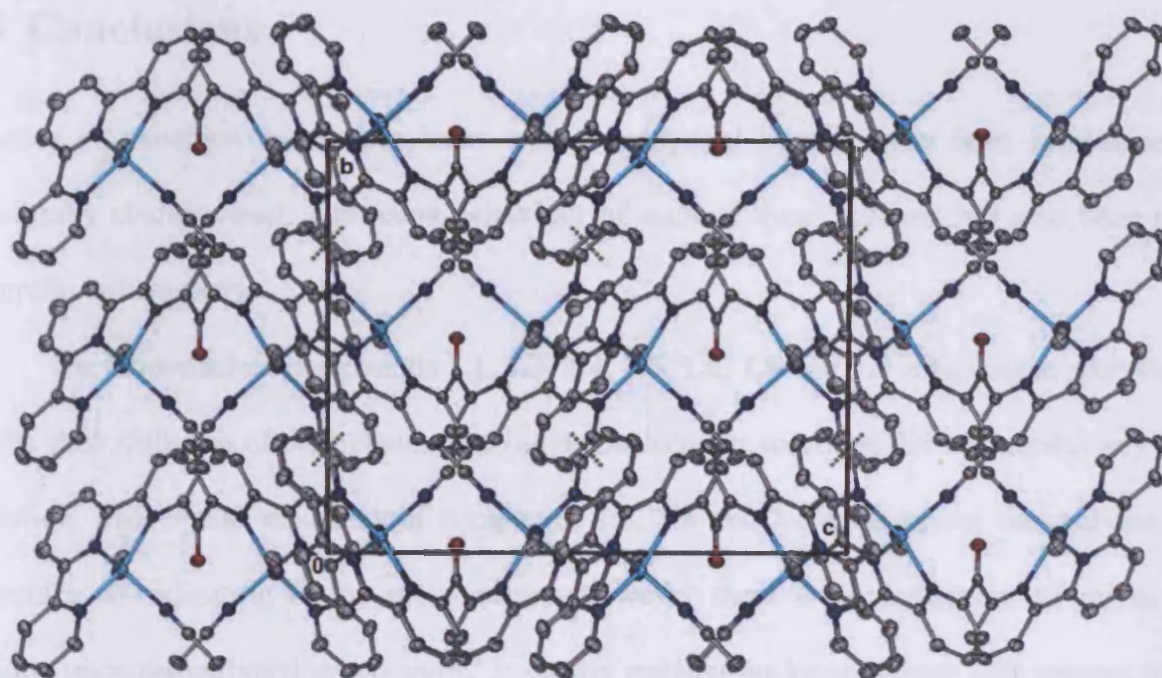


**Figure 36:** A view of the bc plane showing the molecular packing supported by intermolecular  $\pi$ - $\pi$  stacking (gold dotted lines). Hydrogen atoms have been omitted for clarity, as have perchlorate counterions located in the lattice and solvent acetonitrile.

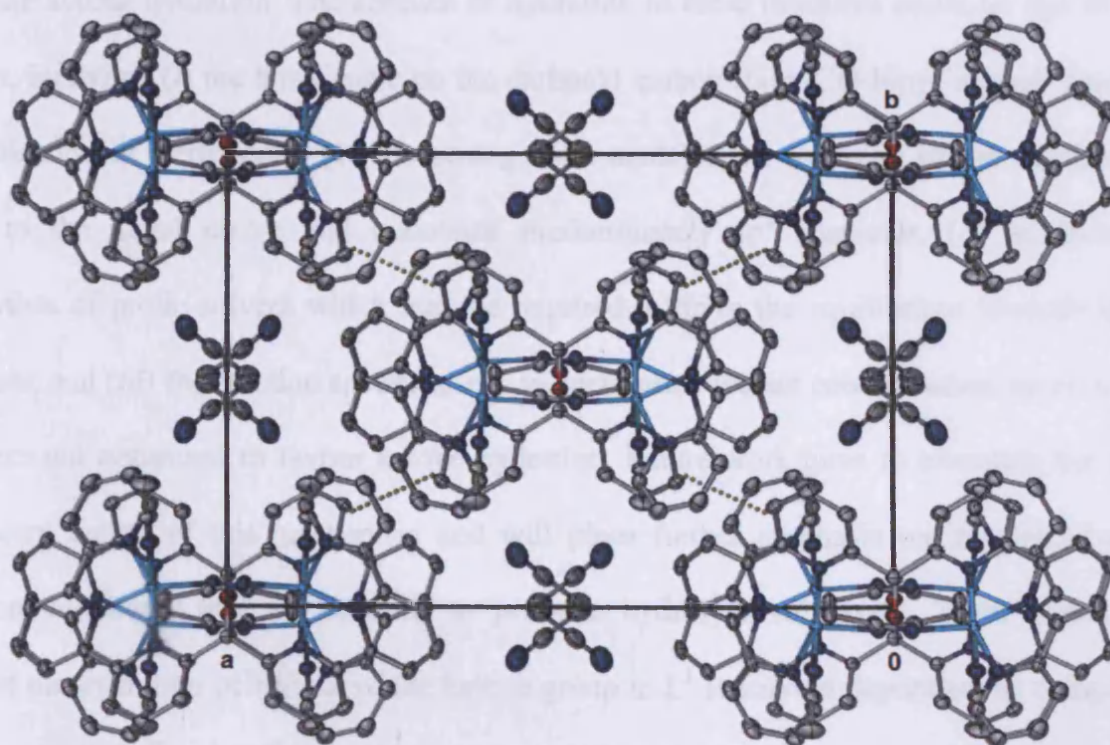


**Figure 37:** An alternative view (ab plane) of the molecular packing. Hydrogen atoms and non-coordinating perchlorate counterions have been omitted for clarity.

## 1.5 Conclusions

A series of transition metal complexes with two bipodal ligands have been synthesised and structurally characterised. The redox-behaviour of each of these systems has also been probed *via* cyclic voltammetry.

The mononuclear compounds **1.1**, **1.3**, **1.4**, **1.5**, **1.6**, **1.8** and **1.9** which were recrystallised *via* the slow diffusion of diethyl ether into acetonitrile/water solutions did not exhibit any ketone hydration. The crystal structures of complexes **1.3**, **1.4** and **1.6** each reveal two solvent water molecules co-ordinating to the metal centre, however there is no indication of nucleophilic addition upon the carbonyl group and  $L^1$  is clearly stable in its ketonic form with respect to *gem*-diol formation. Interestingly, the complexes **1.1**, **1.3**, **1.5** and **1.8** each exhibit a significant disruption of ketone planarity with the bipyridyl groups, a feature which is typically expected to facilitate ketone hydration. The absence of hydration in these instances could be due to several factors, including (i) the bond angle on the carbonyl carbon (bipy-CO-bipy) in each case shows no indication of steric strain (*i.e.* becoming more acute) upon chelation of the adjoining bipy units to the metal centre and maintains predominantly  $sp^2$  character, (ii) an insufficient proportion of protic solvent which may be required to drive the equilibrium towards hydrated products, and (iii) the reaction specifics, *e.g.* temperature, reactant concentration, metal to ligand ratio are not optimised to favour ketone hydration. Future work aims to elucidate the solvent-dependant nature of this mechanism and will place further emphasis on the optimisation of reaction conditions that are required to promote hydrolysis/solvolysis. These initial results suggest the hydration behaviour of the ketone group in  $L^1$  is solvent dependant as complexation reactions with  $Fe^{II}$  and  $Zn^{II}$  in hot methanolic solutions led to the formation of the monoanionic hemiketal species,  $(2\text{-bipy})_2C(OMe)O^-$ . This species exhibited a  $\mu_2:\eta^1:\eta^1:\eta^2:\eta^1:\eta^1$  binding mode

## Chapter 1: Two Bipodal Ligand Frameworks: A Structural Exploration *via* X-Ray Diffraction Methods

in which the deprotonated hydroxyl group bridged two metal centres, yielding dinuclear complexes of the form  $[M_2\{(2\text{-bipy})_2\text{C}(\text{OMe})\text{O}^-\}_2][\text{ClO}_4]_2$  ( $M = \text{Fe}^{\text{II}}$  or  $\text{Zn}^{\text{II}}$ ). Conducting the same experiment with a hot acetonitrile/water mixture led to the unhydrated ketonic mononuclear  $\text{Zn}^{\text{II}}$  complex, however initial attempts at crystallising the analogous mononuclear iron complex have been unsuccessful. In accordance with these observations, the copper complex of the terpyridine ligand,  $L^2$ , which was crystallised from a hot acetonitrile/water mixture did not reveal any *gem*-diol formation.

The crystal structures of the transition metal complexes of  $L^1$  and  $L^2$  reveal self-assembled supramolecular architectures supported by non-covalent interactions such as hydrogen bonding and  $\pi$ - $\pi$  stacking. These attractive structures deserve further investigation in terms of the assembly of supramolecular arrays of metal ions, particularly due to the ligands potential to demonstrate a range of binding modes following hydration.

### 1.6 References

1. J.-M. Lehn, *Supramolecular Chemistry: Concepts and Perspectives*, 1995, Weinheim, VCH.
2. J.-M. Lehn, *Science*, 2002, 295, 2400.
3. J.-M. Lehn, *Supramolecular Science: Where It Is and Where It Is Going*, 1999, Kluwer, Dordrecht, Netherlands.
4. J.-M. Lehn, *Rep. Prog. Phys.*, 2004, 67, 249-265.
5. J.-M. Lehn, *Chem. Soc. Rev.*, 2007, 36, 151-160.
6. S. P. Argent, T. Riis-Johannessen, J. C. Jeffery, L. P. Harding and M. D. Ward, *Chem. Commun.*, 2005, 4647-4649.

Chapter 1: Two Bipodal Ligand Frameworks:  
A Structural Exploration *via* X-Ray Diffraction Methods

7. S. P. Argent, H. Adams, T. Riis-Johannessen, J. C. Jeffery, L. P. Harding and M. D. Ward, *J. Am. Chem. Soc.*, 2006, 128, 72–73.
8. S. P. Argent, H. Adams, T. Riis-Johannessen, J. C. Jeffery, L. P. Harding, O. Mamula and M. D. Ward, *Inorg. Chem.*, 2006, 45, 3905–3919.
9. E. C. Constable, *Angew. Chem. Int. Ed. Engl.*, 1991, 30, No. 11.
10. E. C. Constable, *Chem. Soc. Rev.*, 2007, 36, 246-253.
11. E. C. Constable, *Coord. Chem. Rev.*, 2008, 252, 842-855.
12. J.-P. Collin, C. Dietrich-Buchecker, C. Hamann, D. Jouvenot, J.-M. Kern, P. Mobian, J.-P. Sauvage, *Comprehensive Coordination Chemistry II*, 2004, 7, 303-326.
13. N. Dalla-Favera, J. Hamacek, M. Borkovec, D. Jeannerat, F. Gumy, J.-C. G. Bünzli, *Chem. Eur. J.*, 2008, 14, 2994-3005.
14. J.-C. G. Bünzli, C. Piguet, *Chem. Rev.*, 2002, 102, 1897-1928.
15. C. Piguet, J.-C. G. Bünzli, *Chem. Soc. Rev.*, 1999, 28, 347.
16. C. Piguet, M. Borkovec, J. Hamacek, K. Zeckert, *Coord. Chem. Rev.*, 2005, 249, 705-726.
17. C. Piguet, G. Bernardinelli, G. Hopfgartner, *Chem. Rev.*, 1997, 97, 6, 2005-2062.
18. J.-M. Lehn, *Science*, 1985, 227, 849-856.
19. B. J. Holliday, C. A. Mirkin, *Angew. Chem. Int. Ed.*, 2001, 40, 2022-2043.
20. J. K. M. Sanders, *Chem. Eur. J.*, 1998, 4, 1378-1383.
21. M.-C. Daniel, D. Astruc, *Chem. Rev.*, 2004, 104, 293-346.
22. C. A. Nijhuis, B. J. Ravoo, J. Huskens, D. N. Reinhoudt, *Coord. Chem. Rev.*, 2007, 251, 1761-1780.
23. P. L. Boulas, M. Gómez-Kaifer, L. Echegoyen, *Angew. Chem. Int. Ed.*, 1998, 37, 216-247.

Chapter 1: Two Bipodal Ligand Frameworks:  
A Structural Exploration *via* X-Ray Diffraction Methods

24. B.-H. Ye, M.-L. Tong, X.-M. Chen, *Coord. Chem. Rev.*, 2005, 249, 545-565.
25. M. A. Camacho, A. K. Kar, W. E. Lindsell, C. Murray, P. N. Preston, B. S. Wherrett, *J. Mater. Chem.*, 1999, 9, 1251-1256.
26. T. Maruyama, T. Yamamoto, *Inorg. Chim. Acta*, 1995, 238, 9-13.
27. C. Y. Liu, H. P. Zeng, Y. Segawa, R. Kira, *Optic. Commun.*, 1999, 162, 53-56.
28. M. Ruben, J.-M. Lehn, G. Vaughan, *Chem. Commun.*, 2003, 1338-1339.
29. K. Kalyanasundaram, M. Grätzel, *Coord. Chem. Rev.*, 1998, 347-414.
30. Y. Rodríguez-Martín, M. Hernández-Molina, F. S. Delgado, J. Pasán, C. Ruiz-Pérez, J. Sanchiz, F. Lloret, M. Julve, *CrystEngComm*, 2002, 4, 522-535.
31. O. Waldmann, J. Hassmann, P. Müller, G. S. Hanan, D. Volkmer, U. S. Schubert, J.-M. Lehn, *Phys. Rev. Lett.*, 1997, 78, 3390.
32. C. Sangregorio, T. Ohm, C. Paulsen, R. Sessoli, D. Gatteschi, *Phys. Rev. Lett.*, 1997, 78, 4645-4648.
33. R. R. Osborne, W. R. McWhinnie, *Inorg. Phys. Theor.*, 1967, 2075-2078.
34. M. C. Feller, R. Robson, *Aust. J. Chem.*, 1968, 21, 2919-2927.
35. M. C. Feller, R. Robson, *Aust. J. Chem.*, 1970, 23, 1997-2003.
36. M. C. Feller, R. Robson, I. J. Bakker, *J. Inorg. Nucl. Chem.*, 1971, 33, 747-754.
37. G. Bandoli, A. Dolmella, T. I. A. Gerber, J. G. H. du Preez, H. J. Kemp, *Inorg. Chim. Acta*, 1994, 217, 141-147.
38. A. D. Q. Ferreira, A. Bino, D. Gibson, *Inorg. Chim. Acta*, 1997, 265, 155-161.
39. C. A. Kavounis, C. Tsiamis, C. J. Cardin, Y. Zubavichus, *Polyhedron*, 1996, 15, 385-390.
40. O. J. Parker, S. L. Aubol, G. L. Breneman, *Polyhedron*, 2000, 19, 623-626.
41. G. Yang, S.-L. Zheng, X.-M. Chen, H. K. Lee, Z.-Y. Zhou, T. C. W. Mak, *Inorg. Chim. Acta*, 2000, 303, 86-93.



Chapter 1: Two Bipodal Ligand Frameworks:  
A Structural Exploration *via* X-Ray Diffraction Methods

42. V. Rattanaphani, W. R. McWhinnie, *Inorg. Chim. Acta*, 1974, 9, 239-244.
43. C. A. Kavounis, C. Tsiamis, C. J. Cardin, Y. Zubavichus, *Polyhedron*, 1996, 15, 385-390.
44. O. J. Parker, S. L. Aubol, G. L. Breneman, *Polyhedron*, 2000, 19, 623-626.
45. P. K. Byers, A. J. Canty, L. M. Engelhardt, J. M. Patrick, A. H. White, *J. Chem. Soc., Dalton Trans.*, 1985, 981-986.
46. G. Natile, G. Annibale, L. Canovese, L. Cattalini, M. Biagini-Cingi, A.-M. Manotti-Lanfredi, A. Tiripicchio, *J. Chem. Soc., Dalton Trans.*, 1981, 2280-2287.
47. B. E Fischer, H. Sigel, *J. Inorg. Nucl. Chem.*, 1975, 37, 2127.
48. K. N. Crowder, S. J. Garcia, R. L. Burr, J. M. North, M. H. Wilson, B. L. Conley, P. E. Fanwick, P. S. White, K. D. Sienerth, R. M. Granger, *Inorg. Chem.*, 2004, 43, 72-78.
49. Z. E. Serna, R. Cortés, M. K. Urtiaga, M. G. Barandika, L. Lezama, M. I. Arriortua, T. Rojo, *Eur. J. Inorg. Chem.*, 2001, 865-872.
50. Z. E. Serna, M. K. Urtiaga, M. G. Barandika, R. Cortés, S. Martin, L. Lezama, M. I. Arriortua, T. Rojo, *Inorg. Chem.*, 2001, 40, 4550.
51. G. S. Papaefstathiou, S. P. Perlepes, A. Escuer, R. Vicente, M. Font-Bardia, X. Solans, *Angew. Chem., Int. Ed. Engl.*, 2001, 40, 884.
52. G. S. Papaefstathiou, A. Escuer, C. P. Raptopoulou, A. Terzis, S. P. Perlepes, R. Vicente, *Eur. J. Inorg. Chem.*, 2001, 1567.
53. S. K. Padhi, R. Sahu, *Polyhedron*, 2008, 27, 2662-2666.
54. Y.-M. Li, J.-J. Zhang, R.-B. Fu, S.-C. Xiang, T.-L. Sheng, D.-Q. Yuan, X.-T. Wu, *Polyhedron*, 2006, 25, 1618-1624.
55. M.-L. Tong, S.-L. Zheng, J.-X. Shi, Y.-X. Tong, H. K. Lee, X.-M. Chen, *J. Chem. Soc., Dalton Trans.*, 2002, 1727-1734.

Chapter 1: Two Bipodal Ligand Frameworks:  
A Structural Exploration *via* X-Ray Diffraction Methods

56. N. Lalioti, C. P. Raptopoulou, A. Terzis, A. E. Aliev, I. P. Gerothanassis, E. Manessi-Zoupa, S. P. Perlepes, *Angew. Chem. Int. Ed.*, 2001, 40, 3211-3214.
57. A. Tsohos, S. Dionyssopoulou, C. P. Raptopoulou, A. Terzis, E. G. Bakalbassis, S. P. Perlepes, *Angew. Chem. Int. Ed.*, 1999, 38, 983-985.
58. T. C. Stamatatos, V. Nastopoulos, A. J. Tasiopoulos, E. E. Moushi, W. Wernsdorfer, G. Christou, S. P. Perlepes, *Inorg. Chem.*, 2008, 47, 10081-10089.
59. A. Erxleben, *Inorg. Chim. Acta*, 2009, 362, 839-834.
60. X.-D. Chen, M. Du, F. He, X.-M. Chen, T. C. W. Mak, *Polyhedron*, 2005, 24, 1047-1053.
61. G. S. Papaefstathiou, C. P. Raptopoulou, A. Tsohos, A. Terzis, E. G. Bakalbassis, S. P. Perlepes, *Inorg. Chem.*, 2000, 39, 4658.
62. H. Nierengarten, J. Rojo, E. Leize, J.-M. Lehn, A. Van Dorsselaer, *Eur. J. Inorg. Chem.*, 2002, 573-579.
63. T. Bark, R. P. Thummel, *Inorg. Chem.*, 2005, 44, 24, 8733-8739.
64. G. S. Hanan, J.-M. Lehn, N. Kyritsakas, J. Fischer, *J. Chem. Soc., Chem. Commun.*, 1995, 7, 765-766.
65. N. Singh, Ph.D. Dissertation, Cardiff University, 2008.
66. M. G. B. Drew, J. Nelson, F. Esho, V. Mckee, S. M. Nelson, *J. Chem. Soc., Dalton Trans.*, 1982, 1837.
67. D. V. Bautista, J. C. Dewan, L. K. Thompson, *Can. J. Chem.*, 1982, 60, 2583.
68. P. Krumholz, *J. Am. Chem. Soc.*, 1953, 75, 2163.
69. P. Krumholz, O. A. Serra, M. A. De Paoli, *Inorg. Chim. Acta*, 1975, 15, 25.
70. R. J. P. Williams, *J. Chem. Soc.*, 1955, 137-145.
71. A. B. P. Lever, J. Lewis, R. S. Nyholm, *J. Chem. Soc.*, 1964, 1187.

Chapter 1: Two Bipodal Ligand Frameworks:  
A Structural Exploration *via* X-Ray Diffraction Methods

72. A. B. P. Lever, *Inorganic Electronic Spectroscopy*, 1984, Elsevier, Amsterdam, The Netherlands.
73. A. B. P. Lever, *Coord. Chem. Rev.*, 1968, 3, 119.
74. B. F. Little, G. J. Long, *Inorg. Chem.*, 1978, 17, 3401.
75. G. M. Bancroft, K. D. Butler, *J. Chem. Soc., Dalton Trans.*, 1972, 1209.
76. F. A. Cotton, G. Wilkinson, *Advanced Inorganic Chemistry*, Wiley, New York, 5th edn., 1988, 733.
77. B. K. Santra, G. K. Lahiri, *J. Chem. Soc., Dalton Trans.*, 1998, 139-145.
78. W. C. Jones, W. E. Ball, *J. Chem. Soc. (A)*, 1968, 1849.
79. J. S. Merriam, J. R. Perrumareddi, *J. Phys. Chem.*, 1975, 79, 142.
80. M. C. Hughes, J. M. Rao, D. J. Macero, *Inorg. Chim. Acta*, 1979, 35, L321-L324.
81. N. G. Connelly, W. E. Geiger, *Chem. Rev.*, 1996, 96, 877-910.
82. M.-L. Tong, H. K. Lee, Y.-X. Tong, X.-M. Chen, T. C. W. Mak, *Inorg. Chem.*, 2000, 39, 4666-4669.
83. M. Bakir, J. A. M. McKenzie, *J. Electroanal. Chem.*, 1997, 425, 61-66.
84. M. Bakir, J. A. M. McKenzie, *J. Chem. Soc., Dalton Trans.*, 1997, 3571-3578.
85. J. E. B. Randles, *Trans. Faraday Soc.*, 1948, 44, 327.
86. A. J. Bard, L. R. Faulkner, *Electrochemical Methods: Fundamentals and Applications*, Wiley, 2001.
87. N. Tanaka, Y. Sato, *Bull. Chem. Soc. Jap.*, 1968, 41, 2059-2064.
88. R. H. Blessing, *Acta Crystallogr.*, 1995, A51, 33-38.
89. A. Altomare, G. Cascarano, C. Giacovazzo and A. Guagliardi, *J. Appl. Crystallogr.*, 1993, 26, 343-350.

Chapter 1: Two Bipodal Ligand Frameworks:  
A Structural Exploration *via* X-Ray Diffraction Methods

90. G. M. Sheldrick, SHELXL-97, Program for the Refinement of Crystal Structures, University of Göttingen, Germany, 1997.
91. L. J. Farrugia, *J. Appl. Crystallogr.*, 1997, 30, 565.
92. C. Ruiz-Perez, Y. Rodriguez-Martin, J. Gonzalez-Platas, *Acta Crystallogr.*, 1999, C55, 186.
93. The Cambridge Structural Database: a quarter of a million structures and rising. F. H. Allen, *Acta Crystallogr.*, 2002, B58, 380-388.
94. New Software for searching the Cambridge Structural Database and visualising crystal structures. I. J. Bruno, J. C. Cole, P. R. Edgington, M. Kessler, C. F. McCabe, J. Pearson, R. Taylor, *Acta Crystallogr.*, 2002, B58, 389-397.
95. S. V. Kryatov, S. Taktak, I. V. Korendovych, E. V. Rybak-Akimova, J. Kaizer, S. Torelli, X. Shaun, S. Mandal, V. L. MacMurdo, A. M. Payeras, L. Que Jr., *Inorg. Chem.*, 2005, 44, 85.
96. R. Atencio, G. Liendo, A. Briceno, T. Gonzalez, *Acta Crystallogr.*, 2004, E60, m1028.
97. C. Ruiz-Perez, Y. Rodriguez-Martin, J. Gonzalez-Platas, *Acta Crystallogr.*, 1999, C55, 1087.
98. E. D. McKenzie, *Coord. Chem. Rev.*, 1971, 6, 187-216.
99. Y. Bai, Y. Li, E. Wang, X. Wang, Y. Lu, L. Xu, *J. Mol. Struct.*, 2005, 752, 54.
100. R.-L. Zhang, J.-S. Zhao, S.-Y. Yang, S. W. Ng, *Acta Crystallogr.*, 2004, E60, m262.
101. B.-H. Ye, F. Xue, G.-Q. Xue, L.-N. Ji, T. C. W. Mak, *Polyhedron*, 1999, 18, 1785, CCDC deposition no. 112076.
102. N. N. Murthy, K. D. Karlin, *Chem. Commun.*, 1993, 1236.
103. Z. R. Ranjbar, A. Morsali, L.-G. Zhu, *J. Coord. Chem.*, 2007, 60, 667-676. CCDC deposition no. 289459.

Chapter 1: Two Bipodal Ligand Frameworks:  
A Structural Exploration *via* X-Ray Diffraction Methods

104. J. Valdes-Martinez, R. A. Toscano, D. Salazar-Mendoza, *Acta Crystallogr.*, 2001, E57, m331. CCDC deposition no. 170860.

Chapter 2: A Bipyridine-based Tripodal Framework with a Strong Preference for Trigonal Prismatic Co-ordination Geometries

# **Chapter 2: A Bipyridine-based Tripodal Framework with a Strong Preference for Trigonal Prismatic Co-ordination Geometries**

## 2.1 Scheme for Chapter 2

Chapter 2 takes a detailed look at a series of transition metal complexes formed by the tripodal bipyridine-based ligand framework,  $L^3$  (Fig. 1). This tris-bipyridyl ligand has been shown to enforce a predominantly trigonal prismatic co-ordination environment around a metal centre, even in cases where the metal has a strong stereoelectronic octahedral preference. The relationship between octahedral and trigonal prismatic character as the d-electron configuration of the metal centre is varied has been examined. Using the Cartesian co-ordinates obtained from crystallographic data sets, continuous shape mapping analysis (CShM) has been employed to assist in the quantification of the distortions away from these two ideal geometries.

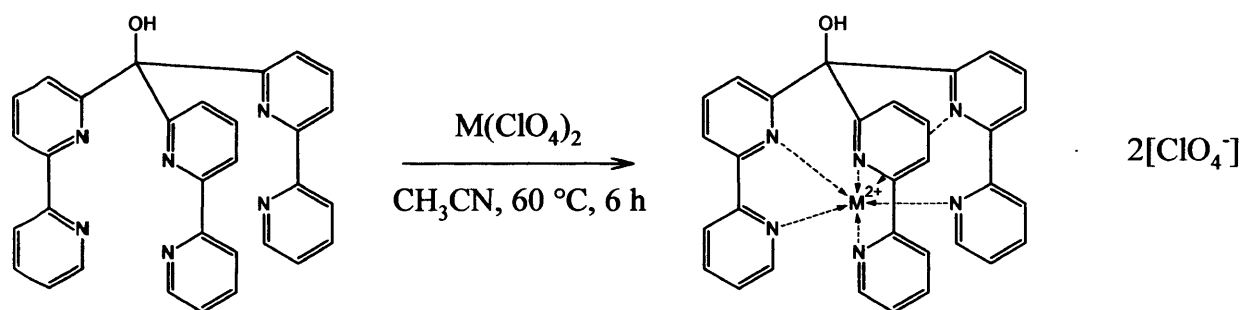


**Figure 1:** The tris-bipyridyl ligand,  $L^3$  (left), undergoes complexation to form monomeric transition metal complexes with varying degrees of Bailar twist.

## 2.2 Introduction

### The Bailar Twist

In 1958, Bailar proposed that six co-ordinate molecular complexes exhibiting trigonal prismatic (TP) geometries could exist as intermediates during the racemisation of tris-chelate complexes.<sup>1</sup>

The ‘Bailar twist’ has since become the conventional means of describing the interconversion of an octahedral and TP co-ordination geometry (Fig. 2). Either geometry can be visualised in terms

of two sets of three donor atoms arranged as equilateral triangles, lying above and below a metal centre. The Bailar twist angle,  $\phi$ , is defined as the mean average torsion  $A'-C_n-C_n'-B'$  angle ( $C_n, C_n'$  = centroids of the triangles;  $A', B'$  = near eclipsed pair of donor atoms) between the two opposite trigonal faces. In the case of a perfect trigonal prism,  $\phi$  is  $0^\circ$  *i.e.* an eclipsed conformation, and rotating one triangular face upon the other by  $60^\circ$  produces a perfect octahedral geometry.

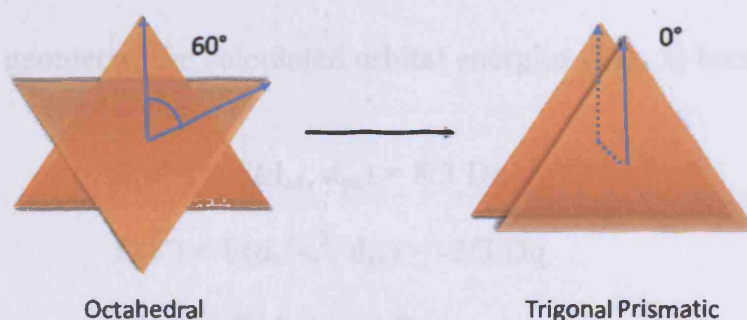


**Figure 2:** The Bailar twist interconversion between octahedral and trigonal prismatic geometries.

### Trigonal Prismatic vs Octahedral Co-ordination Geometries

The TP geometry is typically unfavourable as the internuclear separation between the eclipsed sets of donor atoms is  $\sqrt{2/3}$  the value of an octahedron, consequently the non-bonded contacts are increased and the overall stabilisation is lowered. Such internuclear repulsion could be compensated by lengthening the metal-ligand bond distances, however, this would again lower the stabilisation with respect to an octahedron where the metal-ligand interactions are maximised. Therefore, a ligand framework with strong steric and torsional preferences is typically required to enforce TP co-ordination.

The stereoelectronic preference of the metal cation centre can also have a significant influence upon the resulting co-ordination environment. This can be determined by a comparison of the octahedral and TP ligand field stabilisation energies (LFSE). Wentworth<sup>2</sup> derived a



## Chapter 2: A Bipyridine-based Tripodal Framework with a Strong Preference for Trigonal Prismatic Co-ordination Geometries

formula to approximate the general ligand field potential (assuming a constant polar angle\* of  $\cos^{-1}\sqrt{1/3}$ ) as a function of the twist angle (equation 1):

$$V_{LF} = 14eq\sqrt{\pi} \{-Y_4^0 - \sqrt{5/14} [(1-e^{-i3\alpha})Y_4^3 - (1-e^{i3\alpha})Y_4^{-3}]\} (r^4/R^5)/9 \quad (1)$$

where  $e$  = electronic charge,  $r$  = radius,  $q$  = effective charge,  $R$  = metal-ligand distance, and the  $Y_l^m$  are spherical harmonics.

At  $\phi = 0^\circ$ , *i.e.* a TP geometry, the calculated orbital energies (Fig. 3) become:

$$E(e'') \equiv E(d_{xz}, d_{yz}) = 8/3 Dq \quad (2)$$

$$E(e') \equiv E(d_x^2 - y^2, d_{xy}) = -2/3 Dq \quad (3)$$

$$E(a_1') \equiv E(d_z^2) = -4 Dq \quad (4)$$

In the case of most six-coordinate complexes an octahedral environment is favourable, this is because the energy span of the d-orbitals in a octahedron (30/3) is larger than in a TP arrangement (20/3).<sup>2</sup> Wentworth also carried out a detailed comparison of the LFSE values associated with octahedral and TP co-ordination for the various  $d^n$  electronic configurations, producing a useful diagram reproduced below (Fig. 4). It revealed that while indeed most  $d^n$ -electron configurations do exhibit an octahedral preference over trigonal prismatic, there are a few exceptions which have no octahedral preference:  $d^0$ ,  $d^1$ , low-spin  $d^2$ , high-spin  $d^5$ , high-spin  $d^6$  and  $d^{10}$ .

---

\* The polar angle here refers to the average angle between the  $C_3$  axis and the co-ordinative bonds.

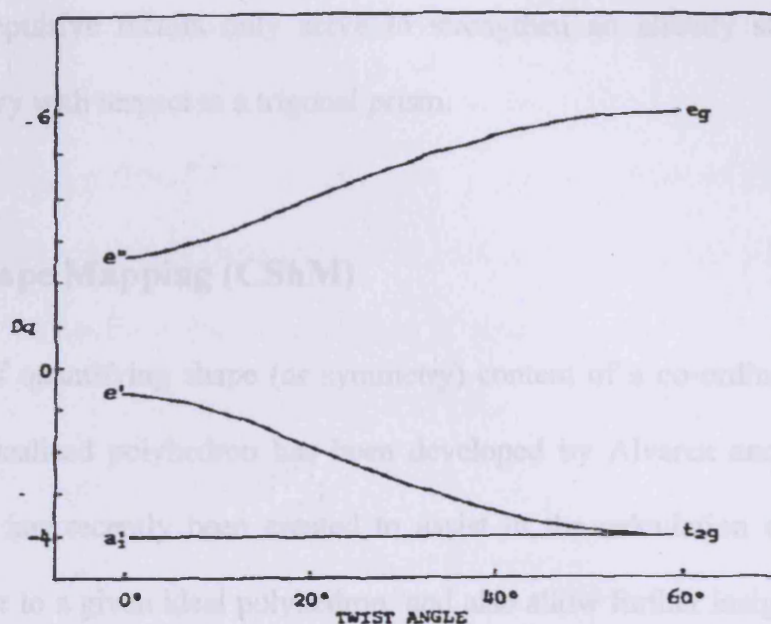


Figure 3: A diagram showing how the energies of the d-orbitals change as a function of the twist angle.

Sourced directly from ref 2.

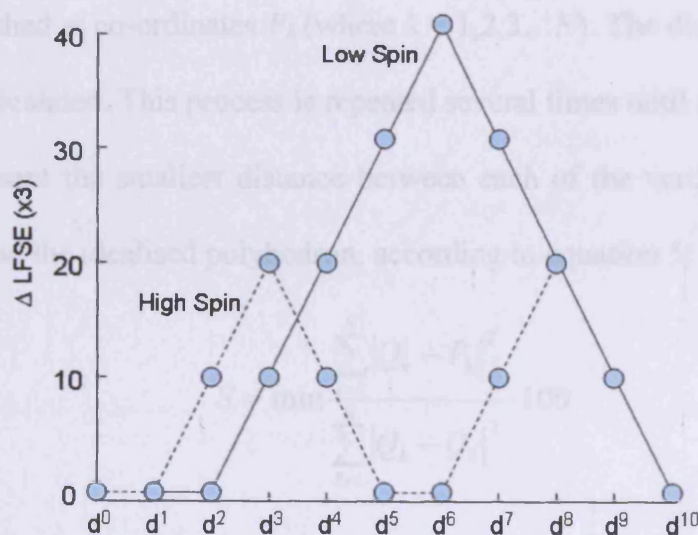


Figure 4: Variation of  $\Delta LFSE$  with the d orbital occupation number, where  $\Delta LFSE = LFSE(\text{octahedron}) - LFSE(\text{trigonal prism})$

It is also important to consider electronic repulsive energies due to electrons occupying the d-orbitals. Most remarkably, in the case of high-spin  $d^7$ , trigonal prismatic geometries become only  $\sim 5\text{kcal}$  more unstable than an octahedron. While in the case of low-spin  $d^6$  and (to a

## Chapter 2: A Bipyridine-based Tripodal Framework with a Strong Preference for Trigonal Prismatic Co-ordination Geometries

degree)  $d^8$ , the repulsive factors only serve to strengthen an already strong preference for octahedral geometry with respect to a trigonal prism.

### Continuous Shape Mapping (CShM)

A useful means of quantifying shape (or symmetry) content of a co-ordination geometry with reference to an idealised polyhedron has been developed by Alvarez and co-workers.<sup>3-8</sup> The program *SHAPE*<sup>\*</sup> has recently been created to assist in the calculation of the *distance* of a molecular structure to a given ideal polyhedron, and also allow further insight into the nature of the distortion. This method first takes into consideration the Cartesian co-ordinates of the polyhedron (with  $N$  vertices) under investigation,  $Q_k$  (where  $k = 1,2,3\dots N$ ). Next, a perfect polyhedron is established at co-ordinates  $P_k$  (where  $k = 1,2,3\dots N$ ). The distance between each of the vertices is then calculated. This process is repeated several times until a set of  $P_k$  co-ordinates is found which represent the smallest distance between each of the vertices of the polyhedron under investigation and the idealised polyhedron, according to equation 5:

$$S = \min \frac{\sum_{k=1}^N |Q_k - P_k|^2}{\sum_{k=1}^N |Q_k - Q_0|^2} \cdot 100 \quad (5)$$

where  $S$  is the shape measure of the investigated structure and  $Q_0$  is the position vector of the geometrical centre of the problem structure.

The vertices of, for example, a metal complex co-ordination geometry which has near-perfect symmetry will therefore lie only a small distance away from the ideal polyhedron and will

---

\* *SHAPE* v1.1b was obtained directly from the authors who assisted in the interpretation of the results.

## Chapter 2: A Bipyridine-based Tripodal Framework with a Strong Preference for Trigonal Prismatic Co-ordination Geometries

consequently have a shape measure,  $S$ , close to zero. A polyhedron which departs significantly from perfect symmetry will naturally have a higher  $S$  value.

Alvarez *et al.* have produced scatter plots (or shape maps) which plot two reference polyhedra (with equal number of vertices) against each other. The placement of a shape on such a map can give useful insight into the exact nature of distortion away from an idealised structure. Figure 5 is a plot of  $S(\text{Octahedron})$  versus  $S(\text{Trigonal Prism})$  showing the Bailar pathway amongst other types of distortions.\*

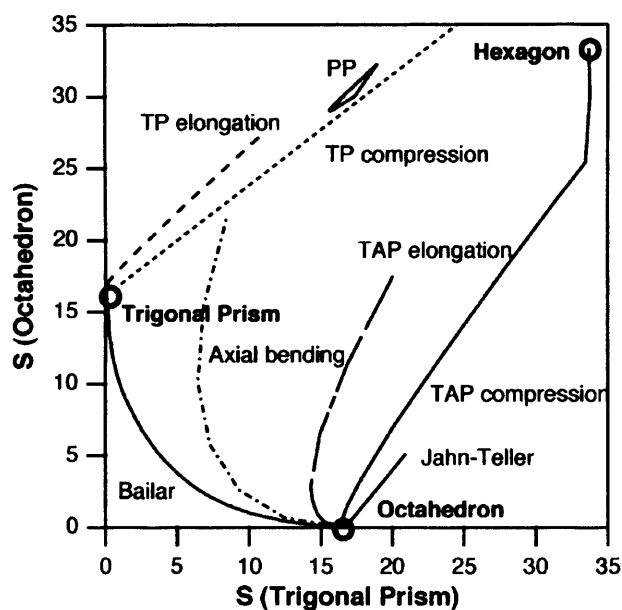


**Figure 5:** Shape map for the geometrical distortions of the octahedron and the trigonal prism. This diagram is sourced directly from reference 3.

The shape measures of a structure which lies on the Bailar pathway must obey the following equation:

$$\arcsin \frac{\sqrt{S(\text{Oct})}}{10} + \arcsin \frac{\sqrt{S(\text{TP})}}{10} = \theta_{\text{Oct,TP}} \quad (6)$$

where  $\theta_{\text{Oct,TP}}$  is a constant for this pair of polyhedra, representing the symmetry angle.

\* A detailed description of each of these distortions can be found in ref 3.

## Chapter 2: A Bipyridine-based Tripodal Framework with a Strong Preference for Trigonal Prismatic Co-ordination Geometries

In cases where a structure does not lie directly along this minimal distortion interconversion pathway, this deviation can be measured *via* the following equation:

$$\Delta(TP, Oct) = \frac{1}{\theta_{Oct,TP}} \left[ \arcsin \frac{\sqrt{S(Oct)}}{10} + \arcsin \frac{\sqrt{S(TP)}}{10} \right] - 1 \quad (7)$$

### A Review of Known Trigonal Prismatic Compounds

Metal complexes with trigonal prismatic co-ordination geometries are comparatively rare with respect to octahedral environments. The first publication featuring trigonal prismatic compounds appeared in 1923, concerning the infinite lattice structures of minerals  $\text{MoS}_2$  and  $\text{WS}_2$ .<sup>9</sup> In 1965, Ibers and Eisenberg<sup>10,11</sup> characterised a dithiolato complex, tris(cis-1,2-diphenylethene-1,2-dithiolato)rhenium (Fig. 6), *via* single-crystal X-ray diffraction studies and established that while the overall molecular symmetry was  $C_3$ , the co-ordination geometry was clearly TP, this was the first discrete molecular compound of this type.

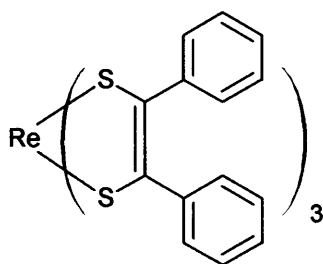


**Figure 6:** The complex tris(cis-1,2-diphenylethene-1,2-dithiolato)rhenium was the first reported discrete molecular compound with a trigonal prismatic co-ordination sphere.

This report was received with much interest and soon afterwards the analogous complexes  $\text{Mo}(\text{S}_2\text{C}_2\text{H}_2)_3$ ,<sup>12</sup>  $\text{V}[\text{S}_2\text{C}_2(\text{C}_6\text{H}_5)_2]_3$ ,<sup>13,14</sup> were also reported to have TP or near-TP co-ordination spheres. Several other dithiolato complexes of these metal ions, as well as chromium

## Chapter 2: A Bipyridine-based Tripodal Framework with a Strong Preference for Trigonal Prismatic Co-ordination Geometries

and tungsten, have also exhibited TP environments. Although the exact cause of these unusual geometries remains uncertain, interligand S-S bonding is thought to be largely responsible for the TP nature of these complexes.<sup>15,16</sup> Furthermore, since the ideal L–M–L bond angle is 90° in an ideal octahedron and 81.8° in an trigonal prism, ligands with a small bite angle are more suited to TP co-ordination.

In a similar investigation into trigonal prismatic co-ordination environments, Wentworth *et al.* investigated the Mn<sup>II</sup>, Fe<sup>II</sup>, Co<sup>II</sup>, Ni<sup>II</sup> and Zn<sup>II</sup> complexes of the Schiff base ligand *cis,cis*-1,3,5-tris(pyridine-2-carboxaldimino)cyclohexane ((py)<sub>3</sub>tach; Fig. 7).<sup>17-19</sup> Space-filling molecular models of this ligand indicated the donor atoms adopt positions on the vertices of a trigonal prism in the absence of a metal. X-ray diffraction studies of the corresponding zinc complex revealed that the TP co-ordination geometry remained largely unperturbed as was expected due to the lack of stereoelectronic preference of the d<sup>10</sup> metal ion. The powder X-ray diffraction patterns of the analogous Mn<sup>II</sup> and Co<sup>II</sup> complexes were essentially indistinguishable from that of the zinc structure, leading to the conclusion that these complexes also maintained TP geometries in the solid state. The powder X-ray diffraction patterns of the Fe<sup>II</sup> and Ni<sup>II</sup> complexes were different with respect to the Mn<sup>II</sup>, Co<sup>II</sup> and Zn<sup>II</sup> complexes, as well as to each other, suggesting non-TP geometries in each case. The electronic spectra of the Fe<sup>II</sup> and Ni<sup>II</sup> complexes also provided strong evidence of octahedral or near-octahedral co-ordination environments. Indeed, single-crystal X-ray diffraction experiments on the complex [Ni<sup>II</sup>(py)<sub>3</sub>tach]<sup>2+</sup> later revealed a Bailar twist angle of 32°. <sup>19</sup> It was concluded, therefore, that while the conformational preference of the ligand is trigonal prismatic, the presence of metal ions which have a strong octahedral preference such as Fe<sup>II</sup> and Ni<sup>II</sup> (low-spin d<sup>6</sup> and d<sup>8</sup> respectively) significantly influence the resulting conformation, forcing it to adopt a non-TP geometry. While the Co<sup>II</sup> (high-spin d<sup>7</sup>) ion does have an electronic preference for octahedral configurations, the difference in ligand-field

## Chapter 2: A Bipyridine-based Tripodal Framework with a Strong Preference for Trigonal Prismatic Co-ordination Geometries

stabilisation between octahedral and trigonal prismatic configurations is comparatively much less and evidently not sufficient to influence the ligand conformation to the same extent.

A similar example is provided in the ligand 1,1',1''-tris(pyridine-2-carboxaldiminomethyl)ethane ((py)<sub>3</sub>tame; Fig. 7).<sup>20</sup> In this instance, whilst this compound also adopts a near-TP configuration in the absence of a metal, the structural rigidity of the ligand framework with respect to (py)<sub>3</sub>tach is reduced. Consequently, the corresponding Zn<sup>II</sup> complex reveals a much larger Bailar twist angle of 28°. The analogous Mn<sup>II</sup>, Co<sup>II</sup> and Ni<sup>II</sup> complexes were isomorphous with the zinc complex and it was proposed that these complexes probably exhibit similar geometries. The Fe<sup>II</sup> complex of this ligand revealed a Bailar twist angle of 43° which is indicative of the strong stereochemical preference low-spin d<sup>6</sup> metal ions have for octahedral geometries.

The even more rigid clathro-chelate fluoroborotris(2-carboxaldoximo-6-pyridyl)phosphine<sup>21-23</sup> (Fig. 7) first reported by Holm *et al.* encapsulates metal ions upon coordination and imposes a strongly trigonal prismatic environment. The clathro-chelates provide high thermodynamic stability and virtual kinetic inertness. The low-spin Fe<sup>II</sup> complex exhibited a Bailar twist angle of *ca.* 21° which indicates that even in the presence of a metal ion with a very strong octahedral preference, this framework still maintains predominantly TP character. A similar clathro-chelate 1,8-bis(fluoroboro)-2,7,9,14,15,20-hexaoxa-3,6,10,13,16,19-hexaaza-4,5,11,12,17,18-hexamethylbicyclo[6.6.6]eicosa-3,5,10,12,16,18-hexaene<sup>24</sup> (Fig. 7) reported by Rose *et al.* reveals similar behaviour. The Co<sup>II</sup> and Co<sup>III</sup> complexes of this ligand were investigated by single-crystal X-ray diffraction and exhibited Bailar twist angles of 8.6° and *ca.* 22° respectively.<sup>25</sup>

## Chapter 2: A Bipyridine-based Tripodal Framework with a Strong Preference for Trigonal Prismatic Co-ordination Geometries

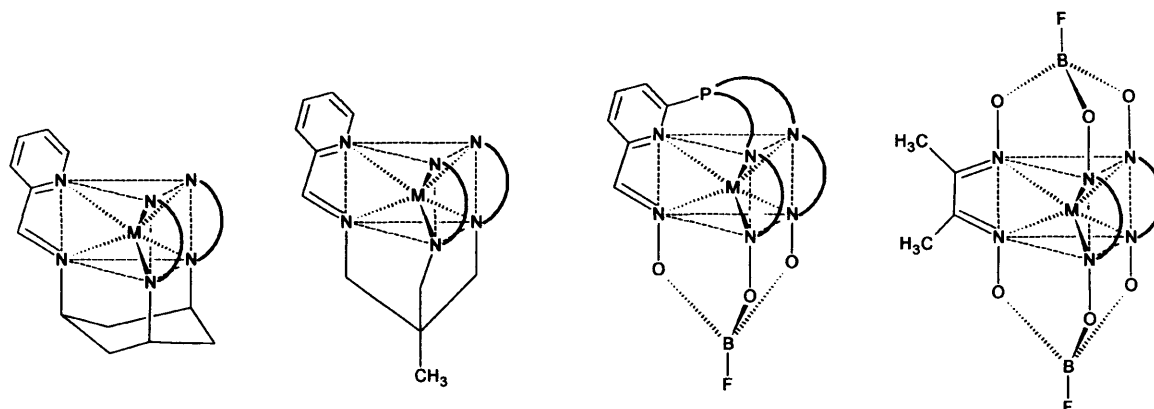
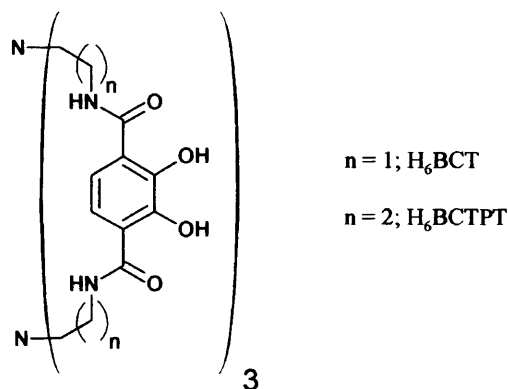


Figure 7: Various metal complexes of the ligands (py)<sub>3</sub>tach, (py)<sub>3</sub>tame, and the clathro-chelates reported by Holm and Rose (left to right) have revealed predominantly trigonal prismatic co-ordination geometries.<sup>26</sup>

Raymond *et al.* reported the bimakrocyclic ligands bicappedTRENAM (BCT) and bicappedTPTCAM (BCTPT) which also exhibit predisposition for TP co-ordination (Fig. 8).<sup>16</sup> The complexes of BCT with the metals Ti<sup>IV</sup>, V<sup>IV</sup> and Fe<sup>III</sup> each reveal pseudo-TP environments, however the complexes involving Al<sup>III</sup> and Ga<sup>III</sup> metal ions were better described as pseudo-octahedral. Spectroscopic evidence was provided indicating that the TP geometries of the d-block metal complexes are stabilised by  $\pi$ -bonding. These d-orbitals are filled in the case of Ga<sup>III</sup> and not accessible in energy for Al<sup>III</sup>, therefore in these instances the resulting co-ordination geometry is decided largely by repulsive interactions. The Fe<sup>III</sup> complex of the larger macrobicycle BCTPT was shown by X-ray structural analysis to have a twist angle of 39.5°, indicative of pseudo-octahedral character, however the overall co-ordination environment was reported to more closely resemble a TP geometry. Evidently, the introduction of additional carbon spacer atoms in the case of BCTPT leads to a reduction in the structural rigidity of the ligand framework and, consequently, repulsive interactions have more bearing on the resulting conformation.



Chapter 2: A Bipyridine-based Tripodal Framework with a Strong Preference for Trigonal Prismatic Co-ordination Geometries



**Figure 8:** The bimacrocyclic ligands bicappedTREN CAM ( $H_6BCT$ ) and bicappedTPTCAM ( $H_6BCTPT$ )

Structurally rigid ligand frameworks with a predisposition for TP co-ordination are not necessarily a prerequisite for generating TP complexes. Peacock *et al.* reported the first examples of trigonal prismatic cobalt complexes incorporating non-rigid ligands.<sup>27</sup> This group had previously studied the hexadentate pendant-arm macrocyclic ligand  $N,N',N''$ -tris-(2*R*)-2-hydroxypropyl-1,4,7-[9]aneN<sub>3</sub> (Fig. 9; left) and suggested the likely formation of octahedral geometries with  $Co^{II}$ . However, expanding the macrocyclic ring led to, in the case of  $H_3L^2$  and  $H_3L^4$ , trigonal prismatic complexes with  $Co^{II}$ , which were confirmed by single-crystal X-ray diffraction. While no crystal structure was obtained for  $H_3L^3$ , it was anticipated that this ligand would most likely adhere to this trend and also form a trigonal prismatic complex with  $Co^{II}$ . Interestingly, while the ligand  $H_3L^2$  probably imposed the trigonal prismatic environment in the  $Co^{II}$  complex, this ligand was previously found to form octahedral co-ordination geometries in a ( $Mn^{II}, Mn^{IV}$ ) hydrogen-bridged dimer.<sup>28-29</sup>

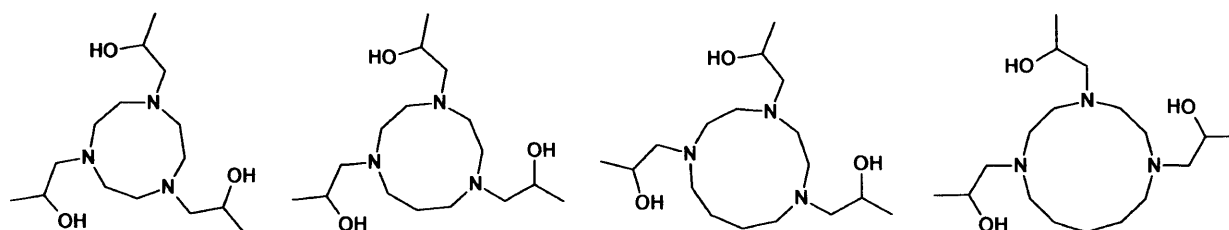


**Figure 9:** Examples of non-rigid ligand frameworks leading to trigonal prismatic co-ordination geometries.  $H_3L^1$ ,  $H_3L^2$ ,  $H_3L^3$  and  $H_3L^4$  (left to right).

## Chapter 2: A Bipyridine-based Tripodal Framework with a Strong Preference for Trigonal Prismatic Co-ordination Geometries

Another interesting example is provided in the compound  $[\text{Li}(\text{tmed})]_2[\text{Zr}(\text{Me})_6]$  (where  $\text{tmed} = N,N,N',N'$ -tetramethylethylenediamine), reported by Girolami *et al.* in 1989.<sup>30</sup> In this instance, the zirconium is situated within an essentially perfect trigonal prism of six homoleptic donors. It was proposed that the resulting geometry was “probably *intrinsic* to the  $[\text{Zr}(\text{Me})_6]^{2-}$  anion” and not influenced by the two  $[\text{Li}(\text{tmed})]^+$  cations. For a  $d^0$  ion of  $O_h$  symmetry, the HOMO (which is composed of metal p-orbitals and ligand  $\sigma$ -orbitals of  $T_{1u}$  symmetry) and the LUMO (composed of the non-bonding metal d-orbitals of  $T_{2g}$  symmetry) cannot mix by symmetry. Upon lowering the symmetry to  $D_{3h}$  (a second-order Jahn-Teller effect), the HOMO and LUMO undergo a conversion to  $E' + A_2''$  and  $E' + A_2'$  respectively. Following this transformation, the  $E'$  ( $d_x^2 - y^2, d_{xy}$ ) set of orbitals that constitute the LUMO can mix with the occupied metal-ligand  $\sigma$ -bonding orbitals. The overall result of this mixing lowers the energy of the HOMO and therefore it was concluded that  $d^0$   $\text{ML}_6$  complexes evidently have an intrinsic electronic preference for adopting non-octahedral co-ordination geometries.

More recently, Ward and McCleverty *et al.* showed that the ligand tris(pyrazolyl)borate ( $\text{Tp}^{\text{py}}$ ; Fig. 10) can be co-ordinated with  $\text{Zn}^{\text{II}}$  and  $\text{Mn}^{\text{II}}$  to give tetrameric  $[\text{M}_4\text{L}_4]^{4+}$  octahedral complexes<sup>31,32</sup> or with  $\text{Co}^{\text{II}}$  to give the monomeric trigonal prismatic species,  $[\text{Co}(\text{Tp}^{\text{py}})][\text{PF}_6]$ .<sup>33-</sup>  
<sup>35</sup> The ligand in this instance naturally adopts a trigonal prismatic conformation, furthermore simple molecular modelling studies have indicated that the formation of an octahedral geometry in a 1:1 metal to ligand complex would cause significant ligand strain. At first glance, the co-ordination environments of these complexes seem contrary to that predicted by simple LSFE arguments; it would be reasonable to assume the high-spin ( $d^7$ )  $\text{Co}^{\text{II}}$  complex would prefer the octahedral tetrameric environment and the  $\text{Mn}^{\text{II}}$  and  $\text{Zn}^{\text{II}}$  with no stereoelectronic preference would be co-ordinated in a trigonal prismatic fashion, leaving the natural conformation of the ligand largely undistorted. However, one must also consider the electronic repulsive energies due

## Chapter 2: A Bipyridine-based Tripodal Framework with a Strong Preference for Trigonal Prismatic Co-ordination Geometries

to electrons occupying the d-orbitals. This now leads to, in the case of high-spin  $d^7$ , TP geometries being only  $\sim 5$  kcal more unstable than the octahedral analogue. The tetrameric  $Mn^{II}$  and  $Zn^{II}$  complexes both involve the ligand co-ordinating one arm to each of the three metal ions, generating a tetrahedral cluster with each ligand face-capping. Various forms of spectroscopic evidence indicated that all three complexes were maintained in solution and there was no indication of any interconversion between these forms. It was proposed that the basis for the different binding modes of the  $Tp^{py}$  ligand was driven by the stereoelectronic preferences of the metal ions involved.

The work presented in this chapter describes the co-ordination chemistry of a rigid hexadentate tripodal ligand, tris(2,2'-bipyrid-6-yl)methanol ( $L^3$ ; Fig. 10), which enforces pseudo-TP geometries upon co-ordination to a series of transition metals. Furthermore, this work examines the relationship between the octahedral and trigonal prismatic character of these complexes as the d-electron configuration of the metal centre is varied. Unlike  $Tp^{py}$ ,  $L^3$  is (i) a neutral ligand meaning that the formation of tetrameric species would lead to greater unfavourable electrostatic repulsions and (ii) having no 5-membered rings it is better sterically suited to chelating a single metal.

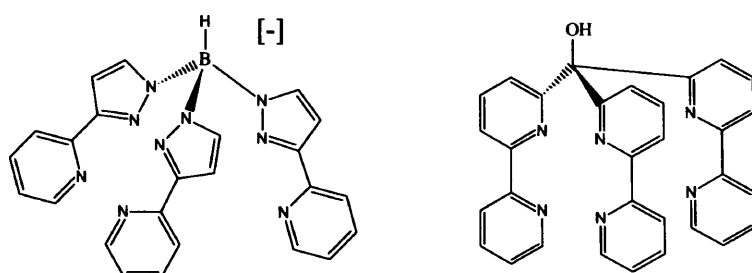


**Figure 10:** The tripodal framework tris(pyrazolyl)borate ( $Tp^{py}$ ; left) alongside  $L^3$  (right) for comparison.

## 2.3 Experimental

### 2.3.1 General

The details regarding the collection of experimental data are the same as those reported in Chapter 1 (p.16).

### 2.3.2 Preparations

#### 2.3.2.1 General Procedure for the synthesis of metal complexes

Ligand  $L^3$  (1 equivalent, typically 0.1 mmol) was dissolved in the minimum amount of acetonitrile (typically 3 mL). The solutions were warmed to *ca.* 60°C to ensure that the ligand fully dissolved. To this stirred solution, the metal perchlorate salt (1 equivalent) dissolved in either acetonitrile or water (typically ~2 mL) was added dropwise. In all cases, a precipitate formed and was collected and dried in air. Recrystallisation of the compounds typically involved the diffusion of diethyl ether into acetonitrile or methanolic solutions which were filtered through Celite.

**WARNING:** Perchlorate salts of metal complexes are potentially explosive. Care should be taken while handling such complexes.

$[\text{Mn}^{\text{II}}(L^3)]_2[\text{ClO}_4]_2 \cdot \text{H}_2\text{O}$  (2.1): Pale yellow crystals (62% yield). Found: C, 48.79; H, 3.30; N, 11.10%.  $\text{MnC}_{31}\text{H}_{22}\text{N}_6\text{O}(\text{ClO}_4)_2 \cdot \text{H}_2\text{O}$  requires C, 48.58; H, 3.16; N, 10.97%; HRMS (ES) *m/z* (%): 648.0695 (100) ( $[\text{Mn}(L^3) + \text{ClO}_4]^+$ ;  $\text{MnC}_{31}\text{H}_{22}\text{ClN}_6\text{O}_5$  requires 648.0721); IR (KBr pellet,

Chapter 2: A Bipyridine-based Tripodal Framework with a Strong Preference for Trigonal Prismatic Co-ordination Geometries

$\text{cm}^{-1}$ ): 3398(br), 3093(m), 1597(s), 1453(s), 1101(s), 768(s), 623(s); UV/Vis [ $\lambda_{\text{max}}$ , nm ( $\epsilon_{\text{M}}$ ,  $\text{M}^{-1}\text{cm}^{-1}$ )] in  $\text{CH}_3\text{CN}$ : 241(21,250), 295(23,000), 314(6,500).

**[Fe<sup>II</sup>(L<sup>3</sup>)](ClO<sub>4</sub>)<sub>2</sub>·0.5CH<sub>3</sub>CN (2.2)**: Purple crystals (58% yield). Found: C, 50.19; H, 3.24; N, 12.49%. FeC<sub>31</sub>H<sub>22</sub>N<sub>6</sub>O(ClO<sub>4</sub>)<sub>2</sub>·CH<sub>3</sub>CN requires C, 50.15; H, 3.19; N, 12.41%; HRMS (ES)  $m/z$  (%): 549.1113 (100) ([Fe(L<sup>3</sup>) - H]<sup>+</sup>; FeC<sub>31</sub>H<sub>21</sub>N<sub>6</sub>O requires 549.1126); IR (KBr pellet,  $\text{cm}^{-1}$ ): 3421(br), 3096(m), 1604(s), 1453(s), 1093(s), 769(s), 623(s); UV/Vis [ $\lambda_{\text{max}}$ , nm ( $\epsilon_{\text{M}}$ ,  $\text{M}^{-1}\text{cm}^{-1}$ )] in  $\text{CH}_3\text{CN}$ : 245(22,500), 296(25,000), 316(7,000), 497(57), 557(79).

**[Co<sup>II</sup>(L<sup>3</sup>)](ClO<sub>4</sub>)<sub>2</sub>·0.5CH<sub>3</sub>CN (2.3)**: Orange crystals (65% yield). Found: C, 50.09; H, 3.20; N, 12.46%. CoC<sub>31</sub>H<sub>22</sub>N<sub>6</sub>O(ClO<sub>4</sub>)<sub>2</sub>·CH<sub>3</sub>CN requires C, 49.95; H, 3.18; N, 12.36%; HRMS (ES)  $m/z$  (%): 652.0673 (100) ([Co(L<sup>3</sup>) + ClO<sub>4</sub>]<sup>+</sup>; CoC<sub>31</sub>H<sub>22</sub>N<sub>6</sub>O<sub>5</sub>Cl requires 652.0672); IR (KBr pellet,  $\text{cm}^{-1}$ ): 3399(br), 3091(m), 1603(s), 1454(s), 1095(s), 769(s), 623(s); UV/Vis [ $\lambda_{\text{max}}$ , nm ( $\epsilon_{\text{M}}$ ,  $\text{M}^{-1}\text{cm}^{-1}$ )] in  $\text{CH}_3\text{CN}$ : 242(24,200), 294(21,000), 314(3,300), 468(112), 1052(14).

**[Ni<sup>II</sup>(L<sup>3</sup>)](ClO<sub>4</sub>)<sub>2</sub>·0.5CH<sub>3</sub>CN (2.4)**: Purple crystals (78% yield). Found: C, 50.03; H, 3.24; N, 12.48%. NiC<sub>31</sub>H<sub>22</sub>N<sub>6</sub>O(ClO<sub>4</sub>)<sub>2</sub>·CH<sub>3</sub>CN requires C, 49.97; H, 3.18; N, 12.36%; HRMS (EI)  $m/z$  (%): 651.0668 (100) ([Ni(L<sup>3</sup>) + ClO<sub>4</sub>]<sup>+</sup>; NiC<sub>31</sub>H<sub>22</sub>N<sub>6</sub>O<sub>5</sub>Cl requires 651.0694); IR (KBr pellet,  $\text{cm}^{-1}$ ): 3388(br), 3092(m), 1605(s), 1453(s), 1104(s), 771(s), 623(s); UV/Vis [ $\lambda_{\text{max}}$ , nm ( $\epsilon_{\text{M}}$ ,  $\text{M}^{-1}\text{cm}^{-1}$ )] in  $\text{CH}_3\text{CN}$ : 248(23,050), 295(25,600), 315(6,200), 532(9), 827(2), 958(56).

**[Cu<sup>II</sup>(L<sup>3</sup>)](ClO<sub>4</sub>)<sub>2</sub>·2CH<sub>3</sub>CN (2.5)**: Blue crystals (52% yield). Found: C, 50.05; H, 3.38; N, 13.49%. CuC<sub>31</sub>H<sub>22</sub>N<sub>6</sub>O(ClO<sub>4</sub>)<sub>2</sub>·2CH<sub>3</sub>CN requires C, 50.10; H, 3.36; N, 13.35%. HRMS (ES)  $m/z$  (%): 656.0611 (100) ([Cu(L<sup>3</sup>) + ClO<sub>4</sub>]<sup>+</sup>; CuC<sub>31</sub>H<sub>22</sub>N<sub>6</sub>O<sub>5</sub>Cl requires 656.0636); IR (KBr pellet,

## Chapter 2: A Bipyridine-based Tripodal Framework with a Strong Preference for Trigonal Prismatic Co-ordination Geometries

$\text{cm}^{-1}$ ): 3448(br), 3093(m), 1609(s), 1453(s), 1101(s), 770(s), 622(s); UV/Vis [ $\lambda_{\text{max}}$ , nm ( $\epsilon_{\text{M}}$ ,  $\text{M}^{-1}\text{cm}^{-1}$ )] in  $\text{CH}_3\text{CN}$ : 246(22,350), 301(29,650), 315(4,900), 636(61), 754(32).

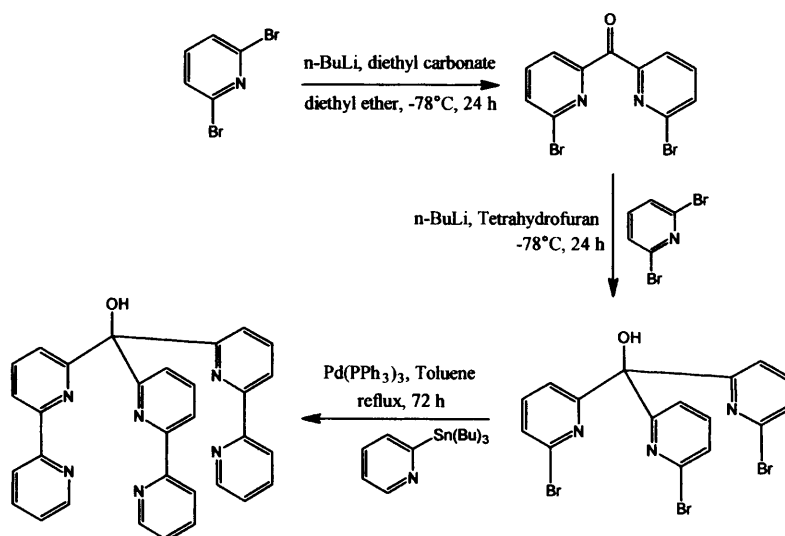
**[Zn<sup>II</sup>(L<sup>3</sup>)](ClO<sub>4</sub>)<sub>2</sub> (2.6)**: Colourless crystals (71% yield). Found: C, 48.97; H, 2.99; N, 10.97%.  $\text{ZnC}_{31}\text{H}_{22}\text{N}_6\text{O}(\text{ClO}_4)_2$  requires C, 49.06; H, 2.92; N, 11.07%; HRMS (ES)  $m/z$  (%): 657.0614 (100) ([Zn(L<sup>3</sup>) + ClO<sub>4</sub>]<sup>+</sup>;  $\text{ZnC}_{31}\text{H}_{22}\text{N}_6\text{O}_5\text{Cl}$  requires 657.0632); <sup>1</sup>H NMR (400MHz; CD<sub>3</sub>CN): 8.80 (d, 3H,  $J$  7.7 Hz), 8.53 (d, 3H,  $J$  7.6 Hz), 8.42-8.36 (m, 6H), 8.35-8.29 (m, 6H), 7.89 (t, 3H,  $J$  7.6 Hz), 6.73 (s, 1H); <sup>13</sup>C NMR: (125 MHz; CD<sub>3</sub>CN): 157.1, 149.5, 149.1, 148.6, 142.2, 141.8, 127.3, 123.3, 122.3, 120.7, 75.0; IR (KBr pellet,  $\text{cm}^{-1}$ ): 3407(br), 3096(m), 1605(s), 1454(s), 1093(s), 769(s), 623(s).

**[Cd<sup>II</sup>(L<sup>3</sup>)](ClO<sub>4</sub>)<sub>2</sub>·2CH<sub>3</sub>OH (2.7)**: Colourless crystals (59% yield). Found: C, 45.67; H, 3.55; N, 9.87%.  $\text{CdC}_{31}\text{H}_{22}\text{N}_6\text{O}(\text{ClO}_4)_2\cdot 2\text{CH}_3\text{OH}$  requires C, 45.56; H, 3.48; N, 9.66%; HRMS (ES)  $m/z$  (%): 703.0366 (100) ([Cd(L<sup>3</sup>) + ClO<sub>4</sub>]<sup>+</sup>;  $\text{CdC}_{31}\text{H}_{22}\text{N}_6\text{O}_5\text{Cl}$  requires 703.0370); <sup>1</sup>H NMR: (500 MHz; CD<sub>3</sub>CN):  $\delta_{\text{H}}$  9.32 (d, 3H,  $J$  7.9 Hz), 8.53-8.40 (m, 12H), 8.31 (t, 3H,  $J$  7.4 Hz), 7.94 (t, 3H,  $J$  7.0), 6.61 (s, 1H); <sup>13</sup>C NMR (125 MHz; CD<sub>3</sub>CN): 158.3, 150.2, 149.8, 148.9, 141.7, 141.4, 127.2, 123.8, 122.8, 121.8, 75.6; IR (KBr pellet,  $\text{cm}^{-1}$ ): 3435(br), 3113(m), 1592(s), 1452(s), 1097(s), 768(s), 623(s).

## 2.4 Results and Discussion

### 2.4.1 Ligand Synthesis

The synthesis of ligand  $L^3$  was reported by Dr. Neha Singh<sup>36</sup> and is summarised in Scheme 2.1. The bromo derivatives were readily prepared in reasonable yields. In turn, the bromo derivative was suspended in toluene and treated with an excess of 2-tributylstannylpyridine in the presence of the palladium catalyst,  $Pd(PPh_3)_4$ , for 24 hours at  $110^\circ C$  to generate the bipy derivative,  $L^3$ . This was formed *via* a Stille coupling reaction. The crude product of  $L^3$  was acidified and extracted with DCM to remove the excess 2-tributylstannylpyridine and other impurities. The aqueous layer was then basified and again extracted with DCM. The removal of the solvent under a vacuum gave the purified product, tris(2,2'-bipyrid-6-yl) methanol,  $L^3$ , as a yellow solid (42%).



Scheme 2.1: Synthetic route to  $L^3$

## 2.4.2 Synthesis of Complexes

Preliminary studies of complexes **2.2**, **2.4**, **2.5** and **2.6** have previously been reported,<sup>36</sup> and some of this data has been used to aid in the discussion. This work represents the first detailed examination of this series of compounds.

The ligand was dissolved in the minimum amount (typically 3 mL) of warm acetonitrile. In each case, the dropwise addition of the relevant metal perchlorate salt dissolved in either water or acetonitrile instantly yielded a precipitate. These compounds were recrystallised *via* the diffusion of diethyl ether into acetonitrile or methanolic solutions resulting in crystals suitable for single-crystal X-ray diffraction. The yields from these reactions were moderate (52-78%) and this crystalline material was then subsequently used for all spectroscopic measurements.

## Spectroscopic Properties of Complexes

### 2.4.3 Vibrational Spectroscopy

The tentative assignments for the IR spectral bands useful for determining the ligands mode of co-ordination are listed in Table 1. Compounds **2.1-2.7** all display a shift of the strong  $1,580\text{ cm}^{-1}$  band to higher frequency (*ca.*  $1,600\text{ cm}^{-1}$ ), indicative of pyridyl co-ordination. The striking similarities between the vibrational spectra of compounds **2.1-2.7** suggests similar electronic density over the ring systems caused primarily by back-bonding from the metal ion to the low-lying  $\pi$ -orbitals of the bipyridine groups. All compounds reveal two characteristic unsplit infrared active bands at  $\sim 1,100\text{ cm}^{-1}$  and  $\sim 623\text{ cm}^{-1}$  indicative of ionic perchlorate ( $T_d$  symmetry). The formation of a covalent bond to a metal ion through a perchlorate oxygen atom would lower the symmetry of the perchlorate to  $C_{3v}$  (or lower still to  $C_{2v}$  if co-ordination occurs



## Chapter 2: A Bipyridine-based Tripodal Framework with a Strong Preference for Trigonal Prismatic Co-ordination Geometries

through two oxygen atoms), and hence, the number of observed bands would increase to six (or nine if  $C_{2v}$ ). Since only two bands are observed in each of the infrared spectra, the perchlorate counterions are non-coordinating which is in accordance with crystallographic data.

**Table 1: IR Stretching Frequencies of  $L^3$  and Complexes 2.1-2.7**

Compound	Characteristic vibrations/cm <sup>-1</sup>				
	aromatic $\nu(\text{C-H})$	$\nu(\text{O-H})$	$\nu(\text{C=N})$ and $\nu(\text{C=C})$	$\pi(\text{C-H})$	$\nu(\text{Cl-O})$
$L^3$	3072(m)	3322(br)	1580(m), 1453(m)	766(s)	-
<b>2.1</b>	3093(m)	3398(br)	1597(s), 1453(s)	768(s)	1101(s), 623(s)
<b>2.2</b>	3096(m)	3421(br)	1604(s), 1453(s)	769(s)	1093(s), 623(s)
<b>2.3</b>	3091(m)	3399(br)	1603(s), 1454(s)	769(s)	1095(s), 623(s)
<b>2.4</b>	3092(m)	3388(br)	1605(s), 1453(s)	771(s)	1104(s), 623(s)
<b>2.5</b>	3093(m)	3448(br)	1609(s), 1453(s)	770(s)	1101(s), 622(s)
<b>2.6</b>	3096(m)	3407(br)	1605(s), 1454(s)	769(s)	1093(s), 623(s)
<b>2.7</b>	3113(m)	3435(br)	1592(s), 1452(s)	768(s)	1097(s), 623(s)

<sup>a</sup> IR spectra measured as KBr discs.

### 2.4.4 $^1\text{H}$ and $^{13}\text{C}$ NMR of Zn and Cd Complexes

The  $^1\text{H}$  and  $^{13}\text{C}$  NMR spectra of  $L^3$ , **2.6** and **2.7** were measured in  $\text{CD}_3\text{CN}$  solutions. At ambient temperature both complexes produce relatively simple spectra as a consequence of the three-fold axis of symmetry. The proton resonance frequencies of the zinc complex, **2.6**, have experienced a significant downfield shift on comparison to the parent ligand\* which is clearly caused by a negative inductive effect upon co-ordination to the strongly Lewis acidic  $\text{Zn}^{2+}$  cation. The  $^1\text{H}$ -NMR of the cadmium complex, **2.7** (Fig. 11), much like the analogous zinc complex, is also shifted downfield significantly compared to the free ligand. Interestingly, this effect is greater in the cadmium complex which is surprising considering the poorer Lewis acidity of  $\text{Cd}^{\text{II}}$ .

\*  $^1\text{H}$  NMR (400 MHz:  $\text{CDCl}_3$ );  $\delta$  8.55 (d, 3H,  $J$  7.8 Hz), 8.28 (d, 3H,  $J$  7.5 Hz), 8.12 (d, 3H,  $J$  7.2 Hz), 7.89-7.72 (m, 6H), 7.67 (t, 3H,  $J$  7.5 Hz), 7.21 (t, 3H,  $J$  7.2 Hz), 5.21 (s, 1H).

Attempts were made to collect the  $^1\text{H}$  NMR of the  $\text{Fe}^{\text{II}}$  complex, **2.2**, however no signals were observable which is suggestive of a high-spin paramagnetic  $d^6$  electron configuration. This is interesting as the octahedral compound  $[\text{Fe}^{\text{II}}(\text{bipy})_3]^{2+}$  is known to have a low-spin electronic configuration, however, the crystal structure of compound **2.2** (*cf.* Section 2.4.7.2, p. 115) reveals a predominantly trigonal prismatic co-ordination geometry, which would help facilitate a high-spin configuration due to the smaller span of the d-orbitals.

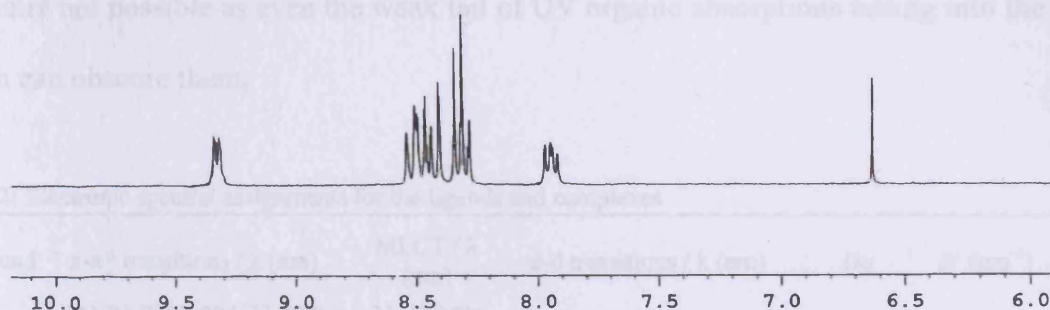


Figure 11:  $^1\text{H}$  NMR of the the cadmium complex of  $\text{L}^3$  (**2.7**).

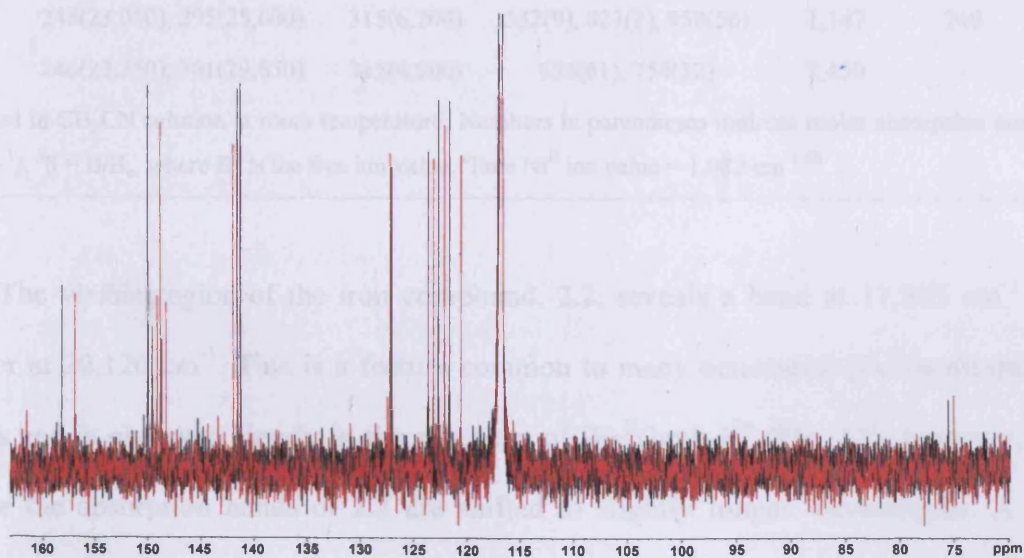


Figure 12: Superimposed  $^{13}\text{C}$  NMR spectra of both the zinc (red) and cadmium (black) complexes of  $\text{L}^3$ .

## 2.4.5 Electronic Absorption Spectra

The electronic spectra of complexes **2.1**, **2.2**, **2.3**, **2.4** and **2.5** have been measured in solution and the significant absorption bands are presented in Table 2. The electronic absorption spectra for all complexes of  $L^3$  possess two strong peaks between 241 nm and 301 nm which are characteristic of intra-ligand bipyridine  $\pi-\pi^*$  transitions. The manganese(II) complex, **2.1**, did not reveal any indication of a d-d transition even in highly concentrated solutions. Spin-forbidden d-d transitions of  $Mn^{II}$  complexes are typically very weak and identification is usually not possible as even the weak tail of UV organic absorptions tailing into the visible region can obscure them.

**Table 2:** Electronic spectral assignments for the ligands and complexes

Compound	$\pi-\pi^*$ transitions / $\lambda$ (nm)	MLCT / $\lambda$ (nm)	d-d transitions / $\lambda$ (nm)	$Dq$	$B'$ ( $cm^{-1}$ )	$\beta^b$
<b>2.1</b>	241(21,250), 295(23,000)	314(6,500)	-	-	-	-
<b>2.2</b>	245(22,500), 296(25,000)	316(7,000)	497(57), 557(79)	-	-	-
<b>2.3</b>	242(24,200), 294(21,000)	314(3,300)	468(112), 1052(14)	1,620	899	0.926
<b>2.4</b>	248(23,050), 295(25,600)	315(6,200)	532(9), 827(2), 958(56)	1,147	740	0.684 <sup>c</sup>
<b>2.5</b>	246(22,350), 301(29,650)	315(4,900)	636(61), 754(32)	2,450	-	-

<sup>a</sup>performed in  $CH_3CN$  solution at room temperature; Numbers in parentheses indicate molar absorption coefficients  $\epsilon$  ( $M^{-1}cm^{-1}$ ). <sup>b</sup> $\beta = B/B_0$ , where  $B_0$  is the free ion value. <sup>c</sup>Free  $Ni^{II}$  ion value =  $1,082 cm^{-1}$ .<sup>38</sup>

The visible region of the iron compound, **2.2**, reveals a band at  $17,945 cm^{-1}$  with a shoulder at  $20,120 cm^{-1}$ . This is a feature common to many octahedral  $[Fe^{II}(\alpha\text{-dimmine})_3]^{2+}$  systems and is observed clearly in the spectrum of  $[Fe^{II}(bpy)_3]^{2+}$  (Fig. 13), however, in this instance the absorption bands of **2.2** are shifted to slightly longer wavelengths. A similar observation was made by Wentworth *et al.* while studying the iron(II) complex of *cis,cis-*

1,3,5-tris(pyridine-2-carboxaldimino)cyclohexane ((py)<sub>3</sub>tach), a ligand which also exhibits a sterically-induced preference for trigonal prismatic geometries.<sup>17</sup> Higher molar absorption coefficients for both compound **2.2** and [Fe<sup>II</sup>](py)<sub>3</sub>tach]<sup>2+</sup> suggest these complexes may maintain predominantly trigonal prismatic character in solution, however similar differences have also been reported to occur with the octahedral [Fe<sup>II</sup>(*o*-phenanthroline)<sub>3</sub>]<sup>2+</sup> complex.<sup>39</sup> Further investigations involving energy level calculations are required before any any meaningful conclusions can be drawn.

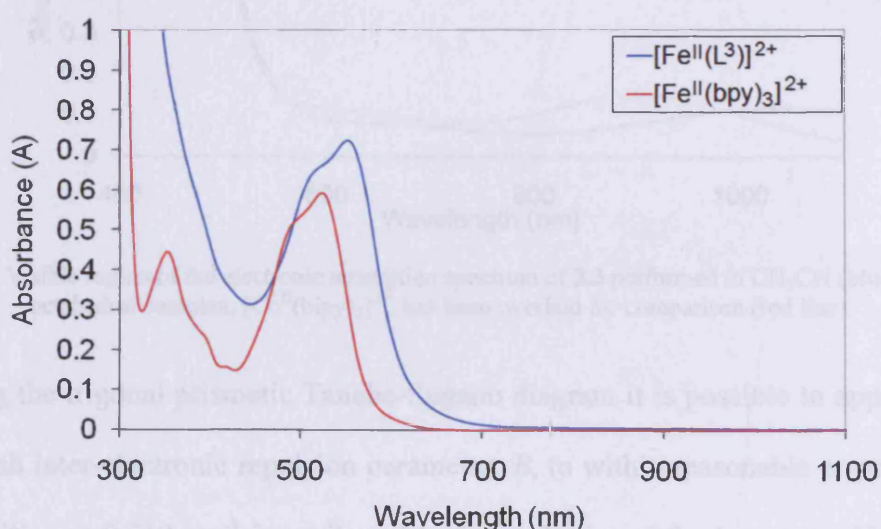


**Figure 13:** Visible region of the electronic absorption spectrum of **2.2** performed in CH<sub>3</sub>CN (blue line). The octahedral complex, [Fe<sup>II</sup>(bpy)<sub>3</sub>]<sup>2+</sup>, has been overlaid for comparison (red line).

The absorption bands of the cobalt compound, **2.3** (Fig. 14; blue line), which has been assumed to be trigonal prismatic based upon single crystal X-ray diffraction data, have been assigned using the appropriate Tanabe-Sugano diagram (Fig. 15).<sup>17</sup> The visible region consists of two observable bands, the very broad band at lowest energy 9,510 cm<sup>-1</sup> is assigned to the combination of three spin-allowed transitions; <sup>4</sup>A<sub>2</sub>', <sup>4</sup>A<sub>2</sub>' + <sup>4</sup>A<sub>1</sub>'', <sup>4</sup>E''(F) ← <sup>4</sup>E'. The second observable band which is seen as a shoulder to a charge transfer band has been deconvoluted *via* computational analysis of the spectrum using the software PeakFit version

4.12 (SeaSolve Software, Richmond, CA, USA) which applies a Gaussian response function with a Fourier deconvolution algorithm. This peak reaches an absorbance maxima at 21,370  $\text{cm}^{-1}$  and corresponds to the transition  ${}^4E''(\text{P}) \leftarrow {}^4E'(\text{F})$ .

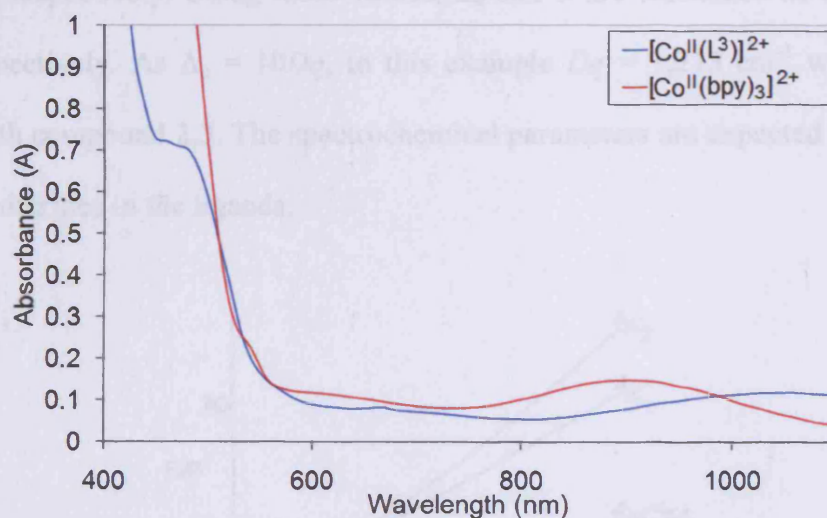


**Figure 14:** Visible region of the electronic absorption spectrum of **2.3** performed in  $\text{CH}_3\text{CN}$  (blue line). The octahedral complex,  $[\text{Co}^{\text{II}}(\text{bipy})_3]^{2+}$ , has been overlaid for comparison (red line).

Using the trigonal prismatic Tanabe-Sugano diagram it is possible to approximate  $Dq$  and the Racah inter-electronic repulsion parameter,  $B$ , to within reasonable error. The lowest energy transition at  $9,510 \text{ cm}^{-1}$  is attributed to the midpoint of the lower manifold, and thus  $Dq$  was found to be  $1,521 \text{ cm}^{-1}$  and  $B$  to be  $869 \text{ cm}^{-1}$  ( $Dq/B = 1.75$ ). It was possible therefore to predict the location of the third spin-allowed transition  ${}^4A_2'(\text{P}) \leftarrow {}^4E'(\text{F})$  to occur at  $22,590 \text{ cm}^{-1}$ , an energy which is obscured by a  $\text{Co}^{\text{II}}$  to diimine metal to ligand charge transfer band (MLCT). The nephelauxetic ratio,  $\beta = 0.894$  (assuming free ion  $[\text{Co}^{\text{II}}]$ ,  $B = 971 \text{ cm}^{-1}$ ), indicates a significant degree of covalency. On the basis of the d-orbital splitting of a trigonal prism (Fig. 2), two ligand field splitting parameters have been proposed;  $\Delta_1 \equiv E(d_{x^2-y^2}, d_{xy}) - E(d_{z^2})$  and  $\Delta_2 \equiv E(d_{xz}, d_{yz}) - E(d_{x^2-y^2}, d_{xy})$ . In this instance, assuming a perfect trigonal prism,  $\Delta_1 = \Delta_2 = 3^{1/3}Dq = 5,070 \text{ cm}^{-1}$ .

The known octahedral complex,  $[\text{Co}^{\text{II}}(\text{bipy})_3]^{2+}$ , has been prepared for comparative purposes. In this instance, two spin-allowed transitions are observed at  $11,030 \text{ cm}^{-1}$  and  $19,080 \text{ cm}^{-1}$  (Fig. 14; red line), corresponding to the transitions  ${}^3\text{T}_{2g}(\text{F}) \leftarrow {}^3\text{T}_{1g}$  and  ${}^3\text{T}_{1g}(\text{F}) \leftarrow {}^3\text{T}_{1g}$  respectively. Using these values,  $\Delta_0$  and  $B$  are calculated as  $12,130 \text{ cm}^{-1}$  and  $610 \text{ cm}^{-1}$  respectively. As  $\Delta_0 = 10Dq$ , in this example  $Dq = 1,213 \text{ cm}^{-1}$  which is in good agreement with compound **2.3**. The spectrochemical parameters are expected to be very close due to the similarities in the ligands.

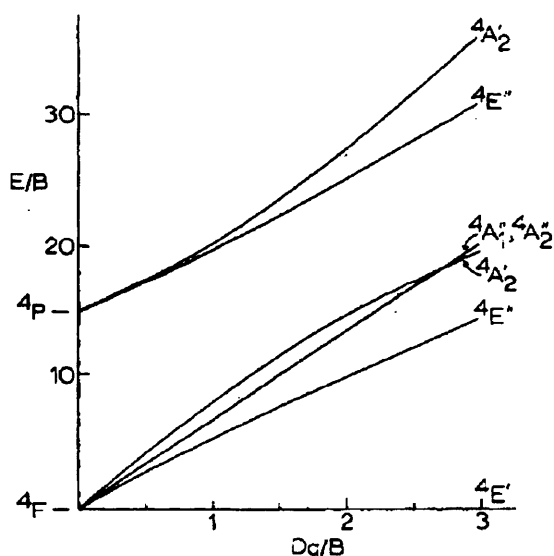
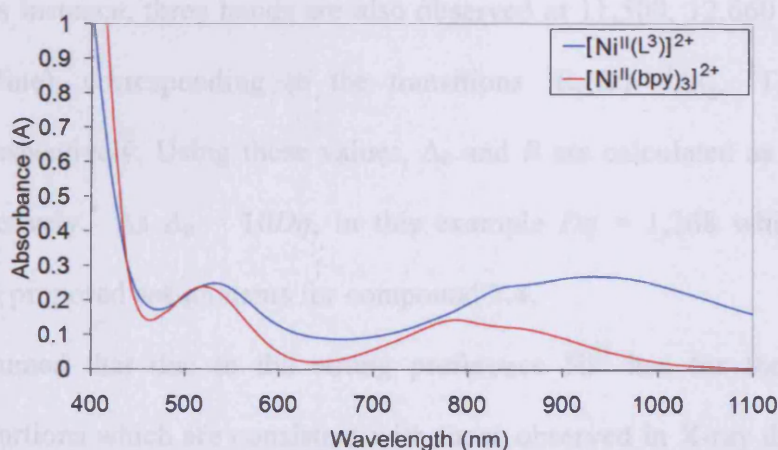


Figure 15: Energy level diagram for a  $d^7$  trigonal prismatic complex, taken directly from reference 17.

Deconvolution of the visible region of the nickel compound, **2.4**, yields three absorption bands (Fig. 16; blue line). This compound exhibits a strongly trigonal prismatic geometry in the solid state (*cf.* Section 2.4.7.4; p. 119) and accordingly these bands have been assigned using an energy level diagram for a  $d^8$  trigonal prismatic complex (Fig. 17). If the lowest energy transition at  $10,440 \text{ cm}^{-1}$  is ascribed to the spin-allowed transition  ${}^3\text{E}'(\text{P}) \leftarrow {}^3\text{A}_2'$  and the subsequent band at  $12,090 \text{ cm}^{-1}$  is attributed to the spin-forbidden transition  ${}^1\text{E}' \leftarrow {}^3\text{A}_2'$  then, using these values, the third band,  ${}^3\text{E}''(\text{P}) + {}^3\text{A}_2'(\text{P}) \leftarrow {}^3\text{A}_2'$ , is

predicted to occur at  $19,390\text{ cm}^{-1}$  which is quite close to the observed  $18,800\text{ cm}^{-1}$ . The spectroscopic parameters  $Dq$  and  $B$  are  $1,147\text{ cm}^{-1}$  and  $740\text{ cm}^{-1}$  respectively ( $Dq/B = 1.55$ ). The two ligand field splitting parameters, assuming a perfect trigonal prism, are  $\Delta_1 = \Delta_2 = 3,823\text{ cm}^{-1}$ .



**Figure 16:** Visible region of the electronic absorption spectrum of **2.4** performed in  $\text{CH}_3\text{CN}$  (blue line). The octahedral complex,  $[\text{Ni}^{\text{II}}(\text{bipy})_3]^{2+}$ , has been overlaid for comparison (red line).

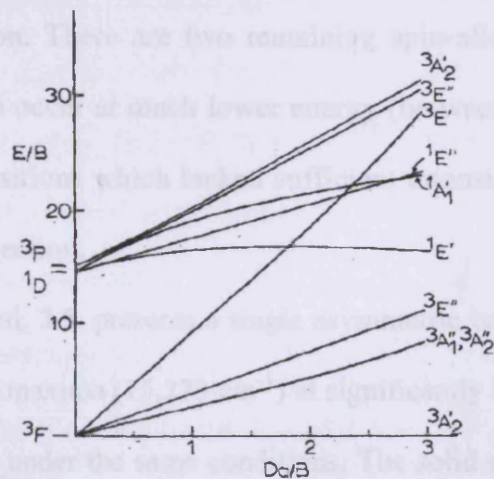


**Figure 17:** Energy level diagram for a  $d^8$  trigonal prismatic complex, taken directly from reference 17.

There is an alternative assignment of the transition terms in which the ordering is reversed and the transition  $1E' \leftarrow 3A_2'$  is ascribed to the lowest energy transition. In this case, the spectroscopic parameters become  $Dq = 1,323\text{ cm}^{-1}$  and  $B = 630\text{ cm}^{-1}$  ( $Dq/B = 2.1$ ). The

third band in this instance is predicted to occur at  $16,510\text{ cm}^{-1}$ , which contradicts what has been observed experimentally. Therefore, on this basis, the previous assignment is the most likely.

The known octahedral complex,  $[\text{Ni}^{\text{II}}(\text{bipy})_3]^{2+}$ , has been prepared for comparative purposes. In this instance, three bands are also observed at  $11,500$ ,  $12,660$  and  $19,160\text{ cm}^{-1}$  (Fig. 16; red line), corresponding to the transitions  ${}^1\text{E}_g(\text{D}) \leftarrow {}^3\text{A}_{2g}$ ,  ${}^3\text{T}_{2g}(\text{F}) \leftarrow {}^3\text{A}_{2g}$ , and  ${}^3\text{T}_{1g}(\text{F}) \leftarrow {}^3\text{A}_{2g}$  respectively. Using these values,  $\Delta_o$  and  $B$  are calculated as  $12,680\text{ cm}^{-1}$  and  $728\text{ cm}^{-1}$  respectively.\* As  $\Delta_o = 10Dq$ , in this example  $Dq = 1,268$  which lies mid-way between the two proposed assignments for compound **2.4**.

It is assumed that due to the strong preference  $\text{Ni}^{\text{II}}$  has for forming octahedral geometries, distortions which are consistent with those observed in X-ray diffraction studies are also likely to occur in solution. Therefore, whilst the energy level diagram provides a satisfactory ordering of the terms involved, the spectroscopic parameters derived must be treated with some suspicion. There are two remaining spin-allowed transitions,  ${}^3\text{E}'' \leftarrow {}^3\text{A}_2'$  and  ${}^3\text{A}_1'' \leftarrow {}^3\text{A}_2'' \leftarrow {}^3\text{A}_2'$  which occur at much lower energy (between  $3,000$  and  $5,000\text{ cm}^{-1}$ ) and several spin-forbidden transitions which lacked sufficient intensity to be observed within the spectra despite careful inspection.

The copper compound, **2.5**, presents a single asymmetric band in the visible region (Fig. 18), reaching an absorbance maxima ( $15,273\text{ cm}^{-1}$ ) at significantly higher energy than is seen for  $[\text{Cu}^{\text{II}}(\text{bpy})_3]^{2+}$  ( $14,809\text{ cm}^{-1}$ ) under the same conditions. The solid state geometry is intermediate between octahedral and trigonal prismatic, and a distortion from octahedral geometry is expected to cause a decrease in ligand field strength and thus an increase in  $\lambda_{\text{max}}$ . Deconvolution of the

\* This is in excellent agreement with previous literature data<sup>40</sup> for the compound  $[\text{Ni}^{\text{II}}(\text{bipy})_3]^{2+}$ , where transitions at  $11,500\text{ cm}^{-1}$ ,  $12,650\text{ cm}^{-1}$  and  $19,200\text{ cm}^{-1}$  were located and assigned to the same transitions. In this example,  $\Delta_o = 12,650\text{ cm}^{-1}$ .



visible region reveals two bands corresponding to the two spin-allowed transitions for a  $d^9$  metal ion in a TP environment. The lowest energy transition,  ${}^2E' \leftarrow {}^2E''$ , occurs at  $13,260\text{cm}^{-1}$  and the next transition,  ${}^2A_1' \leftarrow {}^2E''$ , at  $15,710\text{cm}^{-1}$ .

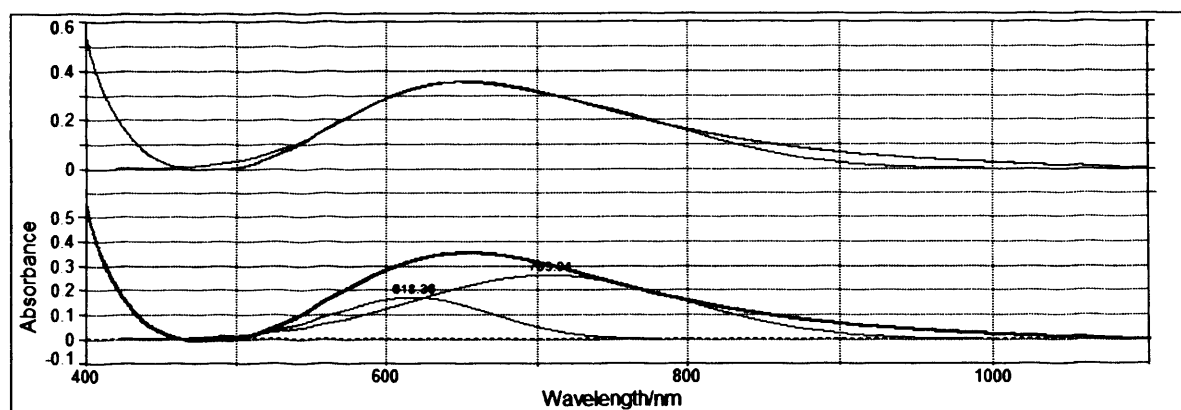


**Figure 18:** Deconvolution of the electronic spectra of 2.5. The lower graph contains a trace revealing the individual component peaks, while the upper graph has a trace which reflects the sum curve of these peaks. Both the upper and lower graphs also contain a trace of the raw input data.

A perfect trigonal prismatic conformation would lead to two transitions, one at half the energy of the other. In this instance, however, the ratio  $v_2/v_1 = 0.844$ . Using Figure 3, this corresponds to a Bailar twist angle of *ca.*  $30^\circ$  (where  $v_2/v_1 = 0.846$ ; Fig. 19). It should be noted that the crystal structure of this complex (*cf.* Section 2.4.7.5, p. 121) reveals a pronounced Jahn-Teller distortion which has not been taken into consideration here. This distortion would clearly have an impact upon the electronic spectrum and therefore these conclusions should be treated with caution. In the solid state, the mean Bailar twist angle is  $17.0^\circ$ .

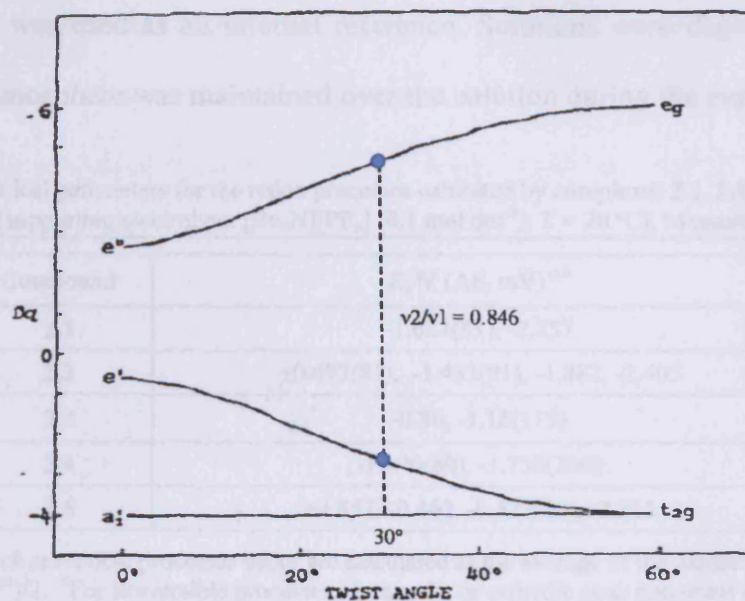


Figure 19: The ratio  $v_2/v_1$  between the transitions in the visible region of the electronic spectrum of compound 2.5 is 0.844. This approximates well to a  $30^\circ$  Bailar twist where this ratio is 0.846.

#### 2.4.6 Electrochemical Studies

The cyclic voltammetry experiments were carried out with an AUTOLAB PGSTAT12 potentiostat in conjunction with General Purpose Electrochemical System software (GPES version 4.7 for Windows) in a specially designed three-electrode glass cell with a Teflon-coated cell cap. A Bioanalytical platinum working electrode (model no. MF2013) with a 1.6 mm disk was used for all experiments. The counter electrode was a platinum wire and the reference electrode an Ag/AgNO<sub>3</sub> electrode. To regain electrochemical sensitivity and reproducibility the working electrode was polished, with 600 grid emery paper, to a mirror surface and then ultrasonicated. Prior to each experiment, the electrode was washed with high performance liquid chromatography (HPLC) grade CH<sub>3</sub>CN and dried in air for about 15 min. A 0.1 M [Bu<sub>4</sub>N][PF<sub>6</sub>] solution in CH<sub>3</sub>CN was used as supporting electrolyte. In all

cases, ferrocene was used as an internal reference. Solutions were degassed with nitrogen and a nitrogen atmosphere was maintained over the solution during the experiment.

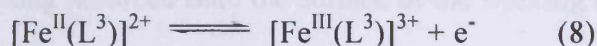
**Table 3:** Electrochemical parameters for the redox processes exhibited by complexes **2.1**, **2.2**, **2.3**, **2.4** and **2.5** in acetonitrile solution (supporting electrolyte: [Bu<sub>4</sub>N][PF<sub>6</sub>] (0.1 mol dm<sup>-3</sup>); T = 20 °C). Measured at 0.1 Vs<sup>-1</sup>.

Compound	$E_p/V$ ( $\Delta E$ , mV) <sup>a,b</sup>
<b>2.1</b>	-1.621(81), -2.357
<b>2.2</b>	+0.693(81), -1.433(91), -1.882, -2.405
<b>2.3</b>	-0.86, -1.18(119)
<b>2.4</b>	-1.390(60), -1.750(100)
<b>2.5</b>	+0.857, -0.462, -0.523(80), -2.315

<sup>a</sup>the potentials at which reversible processes occur are calculated as the average of the oxidative and reductive peak potentials ( $E_p^{ox} + E_p^{red}$ )/2. <sup>b</sup>For irreversible processes, the anodic or cathodic peak potentials are given. Potentials are given in volts *versus* Ferrocenium/Ferrocene.

The cyclic voltammogram of the manganese compound, **2.1**, reveals two reduction processes. The reduction process located at the cathodic potential of -1.621 V referenced against ferrocenium/ferrocene (Fc<sup>+</sup>/Fc) was reversible over the scan rate range of 50 – 1000 mVs<sup>-1</sup>. This was demonstrated by plotting the square root of the scan rate against the peak current. A linear relationship was observed which confirmed an ideal diffusion controlled response, adhering to the Randles-Sevcik equation (*cf.* Section 1.4.6; p. 32). This process is most likely attributable to the Mn<sup>III/I</sup> redox couple. The complex [Mn<sup>II</sup>(bpy)<sub>3</sub>][ClO<sub>4</sub>]<sub>2</sub> has been shown to undergo a well-defined reversible reduction at -1.314 V (*vs* Ag/AgCl) which has been attributed to the same process.<sup>41</sup> The second reduction peak at the more negative potential of -2.357 V is irreversible and most likely attributable to a ligand process. Electrochemical studies on related [Mn<sup>II</sup>(bpy)<sub>3</sub>]<sup>2+</sup> salts<sup>41,42</sup> also reveal a reversible oxidation attributed to the Mn<sup>III/II</sup> couple in the anodic region (*ca.* +1.5 V *vs* Ag/AgCl), however compound **2.1** does not show any evidence of this redox couple within the bounds of the potential window as limited by the electrolysis of the acetonitrile solvent.

The voltammogram of the iron complex, **2.2**, reveals two reversible and two irreversible processes. Chen<sup>43</sup> examined the related compound  $[\text{Fe}^{\text{II}}(\text{bpy})_3]^{2+}$  and established that the reversible oxidation feature at +0.89 V vs Ag/AgCl was due to the  $\text{Fe}^{\text{II/III}}$  process, likewise the reversible oxidation feature at +0.693 V (Fig. 20) has been assigned to this redox couple (equation 8).



The plot of the square root of the scan rate (50 – 1000  $\text{mVs}^{-1}$ ) vs peak current was again consistent with the Randles-Sevcik equation for a reversible process. A second reversible feature at -1.433 V with a peak-to-peak separation of 91 mV is most likely attributable to a bipy-based redox couple, corresponding to the addition, and subsequent removal, of an electron from the low lying unoccupied  $\pi^*$  orbital. Likewise, the two irreversible cathodic reduction waves at -1.882 and -2.405 V are both most likely associated with the hexadentate ligand.

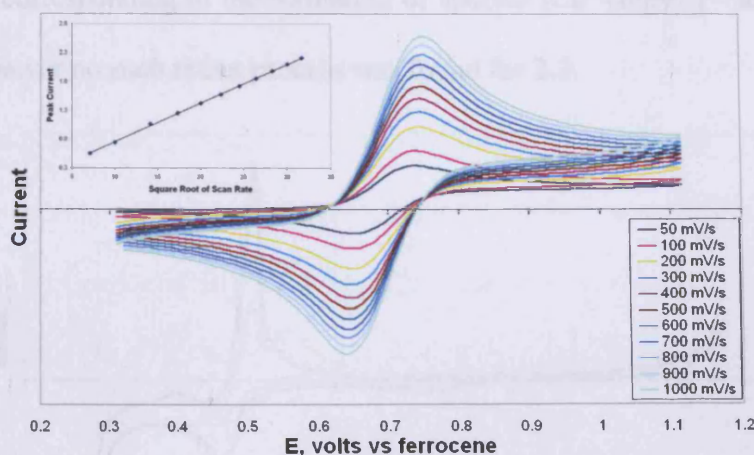


Figure 20: Isolation of the  $\text{Fe}(\text{II/III})$  redox couple for **2.2**

A quasi-reversible reduction peak is observed in the cathodic region for the cobalt complex, **2.3**, at -1.18 V which is very likely attributable to a  $\text{Co}^{\text{III/I}}$  redox process based upon

electrochemical studies of other cobalt(II) complexes. For instance, the compound  $[\text{Co}^{\text{II}}(\text{bipy})_3][\text{ClO}_4]_2$  was shown to undergo a reversible one-electron reduction at -1.2 V (*vs* SCE, acetonitrile).<sup>44</sup> However, the observed peak separation is too broad (119 mV) to establish whether this process is fully reversible. Upon scanning the full potential window (Fig. 21), this process is obscured by a sharp, asymmetric oxidation at -1.06 V, typically indicative of an insoluble material becoming adsorbed onto the surface of the working electrode. Narrowing the potential window to between -1.5 V and -0.5 V eliminates this oxidation feature, revealing the  $\text{Co}^{\text{II}}/\text{Co}^{\text{I}}$  couple (Fig. 21; orange overlay). A further irreversible oxidation at -0.86 V is also revealed and is assigned to the formation of an unidentified species, formed immediately after the reduction of the starting complex. On scanning through a second cycle, no change of the cathodic or anodic waves was observed for these electrode processes; the reductions occurred at the same potentials as observed in the first cycle. Multiple scans resulted in nearly superimposable cyclic voltammograms, thereby showing the marked stability of the reduced complex involved in the electrochemical study. The related compound  $[\text{Co}^{\text{II}}(\text{bipy})_3]^{2+}$  reveals an oxidation process corresponding to the formation of species  $[\text{Co}^{\text{III}}(\text{bipy})_3]^{3+}$  at +0.2 V (*vs* SCE, acetonitrile),<sup>44</sup> however no such redox process was found for **2.3**.

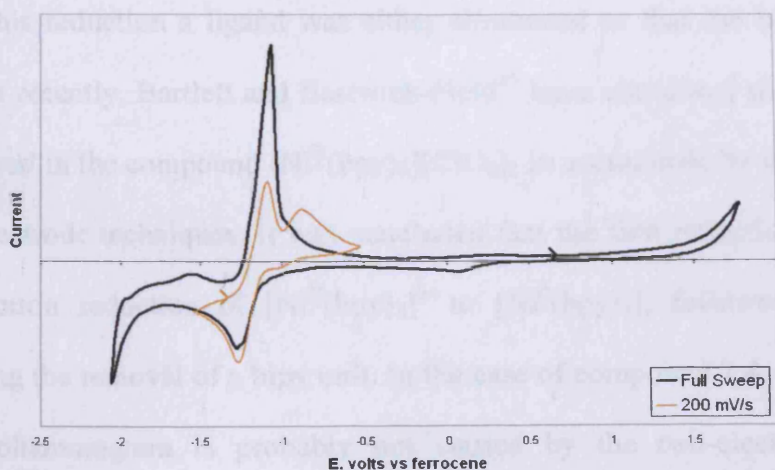


Figure 21: Cyclic voltammogram of **2.3**

The nickel complex, **2.4**, shows reversible reduction waves at cathodic potentials of -1.390 and -1.750 V (Fig. 22). These have peak-to-peak separations of 60 mV and 100 mV respectively. Many groups<sup>45,46</sup> have investigated the electrochemistry of the related compound  $[\text{Ni}^{\text{II}}(\text{bpy})_3]^{2+}$  reaching slightly different conclusions. Tanaka and Sato attributed the first reduction wave in the voltammogram, in the presence of excess bipy, to a two-electron reduction of  $[\text{Ni}^{\text{II}}(\text{bpy})_3]^{2+}$  to  $[\text{Ni}^0(\text{bpy})_3]$ . The second wave was attributed to the one-electron reduction of  $[\text{Ni}^0(\text{bpy})_3]$  to  $[\text{Ni}^{\text{I}}(\text{bpy})_3]^-$ .<sup>47</sup> It was also observed that, in the absence of excess bipy, the first wave is complicated by the presence of a pre-wave which suggested that some  $[\text{Ni}^{\text{II}}(\text{bpy})_3]^{2+}$  underwent loss of a ligand or ligands and the resultant  $[\text{Ni}^{\text{II}}(\text{bpy})_{3-n}]^{2+}$  was subsequently reduced to  $[\text{Ni}^0(\text{bpy})_{3-n}]$ . It is worth noting that Tanaka *et al.* later performed electron spin resonance measurements and reported the formation of  $[\text{Ni}^{\text{I}}(\text{bpy})_3]^+$ , suggesting the first polarographic wave was indeed the summation of two one-electron reductions;  $[\text{Ni}^{\text{II}}(\text{bpy})_3]^{2+}$  to  $[\text{Ni}^{\text{I}}(\text{bpy})_3]^+$  subsequently leading to  $[\text{Ni}^0(\text{bpy})_3]$ .<sup>48</sup> Henne and Bartak also examined the  $[\text{Ni}^{\text{II}}(\text{bpy})_3]^{2+}$  complex and observed five reduction waves between -1.26 and -2.34 V (vs SCE).<sup>49</sup> The first reduction wave was similarly attributed to the two-electron reduction of  $[\text{Ni}^{\text{II}}(\text{bpy})_3]^{2+}$  to  $[\text{Ni}^0(\text{bpy})_3]$  and it was suggested that following this reduction a ligand was either eliminated or that the bipy units became unidentate. Most recently, Bartlett and Eastwick-Field<sup>45</sup> have elucidated the electrochemical processes observed in the compound  $[\text{Ni}^{\text{II}}(\text{bpy})_3][\text{ClO}_4]_2$  in acetonitrile by using rotating disk and ring-disk electrode techniques. It was concluded that the first reduction wave is caused by the two-electron reduction of  $[\text{Ni}^{\text{II}}(\text{bpy})_3]^{2+}$  to  $[\text{Ni}^0(\text{bpy})_3]$ , followed by a chemical reaction involving the removal of a bipy unit. In the case of compound **2.4**, the first reduction wave in the voltammogram is probably not caused by the two-electron reduction of  $[\text{Ni}^{\text{II}}(\text{L}^3)]^{2+}$  to  $[\text{Ni}^0(\text{L}^3)]$  as the peak to peak separation of 60 mV is instead suggestive of a

one-electron process. The second reduction wave has therefore been tentatively attributed to the one-electron reduction of  $[\text{Ni}^{\text{I}}(\text{L}^3)]^+$  to  $[\text{Ni}^0(\text{L}^3)]$ , however additional coulometry experiments are required to assist in the interpretation of the electrochemical behaviour of this species.

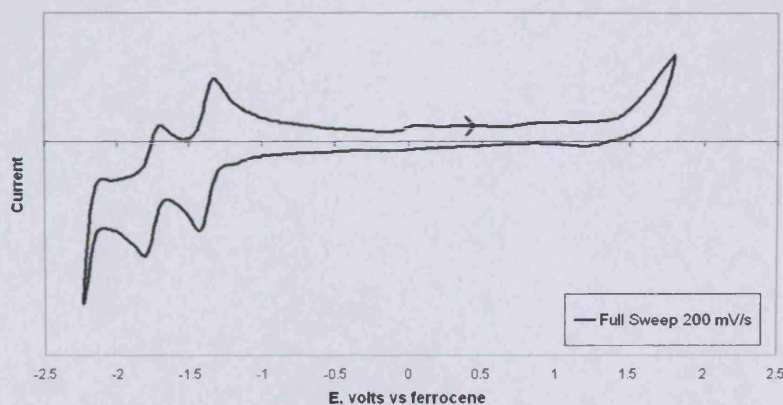


Figure 22: Cyclic voltammogram of 2.4

The voltammogram of the copper compound, 2.5, reveals a reduction process at -0.523 V (Fig. 23) with a peak-to-peak separation of 80 mV, most likely attributable to the  $\text{Cu}^{\text{II/I}}$  redox couple. This couple is representative of an ideal diffusion controlled response which abides by the Randles-Sevcik equation, confirming that the couple is reversible.

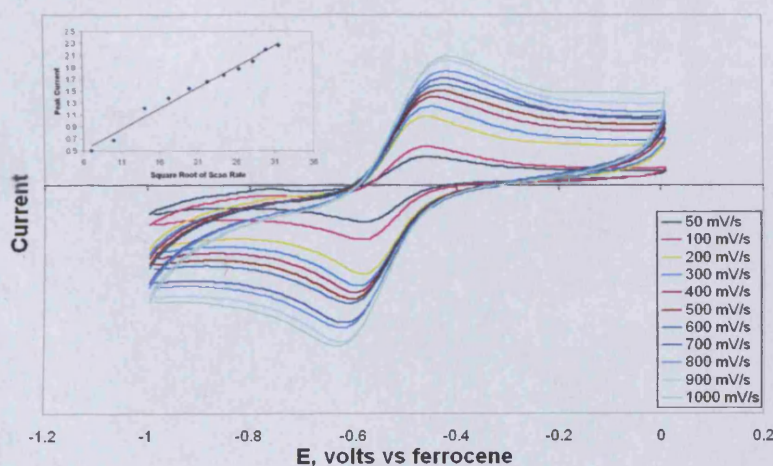


Figure 23: Isolation of the  $\text{Cu}^{\text{II/I}}$  redox couple for 2.5

Several groups<sup>50-52</sup> have studied the similar tris(2,2'-bipy) copper(II) complex and have noted that the reduction of  $[\text{Cu}^{\text{II}}(\text{bpy})_3]^{2+}$  results in the dissociation of a bpy unit, yielding the product  $[\text{Cu}^{\text{I}}(\text{bpy})_2]^+$ . The reduction potential for this reversible couple has been found to be heavily solvent and counterion dependant. Ruminski, performing this experiment in acetonitrile and under similar conditions to those used in this work, observed the reduction potential at -0.03 V (*vs* SCE).<sup>53</sup> A scan of the full window (Fig. 24) shows the reversible couple is obscured by a sharp, asymmetric irreversible oxidation process at -0.462 V, typically indicative of an insoluble material becoming adsorbed onto the surface of the working electrode. The origin of this feature is linked to an irreversible oxidation process present at +0.857 V. Curiously, this oxidation process does not affect the position or size of the current for the reduction associated with the  $\text{Cu}^{\text{I}}/\text{Cu}^{\text{II}}$  process. A reduction process most likely attributable to the addition of an electron to the low lying unoccupied  $\pi^*$  orbital is also present at -2.315 V.

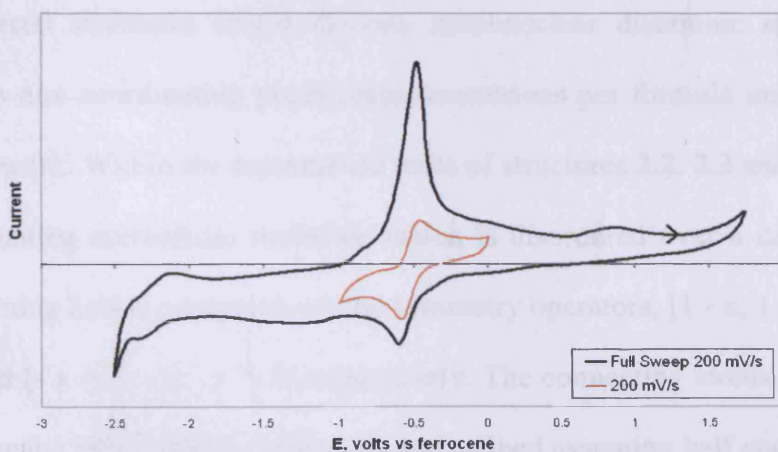


Figure 24: Cyclic voltammogram of compound 2.5



### 2.4.7 Crystallographic Studies

All single crystal X-ray data was collected at 150 K on a Bruker/Nonius Kappa CCD diffractometer using graphite monochromated Mo-K $\alpha$  radiation ( $\lambda = 0.71073 \text{ \AA}$ ), equipped with an Oxford Cryostream cooling apparatus. Crystal parameters and details of the data collection, solution and refinement are presented in Table 4. The data was corrected for Lorentz and polarisation effects and for absorption using SORTAV.<sup>54</sup> Structure solution was achieved by direct methods (Sir-92 program system<sup>55</sup>) and refined by full-matrix least-squares on  $F^2$  (SHELXL-97<sup>56</sup>) with all non-hydrogen atoms assigned anisotropic displacement parameters. Hydrogen atoms attached to carbon atoms were placed in idealised positions and allowed to ride on the relevant carbon atom. In the final cycles of refinement, a weighting scheme that gave a relatively flat analysis of variance was introduced and refinement continued until convergence was reached. Molecular structures in the figures were drawn with ORTEP 3.0 for Windows (version 1.08).<sup>57</sup> Consistent with spectroscopic analysis, all crystal structures reveal discrete mononuclear dicationic species which are balanced by two non-coordinating perchlorate counterions per formula unit residing within the lattice framework. Within the asymmetric units of structures 2.2, 2.3 and 2.4 lies one half of a non-coordinating acetonitrile molecule which is disordered over a centre of inversion (C33), the remaining half is generated *via* the symmetry operators,  $[1 - x, 1 - y, 1 - z]$ ,  $[1 - x, 1 - y, 1 - z]$ , and  $[-x + 2, -y, -z + 2]$  respectively. The connecting atoms in these instances were restrained using DFIX shelxl commands and refined assuming half occupancy.

**Table 4: Crystal Structure Data for Complexes 2.1-2.7**

Compound	Chemical Formula	Mr, g mol	Crystal System	Space group	T(K)	a, Å	b, Å	c, Å	α, deg	β, deg	γ, deg	Z	Dc, Mg/m <sup>3</sup>	μ(Mo K α), mm <sup>-1</sup>	Observed Reflections	Unique Reflections	R <sub>int</sub>	R <sub>1</sub> [I>2σ(I)]	wR <sub>2</sub> (all data)
2.1	[Mn(L <sup>3</sup> )](ClO <sub>4</sub> ) <sub>2</sub> ·H <sub>2</sub> O	766.4	triclinic	P-1	150	11.5618(2)	15.9279(3)	19.0219(5)	92.0290(10)	103.4120(10)	98.5920(10)	4	1.515	0.618	7306	15338	0.195	0.0738	0.1885
2.2	[Fe(L <sup>3</sup> )](ClO <sub>4</sub> ) <sub>2</sub> ·0.5CH <sub>3</sub> CN	1539.65	monoclinic	P 21/n	150	11.4113(3)	13.4325(3)	20.8164(7)	90	95.8420(10)	90	2	1.611	0.712	3548	7223	0.147	0.0676	0.1891
2.3	[Co(L <sup>3</sup> )](ClO <sub>4</sub> ) <sub>2</sub> ·0.5CH <sub>3</sub> CN	1545.81	monoclinic	P 21/n	150	11.4027(3)	13.4301(3)	20.7683(6)	90	95.7710(10)	90	2	1.622	0.78	3979	7227	0.103	0.0644	0.1792
2.4	[Ni(L <sup>3</sup> )](ClO <sub>4</sub> ) <sub>2</sub> ·0.5CH <sub>3</sub> CN	1545.33	monoclinic	P 21/n	150	11.4636(2)	13.4293(2)	20.7077(4)	90	95.0130(10)	90	2	1.616	0.848	4025	7268	0.145	0.0866	0.2884
2.5	[Cu(L <sup>3</sup> )](ClO <sub>4</sub> ) <sub>2</sub> ·2CH <sub>3</sub> CN	798.04	monoclinic	C 2/c	150	20.7459(4)	12.2533(3)	26.2774(6)	90	99.3110(10)	90	8	1.608	0.893	4441	7489	0.095	0.0627	0.1721
2.6	[Zn(L <sup>3</sup> )](ClO <sub>4</sub> ) <sub>2</sub>	758.82	monoclinic	P 21/n	150	11.1983(3)	13.3434(3)	20.7361(6)	90	95.7470(10)	90	4	1.635	1.038	4117	7051	0.093	0.059	0.1319
2.7	[Cd(L <sup>3</sup> )](ClO <sub>4</sub> ) <sub>2</sub> ·2CH <sub>3</sub> OH	869.94	triclinic	P-1	150	14.7638(3)	15.4130(3)	15.9828(4)	109.1960(10)	94.1520(10)	95.3900(10)	4	1.7	0.872	10533	15554	0.11	0.0599	0.1415

### 2.4.7.1 Crystal Structure of $[\text{Mn}^{\text{II}}(\text{L}^3)][\text{ClO}_4]_2 \cdot \text{H}_2\text{O}$ (2.1)

Compound **2.1** crystallises in the triclinic space group P-1 and contains two monomeric complexes within the asymmetric unit. The  $\text{Mn}^{\text{II}}$  cation in each case is co-ordinated *via* all six bipy N-donors (Fig. 25), and whilst the overall molecular symmetry of both complexes is approximately  $\text{C}_3$ , the core geometries are predominantly trigonal prismatic in character. The co-ordinative bond lengths range from 2.221(4) Å to 2.278(4) Å and are statistically identical to those of the octahedral compound  $[\text{Mn}^{\text{II}}(\text{bpy})_3][\text{ClO}_4]_2$  reported by Chen *et al.* which range from 2.214(4) Å to 2.294(4) Å.<sup>58</sup> The mean Bailar twist angles,  $\phi$ , for both unique complexes are just 10.4° and 7.7° and the corresponding dihedral angles between the two trigonal faces are 0.10(18)° and 0.39(18)° respectively, which shows that in each case they are essentially parallel. These values illustrate the high trigonal prismatic content of the co-ordination sphere around the  $\text{Mn}^{\text{II}}$  cation. Table 14 (p. 129) compiles the Bailar twist angles for complexes **2.1** – **2.7** and is accompanied by a discussion highlighting the structural differences between each complex.

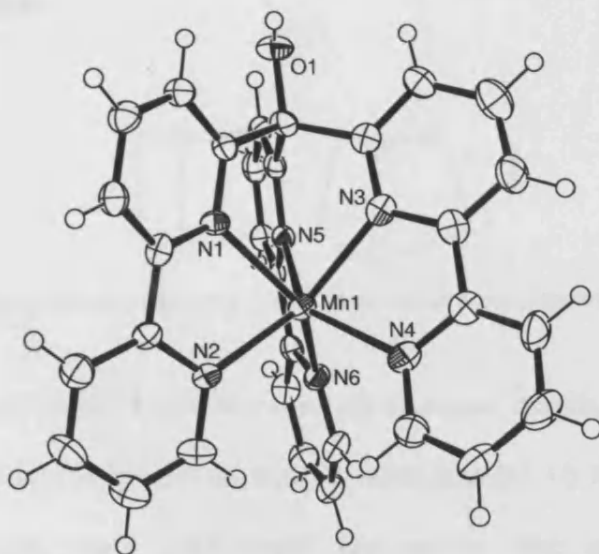


**Figure 25:** Perspective view of the asymmetric unit showing the atom numbering. Displacement ellipsoids are shown at the 50% probability level. H atoms are represented by circles of arbitrary size. Only one of the crystallographically independent complex units is shown; the other is similar.

## Chapter 2: A Bipyridine-based Tripodal Framework with a Strong Preference for Trigonal Prismatic Co-ordination Geometries

The  $S(\text{TP})$  values are 1.63 and 1.35 respectively which confirms the small distance from an ideal trigonal prism. Accordingly, the  $S(\text{Oct})$  values are comparatively high, 12.21 and 13.33 respectively (see Table 15; p. 129 for CShM values for this series of complexes). A representation of the calculated values in a shape map (Fig. 42; p. 131) does however suggest that the co-ordination sphere of the Mn atom in each unique complex deviates significantly from the Bailar path (15 and 17% respectively). It is likely that the constrained geometry of the hexadentate ligand is responsible for the deviations from the ideal shape. A closer look at the structures reveals that the N...N distances within each bipyridine unit (mean distance 2.675(4) Å) are generally significantly shorter than those between different bipyridines within the same triangular face (mean distance 3.116(5) Å). Accordingly, the mean  $s/h$  ratios are 1.19 and 1.17, indicating a significant compression relative to an ideal trigonal prism. The extent of this difference is much greater between the distal pyridyl N-donors on separate bipy units (3.351(5) Å) than it is between those pyridyl N-donors closer to the methine bridge (2.885(4) Å), indicating a significant degree of truncation in the geometry (Fig. 26) due to the divergent geometry of the three arms.

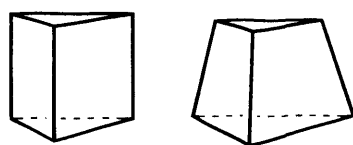


**Figure 26:** The co-ordination geometry is best described as a truncated trigonal prism ( $C_{3v}$ ).

An ideal trigonal prism has nine edges all of equal length, clearly in this case the major deviations could be due to several factors, including the (i) the constrained geometry of the ligand framework itself, particularly the narrow bite angle of the bipy units compressing the trigonal prism, (ii) the ionic radius of the metal centre may not be optimal

for the size of the cavity, forcing the ligand to twist in order to maximise the Mn<sup>II</sup>-N bonding interactions, and (iii) the molecular packing forces may have some impact of the ligand conformation, although this is difficult to quantify.

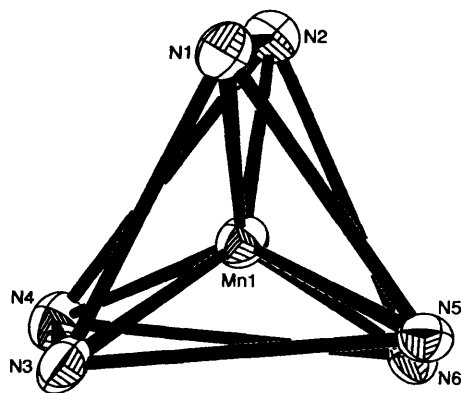


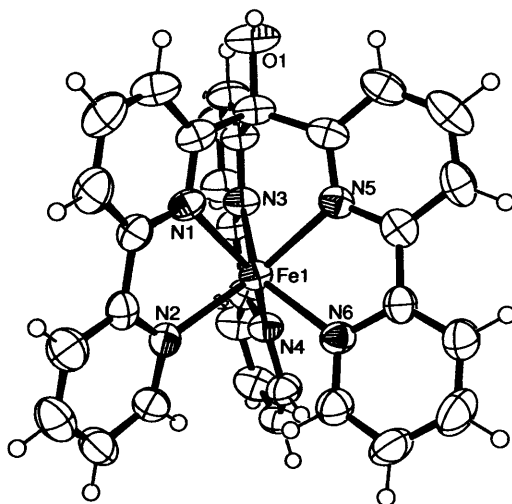
Figure 27: A view of the core geometry of 2.1 showing the atom numbering. Displacement ellipsoids are shown at the 50% probability level.

Table 5: Significant Bond lengths (Å) and Angles (°) for [Mn<sup>II</sup>(L<sup>3</sup>)](ClO<sub>4</sub>)<sub>2</sub>·H<sub>2</sub>O

Mn(1)-N(1)	2.227(3)		Mn(2)-N(7)	2.259(3)
Mn(1)-N(2)	2.242(4)		Mn(2)-N(8)	2.238(3)
Mn(1)-N(3)	2.245(4)		Mn(2)-N(9)	2.249(3)
Mn(1)-N(4)	2.263(4)		Mn(2)-N(10)	2.278(4)
Mn(1)-N(5)	2.252(3)		Mn(2)-N(11)	2.236(3)
Mn(1)-N(6)	2.229(3)		Mn(2)-N(12)	2.221(4)
N(1)-Mn(1)-N(6)	138.54(13)		N(12)-Mn(2)-N(11)	73.68(12)
N(1)-Mn(1)-N(2)	73.46(12)		N(12)-Mn(2)-N(8)	97.87(13)
N(6)-Mn(1)-N(2)	96.95(13)		N(11)-Mn(2)-N(8)	137.89(13)
N(1)-Mn(1)-N(3)	80.48(12)		N(12)-Mn(2)-N(9)	136.37(12)
N(6)-Mn(1)-N(3)	122.57(13)		N(11)-Mn(2)-N(9)	79.71(12)
N(2)-Mn(1)-N(3)	139.73(12)		N(8)-Mn(2)-N(9)	124.63(12)
N(1)-Mn(1)-N(5)	79.28(12)		N(12)-Mn(2)-N(7)	126.15(13)
N(6)-Mn(1)-N(5)	72.80(13)		N(11)-Mn(2)-N(7)	79.18(12)
N(2)-Mn(1)-N(5)	123.26(13)		N(8)-Mn(2)-N(7)	73.16(12)
N(3)-Mn(1)-N(5)	79.85(13)		N(9)-Mn(2)-N(7)	80.30(13)
N(1)-Mn(1)-N(4)	125.15(12)		N(12)-Mn(2)-N(10)	96.07(14)
N(6)-Mn(1)-N(4)	95.78(13)		N(11)-Mn(2)-N(10)	126.21(12)
N(2)-Mn(1)-N(4)	97.64(14)		N(8)-Mn(2)-N(10)	95.35(12)
N(3)-Mn(1)-N(4)	72.96(14)		N(9)-Mn(2)-N(10)	72.71(13)
N(5)-Mn(1)-N(4)	138.17(13)		N(7)-Mn(2)-N(10)	136.97(13)

### 2.4.7.2 Crystal Structure of $[\text{Fe}^{\text{II}}(\text{L}^3)][\text{ClO}_4]_2$ (2.2)

Compound **2.2** crystallises in the monoclinic space group  $P2_1/n$  and contains one complex within the asymmetric unit (Fig. 28). The central  $\text{Fe}^{\text{II}}$  cation again lies within the central cavity of the discrete complex and is co-ordinated by all six bipy N-donors.



**Figure 28:** Perspective view of the asymmetric unit showing the atom numbering. Displacement ellipsoids are shown at the 50% probability level. H atoms are represented by circles of arbitrary size.

The co-ordination geometry (Fig. 29) is predominantly trigonal prismatic, which is confirmed by the  $S(\text{TP})$  value of 1.89. The mean Bailar twist angle,  $\phi$ , is  $14.6^\circ$  and the dihedral angle between the trigonal faces is just  $0.10(19)^\circ$ . The co-ordination spheres of the Fe atom does however, in a similar manner to the Mn complex, deviate significantly (10%) from the Bailar path. The co-ordinative  $\text{Fe}^{\text{II}}\text{-N}(\text{bipy})$  bond lengths range from  $2.152(3)$  Å to  $2.223(4)$  Å, which are significantly longer than the similar example,  $[\text{Fe}^{\text{II}}(\text{bipy})_3][\text{ClO}_4]_2$ , reported by Batten *et al.*<sup>59</sup> which range from  $1.953(3)$  Å to  $1.972(3)$  Å in an unconstrained octahedral environment. This difference could be due to the system compensating for the increased internuclear repulsion by lengthening the metal-ligand bond distances. The  $\text{N}\cdots\text{N}$  distances within each bipyridine unit (mean distance  $2.639(5)$  Å) are also significantly shorter than those between different bipyridines within the same triangular face (mean distance  $3.034(5)$  Å). Accordingly, the mean  $s/h$  ratio is

1.17 indicating a significant compression relative to an ideal trigonal prism. As observed for all the complexes in this series, a significant degree of truncation is present, lowering the overall symmetry of the core from  $D_{3h}$  to  $C_{3v}$  (Fig. 26).

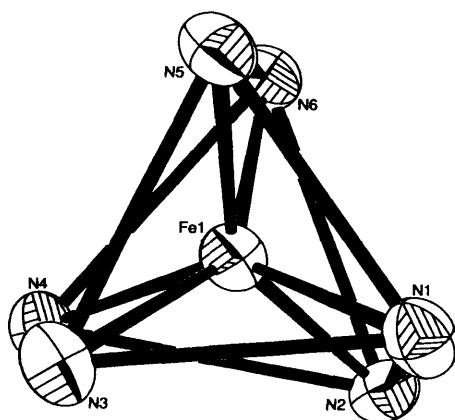


Figure 29: A view of the core geometry of 2.2 showing the atom numbering. Displacement ellipsoids are shown at the 50% probability level.

The molecular packing framework is supported by one classical hydrogen bond (Table 7), notably between the tertiary alcohol and an oxygen acceptor (O2) located on a symmetry generated perchlorate counterion [ $-\frac{1}{2} + x, \frac{1}{2} - y, -\frac{1}{2} + z$ ].

Table 6: Significant Bond lengths (Å) and Angles (°) for  $[\text{Fe}^{\text{II}}(\text{L}^3)][\text{ClO}_4]_2$

Fe(1)-N(1)	2.152(3)		Fe(1)-N(4)	2.209(4)
Fe(1)-N(2)	2.223(4)		Fe(1)-N(5)	2.157(3)
Fe(1)-N(3)	2.192(3)		Fe(1)-N(6)	2.179(3)
N(1)-Fe(1)-N(5)	82.31(13)		N(6)-Fe(1)-N(4)	93.33(13)
N(1)-Fe(1)-N(6)	122.60(13)		N(3)-Fe(1)-N(4)	73.66(13)
N(5)-Fe(1)-N(6)	74.91(14)		N(1)-Fe(1)-N(2)	74.30(14)
N(1)-Fe(1)-N(3)	81.73(13)		N(5)-Fe(1)-N(2)	143.89(14)
N(5)-Fe(1)-N(3)	81.13(13)		N(6)-Fe(1)-N(2)	94.87(13)
N(6)-Fe(1)-N(3)	142.12(13)		N(3)-Fe(1)-N(2)	121.12(13)
N(1)-Fe(1)-N(4)	142.74(13)		N(4)-Fe(1)-N(2)	94.86(14)
N(5)-Fe(1)-N(4)	119.88(13)			

Table 7: H-bonding geometry (Å, °) for 2.2

D-H...A	D - H	H...A	D...A	D - H...A
O(1)-H(1)...O(2)#1	0.84	2.06	2.825(6)	152

Symmetry transformations used to generate equivalent atoms:

#1 =  $-1/2+x, 1/2-y, -1/2+z$ . #2 =  $3/2-x, 1/2+y, 1/2-z$

### 2.4.7.3 Crystal Structure of $[\text{Co}^{\text{II}}(\text{L}^3)][\text{ClO}_4]_2 \cdot 0.5\text{CH}_3\text{CN}$ (2.3)

Compound **2.3** crystallises in the monoclinic space group  $P2_1/n$  and contains one complex within the asymmetric unit (Fig. 30). The mean Bailar twist angle in this instance is  $16.8^\circ$  which is large in comparison to the other complexes in this series (with the exception of the  $\text{Ni}^{\text{II}}$  complex, **2.4**, which exhibits the highest twist angle of  $25.1^\circ$ ). However, the core geometry is still best described as trigonal prismatic, with the  $S(\text{TP})$  and  $S(\text{Oct})$  values of 2.05 and 9.25 respectively. The strong trigonal prismatic preference of the ligand appears to prevent the adoption of an octahedral environment even in the presence of metals with strong stereoelectronic preferences. As a result, the adoption of high-spin electronic configurations is more favourable and the trend of Bailar twist angles for this series of complexes appears to support this theory (*cf.* Section 2.2, Fig. 4, p. 79).

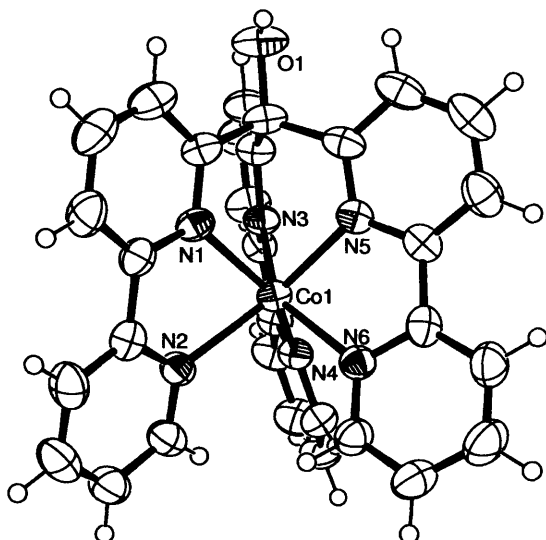


**Figure 30:** Perspective view of the asymmetric unit showing the atom numbering. Displacement ellipsoids are shown at the 50% probability level. H atoms are represented by circles of arbitrary size.

The dihedral angle between the trigonal faces is just  $0.15(18)^\circ$  and there is negligible deviation away from the  $C_3$  axis. The co-ordinative bond lengths range from  $2.111(3)$  Å to  $2.200(3)$  Å which are similar to those within the octahedral complex,  $[\text{Co}^{\text{II}}(\text{bpy})_3][\text{ClO}_4]_2$ ,



reported by Yao *et al.* which range between 2.119(2) and 2.136(2) Å.<sup>60</sup> The mean N···N distance within each bipyridine unit (2.623(3) Å) is significantly shorter than those between different bipyridines within the same triangular face (2.978(3) Å) and leads to a compression along one axis ( $s/h = 1.16$ ). The trigonal prism is again truncated, in this case the mean distance between the distal pyridyl-N donors is 0.342(3) Å larger than those donors lying closest to the methine bridge. Analysis of the deviation from the Bailar path (7%) reveals that this compound has a similar value to that found in the nickel (5%) and the zinc (9%) compounds, suggesting that these structures are very close to the Bailar path for the interconversion of the trigonal prism and the octahedron.

Intermolecular  $\pi$ - $\pi$  stacking interactions are not present, however there is a classical hydrogen bond supporting the molecular packing framework between the hydroxyl oxygen atom (O1) and the acceptor perchlorate oxygen (O5) (Table 9).

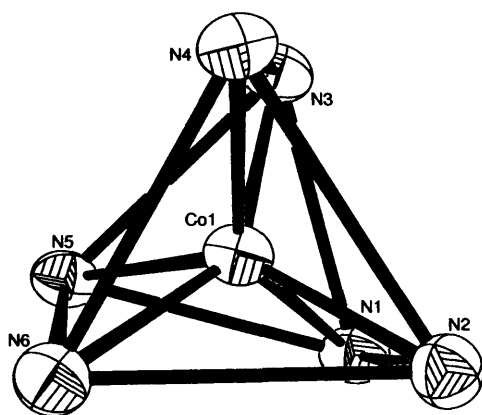


**Figure 31:** A view of the core geometry of 2.3 showing the atom numbering. Displacement ellipsoids are shown at the 50% probability level.

Chapter 2: A Bipyridine-based Tripodal Framework with a Strong Preference for Trigonal Prismatic Co-ordination Geometries

**Table 8:** Significant Bond lengths (Å) and Angles (°) for  $[\text{Co}^{\text{II}}(\text{L}^3)][\text{ClO}_4]_2 \cdot 0.5\text{CH}_3\text{CN}$

Co(1)-N(1)	2.111(3)		Co(1)-N(4)	2.181(3)
Co(1)-N(2)	2.200(3)		Co(1)-N(5)	2.116(3)
Co(1)-N(3)	2.141(3)		Co(1)-N(6)	2.147(3)
N(1)-Co(1)-N(5)	83.38(13)		N(3)-Co(1)-N(4)	74.56(12)
N(1)-Co(1)-N(3)	82.90(13)		N(6)-Co(1)-N(4)	91.66(13)
N(5)-Co(1)-N(3)	82.01(13)		N(1)-Co(1)-N(2)	74.99(13)
N(1)-Co(1)-N(6)	121.66(13)		N(5)-Co(1)-N(2)	146.48(13)
N(5)-Co(1)-N(6)	75.98(13)		N(3)-Co(1)-N(2)	119.44(13)
N(3)-Co(1)-N(6)	143.99(13)		N(6)-Co(1)-N(2)	93.81(13)
N(1)-Co(1)-N(4)	144.61(13)		N(4)-Co(1)-N(2)	92.61(13)
N(5)-Co(1)-N(4)	119.13(12)			

**Table 9:** H-bonding geometry (Å, °) for 2.3

D-H...A	d(D-H)	d(H...A)	d(D...A)	<(DHA)
O(1)-H(1)...O(5)	0.84	2.04	2.809(5)	152.2

#### 2.4.7.4 Crystal Structure of $[\text{Ni}^{\text{II}}(\text{L}^3)][\text{ClO}_4]_2 \cdot 0.5\text{CH}_3\text{CN}$ (2.4)

Compound 2.4 crystallises in the monoclinic space group  $P2_1/n$  and contains a single complex within the asymmetric unit (Fig. 32). The co-ordinative bond lengths range from 2.055(4) Å to 2.155(5) Å and span a significantly larger range compared to that of the related compound  $[\text{Ni}^{\text{II}}(\text{bpy})_3][\text{ClO}_4]_2$  reported by Hong *et al.*<sup>61</sup> which range between 2.071(3) Å and 2.090(3) Å in an unconstrained octahedral environment. This may be caused by the system attempting to compensate for the increased non-bonded contacts which are imposed by the natural TP conformation of the ligand framework by lengthening the metal-ligand bond distances.

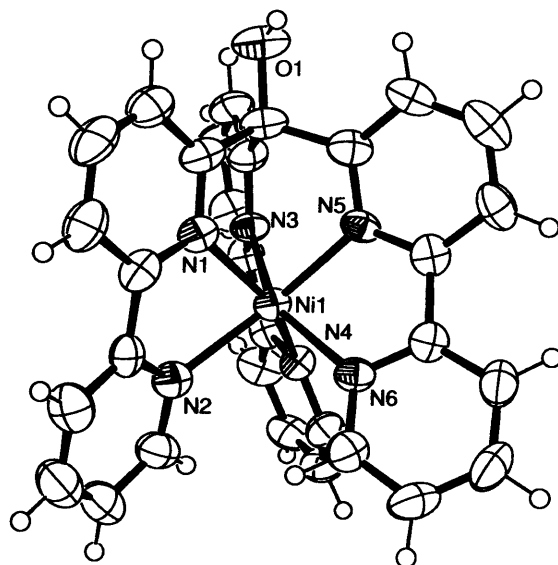


**Figure 32:** Perspective view of the asymmetric unit showing the atom numbering. Displacement ellipsoids are shown at the 50% probability level. H atoms are represented by circles of arbitrary size.

The mean Bailar twist angle is  $25.1^\circ$  which is the largest for all the complexes in this series and is an indication of the strong octahedral preference displayed by the  $d^8$  metal ion. However, despite this being the largest twist, the complex still retains predominantly trigonal prismatic character (Fig. 33) with  $S(\text{TP})$  and  $S(\text{Oct})$  values of 3.62 and 6.19 respectively. The dihedral angle between the trigonal faces is just  $0.1(3)^\circ$  and there is negligible deviation of the metal co-ordination sphere from the Bailar path.

The mean  $\text{N}\cdots\text{N}$  distance within each bipyridine unit ( $2.613(3)$  Å) is significantly shorter than those between different bipyridines within the same triangular face ( $2.917(3)$  Å) and leads to a compression along one axis ( $s/h = 1.16$ ). The trigonal prism is again truncated, in this case the mean distance between the distal pyridyl-N donors is  $0.312(5)$  Å larger than those donors lying closest to the methine bridge. Despite the distortions from the trigonal prism, arising both from the unequal  $\text{N}\cdots\text{N}$  edges and the Bailar twist, the negligible deviation of the CSOM tells us that this complex clearly retains the  $C_3$  axis.

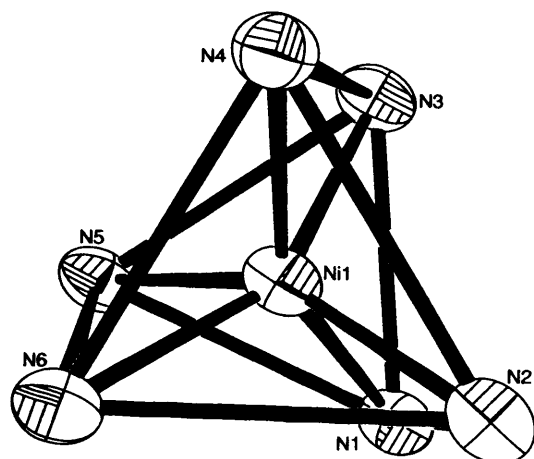


Figure 33: A view of the core geometry of 2.4 showing the atom numbering. Displacement ellipsoids are shown at the 50% probability level.

Table 10: Significant Bond lengths (Å) and Angles (°) for  $[\text{Ni}^{\text{II}}(\text{L}^3)][\text{ClO}_4]_2 \cdot 0.5\text{CH}_3\text{CN}$

Ni(1)-N(1)	2.057(5)		Ni(1)-N(4)	2.145(5)
Ni(1)-N(2)	2.155(5)		Ni(1)-N(5)	2.055(4)
Ni(1)-N(3)	2.072(4)		Ni(1)-N(6)	2.115(5)
N(5)-Ni(1)-N(1)	84.0(2)		N(3)-Ni(1)-N(4)	76.64(19)
N(5)-Ni(1)-N(3)	83.53(19)		N(6)-Ni(1)-N(4)	90.96(19)
N(1)-Ni(1)-N(3)	84.66(19)		N(5)-Ni(1)-N(2)	151.76(19)
N(5)-Ni(1)-N(6)	77.34(19)		N(1)-Ni(1)-N(2)	76.8(2)
N(1)-Ni(1)-N(6)	114.51(19)		N(3)-Ni(1)-N(2)	114.53(19)
N(3)-Ni(1)-N(6)	150.87(19)		N(6)-Ni(1)-N(2)	91.97(19)
N(5)-Ni(1)-N(4)	113.41(18)		N(4)-Ni(1)-N(2)	92.57(18)
N(1)-Ni(1)-N(4)	152.38(19)			

#### 2.4.7.5 Crystal Structure of $[\text{Cu}^{\text{II}}(\text{L}^3)][\text{ClO}_4]_2 \cdot 2\text{CH}_3\text{CN}$ (2.5)

Compound 2.5 crystallises in the monoclinic space group  $C2/c$  and contains a single complex within the asymmetric unit (Fig. 34). A closer look at the structure of the  $\text{Cu}^{\text{II}}$  complex (Fig. 35) shows that it has four short (between 1.995(3) and 2.030(3) Å) and two long (2.349(3) and 2.859(4) Å) distances, indicative of a Jahn-Teller distortion. However, this is not the well-known Jahn-Teller distortion of a purported octahedral  $\text{Cu}^{\text{II}}$  ion that becomes an elongated square bipyramid, but an unprecedented Jahn-Teller distortion of a trigonal prism

schematically shown below (Fig. 36). The octahedral complex  $[\text{Cu}^{\text{II}}(\text{bpy})_3][\text{ClO}_4]_2$ , exhibits a Jahn-Teller distortion in which the two long bonds are mutually *trans* as expected, however, as in **2.5**, they are of unequal length (2.226(7) and 2.450(7) Å).<sup>62</sup> In this example, despite calculations failing to indicate the presence of any significant inter- or intramolecular ionic contacts of the van der Waals type, it was concluded that the crystal packing remained the most likely cause of the inequality.

The mean Bailar twist angle is  $17.0^\circ$  and the dihedral angle between the two trigonal faces is  $1.6(2)^\circ$ . The mean  $\text{N}\cdots\text{N}$  distance within each bipyridine unit (2.648(6) Å) is significantly shorter than those between different bipyridines within the same triangular face (3.038(5) Å) and leads to a compression along one axis ( $s/h = 1.18$ ). The mean  $\text{N}\cdots\text{N}$  distance between pyridyl N-donors closest to the methine bridge (2.804(8) Å) is significantly shorter than between that of the distal pyridyl-N donors (3.272(9) Å), indicative of the truncation seen across this series of complexes.

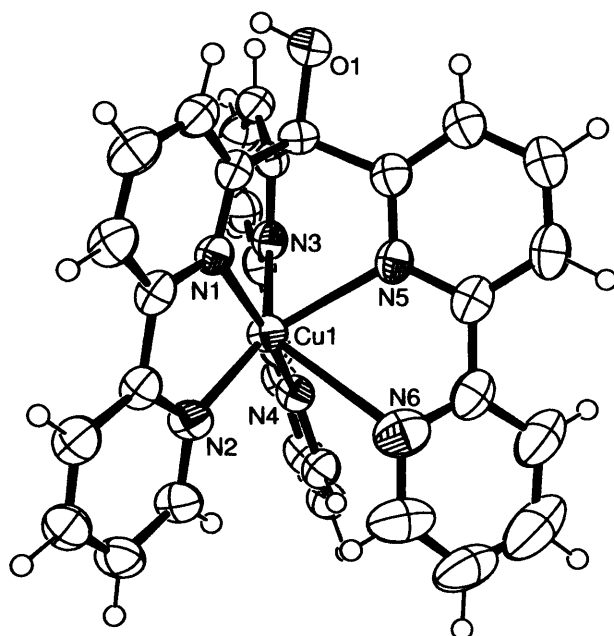


**Figure 34:** Perspective view of the asymmetric unit of **2.5** showing the atom numbering. Displacement ellipsoids are shown at the 50% probability level. H atoms are represented by circles of arbitrary size.

Chapter 2: A Bipyridine-based Tripodal Framework with a Strong Preference for Trigonal Prismatic Co-ordination Geometries

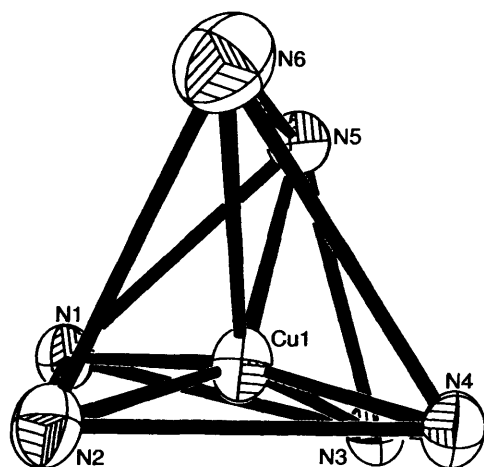


Figure 35: A view of the core geometry of 2.5 showing the atom numbering. Displacement ellipsoids are shown at the 50% probability level.

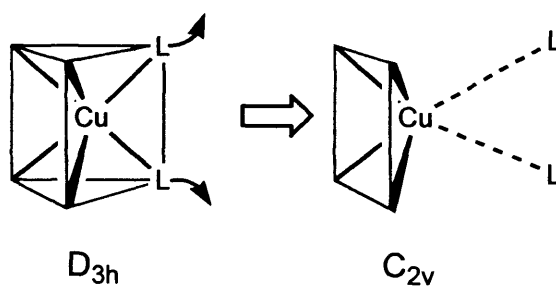


Figure 36: An unprecedented Jahn-Teller distortion of a trigonal prism.

Table 11: Significant Bond lengths (Å) and Angles (°) for  $[\text{Cu}^{\text{II}}(\text{L}^3)][\text{ClO}_4]_2 \cdot 2\text{CH}_3\text{CN}$

Cu(1)-N(1)	1.995(3)		Cu(1)-N(4)	2.023(3)
Cu(1)-N(2)	2.030(3)		Cu(1)-N(5)	2.349(3)
Cu(1)-N(3)	2.005(3)		Cu(1)-N(6)	2.859(4)
N(1)-Cu(1)-N(3)	89.46(13)		N(4)-Cu(1)-N(5)	107.95(12)
N(1)-Cu(1)-N(4)	164.86(14)		N(2)-Cu(1)-N(5)	130.84(13)
N(3)-Cu(1)-N(4)	79.97(13)		N(1)-Cu(1)-N(6)	106.18(12)
N(1)-Cu(1)-N(2)	81.06(13)		N(3)-Cu(1)-N(6)	134.44(13)
N(3)-Cu(1)-N(2)	145.54(14)		N(4)-Cu(1)-N(6)	88.95(12)
N(4)-Cu(1)-N(2)	101.57(13)		N(2)-Cu(1)-N(6)	79.91(13)
N(1)-Cu(1)-N(5)	80.29(12)		N(5)-Cu(1)-N(6)	62.62(12)
N(3)-Cu(1)-N(5)	79.02(13)			

#### 2.4.7.6 Crystal Structure of $[\text{Zn}^{\text{II}}(\text{L}^3)][\text{ClO}_4]_2$ (2.6)

Compound 2.6 crystallises in the monoclinic space group  $P2_1/n$  with a single complex in the asymmetric unit (Fig. 37). The  $d^{10}$   $\text{Zn}^{\text{II}}$  ion has no stereochemical preference and it is reasonable to assume that this complex would be highly similar to the  $\text{Mn}^{\text{II}}$  and  $\text{Cd}^{\text{II}}$  complexes, exhibiting a very small Bailar twist angle, however the twist angle seen in 2.6 is significantly larger at  $15.5^\circ$  (Fig. 38). Furthermore, the dihedral angle between trigonal faces is  $0.16(17)^\circ$  and the calculated deviation from the Bailar twist is relatively small (9%), values which are similar than the cobalt (7%) and nickel (5%) analogues.

The co-ordinative bond lengths vary from  $2.140(3)$  Å to  $2.211(3)$  Å which is a slightly larger range on comparison to the similar compound  $[\text{Zn}^{\text{II}}(\text{bpy})_3][\text{PF}_6]_2$  reported by Breu *et al.*<sup>63</sup> which range from  $2.147(3)$  Å to  $2.182(4)$  Å in an octahedral environment. In a similar manner to each of the other complexes in this series, the  $\text{N}\cdots\text{N}$  distances within each bipyridine unit (mean distance  $2.646(3)$  Å) are shorter than those between different bipyridines within the same triangular face ( $3.013(4)$  Å) leading to a compressed trigonal prism ( $s/h = 1.16$ ). Again, the extent of this difference is much greater between the distal pyridyl N-donors on separate bipy units ( $3.198(3)$  Å) than it is between those pyridyl N-donors closer to the methine bridge ( $2.827(3)$  Å) resulting in an approximately truncated trigonal prism.

Chapter 2: A Bipyridine-based Tripodal Framework with a Strong Preference for Trigonal Prismatic Co-ordination Geometries

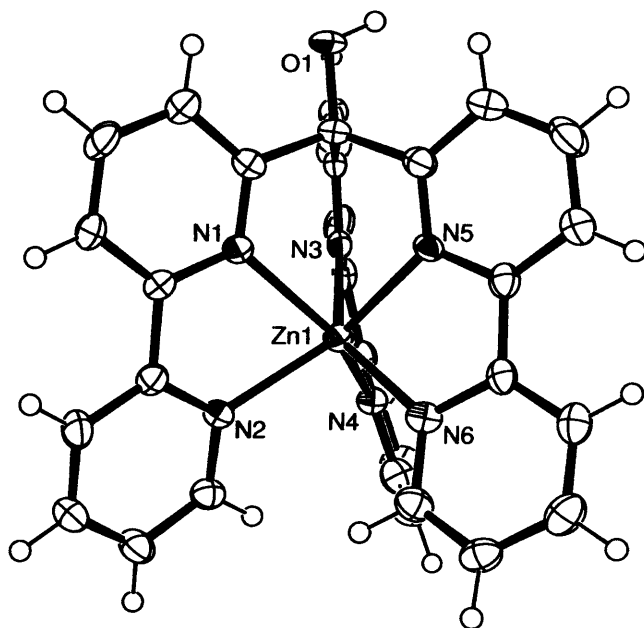


**Figure 37:** Perspective view of the asymmetric unit of **2.6** showing the atom numbering. Displacement ellipsoids are shown at the 50% probability level. H atoms are represented by circles of arbitrary size.

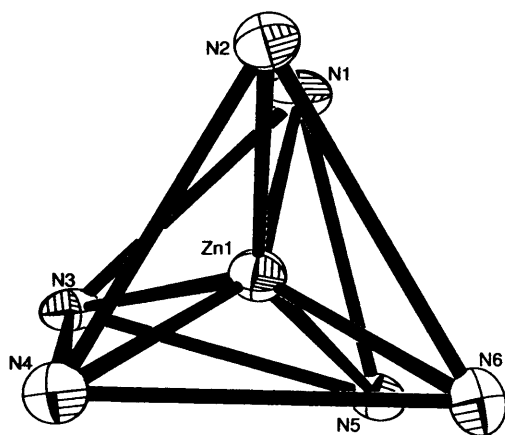


**Figure 38:** A view of the core geometry of **2.6** showing the atom numbering. Displacement ellipsoids are shown at the 50% probability level.



**Table 12:** Significant Bond lengths (Å) and Angles (°) for  $[\text{Zn}^{\text{II}}(\text{L}^3)][\text{ClO}_4]_2$

Zn(1)-N(1)	2.196(3)		Zn(1)-N(4)	2.140(3)
Zn(1)-N(2)	2.174(3)		Zn(1)-N(5)	2.154(3)
Zn(1)-N(3)	2.164(3)		Zn(1)-N(6)	2.211(3)
N(4)-Zn(1)-N(5)	121.54(11)		N(3)-Zn(1)-N(1)	80.49(11)
N(4)-Zn(1)-N(3)	75.62(12)		N(2)-Zn(1)-N(1)	74.31(11)
N(5)-Zn(1)-N(3)	81.64(11)		N(4)-Zn(1)-N(6)	94.51(11)
N(4)-Zn(1)-N(2)	93.86(11)		N(5)-Zn(1)-N(6)	74.56(11)
N(5)-Zn(1)-N(2)	143.26(11)		N(3)-Zn(1)-N(6)	144.31(10)
N(3)-Zn(1)-N(2)	119.80(10)		N(2)-Zn(1)-N(6)	94.70(10)
N(4)-Zn(1)-N(1)	143.25(11)		N(1)-Zn(1)-N(6)	120.64(11)
N(5)-Zn(1)-N(1)	81.26(11)			

#### 2.4.7.7 Crystal Structure of $[\text{Cd}^{\text{II}}(\text{L}^3)][\text{ClO}_4]_2 \cdot 2\text{CH}_3\text{OH}$ (2.7)

Compound 2.7 crystallises in the triclinic space group P-1 with two unique complexes residing within the asymmetric unit (Fig. 39). The co-ordination spheres of these two complexes (Fig. 40) have the smallest Bailar twist angles within this series of complexes, at  $4.4^\circ$  and  $1.7^\circ$  respectively. Furthermore, the dihedral angles between the trigonal faces are just  $0.4(2)^\circ$  and  $0.2(2)^\circ$  and the negligible deviation of the CSOM demonstrates that this complex clearly retains the  $C_3$  axis. Therefore the co-ordination environment is strongly trigonal prismatic, albeit with a compression along one axis caused by the acute bite angle of the three bipy groups. The co-ordinative bond lengths range from 2.286(4) Å to 2.358(4) Å and span a slightly larger range compared to that of the compound  $[\text{Cd}^{\text{II}}(\text{bpy})_3][\text{ClO}_4]_2$  reported by Chaudhury *et al.*<sup>64</sup> which range between 2.308(5) Å and 2.355(5) Å in an unconstrained octahedral environment. In contrast to each of the other complexes in this series, the trigonal prismatic environments of these two unique complexes do not exhibit significant signs of compression ( $s/h = 1.03$  and  $1.02$ ). However, the trigonal prisms are again truncated; the mean distance between the distal

pyridyl-N donors is 0.605(4) Å larger than those donors lying closest to the methine bridge in complex 1, and 0.598(4) Å larger in complex 2.

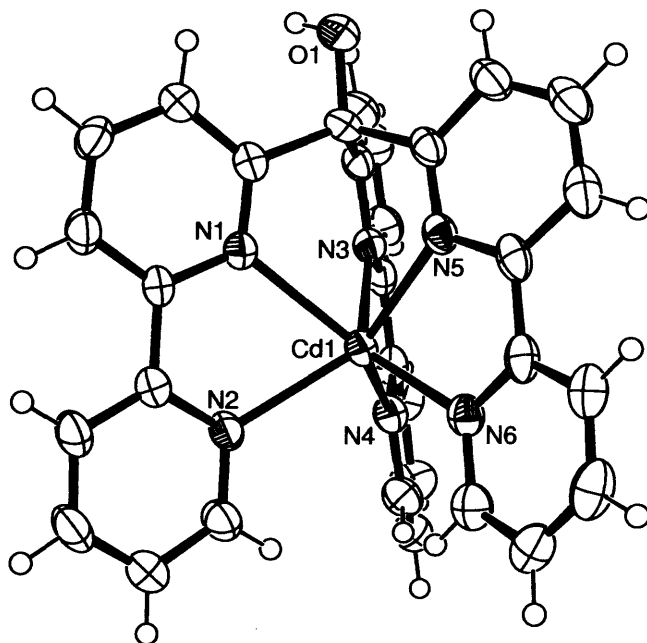


**Figure 39:** Perspective view of the asymmetric unit showing the atom numbering. Displacement ellipsoids are shown at the 50% probability level. H atoms are represented by circles of arbitrary size. Only one of the crystallographically independent complex units is shown; the other is similar.

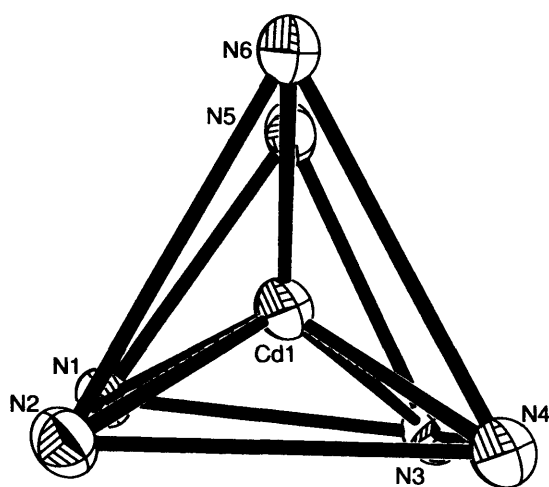


**Figure 40:** A view of the core geometry of 2.7 showing the atom numbering. Displacement ellipsoids are shown at the 50% probability level.

Chapter 2: A Bipyridine-based Tripodal Framework with a Strong Preference for Trigonal Prismatic Co-ordination Geometries

**Table 13:** Significant Bond lengths (Å) and Angles (°) for  $[\text{Cd}^{\text{II}}(\text{L}^3)][\text{ClO}_4]_2 \cdot 2\text{C}_2\text{H}_3\text{N}$

Cd(1)-N(1)	2.349(4)		Cd(2)-N(7)	2.348(4)
Cd(1)-N(2)	2.344(4)		Cd(2)-N(8)	2.337(4)
Cd(1)-N(3)	2.358(4)		Cd(2)-N(9)	2.312(4)
Cd(1)-N(4)	2.321(4)		Cd(2)-N(10)	2.286(4)
Cd(1)-N(5)	2.308(4)		Cd(2)-N(11)	2.337(4)
Cd(1)-N(6)	2.308(4)		Cd(2)-N(12)	2.349(4)
N(6)-Cd(1)-N(5)	72.26(14)		N(10)-Cd(2)-N(9)	72.18(17)
N(6)-Cd(1)-N(4)	103.22(14)		N(10)-Cd(2)-N(11)	127.35(15)
N(5)-Cd(1)-N(4)	131.03(13)		N(9)-Cd(2)-N(11)	76.77(14)
N(6)-Cd(1)-N(2)	101.81(13)		N(10)-Cd(2)-N(8)	101.95(17)
N(5)-Cd(1)-N(2)	134.26(13)		N(9)-Cd(2)-N(8)	132.06(15)
N(4)-Cd(1)-N(2)	94.70(13)		N(11)-Cd(2)-N(8)	130.20(15)
N(6)-Cd(1)-N(1)	127.19(13)		N(10)-Cd(2)-N(7)	134.73(16)
N(5)-Cd(1)-N(1)	77.86(13)		N(9)-Cd(2)-N(7)	80.45(14)
N(4)-Cd(1)-N(1)	129.04(13)		N(11)-Cd(2)-N(7)	77.81(14)
N(2)-Cd(1)-N(1)	70.44(13)		N(8)-Cd(2)-N(7)	70.95(15)
N(6)-Cd(1)-N(3)	136.09(13)		N(10)-Cd(2)-N(12)	97.00(15)
N(5)-Cd(1)-N(3)	79.91(13)		N(9)-Cd(2)-N(12)	128.54(14)
N(4)-Cd(1)-N(3)	70.82(13)		N(11)-Cd(2)-N(12)	71.09(14)
N(2)-Cd(1)-N(3)	121.82(13)		N(8)-Cd(2)-N(12)	99.27(15)
N(1)-Cd(1)-N(3)	76.78(13)		N(7)-Cd(2)-N(12)	128.14(14)

## 2.5 Conclusions

### Structural Overview and Continuous Shape Mapping

It was anticipated that the Bailar twist angles (Table 14) observed for complexes **2.1-2.7** would be largely dependent upon the stereochemical preferences of the metal ions with respect to octahedral and trigonal prismatic geometries, *i.e.* metals with no discernible octahedral preference were expected to distort the ligands natural near-TP conformation to a much smaller degree than metal ions with an octahedral preference. The strong trigonal prismatic preference of the ligand appears to prevent the adoption of an octahedral environment even in the presence of metals with strong stereoelectronic preferences. As a result, the adoption of high-spin electronic

configurations is more favourable and the trend of Bailar twist angles for this series of complexes appears to support this theory (*cf.* Section 2.2, Fig. 4, p. 79). For example, the metal ions  $\text{Co}^{\text{II}}$ ,  $\text{Ni}^{\text{II}}$  and  $\text{Cu}^{\text{II}}$  all result in the most significant trigonal twists towards octahedral configurations, with the  $d^8$   $\text{Ni}^{\text{II}}$  ion providing the largest twist angle. In contrast the  $\text{Mn}^{\text{II}}$ , high-spin  $\text{Fe}^{\text{II}}$ ,  $\text{Zn}^{\text{II}}$  and  $\text{Cd}^{\text{II}}$  cations exhibit the smallest Bailar twist angles. Another point of note is the case of  $\text{Fe}^{\text{II}}$  where the low-spin example would have the strongest octahedral preference, however in this case the sterical constraints of the ligand prevent an octahedral co-ordination geometry. It can be reasonably concluded therefore that the ligand field is weaker due to the poorer orbital overlap between the six homoleptic donors and the metal centre and consequently a high-spin d-electron configuration is obtained.

**Table 14:** The mean average Bailar twist angles for complexes 2.1-2.7 amongst other pertinent data.

Compound	Bailar twist angle, $\phi$ , $^\circ$	$s/h$	Mean bond $\text{M}\cdots\text{N}$ length, $\text{\AA}$	Dihedral angle between trigonal faces, $^\circ$	Effective ionic radius of the metal ion (pm) <sup>b</sup>
2.1	10.4	1.19	2.243	0.10(18)	67
2.1 <sup>a</sup>	7.7	1.17	2.246	0.39(18)	67
2.2	14.6	1.17	2.218	0.10(19)	61(ls), 78(hs)
2.3	16.8	1.16	2.149	0.15(18)	65(ls), 74.5(hs)
2.4	25.1	1.16	2.100	0.1(3)	69
2.5	17.0	1.18	2.210	1.6(2)	73
2.6	15.5	1.16	2.173	0.16(17)	74
2.7	4.4	1.03	2.331	0.4(2)	95
2.7 <sup>a</sup>	1.7	1.02	2.328	0.2(2)	95

<sup>a</sup> Compounds 2.1 and 2.7 each contain two crystallographically independent complexes present within the asymmetric unit. <sup>b</sup> Values taken from reference 65.

The ionic radius of the metal ion clearly has some bearing upon the core geometry, the larger metals ion appear to be associated with the smallest Bailar twist angles. The cadmium ion has the largest ionic radius and accordingly has the most trigonal prismatic character. There is also a strong correlation between the Bailar twist angle and the mean  $\text{M}\cdots\text{N}$  co-ordinative bond lengths (Fig. 41). The complexes with the longest bond lengths display the least distortion

towards an octahedral configuration. This is probably due to the non-bonded contacts within the TP environment being reduced, providing extra stabilisation to the normally unfavourable geometry.

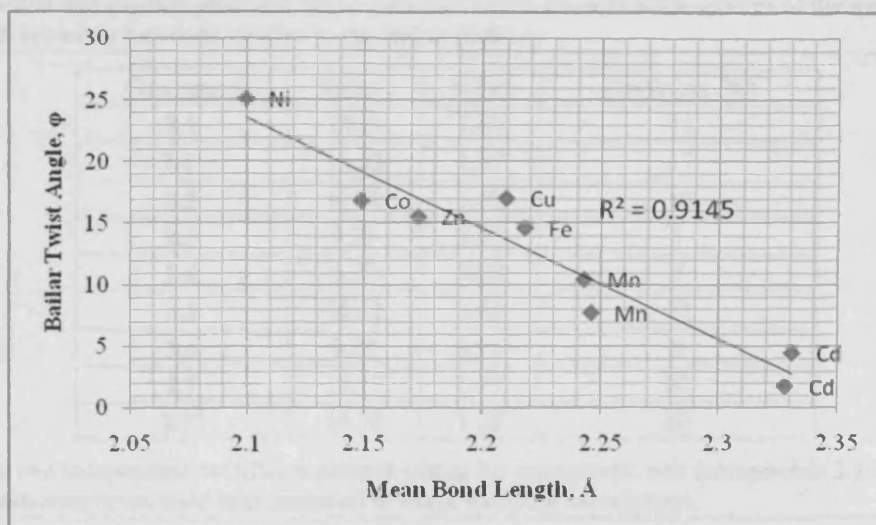


**Figure 41:** A scatter plot illustrating the correlation between the Bailar twist angle and the mean co-ordinative M...N bond distance.\*

A comparison of the shape measures relative to the octahedron and the trigonal prism for each metal atom has led to the following conclusions:

- (i) All structures are much closer to the trigonal prism than to the octahedron, even if none of them can be said to be a nearly perfect trigonal prism.
- (ii) A representation of the calculated values in a shape map (Fig. 42; Table 15) suggests that all structures are close to the Bailar path for the interconversion of the trigonal prism and the octahedron.

\* The  $R^2$  value is a number between 0 and 1 which reveals how closely the estimated values for the trendline correspond to the experimental data. A trend line is most reliable when its  $R^2$  value is at or near 1.

- (iii) The path deviation functions collected in Table 15 show that the  $\text{Co}^{\text{II}}$ ,  $\text{Ni}^{\text{II}}$  and  $\text{Zn}^{\text{II}}$  complexes contain co-ordination environments which are very close to the Bailar path and can be said to be trigonal metaprisms.

**Table 15:** Octahedral and trigonal prismatic shape measures of the co-ordination spheres of the metal atoms, and values of the path deviation functions relative to the Bailar pathway.

Compound	S(Oct)	S(TP)	Deviation (%)
2.1	12.21	1.63	15
2.1 <sup>a</sup>	13.33	1.35	17
2.2	10.20	1.89	10
2.3	9.25	2.05	7
2.4	6.17	3.62	5
2.5	10.32	3.43	22
2.6	9.80	1.94	9
2.7	15.27	1.77	27
2.7 <sup>a</sup>	16.78	1.58	30

<sup>a</sup> Where there are two independent complexes present within the asymmetric unit (compounds 2.1 and 2.7), co-ordinates from both complexes have been included in shape mapping calculations.

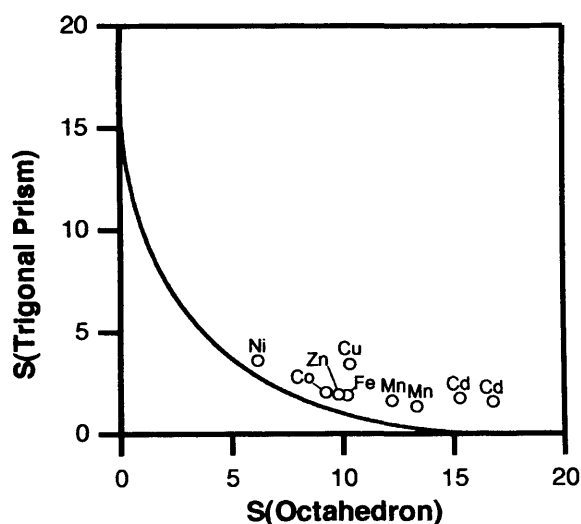


**Figure 42:** Octahedron – Trigonal Prism shape map showing the Bailar pathway (continuous line) and the experimental data (circles).

- (iv) The co-ordination spheres of the  $\text{Fe}^{\text{II}}$  and  $\text{Mn}^{\text{II}}$  complexes deviate significantly from the Bailar path, while the  $\text{Cu}^{\text{II}}$  and  $\text{Cd}^{\text{II}}$  complexes are quite far from that path. Since the

regular trigonal prism with which we are comparing the co-ordination spheres is one that has all its edges identical, it is likely that the constrained geometry of the hexadentate ligand is responsible for the deviations from the ideal shape. A closer look at the structures shows that the N...N distances within each bipyridine unit are shorter than those between different bipyridines, while the N...N distances between different bipyridine units closer to the methine bridge are shorter than those between distal nitrogen atoms, resulting in an approximately truncated pyramidal shape of the co-ordination sphere (Fig. 26; p. 113). Continuous symmetry operation measures (CSOM's) have been calculated in order to determine whether the distortions from the trigonal prism, arising both from the unequal N...N edges and the varying degrees of Bailar twist, cause a deviation from trigonal symmetry. The CSOM's for a three-fold rotation in the complexes under study are presented in Table 16. The negligible values found for most metal atoms clearly tell us that the  $C_3$  axis is retained in most cases, except in the copper compound.

**Table 16:**  $C_3$  Symmetry operation measures of the metal co-ordination spheres

Compound	S( $C_3$ )
<b>2.1</b>	0.01
<b>2.1a</b>	0.01
<b>2.2</b>	0.01
<b>2.3</b>	0.01
<b>2.4</b>	0.01
<b>2.5</b>	0.86
<b>2.6</b>	0.01
<b>2.7</b>	0.03
<b>2.7a</b>	0.06

- (v) A closer look at the structure of the Cu complex shows that it has four short (2.02 Å) and two long (2.35 and 2.86 Å) distances, indicative of a Jahn-Teller distortion. However,

this is not the well-known Jahn-Teller distortion of a purported octahedral Cu(II) ion that becomes an elongated square bipyramid, but an unprecedented Jahn-Teller distortion of a trigonal prism schematically shown in Fig. 36 (p. 123).

## 2.6 References

1. J. C. Bailar, *J. Inorg. Nucl. Chem.*, 1958, 8, 165.
2. R. A. D. Wentworth, *Coord. Chem. Rev.*, 1972, 9, 171-187.
3. S. Alvarez, D. Avnir, M. Lluell, M. Pinsky, *New J. Chem.*, 2002, 26, 996-1009.
4. S. Alvarez, D. Avnir, P. Alemany, *Chem. Soc. Rev.*, 2005, 34, 313-326.
5. S. Alvarez, D. Avnir, P. Alemany, D. Casanova, M. Lluell, J. Cirera, *Coord. Chem. Rev.*, 2005, 249, 1693-1708.
6. S. Alvarez, D. Avnir, M. Pinsky, M. Lluell, *Cryst. Engineer.* 2001, 4, 179-200.
7. M. Pinsky, D. Avnir, *Inorg. Chem.*, 1998, 37, 5575-5582.
8. M. Pinsky, K. B. Lipkowitz, D. Avnir, *J. Math. Chem.*, 2001, 30, 1, 109-120.
9. R. G. Dickinson, L. Pauling, *J. Am. Chem. Soc.*, 1923, 45, 1466.
10. R. Eisenberg, J. A. Ibers, *J. Am. Chem. Soc.*, 1965, 87, 3776.
11. R. Eisenberg, J. A. Ibers, *Inorg. Chem.*, 1966, 5, 411.
12. A. E. Smith, G. N. Schrauzer, V. P. Mayweg, W. Heinrich, *J. Am. Chem. Soc.*, 1965, 87, 5798.
13. R. Eisenberg, E. I. Stiefel, R. C. Rosenberg, H. B. Gray, *J. Am. Chem. Soc.*, 1966, 88, 2874.
14. R. Eisenberg, H. B. Gray, *Inorg. Chem.*, 1967, 6, 1844.
15. D. L. Kepert, *Prog. Inorg. Chem.*, 1977, 23, 1.



Chapter 2: A Bipyridine-based Tripodal Framework with a Strong Preference for Trigonal Prismatic Co-ordination Geometries

16. T. B. Karpishin, T. D. P. Stack, K. N. Raymond, *J. Am. Chem. Soc.*, 1993, 115, 182-192.
17. R. A. D. Wentworth, W. O. Gillum, R. F. Childers, *Inorg. Chem.*, 1970, 9, 1825-1832.
18. W. O. Gillum, J. C. Huffman, W. E. Streib, R. A. D. Wentworth, *Chem. Commun.*, 1969, 843.
19. E. B. Fleischer, A. E. Gebala, D. R. Swift, *Chem. Commun.*, 1971, 1280.
20. E. B. Fleischer, A. E. Gebala, P. A. Tasker, *J. Am. Chem. Soc.*, 1970, 92, 6365.
21. J. E. Parks, B. E. Wagner, R. H. Holm, *J. Am. Chem. Soc.*, 1970, 92, 3500.
22. J. E. Parks, B. E. Wagner, R. H. Holm, *Inorg. Chem.*, 1971, 10, 2472.
23. M. R. Churchill, A. H. Reis, *Inorg. Chem.*, 1972, 11, 1811-1818.
24. D. R. Boston, N. J. Rose, *J. Am. Chem. Soc.*, 1968, 90, 6859.
25. G. A. Zakrzewski, C. A. Ghilardi, E. C. Lingafelter, *J. Am. Chem. Soc.*, 1971, 93, 4411.
26. E. Larsen, G. N. La Mar, B. E. Wagner, J. E. Parks, R. H. Holm, *Inorg. Chem.*, 1972, 11, 2652-2668.
27. H. Al-Sagher, I. Fallis, L. J. Farrugia, R. D. Peacock, *J. Chem. Soc., Chem. Commun.*, 1993, 1499-1500.
28. A. A. Belal, I. Fallis, L. J. Farrugia, N. M. Macdonald, R. D. Peacock, *J. Chem. Soc., Chem. Commun.*, 1991, 402.
29. A. A. Belal, P. Chaudhuri, I. Fallis, L. J. Farrugia, R. Hartung, N. M. Macdonald, B. Nuber, R. D. Peacock, J. Weiss, K. Wieghardt, *Inorg. Chem.*, 1991, 30, 4397.
30. P. M. Morse, G. S. Girolami, *J. Am. Chem. Soc.*, 1989, 111, 4114-4116.
31. R. L. Paul, A. J. Amoroso, P. L. Jones, S. M. Couchman, Z. R. Reeves, L. H. Rees, J. C. Jeffery, J. A. McCleverty, M. D. Ward, *J. Chem. Soc. Dalton Trans.*, 1999, 1563.
32. A. J. Amoroso, J. C. Jeffery, P. L. Jones, J. A. McCleverty, P. Thornton, M. D. Ward, *Angew. Chem. Int. Ed. Engl.*, 1995, 34, 1443.

Chapter 2: A Bipyridine-based Tripodal Framework with a Strong Preference for Trigonal Prismatic Co-ordination Geometries

33. R. L. Paul, A. J. Amoroso, P. L. Jones, S. M. Couchman, Z. R. Reeves, L. H. Rees, J. C. Jeffery, J. A. McCleverty, M. D. Ward, *J. Chem. Soc., Dalton Trans.*, 1999, 1563-1568.
34. M. D. Ward, J. A. McCleverty, J. C. Jeffery, *Coord. Chem. Rev.*, 2001, 222, 251-272.
35. M. D. Ward, *Annu. Rep. Prog. Chem., Sect. A*, 2000, 96, 345-385.
36. N. Singh, Ph.D. Dissertation, Cardiff University, 2008.
37. H. Nierengarten, J. Rojo, E. Leize, J.-M. Lehn, A. V. Dorselaer, *Eur. J. Inorg. Chem.* 2002, 573.
38. S. F. A. Kettle, *Physical Inorganic Chemistry*, Oxford University Press, New York, 1998, p. 163.
39. P. Krumholtz, *J. Amer. Chem. Soc.*, 1953, 75, 2163.
40. C. K. Jorgensen, *Acta Chem. Scand.*, 1955, 9, 1362.
41. M. C. Hughes, J. M. Rao, D. J. Macero, *Inorg. Chim. Acta*, 1979, 35, L321-L324.
42. D. T. Sawyer, M. M. Morrison, *Inorg. Chem.*, 1978, 17, 333-337.
43. S.-M. Chen, *Inorg. Chim. Acta*, 1996, 249, 143-150.
44. N. Tanaka, Y. Sato, *Bull. Chem. Soc. Jap.*, 1968, 41, 2059-2064.
45. P. N. Bartlett, V. Eastwick-Field, *Electrochimica Acta*, 1993, 38, 2515-2523.
46. J. Lewis, M. Schröder, *J. Chem. Soc. Dalton Trans.*, 1982, 1085-1089.
47. N. Tanaka, Y. Sato, *Inorg. Nucl. Letts.*, 1968, 4, 487.
48. N. Tanaka, T. Ogata, S. Niizuma, *Inorg. Nucl. Letts.*, 1972, 8, 965.
49. B. Henne, D. Bartak, *Inorg. Chem.*, 1984, 23, 369.
50. K. Tanaka, K. Nakano, *Bull. Chem. Soc. Jpn.*, 1974, 47, 2222.
51. I. Pecht, M. Anbar, *J. Chem. Soc. A*, 1968, 1902.
52. M. Munakata, S. Nishibayashi, H. Sakamoto, *J. Chem. Soc. Chem. Commun.*, 1980, 219.

## Chapter 2: A Bipyridine-based Tripodal Framework with a Strong Preference for Trigonal Prismatic Co-ordination Geometries

53. R. R. Ruminski, *Inorg. Chim. Acta*, 1985, 103, 159.
54. R. H. Blessing, *Acta Crystallogr.*, 1995, A51, 33-38.
55. A. Altomare, G. Cascarano, C. Giacovazzo, A. Guagliardi, *J. Appl. Crystallogr.*, 1993, 26, 343-350.
56. G. M. Sheldrick, *SHELXL-97, Program for the Refinement of Crystal Structures*, University of Göttingen, Germany, 1997.
57. L. J. Farrugia, *J. Appl. Crystallogr.*, 1997, 30, 565.
58. X.-M. Chen, R.-Q. Wang, Z.-T. Xu, *Acta Crystallogr.*, 1995, C51, 820.
59. S. R. Batten, K. S. Murray, N. J. Sinclair, *Acta Crystallogr.*, 2000, C56, e320.
60. J.-C. Yao, L.-F. Ma, F.-J. Yao, *Z. Kristallogr.-New Cryst. Struct*, 2005, 220, 483. CCDC deposition no. 240261.
61. M. Hong, Y. Zhou, X. Li, Y. Xu, R. Cao, *Acta Crystallogr.*, 2003, E59, m300-m302.
62. O. P. Anderson, *J. Chem. Soc., Dalton Trans.*, 1972, 2597-2601.
63. J. Breu, H. Domel, A. Stoll, *Eur. J. Inorg. Chem.*, 2000, 2401-2408.
64. M. Chaudhury, E. R. T. Tiekink, D. Mandal, N. Kundu, *Appl. Organomet. Chem.*, 2005, 19, 1268. CCDC deposition no. 275094.
65. R. D. Shannon, *Acta Crystallogr.*, 1976, A32, 751-767.

# **Chapter 3: The Co-ordination and Electrochemical Behaviour of Two Analogous Tetra- and Pentadentate Tripodal Ligand Frameworks**

### 3.1 Scheme for Chapter 3

The work presented in this chapter focuses on two analogous tripodal pyridyl-based ligand systems ( $L^4$  and  $L^5$ ; Fig. 1), and examines similar themes to those discussed in the preceding chapter. An investigation into the co-ordination chemistry of the pseudo- $C_{3v}$  symmetric ligand,  $L^3$ , yielded mononuclear complexes with predominantly trigonal prismatic co-ordination polyhedra surrounding the metal centre. The relative scarcity of ligands in the literature capable of enforcing such unfavourable conditions prompted a further exploration into the transition metal complexes formed by the analogous four- and five-coordinate pyridyl-based frameworks. A quantitative structural analysis of the complexes formed by  $L^4$  and  $L^5$ , as well as an investigation into the electrochemistry of these systems, forms the basis of this section.

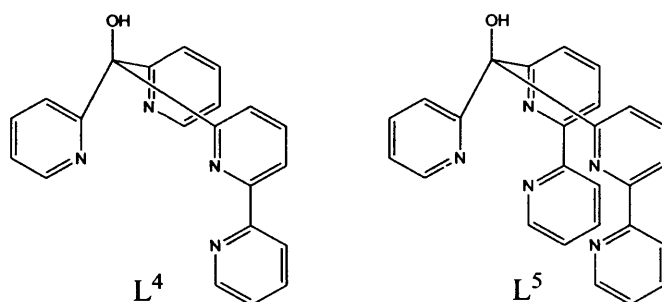


Figure 1: The transition metal complexes of ligands  $L^4$  and  $L^5$  are the focus of investigation in this section.

### 3.2 Introduction

#### Electrochemical Behaviour of Pyridine-Based Frameworks

Pyridine is frequently utilised in a wide variety of structures including cryptates, helicates, dendrimers, molecular wires, and the stacked and grid-like arrays that have recently dominated

the supramolecular literature. Furthermore, metal complexes constructed from polypyridyl systems such as bipyridine<sup>1</sup> have been a highly active area of research for many years.

Tris(bipyridine) complexes, *i.e.*  $[M(\text{bipy})_3]^{n+}$ , have received much attention and have been the focus of several reviews.<sup>2,3</sup> Particular emphasis is often placed upon the rich electrochemistry displayed by these types of complexes,<sup>4,5</sup> with the archetypal example,  $[\text{Ru}^{\text{II}}(\text{bpy})_3]^{2+}$  (Fig. 2; left), being the most commonly discussed.<sup>6</sup> In this example, the  $\text{Ru}^{\text{II}}/\text{Ru}^{\text{III}}$  oxidation occurs at +0.82 V *vs*  $\text{Fc}^+/\text{Fc}$  in  $\text{CH}_3\text{CN}/\text{TEAP}$  (tetraethylammonium perchlorate).<sup>7</sup> This metal-centred process leads to a low-spin  $\pi_{\text{M}}(\text{t}_{2\text{g}})^5$  species which is inert to ligand substitution.<sup>5</sup> This is the only metal-based oxidation which can be observed within the bounds of the potential window in typical solvents. The  $\text{Ru}^{\text{II}}/\text{Ru}^{\text{III}}$  oxidation process in the analogous hexa-aqua species,  $[\text{Ru}^{\text{II}}(\text{H}_2\text{O})_6]^{2+}$ , occurs at a substantially more negative potential (-0.46 V *vs*  $\text{Fc}^+/\text{Fc}$ ),<sup>8</sup> which serves to highlight the stabilisation of the  $\text{Ru}^{\text{II}}$  species by the chelating bipyridine ligands. The first three mono-electron reductions of the bipyridine groups in the  $[\text{Ru}^{\text{II}}(\text{bpy})_3]^{2+}$  complex occur at the successive potentials -1.76, -1.92, and -2.14 V *vs*  $\text{Fc}^+/\text{Fc}$  in  $\text{DMF}/\text{TEAPF}_6$  (tetraethylammonium hexafluorophosphate).<sup>9</sup> These values signify that the reductions occur more readily in comparison to free bipyridine, indicating that upon co-ordination to the metal, the ligand  $\pi^*$  orbitals lower in energy.

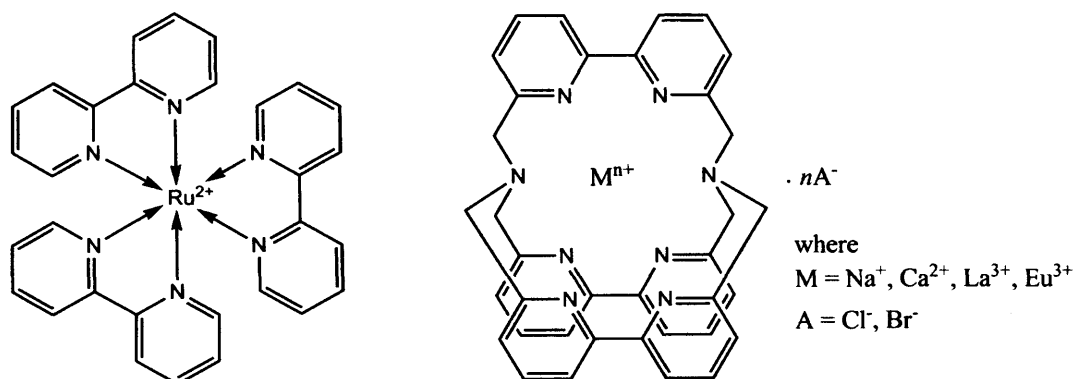


Figure 2:  $[\text{Ru}^{\text{II}}(\text{bipy}_3)]^{2+}$  (left) and a macrobicyclic tris(bipyridine) cryptate (right)

The remaining three reductions of the bipyridine units occur at potentials which are usually too negative to be observed within the bounds of potential window. De Armond *et al.* performed low temperature experiments in DMF/TEAPF<sub>6</sub> and located them at -2.78, -3.00, and -3.30 V vs Fc<sup>+</sup>/Fc.<sup>10</sup> The occurrence of these reductions at six discrete potentials is an indication of the electronic coupling that exists between the bipyridine groups.

Another important class of mononuclear metal complexes which provide a useful comparison are the cryptates, which are the complexes formed between a bi- or polycyclic multidentate ligand (a cryptand) and a cation. These compounds have been very important in the development of supramolecular chemistry over the last four decades since they were first synthesised in the Jean-Marie Lehn laboratory.<sup>11,12</sup> These discoveries were rewarded with a Nobel prize in 1987, which was shared between Lehn, Donald J. Cram and Charles J. Pedersen for their work in this field. A pertinent example of a macrobicyclic tris(bipyridine) cryptand (Fig. 2; right), has been studied in detail and its metal complexes have been shown to possess interesting redox behaviour.<sup>13</sup> The Na<sup>I</sup> complex reveals three reversible reduction waves at -2.40, -2.51 and -2.68 V in DMF-TBAPF<sub>6</sub> vs Fc<sup>+</sup>/Fc, corresponding to the mono-electron reductions of the bipyridine units. Replacement of the Na<sup>I</sup> cation with Ca<sup>II</sup> facilitates the reduction due to simple electrostatic considerations, and the reductions waves accordingly appear at -1.98, -2.14 and -2.18 V. This trend towards more positive potentials as the oxidation state of the metal cation is increased continues with La<sup>III</sup>, which displays ligand-based reduction potentials at -1.76, -1.97 and -2.09 V. This compound also reveals three further mono-electron reductions at the more negative potentials -2.57, -2.80 and -3.09 V, corresponding to the formation of the species [La<sup>III</sup>(L)]<sup>3-</sup> in DMF-TBAPF<sub>6</sub> solution. The large gap between the third and fourth reduction potentials (0.48 V) reflects the difficulty associated with forming the first dianionic

bipyridine, a phenomenon which is mirrored in the ruthenium tris(bipyridine) complex discussed above.

Investigating the electrochemistry of supramolecular systems can lead to pronounced structural transformations. For instance Lehn,<sup>14-16</sup> Constable,<sup>17-19</sup> and Abruña,<sup>20</sup> have all explored helicates and have noted that as the redox state of the chelated ions is altered, it can become possible to systematically 'switch' between di-, tri- and tetranuclear complexes. Electrochemistry can therefore be used to directly influence redox-controlled self-assembly. An example of this phenomenon is the dimerisation of the tetragonal pyramidal monohydrated copper(II) complex of tetramethylquaterpyridine (Fig. 3), which occurs following its mono-electron reduction, leading to the formation of a primitive helicate.<sup>21</sup> The cyclic voltammogram of this compound reveals an irreversible reduction at +0.1 V vs SCE which is attributed to the formation of  $[\text{Cu}^{\text{I}}(\text{L})(\text{H}_2\text{O})]^+$ . This species is unstable and readily dimerises, forming the helicate  $[\{\text{Cu}^{\text{I}}(\text{L})\}_2]^{2+}$ . The reverse sweep reveals two reversible oxidations at half-wave potentials of +0.53 and +0.73 V, which correspond to the processes  $(\text{Cu}^{\text{I}})_2 \rightarrow (\text{Cu}^{\text{II}}-\text{Cu}^{\text{I}}) \rightarrow (\text{Cu}^{\text{II}})_2$ . The presence of two separate oxidations indicates that the two copper centres are not electronically independent of each other. Following these oxidations, the helicate structure gradually decomposes, regenerating the  $[\text{Cu}^{\text{II}}(\text{L})(\text{H}_2\text{O})]^{2+}$  monomer.

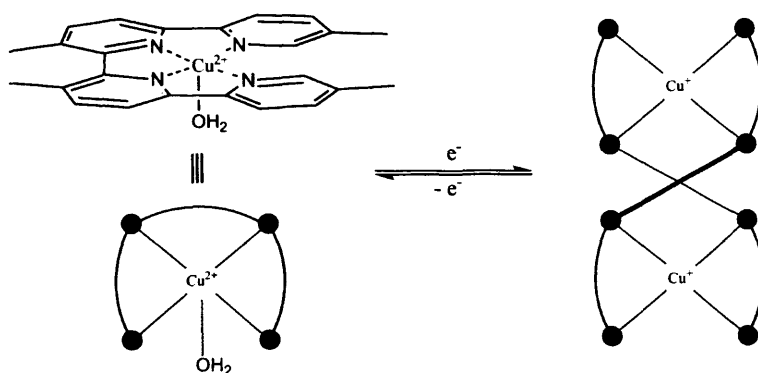


**Figure 3:** The reversible formation of a dimeric helicate (right) via the electrochemical reduction of the monomeric  $\text{Cu}^{\text{II}}$ -tetramethylquaterpyridine complex (top left).



Another example of a redox-controlled interconversion between a monomeric, pseudo-square planar  $\text{Cu}^{\text{II}}$  structure and a dimeric, helical  $\text{Cu}^{\text{I}}$  form can be observed in the copper complexes of the bis-phenanthroline ligand (Fig. 4).<sup>22</sup> The authors were able to isolate and structurally characterise both of these forms, however the cyclic voltammetry experiments performed at a  $500 \text{ mVs}^{-1}$  scan rate revealed that the  $[\text{Cu}_2^{\text{I}}(\text{L})_2]^{2+}$  species undergoes a reversible two-electron oxidation at a half-wave potential of  $+0.64 \text{ V}$  (vs SCE, acetonitrile), while the  $[\text{Cu}^{\text{II}}(\text{L})]^{2+}$  species undergoes a reversible one-electron reduction at  $+0.19 \text{ V}$  under the same conditions. It was therefore reasoned that the  $[\text{Cu}_2^{\text{I}}(\text{L})_2]^{2+}$  species initially oxidises to form  $[\text{Cu}_2^{\text{II}}(\text{L})_2]^{4+}$ , while  $[\text{Cu}^{\text{II}}(\text{L})]^{2+}$  is reduced to form  $[\text{Cu}^{\text{I}}(\text{L})]^+$ . Closer inspection of the cyclic voltammogram of  $[\text{Cu}_2^{\text{I}}(\text{L})_2]^{2+}$  revealed trace peaks corresponding to the formation of  $[\text{Cu}^{\text{II}}(\text{L})]^{2+}$ . Likewise, the cyclic voltammogram of  $[\text{Cu}^{\text{II}}(\text{L})]^{2+}$  showed trace peaks indicating the formation of  $[\text{Cu}_2^{\text{I}}(\text{L})_2]^{2+}$ . It was therefore concluded that the interconversions  $2[\text{Cu}^{\text{I}}(\text{L})]^+ \rightarrow [\text{Cu}_2^{\text{I}}(\text{L})_2]^{2+}$  and  $[\text{Cu}_2^{\text{II}}(\text{L})_2]^{4+} \rightarrow 2[\text{Cu}^{\text{II}}(\text{L})]^{2+}$  do take place, however they occur at a slower rate on comparison to the time-scale of the experiment.

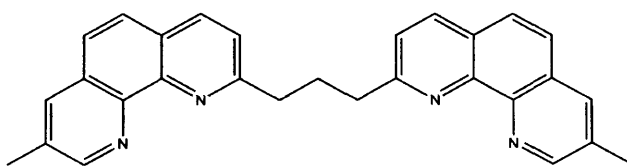


**Figure 4:** The copper complex of this bis-phenanthroline ligand undergoes redox-controlled structural transformation

The mononuclear copper(I) compound,  $[\text{Cu}^{\text{I}}(\text{phen})_2]^+$ , provides a further interesting example of the structural transformations that can occur upon oxidation/reduction.<sup>23</sup> This compound reveals one oxidation and one reduction wave, both of which are poorly reversible and attributed to metal-based processes. The  $\text{Cu}^{\text{I}}/\text{Cu}^{\text{II}}$  oxidation causes the  $\text{Cu}^{\text{II}}$  centre to adopt an octahedral co-ordination geometry in which the vacant sites are filled with molecules of solvent,

while the  $\text{Cu}^{\text{I}}/\text{Cu}^0$  reduction induces ligand dissociation. Replacement of phen with 2,9-dimethyl-1,10-phenanthroline (dmphen) illustrates how introducing two methyl substituents can cause entirely different redox behaviour.<sup>23</sup> The voltammogram of  $[\text{Cu}^{\text{I}}(\text{dmphen})]^+$  also reveals a metal-based oxidation process, however, it is fully reversible and shifted to a more positive potential. This indicates that the  $\alpha$ -substituents to the nitrogen atoms on the ligand prevent both a change in co-ordination geometry and also the addition of solvent into the inner co-ordination sphere. This compound also reveals a reduction process, however it is reversible and corresponds to the addition of an electron to a ligand  $\pi^*$  orbital, rather than a metal-centred process.

The hexakis(bipyridyl)cyclotrimeratrylene ligand (Fig. 5) has been investigated as a redox-induced conformational switch.<sup>24</sup> The six pendant bipyridines allow for the formation of a trinuclear copper(I) complex in which each of the three  $\text{Cu}^{\text{I}}$  centres is co-ordinated by two bipy groups linked to vicinal dioxybenzene units of the calixarene rim. Upon oxidation however, each of the three  $\text{Cu}^{\text{II}}$  centres adopt a square planar co-ordination geometry in which each cuprous ion is co-ordinated by two bipy groups attached to the same dioxybenzene group. Thus, electrochemical oxidation/reduction of this compound induces a de-coordination, rotation, and re-coordination of at least three bipy units. This represents a system in which conformational isomerism exhibits an electrochemical potential hysteresis.

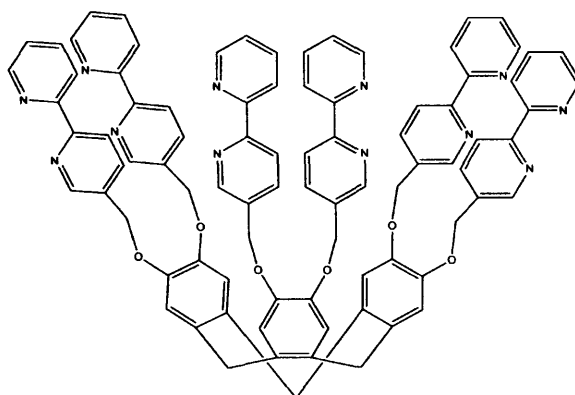


**Figure 5:** Reduction of the trinuclear copper(II) complex containing this hexakis(bipyridyl)cyclotrimeratrylene ligand induces an interesting conformational transformation.

Co-ordination compounds which exhibit redox-controlled linkage isomerism have been the focus of much interest in recent years as molecular memories.<sup>25</sup> An example of such a compound is the bistridentate heteroleptic Ru<sup>II</sup> polypyridyl complex containing the 1-[6-(2,2'-bipyridyl)]-1-(2-pyridyl)-ethanol ligand (Fig. 6; left).<sup>26</sup> The cyclic voltammogram was collected at a low scan-rate (100 mVs<sup>-1</sup>; acetonitrile) and revealed two process; an irreversible anodic wave at +0.79 V vs Fc<sup>+</sup>/Fc, and an irreversible cathodic wave on the reverse scan at +0.34 V. On the basis of UV-Vis spectroelectrochemical changes, the anodic wave was assigned to the metal-based Ru<sup>II/III</sup> oxidation. The irreversibility of this process was attributed to the linkage isomerisation reaction which follows, rapidly switching the donor set from N<sub>6</sub> to N<sub>5</sub>O upon oxidation.

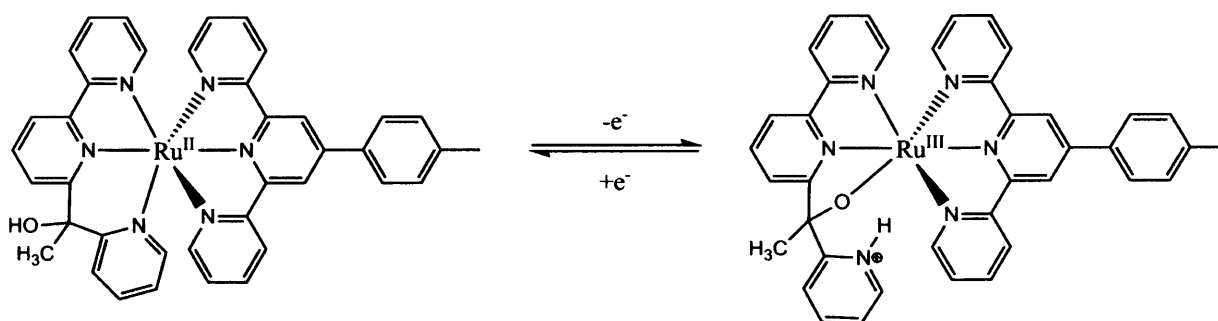


Figure 6: Redox-controlled linkage isomerism in a ruthenium(II) polypyridyl complex.

The objectives of the work presented in this chapter focus upon the co-ordination chemistry of the tetra- and pentadentate tripodal ligands, mono(2,2'-bipyrid-6-yl)bis(pyrid-2-yl)methanol and bis(2,2'-bipyrid-6-yl)mono(pyrid-2-yl)methanol (L<sup>4</sup> and L<sup>5</sup> respectively; Fig. 1) with a series of transition metals. In a similar fashion to the previous chapters, the electrochemical behaviour of these systems will be investigated *via* cyclic voltammetry and the findings will be compared against similar literature compounds. Since these ligands contain fewer bipyridyl arms than the analogous ligand L<sup>3</sup>, a quantitative analysis of the co-ordination

polyhedral *via* continuous shape mapping will examine whether these ligands are still capable of maintaining predominantly trigonal prismatic geometries. It is expected that the stereoelectronic preference of the metal ions will become a more dominant factor in establishing ligand conformation, therefore this work will also focus on the relationship between the co-ordination polyhedra of these complexes and the d-electron configuration of the metal centre.

### 3.3 Experimental

#### 3.3.1 General

The details regarding the collection of experimental data are the same as those reported in Chapter 1 (p.16).

#### 3.3.2 Preparations

##### 3.3.2.1 General Procedure for the synthesis of metal complexes

The ligand (1 equivalent, typically 0.1 mmol) was dissolved in the minimum amount of acetonitrile or methanol (typically 3 mL). The solutions were warmed to *ca.* 60°C to ensure that the ligand fully dissolved. To this stirring solution, the metal perchlorate salt (1 equivalent) dissolved in either acetonitrile or water (typically ~2 mL) was added dropwise. A precipitate was collected and dried in air. Recrystallisation of the compounds typically involved the diffusion of diethyl ether into acetonitrile or methanolic solutions which were filtered through Celite.

**WARNING:** Perchlorate salts of metal complexes are potentially explosive. Care should be taken while handling such complexes.

**[Mn<sup>II</sup>(L<sup>4</sup>)](ClO<sub>4</sub>)<sub>2</sub> (3.1):** White precipitate (47% yield). Found: C, 43.58; H, 2.97; N, 11.09%. MnC<sub>21</sub>H<sub>16</sub>N<sub>4</sub>O(ClO<sub>4</sub>)<sub>2</sub>·CH<sub>3</sub>CN requires C, 43.48; H, 3.01; N, 11.02%; ESMS *m/z* (%): 609.06 (40) [Mn(L<sup>4</sup>) + H<sub>2</sub>O + ClO<sub>4</sub>]<sup>+</sup>; IR (KBr pellet, cm<sup>-1</sup>): 3434(br), 3075(m), 1602(s), 1448(s) 1091(s), 777(s), 623(s); UV/Vis [ $\lambda_{\max}$ , nm ( $\epsilon_M$ , M<sup>-1</sup>cm<sup>-1</sup>)] in CH<sub>3</sub>CN: 242(22,460), 295(24,220), 316(8,070).

**[Fe<sup>II</sup>(L<sup>4</sup>)](ClO<sub>4</sub>)<sub>2</sub> (3.2):** Dark orange precipitate (62% yield). HRMS (ES) *m/z* (%): 436.0881 (100) ([Fe(L<sup>4</sup>) + CH<sub>3</sub>CN - H]<sup>+</sup>; FeC<sub>23</sub>H<sub>18</sub>N<sub>5</sub>O requires 436.0861); IR (KBr pellet, cm<sup>-1</sup>): 3372(br), 3113(m), 1599(s), 1450(s) 1095(s), 772(s), 623(s); UV/Vis [ $\lambda_{\max}$ , nm ( $\epsilon_M$ , M<sup>-1</sup>cm<sup>-1</sup>)] in CH<sub>3</sub>CN: 234(23,110), 287(22,550), 307(6,260), 482(19), 533(31).

**[Co<sup>II</sup>(L<sup>4</sup>)](ClO<sub>4</sub>)<sub>2</sub> (3.3):** Bright orange precipitate (73% yield). Found: C, 43.92; H, 3.33; N, 11.55%. CoC<sub>21</sub>H<sub>16</sub>N<sub>4</sub>O(ClO<sub>4</sub>)<sub>2</sub>·CH<sub>3</sub>CN requires C, 43.21; H, 3.00; N, 10.96%; HRMS (ES) *m/z* (%): 399.0508 (100) ([Co(L<sup>4</sup>)]<sup>+</sup>; CoC<sub>21</sub>H<sub>16</sub>N<sub>4</sub>O requires 399.0656); IR (KBr pellet, cm<sup>-1</sup>): 3419(br), 3109(m), 1606(s), 1449(s), 1111(s), 770(s), 626(s); UV/Vis [ $\lambda_{\max}$ , nm ( $\epsilon_M$ , M<sup>-1</sup>cm<sup>-1</sup>)] in CH<sub>3</sub>CN: 233(19,510), 286(16,350), 459(150), 1051(28).

**[Ni<sup>II</sup>(L<sup>4</sup>)](ClO<sub>4</sub>)<sub>2</sub> (3.4):** Light purple crystals (45% yield). Found: C, 43.32; H, 2.98; N, 11.03%. NiC<sub>21</sub>H<sub>16</sub>N<sub>4</sub>O(ClO<sub>4</sub>)<sub>2</sub>·CH<sub>3</sub>CN requires C, 43.23; H, 3.00; N, 10.96%; HRMS (ES) *m/z* (%): 438.0873 (100) ([Ni(L<sup>4</sup>) + CH<sub>3</sub>CN - H]<sup>+</sup>; NiC<sub>23</sub>H<sub>18</sub>N<sub>5</sub>O requires 438.0865); IR (KBr pellet, cm<sup>-1</sup>): 3415(br), 3092(m) 1601(s), 1452(s), 1114(s), 767(s), 623(s); UV/Vis [ $\lambda_{\max}$ , nm ( $\epsilon_M$ , M<sup>-1</sup>cm<sup>-1</sup>)] in CH<sub>3</sub>CN: 265(21,850), 306(14,300), 714(67), 774(93).

Chapter 3: The Co-ordination and Electrochemical Behaviour of Two Analogous Tetra- and Pentadentate Tripodal Ligand Frameworks

**[Cu<sup>II</sup>(L<sup>4</sup>)](ClO<sub>4</sub>)<sub>2</sub> (3.5):** Dark blue crystals (56% yield). HRMS (ES) *m/z* (%): 402.0535 (50) ([Cu(L<sup>4</sup>) – H]<sup>+</sup>; CuC<sub>21</sub>H<sub>15</sub>N<sub>4</sub>O requires 402.0542); IR (KBr pellet, cm<sup>-1</sup>): 3366(br), 3114(m), 1600(s), 1453(s), 1097(s), 776(s), 624(s); UV/Vis [ $\lambda_{\max}$ , nm ( $\epsilon_M$ , M<sup>-1</sup>cm<sup>-1</sup>)] in CH<sub>3</sub>CN: 251(23,700), 304.7(14,040), 317(9,200), 658(83), 920(37).

**[Zn<sup>II</sup>(L<sup>4</sup>)](ClO<sub>4</sub>)<sub>2</sub> (3.6):** White precipitate (68% yield). Found: C, 42.91; H, 3.05; N, 10.96%. ZnC<sub>21</sub>H<sub>16</sub>N<sub>4</sub>O(ClO<sub>4</sub>)<sub>2</sub>·CH<sub>3</sub>CN requires C, 42.78; H, 2.97; N, 10.85%; <sup>1</sup>H NMR (400 MHz; d<sub>6</sub>-DMSO): 8.74 (d, 2H, *J* 7.0 Hz), 8.67 (d, 1H, *J* 7.0 Hz), 8.55 (m, 2H), 8.11 (dd, 2H, *J* 7.2, 6.9 Hz), 7.99 (dd, 1H, *J* 7.1, 5.0 Hz), 7.78 (d, 2H, *J* 7.0 Hz), 7.69 (t, 1H, *J* 5.4 Hz), 7.51 (d, 1H, *J* 7.1 Hz), 7.47 (t, 2H, *J* 6.9 Hz), 7.19 (dd, 1H, *J* 6.9, 5.4 Hz); HRMS (ES) *m/z* (%): 403.0520 (30) ([Zn(L<sup>4</sup>) – H]<sup>+</sup>; ZnC<sub>21</sub>H<sub>15</sub>N<sub>4</sub>O requires 403.0537); IR (KBr pellet, cm<sup>-1</sup>): 3319(br), 3093(m), 1595(s), 1454(s), 1098(s), 783(s), 622(s).

**[Cd<sup>II</sup>(L<sup>4</sup>)](ClO<sub>4</sub>)<sub>2</sub> (3.7):** Colourless crystals (needles) (40% yield). Found: C, 40.08; H, 2.90; N, 10.30%. CdC<sub>21</sub>H<sub>16</sub>N<sub>4</sub>O(ClO<sub>4</sub>)<sub>2</sub>·CH<sub>3</sub>CN requires C, 39.88; H, 2.76; N, 10.11%; <sup>1</sup>H NMR (500 MHz; d<sub>6</sub>-DMSO): 8.85 (d, 1H, *J* 7.0 Hz), 8.62 (d, 2H, *J* 6.4 Hz), 8.57 (t, 1H, *J* 7.4 Hz), 8.53 (d, 1H, *J* 6.6 Hz), 8.37 (bs, 2H), 8.34-8.25 (m, 4H), 8.11 (d, 2H, *J* 6.4 Hz), 7.92 (t, 1H, *J* 7.0 Hz), 7.61 (t, 2H, *J* 6.8 Hz); <sup>13</sup>C NMR: (125 MHz; d<sub>6</sub>-DMSO): 159.7, 159.0, 150.1, 149.5, 148.7, 148.6, 141.8, 141.0, 140.3, 126.7, 124.2, 123.0, 121.8, 121.7, 75.1; HRMS (ES) *m/z* (%): 490.0552 (30) ([Cd(L<sup>4</sup>) + CH<sub>3</sub>CN – H]<sup>+</sup>; CdC<sub>23</sub>H<sub>18</sub>N<sub>5</sub>O requires 490.0541); IR (KBr pellet, cm<sup>-1</sup>): 3320(br), 3093(m), 1595(s), 1454(s), 1098(s), 800(s), 622(s).

Chapter 3: The Co-ordination and Electrochemical Behaviour of Two Analogous  
Tetra- and Pentadentate Tripodal Ligand Frameworks

**[Mn<sup>II</sup>(L<sup>5</sup>)](ClO<sub>4</sub>)<sub>2</sub> (3.8):** Pale yellow crystals (88% yield). Found: C, 48.51; H, 3.71; N, 14.28%. MnC<sub>26</sub>H<sub>19</sub>N<sub>5</sub>O(ClO<sub>4</sub>)<sub>2</sub>·3CH<sub>3</sub>CN requires C, 48.38; H, 3.55; N, 14.10%; ESMS *m/z* (%): 472.1 (100) [Mn(L<sup>5</sup>) + H]<sup>+</sup>; IR (KBr pellet, cm<sup>-1</sup>): 3367(br), 3087(m), 1603(s), 1449(s), 1117(s), 779(s), 623(s); UV/Vis [ $\lambda_{\text{max}}$ , nm ( $\epsilon_{\text{M}}$ , M<sup>-1</sup>cm<sup>-1</sup>)] in CH<sub>3</sub>CN: 234(23,500), 292(16,600), 314(7,100).

**[Fe<sup>II</sup>(L<sup>5</sup>)](ClO<sub>4</sub>)<sub>2</sub> (3.9):** Purple crystals (55% yield). Found: C, 49.58; H, 4.29; N, 11.90%. FeC<sub>26</sub>H<sub>19</sub>N<sub>5</sub>O(ClO<sub>4</sub>)<sub>2</sub>·2CH<sub>3</sub>CN·(CH<sub>3</sub>CH<sub>2</sub>)<sub>2</sub>O requires C, 49.29; H, 4.26; N, 11.84%; ESMS *m/z* (%): 571.74 (100) [Fe(L<sup>5</sup>) + ClO<sub>4</sub>]<sup>+</sup>; IR (KBr pellet, cm<sup>-1</sup>): 3425(br), 3109(m), 1602(s), 1450(s), 1109(s), 777(s), 624(s); UV/Vis [ $\lambda_{\text{max}}$ , nm ( $\epsilon_{\text{M}}$ , M<sup>-1</sup>cm<sup>-1</sup>)] in CH<sub>3</sub>CN: 239(20,250), 295(18,450), 316(4,400), 419(112), 504(78), 577(133).

**[Co<sup>II</sup>(L<sup>5</sup>)](ClO<sub>4</sub>)<sub>2</sub> (3.10):** Dark orange crystals (33% yield). Found: C, 45.81; H, 2.36; N, 11.50%. CoC<sub>26</sub>H<sub>19</sub>N<sub>5</sub>O(ClO<sub>4</sub>)<sub>2</sub>·CH<sub>3</sub>CN·H<sub>2</sub>O requires C, 45.79; H, 3.29; N, 11.44%; HRMS (ES) *m/z* (%): 575.0406 (50) ([Co(L<sup>5</sup>) + ClO<sub>4</sub>]<sup>+</sup>; CoC<sub>26</sub>H<sub>19</sub>ClN<sub>5</sub>O<sub>5</sub> requires 575.0407); IR (KBr pellet, cm<sup>-1</sup>): 3398(br), 3115(m), 1599(s), 1451(s), 1105(s), 779(s), 623(s); UV/Vis [ $\lambda_{\text{max}}$ , nm ( $\epsilon_{\text{M}}$ , M<sup>-1</sup>cm<sup>-1</sup>)] in CH<sub>3</sub>CN: 231(23,800), 284(19,850), 302(4,150), 463(103), 1030(21).

**[Ni<sup>II</sup>(L<sup>5</sup>)(Br)](ClO<sub>4</sub>) (3.11):** Dark purple crystals (71% yield). ESMS *m/z* (%): 575.2 (100) [Ni(L<sup>5</sup>) + ClO<sub>4</sub>]<sup>+</sup>; IR (KBr pellet, cm<sup>-1</sup>): 3388(br), 3110(m), 1602(s), 1450(s), 1088(s), 782(s), 625(s); UV/Vis [ $\lambda_{\text{max}}$ , nm ( $\epsilon_{\text{M}}$ , M<sup>-1</sup>cm<sup>-1</sup>)] in CH<sub>3</sub>CN: 248(22,000), 298(21,500), 312(9,150), 512(19), 820(15), 956(11).

**[Cu<sup>II</sup>(L<sup>5</sup>)](ClO<sub>4</sub>)<sub>2</sub> (3.12):** Light blue precipitate (62% yield). Found: C, 46.73; H, 3.04; N, 11.75%. CuC<sub>26</sub>H<sub>19</sub>N<sub>5</sub>O(ClO<sub>4</sub>)<sub>2</sub>·CH<sub>3</sub>CN requires C, 46.65; H, 3.08; N, 11.66%; ESMS *m/z* (%): 580.1 (100) [Cu(L<sup>5</sup>) + ClO<sub>4</sub>]<sup>+</sup>; IR (KBr pellet, cm<sup>-1</sup>): 3434(br), 3095(m), 1595(s), 1453(s), 1095(s), 780(s), 624(s); UV/Vis [ $\lambda_{\max}$ , nm ( $\epsilon_M$ , M<sup>-1</sup>cm<sup>-1</sup>)] in CH<sub>3</sub>CN: 245(20,750), 301(29,300), 316(10,300), 639(54).

**[Zn<sup>II</sup>(L<sup>5</sup>)](ClO<sub>4</sub>)<sub>2</sub> (3.13):** White precipitate (80% yield). Found: C, 48.48; H, 4.21; N, 10.68%. ZnC<sub>26</sub>H<sub>19</sub>N<sub>5</sub>O(ClO<sub>4</sub>)<sub>2</sub>·CH<sub>3</sub>CN·(CH<sub>3</sub>CH<sub>2</sub>)<sub>2</sub>O requires C, 48.23; H, 4.05; N, 10.55%; <sup>1</sup>H NMR (400 MHz; d<sub>6</sub>-DMSO): 8.72 (d, 1H, *J* 7.0 Hz), 8.65 (d, 2H, *J* 7.0 Hz), 8.56 (m, 4H), 8.08 (dd, 1H, *J* 7.2, 6.9 Hz), 7.99 (dd, 2H, *J* 7.1, 5.0 Hz), 7.79 (d, 1H, *J* 7.0 Hz), 7.70 (t, 2H, *J* 5.4 Hz), 7.53 (d, 2H, *J* 7.1 Hz), 7.45 (t, 1H, *J* 6.9 Hz), 7.19 (dd, 2H, *J* 6.9, 5.4 Hz); <sup>13</sup>C NMR: (125 MHz; CD<sub>3</sub>CN): 157.2, 157.1, 149.0, 148.6, 148.3, 142.4, 141.6, 140.7, 127.2, 124.4, 122.7, 122.2, 121.3, 120.8, 74.8; ESMS *m/z* (%): 581 (100) [Zn(L<sup>5</sup>) + ClO<sub>4</sub>]<sup>+</sup>; IR (KBr pellet, cm<sup>-1</sup>): 3427(br), 3115(m), 1598(s), 1451(s) 1108(s), 779(s), 624(s).

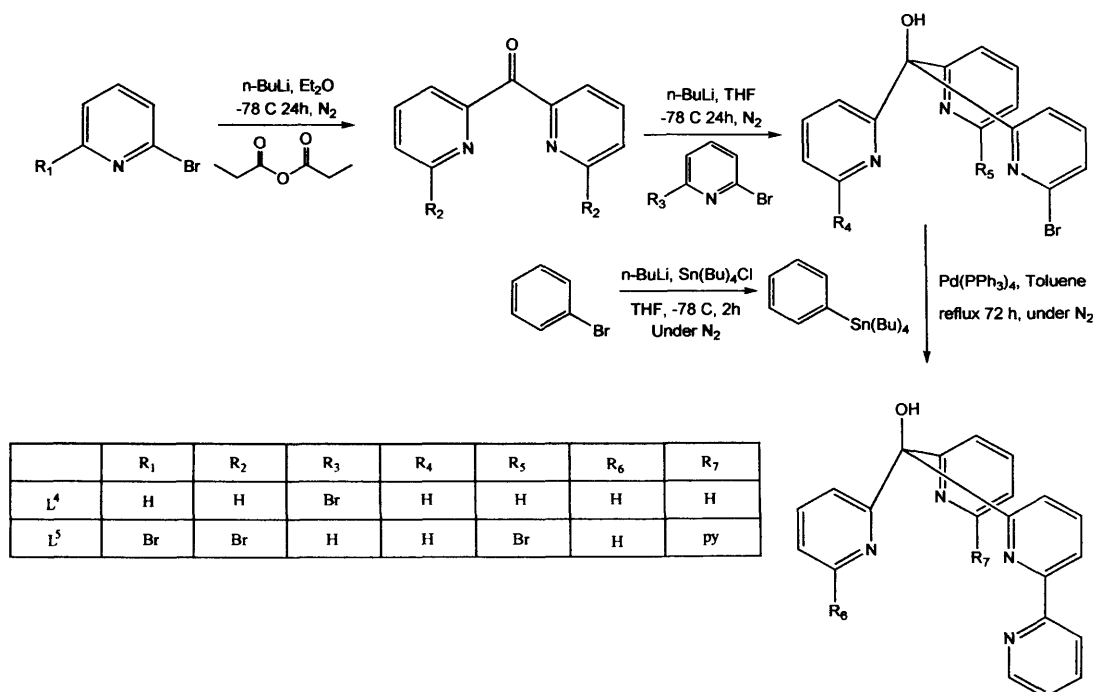
**[Cd<sup>II</sup>(L<sup>5</sup>)](ClO<sub>4</sub>)<sub>2</sub> (3.14):** Colourless crystals (needles) (77% yield). Found: C, 45.20; H, 3.42; N, 13.18%. CdC<sub>26</sub>H<sub>19</sub>N<sub>5</sub>O(ClO<sub>4</sub>)<sub>2</sub>·3CH<sub>3</sub>CN requires C, 45.11; H, 3.31; N, 13.15%; <sup>1</sup>H NMR (250 MHz; CD<sub>3</sub>CN): 9.29 (d, 2H, 6.30 Hz), 9.03 (d, 1H, *J* 6.10 Hz), 8.40-8.53 (m, 6H), 8.27-8.35 (m, 5H), 8.18 (t, 1H, *J* 7.4 Hz), 7.93 (t, 2H, *J* 7.6 Hz), 7.67 (t, 1H, *J* 6.8 Hz), 6.49 (s, 1H); <sup>13</sup>C NMR: (125 MHz; CD<sub>3</sub>CN): 158.4, 158.2, 149.7, 149.2, 149.1, 148.6, 141.8, 141.2, 140.7, 127.0, 124.4, 123.2, 123.1, 122.1, 121.6, 75.2; HRMS (ES) *m/z* (%): 530.0566 (100) ([Cd(L<sup>5</sup>) - H]<sup>+</sup>; CdC<sub>26</sub>H<sub>18</sub>N<sub>5</sub>O requires 530.0545); IR (KBr pellet, cm<sup>-1</sup>): 3398(br), 3114(m), 1595(s), 1448(s), 1097(s), 779(s), 623(s).



## 3.4 Results and Discussion

### 3.4.1 Ligand Synthesis

The preparation of ligands  $L^4$  and  $L^5$  have been previously reported<sup>27</sup> and the synthetic procedure has been summarised in Scheme 3.1. The bromo derivatives were readily prepared in reasonable yields. In turn, the respective bromo derivative was suspended in toluene and treated with an excess of 2-tributylstannylpyridine in the presence of the palladium catalyst,  $\text{Pd}(\text{PPh}_3)_4$ , for 24 hours at  $110^\circ\text{C}$  to generate the respective bipy derivative. These were formed *via* a Stille coupling reaction. The crude products of  $L^4$  and  $L^5$  were flash chromatographed on silica gel. Initially the column was flushed with DCM / MeOH (9.9:0.1) to extract the excess 2-tributylstannylpyridine and finally with MeOH (100%) to obtain the desired product, mono(2,2'-bipyrid-6-yl)bis(2-pyridyl)methanol,  $L^4$ , as a white solid (55%) and bis(2,2'-bipyrid-6-yl)mono(2-pyridyl)methanol,  $L^5$ , as a light brown solid (60%).



Scheme 3.1: Synthetic route to ligands  $L^4$  and  $L^5$ . Corresponding substituents are labelled in the table (inset).

### 3.4.2 Synthesis of Complexes

Initial studies have been conducted on the Fe<sup>II</sup>, Ni<sup>II</sup>, Cu<sup>II</sup> and Zn<sup>II</sup> complexes, however this work represents the first detailed investigation of these systems with particular focus on the electrochemical behaviour and crystallographic data.

The ligand was dissolved in the minimum amount (typically 3 mL) of warm acetonitrile. In each case, the dropwise addition of the relevant metal perchlorate salt dissolved in either water or acetonitrile instantly yielded a precipitate. These compounds were recrystallised *via* the diffusion of diethyl ether into acetonitrile or methanolic solutions resulting in crystals suitable for single-crystal X-ray diffraction. The yields from these reactions were moderate to high (41-87%).

### Spectroscopic Properties of Complexes

#### 3.4.3 Vibrational Spectroscopy

In a similar manner to L<sup>3</sup>, the transition metal complexes of ligands L<sup>4</sup> and L<sup>5</sup> reveal a variety of diagnostic vibrations indicative of pyridine co-ordination to a metal centre. The useful infra-red assignments for determining the ligands mode of co-ordination are listed in Tables 1 and 2. Again, upon complexation a shift of the strong 1580 cm<sup>-1</sup> band to higher frequency (*ca.* 1600 cm<sup>-1</sup>) was observed. The notable similarities between the infra-red spectra for each of the transition metal complexes suggests similar electronic density over the ring systems caused primarily by back-bonding from the metal ion to the low-lying  $\pi$ -orbitals of the bipy units. The unsplit infrared active bands at 1087-1116 cm<sup>-1</sup> and ~623 cm<sup>-1</sup> indicate the perchlorate counterions are of T<sub>d</sub> symmetry and therefore non-coordinating, which is again in accordance with the X-ray diffraction data.

## Chapter 3: The Co-ordination and Electrochemical Behaviour of Two Analogous Tetra- and Pentadentate Tripodal Ligand Frameworks

**Table 1** IR Stretching Frequencies of L<sup>4</sup> and Complexes

Compound	Characteristic vibrations/cm <sup>-1</sup>				
	aromatic ν(C-H)	ν(O-H)	ν(C=N) and ν(C=C)	π(C-H)	ν(Cl-O)
L <sup>4</sup>	3057(m)	3433(br)	1581(s), 1429(s)	774(s)	-
[Mn <sup>II</sup> (L <sup>4</sup> )](ClO <sub>4</sub> ) <sub>2</sub>	3075(m)	3434(br)	1602(s), 1448(s)	777(s)	1091(s), 623(s)
[Fe <sup>II</sup> (L <sup>4</sup> )](ClO <sub>4</sub> ) <sub>2</sub>	3113(m)	3372(br)	1599(s), 1450(s)	772(s)	1095(s), 623(s)
[Co <sup>II</sup> (L <sup>4</sup> )](ClO <sub>4</sub> ) <sub>2</sub>	3109(m)	3419(br)	1606(s), 1449(s)	770(s)	1111(s), 626(s)
[Ni <sup>II</sup> (L <sup>4</sup> )](ClO <sub>4</sub> ) <sub>2</sub>	3092(m)	3415(br)	1601(s), 1452(s)	767(s)	1114(s), 623(s)
[Cu <sup>II</sup> (L <sup>4</sup> )](ClO <sub>4</sub> ) <sub>2</sub>	3114(m)	3366(br)	1600(s), 1453(s)	776(s)	1097(s), 624(s)
[Zn <sup>II</sup> (L <sup>4</sup> )](ClO <sub>4</sub> ) <sub>2</sub>	3093(m)	3319(br)	1595(s), 1454(s)	783(s)	1098(s), 622(s)
[Cd <sup>II</sup> (L <sup>4</sup> )](ClO <sub>4</sub> ) <sub>2</sub>	3093(m)	3320(br)	1595(s), 1454(s)	800(s)	1098(s), 622(s)

<sup>a</sup> IR spectra measured as KBr discs.

**Table 2** IR Stretching Frequencies of L<sup>5</sup> and Complexes

Compound	Characteristic vibrations/cm <sup>-1</sup>				
	aromatic ν(C-H)	ν(O-H)	ν(C=N) and ν(C=C)	π(C-H)	ν(Cl-O)
L <sup>5</sup>	3051(m)	3413(br)	1579(s), 1559(s)	781(s)	-
[Mn <sup>II</sup> (L <sup>5</sup> )](ClO <sub>4</sub> ) <sub>2</sub>	3087(m)	3367(br)	1603(s), 1449(s)	779(s)	1117(s), 623(s)
[Fe <sup>II</sup> (L <sup>5</sup> )](ClO <sub>4</sub> ) <sub>2</sub>	3109(m)	3425(br)	1602(s), 1450(s)	777(s)	1109(s), 624(s)
[Co <sup>II</sup> (L <sup>5</sup> )](ClO <sub>4</sub> ) <sub>2</sub>	3115(m)	3398(br)	1599(s), 1451(s)	779(s)	1105(s), 623(s)
[Ni <sup>II</sup> (L <sup>5</sup> )(Br)](ClO <sub>4</sub> )	3110(m)	3388(br)	1602(s), 1450(s)	782(s)	1088(s), 625(s)
[Cu <sup>II</sup> (L <sup>5</sup> )](ClO <sub>4</sub> ) <sub>2</sub>	3095(m)	3434(br)	1595(s), 1453(s)	780(s)	1095(s), 624(s)
[Zn <sup>II</sup> (L <sup>5</sup> )](ClO <sub>4</sub> ) <sub>2</sub>	3115(m)	3427(br)	1598(s), 1451(s)	779(s)	1108(s), 624(s)
[Cd <sup>II</sup> (L <sup>5</sup> )](ClO <sub>4</sub> ) <sub>2</sub>	3114(m)	3398(br)	1595(s), 1448(s)	779(s)	1097(s), 623(s)

<sup>a</sup> IR spectra measured as KBr discs.

### 3.4.4 <sup>1</sup>H and <sup>13</sup>C NMR of Zn and Cd Complexes

The <sup>1</sup>H NMR spectra of the zinc complexes of L<sup>4</sup> and L<sup>5</sup> are both highly comparable to their parent ligands,<sup>\*</sup> the slight differences arising in the respective chemical shifts. The protons in the zinc complexes are more deshielded and the corresponding signals appear at more downfield positions. This is particularly the case for the protons in *ortho*- positions to the co-ordinating nitrogen atoms which are most affected. It is noted here that the two lone pyridyl units in the

<sup>\*</sup> L<sup>4</sup>: <sup>1</sup>H NMR (CDCl<sub>3</sub>): δ 8.60 (d, 1H, *J* 7.0 Hz), 8.48 (d, 2H, *J* 7.8 Hz), 8.28 (dd, 1H, *J* 6.9, 5.4 Hz), 8.10 (dd, 1H, *J* 7.4, 3.2 Hz), 7.70 (m, 7H), 7.20 (dd, 2H, *J* 7.8, 4.8 Hz), 7.12 (dd, 1H, *J* 7.6, 3.0 Hz).

L<sup>5</sup>: <sup>1</sup>H NMR (CDCl<sub>3</sub>): δ 8.58 (d, 2H, *J* 6.5 Hz), 8.48 (d, 1H, *J* 7.5 Hz), 8.28 (dd, 2H, *J* 7.5, 6.0 Hz), 8.10 (dd, 2H, *J* 7.7, 2.8 Hz), 7.75 (m, 6H), 7.60 (t, 2H, *J* 7.7 Hz), 7.20 (dd, 1H, *J* 7.7, 5.7 Hz), 7.12 (dd, 2H, *J* 7.6, 1.6 Hz).

case of  $L^4$  are equivalent as their chemical shifts are identical, this is also the case for the two bipyridyl units of  $L^5$ . The ordering of the signals has been discussed in more detail in previous work.<sup>27</sup>

For the cadmium complex of  $L^4$ , it is apparent that the ordering of the signals is different on comparison to both the parent ligand and analogous zinc complex. The most upfield aromatic signal, a triplet at 7.61 ppm, is attributed to the protons situated in the 5-position of the two symmetrically equivalent pyridyl groups. The integration in this case corresponds to two protons which supports this explanation. The next signal, another triplet, at 7.92 ppm is half the intensity of the first. This signal is attributed to the proton in the 5-position of the pyridyl unit lying furthest from the methine bridge on the bipyridine group (N4/C17-C21)\*. A doublet, equivalent to two protons, at 8.11 ppm is most likely caused by the protons in the 3-position of the two lone pyridyl units. This is followed by a multiplet, corresponding to four protons, which is composed of a doublet and two triplet signals. The doublet in this instance probably arises from the proton in the 5-position of the pyridyl group lying closest to the methine bridge on the bipyridine group (N3/C12-C16). The two triplets are caused by protons lying on the 4-positions of the two equivalent lone pyridines and by the proton situated on the 4-position of pyridine N4/C17-C21. The next two doublets, each corresponding to one proton at 8.37 and 8.53 ppm are attributed to the protons located on the 3-position of pyridines N3/C12-C16 and N4/C17-C21 respectively. The next signal, a triplet corresponding to one proton, located at 8.57 ppm is attributable to the proton situated on the 4-position of the pyridine lying N3/C12-C16. The finally two doublets at 8.62 and 8.85 ppm, corresponding to two and one protons respectively, are attributed to the protons on the 6-position of lone pyridines and the pyridine N4/C17-C21 respectively.

---

\* The atom numbering here relates to the standard labelling scheme as used for the crystal structures of complexes of  $L^4$  and  $L^5$  which are to be found in the supplementary information (CD).

For the analogous cadmium complex of  $L^5$  (Fig. 7), the most upfield aromatic signal (7.67 ppm) is attributed to the proton in the 5-position of the lone pyridyl group (N1/C2-C6). The integration in this case corresponds to one proton which supports this explanation. The next signal, another triplet, at 7.93 ppm is twice the intensity of the first. This signal is attributed to the protons in the 5-position of the equivalent pyridyl units (N3/C12-C16 and N5/C22-C26) lying furthest from the methine bridge, located on the two bipyridine groups. The next triplet at 8.18 ppm has been ascribed to the proton situated on the 4-position of the lone pyridine. The multiplet from 8.27 – 8.35 ppm most likely consists of two doublets and a triplet. The doublets are attributed to the protons situated on the 5-position of the three pyridines directly attached to the methine bridge, and the triplet to the protons 4-position of symmetrically equivalent pyridines N3/C12-C16 and N5/C22-C26. The next multiplet (8.40 – 8.53 ppm) has an integration corresponding to six protons and consists of two doublets and a triplet. The doublets arise from protons situated on bipyridine units on the 3 and 4 positions of the equivalent pyridine rings lying closest to the methine bridge (N2/C7-C11 and N4/C17-C21), while the triplet is attributable to the protons on the 3-position of the pyridines N3/C12-C16 and N5/C22-C26. The next doublet (9.03 ppm) is most likely caused by the proton in the 6-position of the lone pyridine, the integration which is equivalent to one proton supports this. The most deshielded protons are those on the two bipyridine rings in the 6-position of the pyridine ring lying furthest from the methine bridge (N3/C12-C16 and N5/C22-C26). A sharp singlet at 6.49 ppm corresponds to the methanolic (*O-H*) proton.

The  $^{13}\text{C}$  NMR spectra of both complexes of  $L^5$  have been overlaid in Figure 8. It is clear that the spectra are very similar. The most upfield signal in each case is much weaker on comparison to the other signals and is caused by the bridging carbon atom (C1). Such quaternary

carbons signals are often weak due to slow relaxation and the lack of nuclear Overhauser enhancement. Both  $^{13}\text{C}$  NMR spectra reveal all of the expected sixteen carbon atoms.

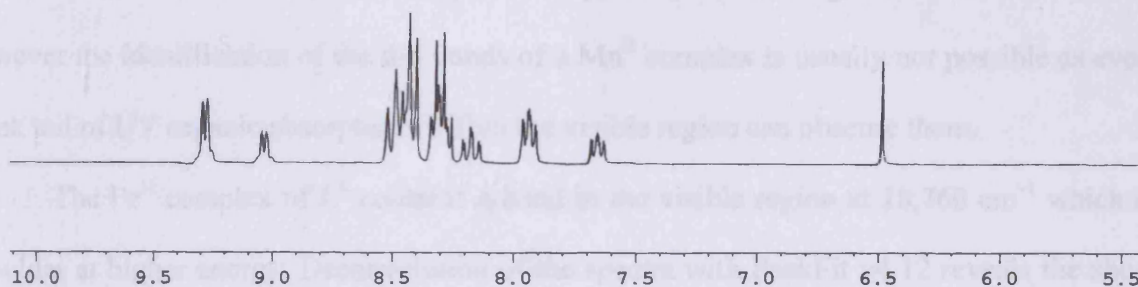


Figure 7:  $^1\text{H}$  NMR of  $[\text{Cd}^{\text{II}}(\text{L}^5)][\text{ClO}_4]_2$

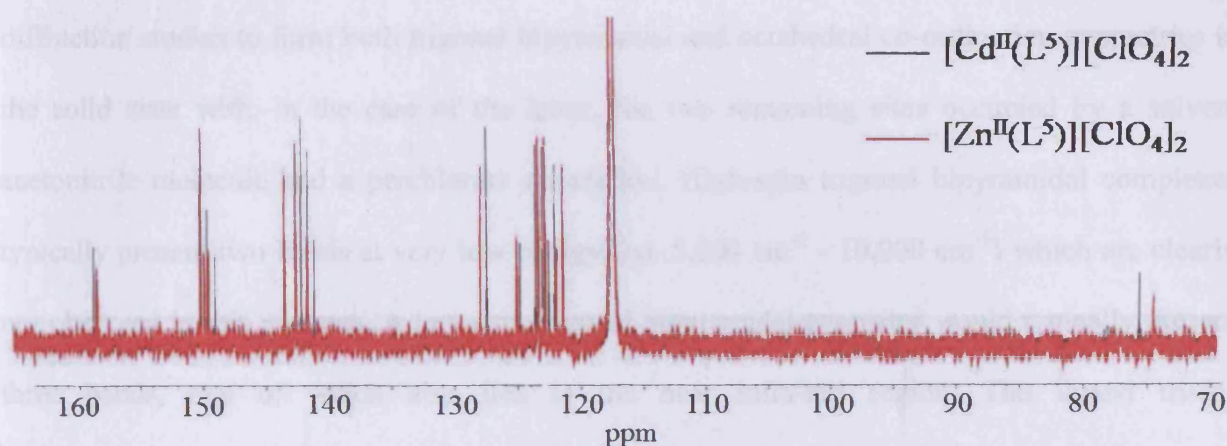


Figure 8: Superimposed  $^{13}\text{C}$  NMR spectra of  $[\text{Zn}^{\text{II}}(\text{L}^5)][\text{ClO}_4]_2$  (red) and  $[\text{Cd}^{\text{II}}(\text{L}^5)][\text{ClO}_4]_2$  (black).

Attempts were made to collect the  $^1\text{H}$  NMR of the  $\text{Fe}^{\text{II}}$  complexes, **3.2** and **3.9**, however no signals were observable which is suggestive of a high-spin paramagnetic  $d^6$  electron configuration.

### 3.4.5 Electronic Absorption Spectroscopy

The electronic absorption spectra for all complexes of  $\text{L}^4$  and  $\text{L}^5$  possess two strong peaks between 231 nm and 306 nm characteristic of intra-ligand bipyridine  $\pi\text{-}\pi^*$  transitions. The

manganese(II) complexes of  $L^4$  and  $L^5$  did not reveal any indication of a d-d transition even in highly concentrated solutions. The molar extinction coefficients for the spin-forbidden d-d transitions of an octahedral  $Mn^{II}$  complex are typically in the range  $10^{-2} - 10^{-1} \text{ dm}^3 \text{ mol}^{-1} \text{ cm}^{-1}$ , however the identification of the d-d bands of a  $Mn^{II}$  complex is usually not possible as even the weak tail of UV organic absorptions within the visible region can obscure them.

The  $Fe^{II}$  complex of  $L^4$  contains a band in the visible region at  $18,760 \text{ cm}^{-1}$  which has a shoulder at higher energy. Deconvolution of the spectra with PeakFit v4.12 reveals the shoulder reaches its absorbance maxima at  $20,750 \text{ cm}^{-1}$  (Fig. 9). Ligand  $L^4$  has been shown by X-ray diffraction studies to form both trigonal bipyramidal and octahedral co-ordination geometries in the solid state with, in the case of the latter, the two remaining sites occupied by a solvent acetonitrile molecule and a perchlorate counterion. High-spin trigonal bipyramidal complexes typically present two bands at very low energy (*ca.*  $5,000 \text{ cm}^{-1} - 10,000 \text{ cm}^{-1}$ ) which are clearly not observed in this instance. A low-spin trigonal bipyramidal geometry would typically present three bands, one of which also lies in the near infra-red region. The ligand tris(o-diphenylphosphinophenyl)phosphine is known to form low-spin trigonal bipyramidal complex with  $Fe^{II}$  and has three bands at *ca.*  $9,000 \text{ cm}^{-1}$ ,  $18,000 \text{ cm}^{-1}$  and  $30,000 \text{ cm}^{-1}$ .<sup>29</sup> As the experimental range in this work was limited to 200 - 1,100 nm ( $50,000 - 9,090 \text{ cm}^{-1}$ ) the lowest energy transition corresponding to  $(e'')^4(e')^2$  to  $(e'')^3(e')^3$  could lie outside the observable range. The two highest energy transitions would therefore correspond to the configurations  $(e'')^4(e')(a_1')$  and  $(e'')^3(e')^2(a_1')$  respectively. In the case of an octahedral co-ordination geometry there is only one spin-allowed transition for a high-spin d-electron configuration  $((t_{2g})^4(e_g)^2 \rightarrow (t_{2g})^3(e_g)^3)$ , *i.e.*  ${}^5E_g \leftarrow {}^5T_{2g}$ , however, the pseudo- $C_{2v}$  symmetry of this system would naturally lead to two transitions resulting from the splitting of the  ${}^5E_g$  state. The resulting splitting into  ${}^5A_1 + {}^5B_1$  means two bands are frequently observed in complexes of this type. The similar  $D_{4h}$

compound,  $\text{Fe}^{\text{II}}(\text{Py})_4\text{Cl}_2$  has absorption bands at  $8,720\text{ cm}^{-1}$  and  $10,520\text{ cm}^{-1}$  which are clearly present at much lower energy than seen for this compound.<sup>30,31</sup> Therefore, the most likely scenario is that of a low-spin octahedral co-ordination geometry. In this case, two transitions ( ${}^1\text{T}_{1g} \leftarrow {}^1\text{A}_{1g}$  and  ${}^1\text{T}_{2g} \leftarrow {}^1\text{A}_{1g}$ ) are typically seen. In some cases, a third transition attributable to the spin-forbidden triplet state  ${}^3\text{T}_1$  is also reported. The compound,  $\text{c-Fe}^{\text{II}}\text{Cl}_2(\text{ArNC})_4$  presents absorption bands at  $17,400\text{ cm}^{-1}$  and  $22,900\text{ cm}^{-1}$  corresponding to the two spin-allowed transitions.<sup>32</sup> It should be noted however that whilst the electron absorption spectra is characteristic of a low-spin diamagnetic d-electron configuration, attempts to obtain the  ${}^1\text{H}$  NMR of this compound were unsuccessful.

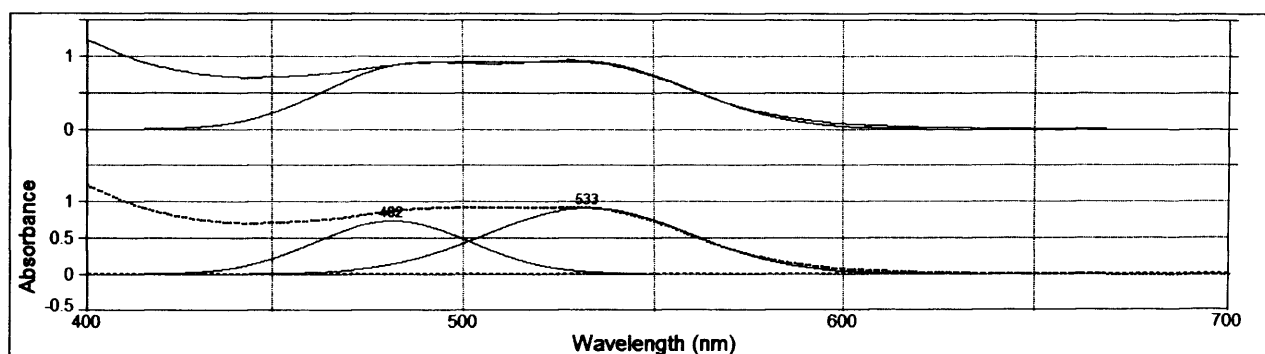


Figure 9: Deconvolution of the Electronic Spectrum of the  $\text{Fe}^{\text{II}}$  complex of Ligand  $\text{L}^4$

The analogous  $\text{Fe}^{\text{II}}$  complex of  $\text{L}^5$  has three bands within the visible region at  $17,330\text{ cm}^{-1}$ ,  $19,840\text{ cm}^{-1}$  and  $23,870\text{ cm}^{-1}$  (Fig. 10). Single crystal X-ray diffraction studies of the compound reveal a distorted octahedral co-ordination geometry. Assuming this geometry is maintained in solution, a low-spin configuration is again the most likely scenario. The lowest energy band in the visible region (which is not observed in the analogous  $\text{Fe}^{\text{II}}$  complex of  $\text{L}^4$ ) is attributable to the spin-forbidden transition to a  ${}^3\text{T}_1$  triplet state. The related compound  $[\text{Fe}^{\text{II}}(\text{das})_3]^{2+}$  exhibits this spin-forbidden transition at  $14,700\text{ cm}^{-1}$ .<sup>33</sup> Again, in a similar manner to the  $\text{Fe}^{\text{II}}$  complex of  $\text{L}^4$ , attempts to obtain the  ${}^1\text{H}$  NMR of this compound were unsuccessful.



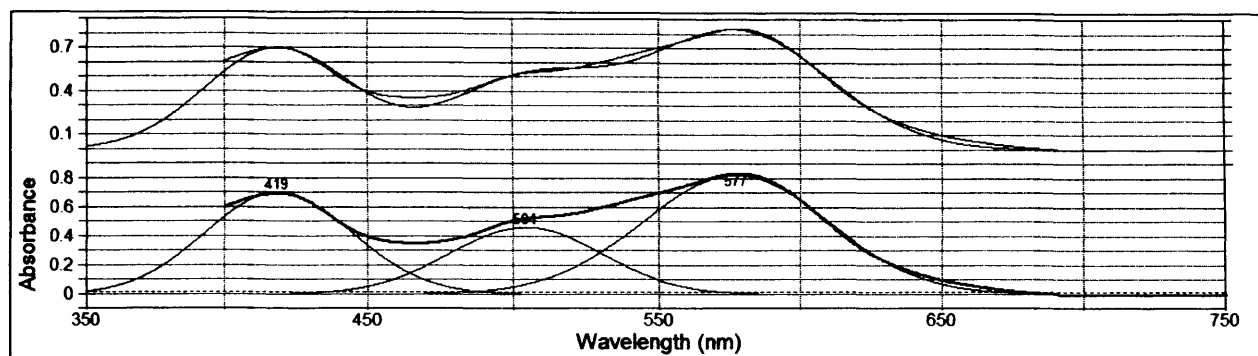


Figure 10: Deconvolution of the Electronic Spectrum of the Fe<sup>II</sup> complex of Ligand L<sup>5</sup>

Ligand L<sup>4</sup> is more likely to form octahedral complexes than L<sup>3</sup> or L<sup>5</sup> because it only has one bipyridine ‘arm’, consequently the steric strain involved in twisting the ligand to force an octahedral geometry is greatly reduced and the ligand field stabilisation energy becomes the leading factor in establishing complex geometry. The complex [Co<sup>II</sup>(L<sup>4</sup>)](ClO<sub>4</sub>)<sub>2</sub> contains two bands in the visible region of its electronic spectrum at 9,520 cm<sup>-1</sup> and 21,790 cm<sup>-1</sup> which is very characteristic of a high-spin octahedral Co<sup>II</sup> complex. High-spin complexes of d<sup>7</sup> ions typically show two transitions; the lowest energy transition is attributed to <sup>4</sup>T<sub>2g</sub> ← <sup>4</sup>T<sub>1g</sub> which usually appears at *ca.* 8,000 - 10,000 cm<sup>-1</sup>. The second transition assigned to <sup>4</sup>T<sub>1g</sub>(P) ← <sup>4</sup>T<sub>1g</sub> typically appears at *ca.* 20,000 cm<sup>-1</sup>. A further spin-allowed transition, <sup>4</sup>A<sub>2g</sub> ← <sup>4</sup>T<sub>1g</sub> is usually not observed as it is very weak, however in some cases it can appear as a shoulder on the second transition. In this instance, this band was not identifiable. The ratio  $\nu_2/\nu_1$  is 2.29 and upon inspection of the appropriate Tanabe-Sugano diagram  $\Delta/B = 15$ . Thus,  $B = 793$  cm<sup>-1</sup> and  $\Delta = 10,313$  cm<sup>-1</sup>. For the free ion [Co<sup>II</sup>],  $B = 971$  cm<sup>-1</sup> therefore the nephelauxetic parameter,  $\beta = 0.817$  indicates a significant degree of covalence. A similar high-spin Co<sup>II</sup> octahedral complex, [Co(py)<sub>6</sub>]<sup>2+</sup>, has absorptions at 9,800 cm<sup>-1</sup> and 20,400 cm<sup>-1</sup>.<sup>34</sup>

The Co<sup>II</sup> complex of L<sup>5</sup> reveals two bands in the visible region at 9,710 cm<sup>-1</sup> and 21,600 cm<sup>-1</sup>. In the solid state, this complex has slightly more trigonal prismatic content than octahedral

### Chapter 3: The Co-ordination and Electrochemical Behaviour of Two Analogous Tetra- and Pentadentate Tripodal Ligand Frameworks

(see Table 22 for results of continuous shape mapping calculations), however the difference is only minor and the electronic spectrum is very similar to that seen for the analogous  $\text{Co}^{\text{II}}$  complex of  $L^4$ . Therefore, the observed transitions have been assigned in an identical manner. The ratio  $v_2/v_1$  is 2.29 and, upon inspection of the appropriate Tanabe-Sugano diagram,  $\Delta/B = 17$ . Thus,  $B = 731 \text{ cm}^{-1}$  and  $\Delta = 12,423 \text{ cm}^{-1}$ . For the free ion  $[\text{Co}^{\text{II}}]$ ,  $B = 971 \text{ cm}^{-1}$  therefore the nephelauxetic parameter,  $\beta = 0.753$  indicates a significant degree of covalence. If the complex maintained predominantly trigonal prismatic character in solution the absorptions in the visible region would look quite different. For instance, three absorption bands corresponding to the transitions:  ${}^4E' \rightarrow {}^4E'' + {}^4A_2' + {}^4A_1''$ ,  ${}^4A_2''$  (unresolved),  ${}^4E' \rightarrow {}^4E''(\text{P})$ , and  ${}^4E' \rightarrow {}^4A_2'(\text{P})$  would be observable at approximately  $8,430 \text{ cm}^{-1}$ ,  $19,000 \text{ cm}^{-1}$  and  $22,200 \text{ cm}^{-1}$  respectively.<sup>35</sup>

The complex  $[\text{Ni}^{\text{II}}(L^4)]_2[\text{ClO}_4]_2$  reveals two regions of absorption in the visible region of its electronic spectrum (Fig. 11). One absorbance maxima occurs at  $19,645 \text{ cm}^{-1}$ , and analysis of the second region reveals two overlapping peaks at  $11,315 \text{ cm}^{-1}$  and  $12,832 \text{ cm}^{-1}$ . The shape mapping results derived from the crystallographic data indicate a clearly octahedral co-ordination geometry, however it is best described as containing pseudo- $C_{2v}$  symmetry. Typically, in  $O_h$  symmetry, three absorption bands are expected corresponding to the spin-allowed transitions from  ${}^3A_{2g}$  to  ${}^3T_{2g}$ ,  ${}^3T_{1g}$  and  ${}^3T_{1g}(\text{P})$  from lowest to highest energy respectively. These three bands are typically observed in the regions  $7,000 - 13,000 \text{ cm}^{-1}$ ,  $11,000 - 20,000 \text{ cm}^{-1}$  and  $19,000 - 27,000 \text{ cm}^{-1}$ . For instance, the related complex  $\text{Ni}^{\text{II}}(\text{bipy})_3$  reveals three transitions at  $12,650$ ,  $19,200$  and  $26,000 \text{ cm}^{-1}$ .<sup>34</sup> The visible region of  $\text{Ni}^{\text{II}}(\text{bipy})_3$  also reveals one further transition at  $11,500 \text{ cm}^{-1}$  which corresponds to the spin-forbidden transition to  ${}^1E_g$ . This is fairly commonly seen as a weak shoulder next to the second transition. As the  $\text{Ni}^{\text{II}}$  complex of  $L^4$  exhibits pseudo- $C_{2v}$  symmetry in the solid state, the spectrum contains some subtle differences

and has been tentatively assigned accordingly. The lowest energy transition  ${}^3A_{1g} \leftarrow {}^3B_{1g}$  most likely occurs in the near-infrared region, outside the operating range of the spectrophotometer. Therefore, the band at  $11,315\text{ cm}^{-1}$  has been ascribed to the second spin-allowed transition  ${}^3A_{2g} + {}^3B_{2g} \leftarrow {}^3B_{1g}$  and the shoulder at  $12,832\text{ cm}^{-1}$  to the spin-forbidden transition  ${}^1B_{1g}(D) + {}^1A_{1g}(D) \leftarrow {}^3B_{1g}$ . The third band in the visible region at  $19,645\text{ cm}^{-1}$  has been attributed to the transition  ${}^3B_{2g} \leftarrow {}^3B_{1g}$ . There are several additional spin-allowed transitions which occur at higher energy which are most likely obscured by charge transfer bands or ligand-based processes.

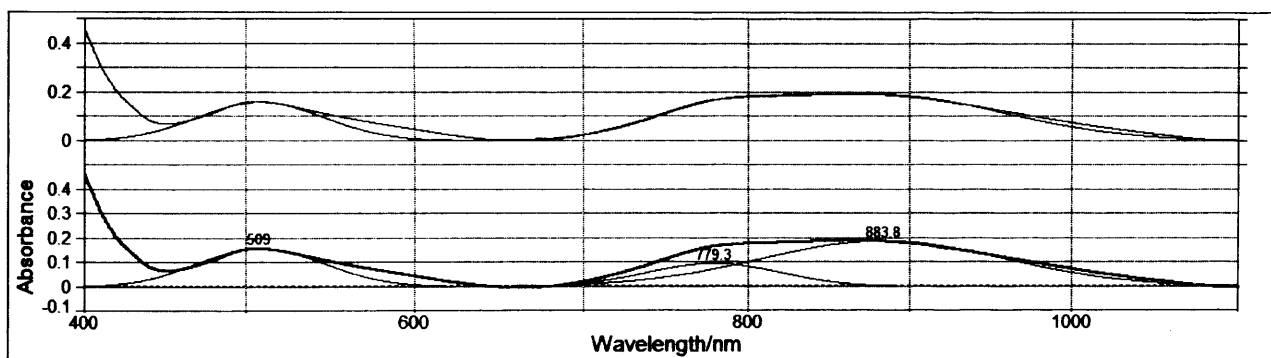


Figure 11: Deconvolution of the Electronic Spectrum of the  $\text{Ni}^{\text{II}}$  complex of Ligand  $L^4$

The  $\text{Ni}^{\text{II}}$  complex of  $L^5$  presents a very similar spectrum (Fig. 12) to that of the analogous  $\text{Ni}^{\text{II}}$  complex of  $L^4$ . There is one absorbance maxima which occurs at  $19,530\text{ cm}^{-1}$ , and deconvolution of the second region reveals two overlapping peaks at  $12,200\text{ cm}^{-1}$  and  $10,460\text{ cm}^{-1}$ . Again, as this complex exhibits a predominantly octahedral co-ordination environment with  $C_{2v}$  symmetry, the absorption bands have been tentatively assigned in an identical manner to the preceding complex.

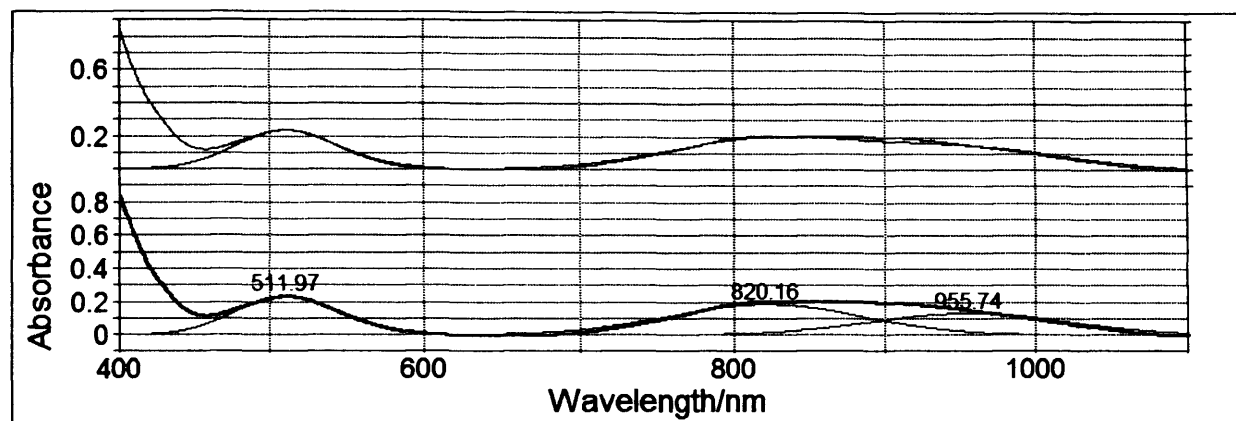


Figure 12: Deconvolution of the Electronic Spectrum of the Ni<sup>II</sup> complex of Ligand L<sup>5</sup>

The complex [Cu<sup>II</sup>(L<sup>4</sup>)](ClO<sub>4</sub>)<sub>2</sub> contains two broad absorption bands in the visible region at 10,875 cm<sup>-1</sup> and 15,189 cm<sup>-1</sup> (Fig. 13). Single crystal X-ray diffraction data indicates the five-coordinate geometry surrounding the metal centre lies almost exactly halfway between trigonal bipyramidal and square pyramidal. The absorption pattern expected for a trigonal bipyramidal copper complex involves peaks extending from *ca.* 10,500 - 14,600 cm<sup>-1</sup> with a greater absorption intensity proceeding from higher to lower energy. A square pyramidal environment would lead to a similar band envelope in the range *ca.* 11,400 - 15,000 cm<sup>-1</sup>, however in this case the absorption intensity is expected to increase to higher energy as shown in the example K[Cu(NH<sub>3</sub>)<sub>5</sub>][PF<sub>6</sub>]<sub>3</sub> provided by Hathaway and Billing.<sup>36</sup> It is also a possibility that [Cu<sup>II</sup>(L<sup>4</sup>)](ClO<sub>4</sub>)<sub>2</sub> forms an octahedral co-ordination environment with C<sub>2v</sub> symmetry in solution. In this case the one electron energy sequence of the Cu<sup>II</sup> ion is approximately the same as that predicted for the square-based pyramidal geometry, *i.e.* (x<sup>2</sup>-y<sup>2</sup>) > (z<sup>2</sup>) > (xy) > (xz) ≈ (yz). Therefore, the broad absorption band at higher energy may be tentatively assigned to transitions from components of t<sub>2g</sub>, *i.e.* (xy, xz ≈ yz) → (x<sup>2</sup> - y<sup>2</sup>), and the lower energy band as (z<sup>2</sup>) → (x<sup>2</sup> - y<sup>2</sup>) transitions. A pertinent example is that of Cu(bipy)<sub>2</sub>(ONO)<sup>+</sup> N<sub>2</sub>N<sub>2</sub>'O<sub>2</sub> which reveals two bands at 9,500 cm<sup>-1</sup> and 14,900 cm<sup>-1</sup>, corresponding to the transitions (z<sup>2</sup> → x<sup>2</sup> - y<sup>2</sup>) and (xy, xz

$\approx yz \rightarrow x^2 - y^2$ ).<sup>37</sup> It should also be mentioned that in such complexes, as the axial bond lengthens, the transitions from the components of  $t_{2g}$  to  $x^2 - y^2$  are shifted to higher energy due to a synergic effect, *i.e.* the copper ion becomes increasingly positive and attracts the equatorial ligands more strongly.

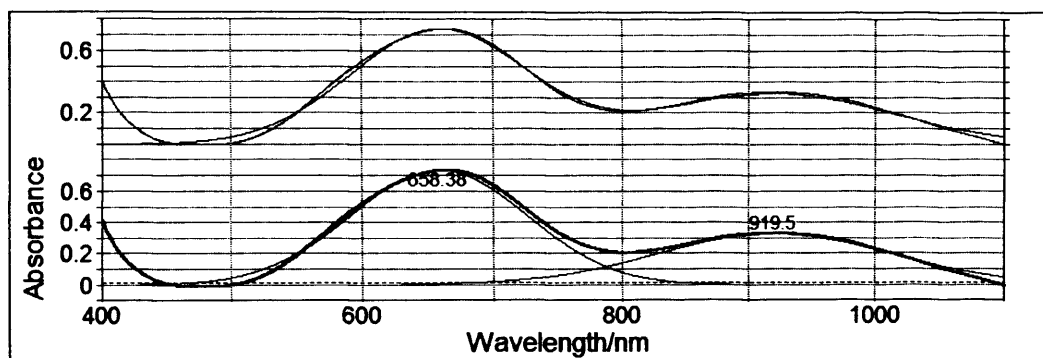


Figure 13: Deconvolution of the Electronic Spectrum of the Cu<sup>II</sup> complex of Ligand L<sup>4</sup>

The analogous Cu<sup>II</sup> complex of L<sup>5</sup> presents a very typical octahedral Cu<sup>II</sup> electronic spectrum *i.e.* a single poorly resolved broad peak in the visible region (15,650 cm<sup>-1</sup>). Here, the unstable <sup>2</sup>E<sub>g</sub> ground state resulting from the asymmetrical filling of the degenerate anti-bonding E<sub>g</sub> subset of orbitals causes a tetragonal distortion. In this instance, the transition  $z^2 \rightarrow x^2 - y^2$  is not observed within the 200 – 1,100 nm window collected here and is most likely located in the near infra-red region. The <sup>2</sup>E<sub>g</sub> term splits into <sup>2</sup>B<sub>1g</sub> and <sup>2</sup>A<sub>1g</sub>, and the <sup>2</sup>T<sub>2g</sub> term splits into <sup>2</sup>B<sub>2g</sub> and <sup>2</sup>E<sub>g</sub>. Therefore, three overlapping bands corresponding to the transitions <sup>2</sup>A<sub>1g</sub> ← <sup>2</sup>B<sub>1g</sub>, <sup>2</sup>B<sub>2g</sub> ← <sup>2</sup>B<sub>1g</sub> and <sup>2</sup>E<sub>g</sub> ← <sup>2</sup>B<sub>1g</sub> are expected to be present. In this instance, identification of these transitions *via* de-convolution could not be performed with confidence owing to the broad symmetrical nature of the absorption band.

## Chapter 3: The Co-ordination and Electrochemical Behaviour of Two Analogous Tetra- and Pentadentate Tripodal Ligand Frameworks

**Table 3** Electronic spectral assignments for complexes of L<sup>4</sup>

Compound	$\pi$ - $\pi^*$ transitions / $\lambda$ (nm)	MLCT / $\lambda$ (nm)	d-d transitions / $\lambda$ (nm)	$\Delta$ (cm <sup>-1</sup> ) <sup>b</sup>	B' (cm <sup>-1</sup> ) <sup>b</sup>	$\beta$
[Mn <sup>II</sup> (L <sup>4</sup> )](ClO <sub>4</sub> ) <sub>2</sub>	242(22,460), 295(24,220)	316(8,070)	-	-	-	-
[Fe <sup>II</sup> (L <sup>4</sup> )](ClO <sub>4</sub> ) <sub>2</sub>	234(23,110), 287(22,550)	307(6,260)	482(19), 533(31)	-	-	-
[Co <sup>II</sup> (L <sup>4</sup> )](ClO <sub>4</sub> ) <sub>2</sub>	233(19,510), 286(16,350)	-	459(150), 1051(28)	10,313	793	0.817
[Ni <sup>II</sup> (L <sup>4</sup> )](ClO <sub>4</sub> ) <sub>2</sub>	265(21,850), 306(14,300)	-	714(67), 774(93)	-	-	-
[Cu <sup>II</sup> (L <sup>4</sup> )](ClO <sub>4</sub> ) <sub>2</sub>	251(23,700), 304.7(14,040)	317(9,200)	658(83), 920(37)	-	-	-

<sup>a</sup>performed in CH<sub>3</sub>CN solution at room temperature; Numbers in parentheses indicate molar absorption coefficients  $\epsilon$  (M<sup>-1</sup>cm<sup>-1</sup>). <sup>b</sup>values calculated by assuming an octahedral geometry

**Table 4** Electronic spectral assignments for complexes of L<sup>5</sup>

Compound	$\pi$ - $\pi^*$ transitions / $\lambda$ (nm)	MLCT / $\lambda$ (nm)	d-d transitions / $\lambda$ (nm)	$\Delta$ (cm <sup>-1</sup> ) <sup>b</sup>	B' (cm <sup>-1</sup> ) <sup>b</sup>	$\beta$
[Mn <sup>II</sup> (L <sup>5</sup> )](ClO <sub>4</sub> ) <sub>2</sub>	234(23,500), 292(16,600)	314(7,100)	-	-	-	-
[Fe <sup>II</sup> (L <sup>5</sup> )](ClO <sub>4</sub> ) <sub>2</sub>	239(20,250), 295(18,450)	316(4,400)	419(112), 504(78), 577(133)	-	-	-
[Co <sup>II</sup> (L <sup>5</sup> )](ClO <sub>4</sub> ) <sub>2</sub>	231(23,800), 284(19,850)	302(4,150)	463(103), 1030(21)	12,423	731	0.753
[Ni <sup>II</sup> (L <sup>5</sup> )(Br)](ClO <sub>4</sub> )	248(22,000), 298(21,500)	312(9,150)	512(19), 820(15), 956(11)	10, 148	220	0.212
[Cu <sup>II</sup> (L <sup>5</sup> )](ClO <sub>4</sub> ) <sub>2</sub>	245(20,750), 301(29,300)	316(10,300)	639(54)	-	-	-

<sup>a</sup>performed in CH<sub>3</sub>CN solution at room temperature; Numbers in parentheses indicate molar absorption coefficients  $\epsilon$  (M<sup>-1</sup>cm<sup>-1</sup>). <sup>b</sup>values calculated by assuming an octahedral geometry

### 3.4.6 Electrochemical Studies

The manganese(II) complexes of L<sup>4</sup> and L<sup>5</sup> reveal very similar cyclic voltammograms. The related Mn<sup>II</sup> compounds [Mn<sup>II</sup>(bipy)<sub>3</sub>](ClO<sub>4</sub>)<sub>2</sub> and [Mn<sup>II</sup>(1,10-phen)<sub>3</sub>](ClO<sub>4</sub>)<sub>2</sub> reveal reversible oxidation processes at +1.36 V and +1.28 V vs SCE respectively (0.1 M TPAP, acetonitrile), which are attributable to the Mn<sup>II/III</sup> redox couple.<sup>38</sup> For both [Mn<sup>II</sup>(L<sup>4</sup>)](ClO<sub>4</sub>)<sub>2</sub> (**3.1**) and [Mn<sup>II</sup>(L<sup>5</sup>)](ClO<sub>4</sub>)<sub>2</sub> (**3.8**), no wave corresponding to this process is observable within the bounds of the potential window. Compound **3.1** reveals three quasi-reversible waves at -1.652, -1.849, and -2.11 V which are attributable to ligand-based processes, specifically the addition and

subsequent removal of an electron from the bipyridyl and pyridyl  $\pi^*$  orbitals. The voltammogram of **3.8** also reveals three quasi-reversible waves at -1.737, -1.964 and -2.236 V. The second value, -1.964 V, corresponds to the cathodic wave only, as it was impossible to measure the corresponding anodic wave. Similarly, these are attributed to ligand-based processes.

**Table 5:** Electrochemical parameters for the redox processes exhibited by complexes of  $L^4$  and  $L^5$  in acetonitrile solution (supporting electrolyte:  $[\text{Bu}_4\text{N}][\text{PF}_6]$  ( $0.1 \text{ mol dm}^{-3}$ );  $T = 20 \text{ }^\circ\text{C}$ ). Measured at  $0.1 \text{ Vs}^{-1}$ .

Compound	$E_p/\text{V} (\Delta E, \text{mV})^{a,b}$
<b>3.1</b>	-1.652(61), -1.849(110), -2.110(90)
<b>3.8</b>	-1.737(62), -1.964, -2.211(60)
<b>3.2</b>	+0.866(70), -1.657(60)
<b>3.9</b>	+0.730(81), -1.552(60), -1.668(61)
<b>3.4</b>	- 1.222(91)
<b>3.11</b>	-1.208(70), -1.677(91)
<b>3.5</b>	+0.965, +0.039, -0.381(70), -2.107, -2.248
<b>3.12</b>	+0.786, -0.460(70), -0.463

<sup>a</sup>the potentials at which reversible processes occur are calculated as the average of the oxidative and reductive peak potentials ( $E_p^{\text{ox}} + E_p^{\text{red}}/2$ ). <sup>b</sup>For irreversible processes, the anodic or cathodic peak potentials are given. Potentials are given in volts *versus* Ferrocenium/Ferrocene.

The  $\text{Fe}^{\text{II}}$  complexes of ligands  $L^4$  and  $L^5$  also present very comparable electrochemical behaviour. In both instances, there is a reversible oxidation process (+0.866 V and +0.730 V respectively) which is attributable to the  $\text{Fe}^{\text{II/III}}$  redox couple (Figs. 14 and 15). Plots of the peak current against the square root of the scan rate confirm that both of these waves are clearly reversible. The  $\text{Fe}^{\text{II}}$  complex of ligand  $L^3$  reveals this reversible oxidation process at +0.693 V (*cf.* Section 2.4.6, p. 105). This trend suggests that as the denticity of the ligand is increased, the  $\text{Fe}^{\text{II}}$  cation becomes progressively easier to oxidise. The potential of these redox couples is in accordance with similar  $\text{Fe}^{\text{II}}$  complexes such as  $\text{Fe}^{\text{II}}(\text{bpy})_3$ ,  $\text{Fe}^{\text{II}}(\text{phen})_3$  and  $\text{Fe}^{\text{II}}(3,4,7,8\text{-Me}_4\text{phen})_3$  which occur at +0.89 V, +0.95 V and +0.66 V respectively.<sup>39</sup>

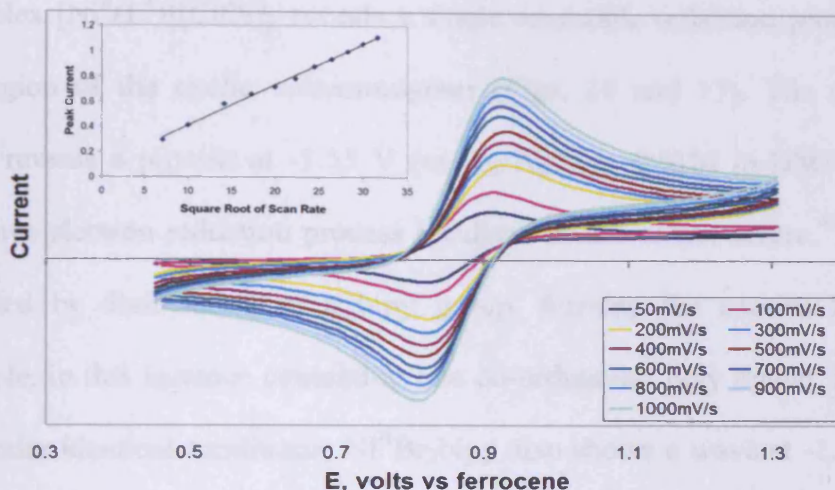


Figure 14: The reversible Fe<sup>II/III</sup> redox couple in [Fe<sup>II</sup>(L<sup>4</sup>)](ClO<sub>4</sub>)<sub>2</sub> (3.2).

In the case of L<sup>4</sup>, the Fe<sup>II</sup> complex (3.2) reveals a single reversible reduction in the cathodic region (-1.657 V) which is assigned to the one-electron reduction of the bipy unit. For the Fe<sup>II</sup> complex of L<sup>5</sup> (3.9), there are two reversible reductions (-1.552 V and -1.668 V) at a similar potential, again similarly assigned to reductions of the two bipy units.

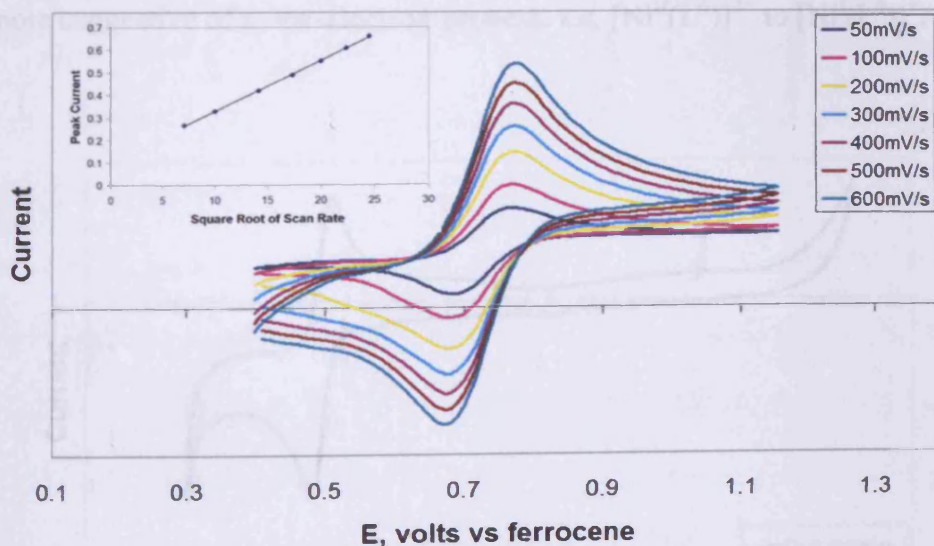


Figure 15: The reversible Fe<sup>II/III</sup> redox couple in [Fe<sup>II</sup>(L<sup>5</sup>)](ClO<sub>4</sub>)<sub>2</sub> (3.9).



The complex  $[\text{Ni}^{\text{II}}(\text{L}^4)][\text{ClO}_4]_2$  reveals a single reversible reduction process (-1.222 V) in the cathodic region of the cyclic voltammogram (Figs. 16 and 17). The similar compound  $\text{Ni}^{\text{II}}(\text{BF}_4)_2\text{bipy}_3$  reveals a process at -1.55 V (vs Ag/AgNO<sub>3</sub>, 0.01M in DMF) which has been attributed to a two electron reduction process localised on the nickel centre.<sup>40</sup> This reduction is also accompanied by dissociation of a bipy group, forming the species  $\text{Ni}^0\text{bipy}_2$ . Another pertinent example, in this instance containing one co-ordinating bipy ligand, is provided by the same authors under identical conditions;  $\text{Ni}^{\text{II}}\text{Br}_2\text{bipy}$  also shows a wave at -1.45 V which again has been ascribed to the two electron reduction of the nickel, forming the species  $\text{Ni}^0\text{bipy}$ . This species has been shown to disproportionate forming the stable species  $\text{Ni}^0\text{bipy}_2$  and metallic nickel. The metallic nickel adsorbs to the surface of the electrode, causing an oxidation at -0.68 V, characteristic of the oxidation of  $\text{Ni}^0$  to  $\text{Ni}^{2+}$ . Considering these examples, it would be reasonable to assume the wave process at -1.222 V in the voltammogram of  $[\text{Ni}^{\text{II}}(\text{L}^4)]^{2+}$  is caused by a two-electron reduction, forming the species  $[\text{Ni}^0(\text{L}^4)]$ , however the peak-to-peak separation (91mV) is more suggestive of a one-electron process, *i.e.*  $[\text{Ni}^{\text{II}}(\text{L}^4)]^{2+}$  to  $[\text{Ni}^{\text{I}}(\text{L}^4)]^+$ .

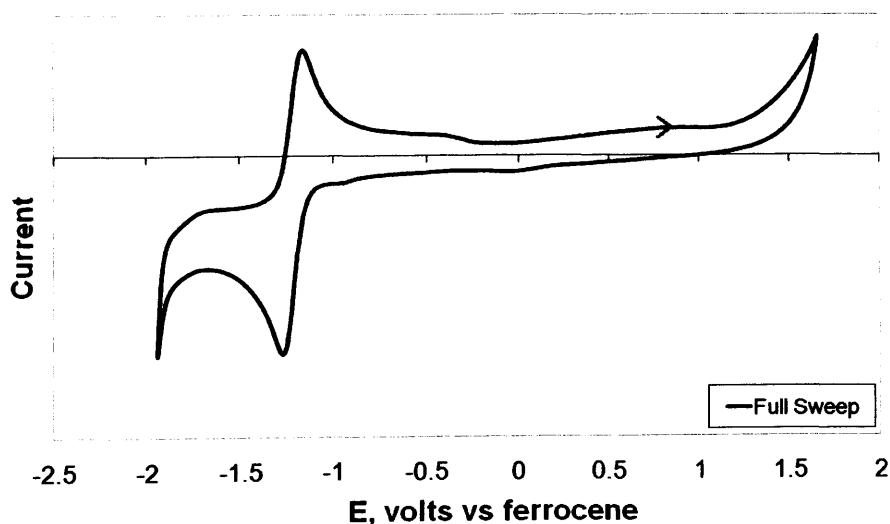


Figure 16: The two-electron reduction of  $[\text{Ni}^{\text{II}}(\text{L}^4)][\text{ClO}_4]_2$  corresponding to the  $\text{Ni}^{\text{II/0}}$  redox couple.

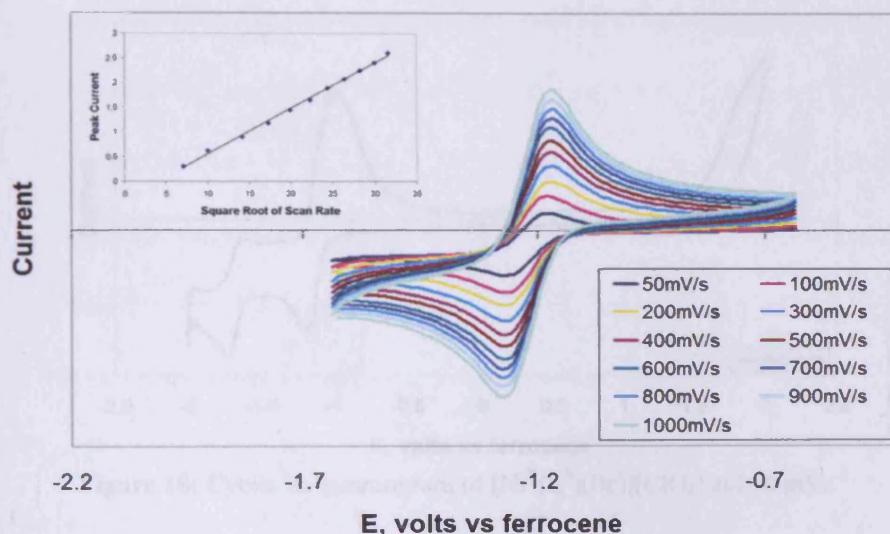
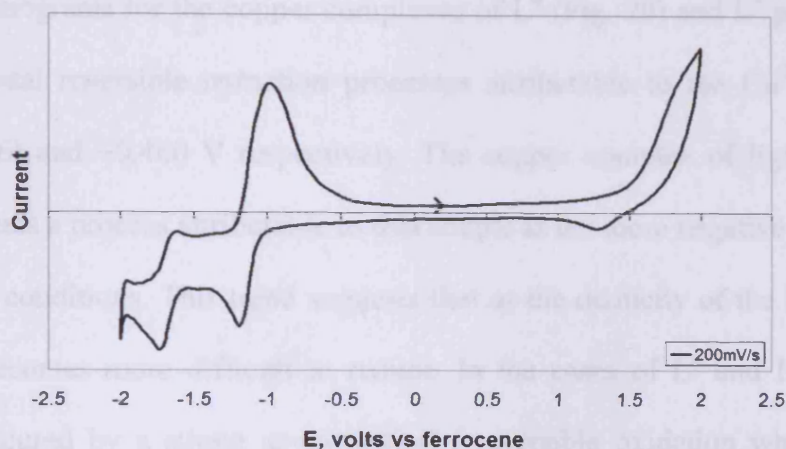


Figure 17: The reversibility of the  $\text{Ni}^{\text{II}/0}$  redox couple in  $[\text{Ni}^{\text{II}}(\text{L}^4)][\text{ClO}_4]_2$ .

The voltammogram of the  $\text{Ni}^{\text{II}}$  complex of  $\text{L}^5$  (Fig. 18) reveals two reversible reduction waves ( $-1.208$  V and  $-1.677$  V). In order to understand the electrochemical processes attributable to these waves, comparisons to related literature compounds must be drawn. Bartlett and Eastwick-Field conducted a thorough analysis of the electrochemical behaviour of  $[\text{Ni}^{\text{II}}(\text{bipy})_3]^{2+}$  in an attempt to resolve the contradictory conclusions of several groups with regards to this complex.<sup>41</sup> After performing controlled potential coulometry experiments, it was concluded that the first reduction wave at  $-1.65$  V was a two-electron process corresponding to the reduction of  $[\text{Ni}^{\text{II}}(\text{bpy})_3]^{2+}$  to  $[\text{Ni}^0(\text{bpy})_3]$ , this was in agreement with the findings of Henne and Bartak.<sup>42</sup> Further experiments revealed the loss of a bipy ligand following this reduction, it was also found that adding excess bipy suppressed this ligand dissociation. A second reduction wave at  $-2.15$  V was attributed to a one-electron reduction of the species  $[\text{Ni}^0(\text{bpy})\text{AN}]$  (where AN = acetonitrile) to  $[\text{Ni}^{-1}(\text{bpy})\text{AN}]^-$ . It was noted, however, that while the fully reduced species was denoted as  $\text{Ni}^{-1}$ , the reduction was probably predominantly ligand based. The formation of the species  $[\text{Ni}^0(\text{bpy})\text{AN}]$  was rationalised following several ring-disk experiments.



**Figure 18:** Cyclic voltammogram of  $[\text{Ni}^{\text{II}}(\text{L}^5)(\text{Br})][\text{ClO}_4]$  at  $200 \text{ mVs}^{-1}$

The voltammogram of compound  $[\text{Ni}^{\text{II}}(\text{L}^5)(\text{Br})][\text{ClO}_4]$  has been interpreted in a similar manner to the analogous  $\text{Ni}^{\text{II}}$  complex of ligand  $\text{L}^3$  which showed two reduction processes at the similar potentials of  $-1.390$  and  $-1.750 \text{ V}$  (*cf.* Section 2.4.6, p. 107). The two reduction waves have been tentatively ascribed to the sequential one-electron reductions of  $[\text{Ni}^{\text{II}}(\text{L}^3)]^{2+}$  to  $[\text{Ni}^{\text{I}}(\text{L}^3)]^+$  and subsequently to  $[\text{Ni}^0(\text{L}^3)]$ . A scan of the full window reveals the first reduction peak is partially obscured by a desorption process, however isolating this wave from the second reduction process eliminates it and enables the measurement of the peak-to-peak separation ( $70 \text{ mV}$ ; Fig. 19) which again supports the theory of a one-electron process. The second reversible wave is attributed to the one-electron reduction of the species  $[\text{Ni}^{\text{I}}(\text{L}^5)]^+$  to  $[\text{Ni}^0(\text{L}^5)]$ .

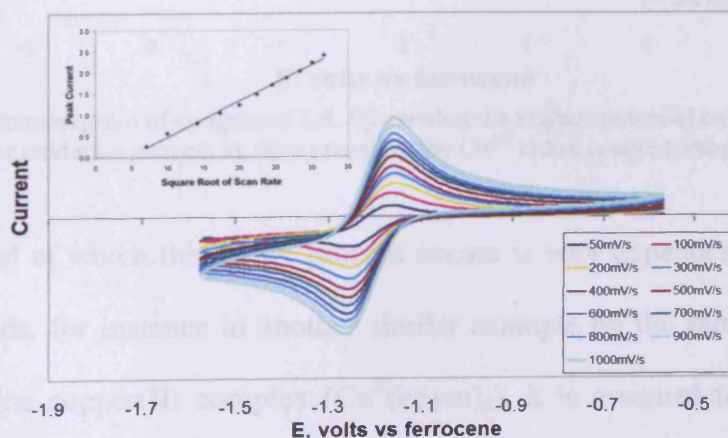


**Figure 19:** The one-electron reduction of  $[\text{Ni}^{\text{II}}(\text{L}^5)(\text{Br})][\text{ClO}_4]$  corresponding to the  $\text{Ni}^{\text{II/I}}$  redox couple.

The voltammograms for the copper complexes of  $L^4$  (Fig. 20) and  $L^5$  present very similar features; both reveal reversible reduction processes attributable to the  $\text{Cu}^{\text{II/I}}$  redox couple at  $-0.381$  V (Fig. 16) and  $-0.460$  V respectively. The copper complex of ligand  $L^3$  (*cf.* Section 2.4.6, p. 108) reveals a process attributable to this couple at the more negative potential of  $-0.523$  V under identical conditions. This trend suggests that as the denticity of the ligand is increased, the  $\text{Cu}^{\text{II}}$  cation becomes more difficult to reduce. In the cases of  $L^4$  and  $L^5$ , these reversible processes are obscured by a strong asymmetrical irreversible oxidation which is related to a further irreversible oxidation occurring at a higher potential in the anodic region. By-passing the highest potential oxidation feature eliminates the other oxidation process, thus revealing the  $\text{Cu}^{\text{II/I}}$  redox couple (Fig. 20; orange overlay). In the related compound,  $\text{Cu}^{\text{II}}(\text{bpy})_3$ , the  $\text{Cu}^{\text{II/I}}$  redox couple occurs at the significantly less negative potential of  $-0.03$  V *vs* SCE.<sup>43</sup>

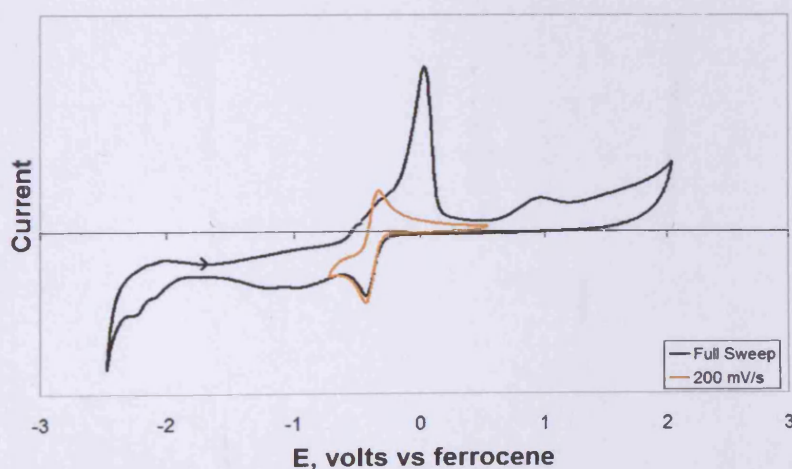


**Figure 20:** Cyclic voltammogram of compound 3.5. By-passing the highest potential oxidation feature eliminates the other oxidation process at, thus revealing the  $\text{Cu}^{\text{II/I}}$  redox couple (orange overlay).

The potential at which this redox process occurs is very dependent on the nature of the co-ordinating ligands, for instance in another similar example by the same authors involving a tris 2,2'-bipyrimidine copper(II) complex ( $\text{Cu}^{\text{II}}(\text{bpym})_3$ ), it is assigned to a reversible process occurring at  $+0.243$  V (*vs* SCE). This shift to more positive potential was attributed to an

increased amount of delocalisation of electron density over bpym ligand orbitals. In the case of 3.5, two further reduction processes ( $-2.107$  V and  $-2.248$  V) are visible and are assigned to the reductions of both bipy units.

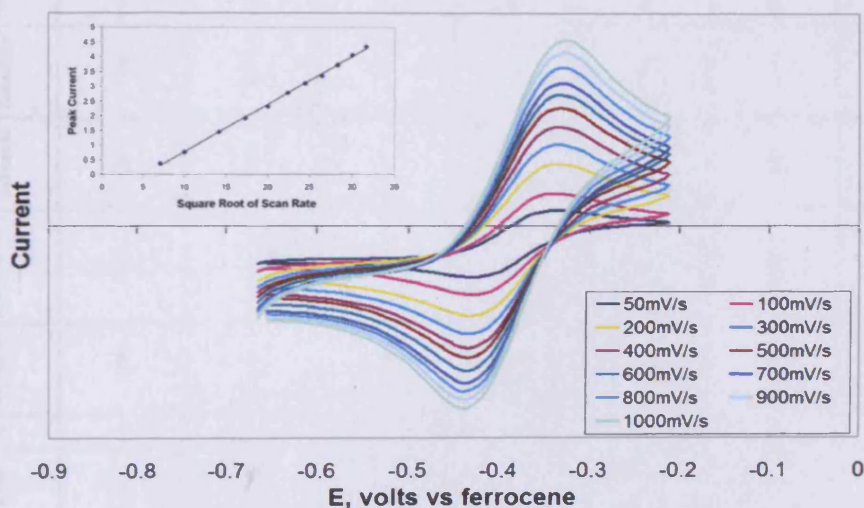


Figure 21: The reversibility of the  $\text{Cu}^{\text{II/I}}$  redox couple in 3.5.

**Table 6: Crystal Structure Data for Complexes 3.4, 3.5, 3.7, 3.8, 3.9, 3.10, 3.11, and 3.14**

Compound	Chemical Formula	Mr, g mol	Crystal System	Space group	T(K)	a, Å	b, Å	c, Å	α, deg	β, deg	γ, deg	Z	Dc, Mg/m <sup>3</sup>	μ(Mo K α), mm <sup>-1</sup>	Observed Reflections	Unique Reflections	Rint	R1 [I>2σ(I)]	wR2 (all data)
3.4	[Ni <sup>II</sup> (L <sup>4</sup> )(ClO <sub>4</sub> )(CH <sub>3</sub> CN)] [ClO <sub>4</sub> ]	639.04	Orthorhombic	Pcab	150(2)	12.8711(3)	16.3092(3)	23.6798(6)	90	90	90	8	1.708	1.061	3538	5680	0.097	0.0553	0.1338
3.5	[Cu <sup>II</sup> (L <sup>4</sup> )(H <sub>2</sub> O)] [ClO <sub>4</sub> ] <sub>2</sub> (CH <sub>3</sub> OH)	652.88	Triclinic	P-1	150(2)	8.5840(2)	11.7848(2)	14.7023(4)	96.7030(10)	96.7020(10)	109.929(1)	2	1.584	1.057	4574	6212	0.115	0.0584	0.1637
3.7	[Cd <sup>II</sup> (L <sup>4</sup> )(ClO <sub>4</sub> )(CH <sub>3</sub> CN)] [ClO <sub>4</sub> ]	692.73	Orthorhombic	Pcab	150(2)	12.6998(2)	17.0177(3)	23.8472(5)	90	90	90	8	1.786	1.118	4317	5876	0.079	0.0430	0.1068
3.8	[Mn <sup>II</sup> (L <sup>4</sup> )(CH <sub>3</sub> CN)] [ClO <sub>4</sub> ] <sub>2</sub> (CH <sub>3</sub> CN) <sub>2</sub>	750.39	Monoclinic	P2 <sub>1</sub> /n	150(2)	12.7935(3)	12.3606(3)	20.9431(6)	90	101.7290(10)	90	4	1.537	0.632	4971	7353	0.0933	0.0665	0.1886
3.9	[Fe <sup>II</sup> (L <sup>3</sup> )(CH <sub>3</sub> CN)] [ClO <sub>4</sub> ] <sub>2</sub> (C <sub>6</sub> H <sub>10</sub> O)	828.44	Triclinic	P-1	150(2)	10.1576(2)	11.9556(3)	15.5564(5)	95.1700(10)	100.1480(10)	93.1100(10)	2	1.489	0.619	5920	8315	0.1013	0.0805	0.2225
3.10	[Co <sup>II</sup> (L <sup>3</sup> )(CH <sub>3</sub> CN)] [ClO <sub>4</sub> ] <sub>2</sub> ·0.5(H <sub>2</sub> O)	1448.69	Monoclinic	P2 <sub>1</sub> /C	150(2)	14.0840(2)	21.3004(3)	19.6325(3)	90	94.2450(10)	90	4	1.638	0.835	6983	13449	0.1788	0.0686	0.1893
3.11	[Ni <sup>II</sup> (L <sup>3</sup> )(Br)] [ClO <sub>4</sub> ]	655.50	Monoclinic	P2 <sub>1</sub> /n	150(2)	12.4513(3)	10.2182(3)	20.2607(6)	90	101.8620(10)	90	4	1.726	2.508	3893	5720	0.1531	0.0666	0.1839
3.14	[Cd <sup>II</sup> (L <sup>3</sup> )(CH <sub>3</sub> CN)] [ClO <sub>4</sub> ] <sub>2</sub> (CH <sub>3</sub> CN) <sub>2</sub>	807.86	Monoclinic	P2 <sub>1</sub> /n	150(2)	12.8927(2)	12.4047(3)	20.9303(5)	90	102.3110(10)	90	4	1.641	0.896	5110	7447	0.0785	0.0531	0.1366

### 3.4.7 Crystallographic Studies

#### 3.4.7.1 Crystal Structure of $[\text{Ni}^{\text{II}}(\text{L}^4)(\text{ClO}_4)(\text{CH}_3\text{CN})][\text{ClO}_4]$ (3.4)

The  $\text{Ni}^{\text{II}}$  complex of  $\text{L}^4$  crystallises in the orthorhombic space group  $\text{Pcab}$  with one molecule in the asymmetric unit (Fig. 22). The  $\text{Ni}^{\text{II}}$  ion lies at the centre of a significantly distorted octahedral environment ( $S(\text{Oct}) = 1.44713$  vs  $S(\text{TP}) = 10.67394$ ) and is co-ordinated by two types of donor atom: five nitrogens and one oxygen. All four pyridyl N-donors are involved in co-ordination to the metal, the fifth nitrogen donor (N5) is located on a molecule of acetonitrile and the oxygen donor (O2) originates from a perchlorate counterion. This donor set is identical to the analogous  $\text{Cd}^{\text{II}}$  complex, 3.7. One prominent distortion arises from the acute nature of the bipyridine bite angle  $\text{N3-Ni1-N4}$  ( $78.74(12)^\circ$ ) which varies significantly from the  $90^\circ$  angle expected for a regular octahedron. Further distortions involve the bond angles between the three mutually trans sets of donor atoms,  $\text{N1-Ni1-N4}$  ( $163.50(12)^\circ$ ),  $\text{N2-Ni1-O2}$  ( $169.53(10)^\circ$ ) and  $\text{N3-Ni1-N5}$  ( $173.03(12)^\circ$ ) which all vary considerably from the theoretical  $180^\circ$ . The mean average of the co-ordinative bond angles between the three pyridines which are directly attached to the methine bridge is  $86.59(11)^\circ$ , indicating some degree of steric strain caused by the small linking group (C1). All but one of the pyridyl  $\text{N-Ni}^{\text{II}}$  bond lengths closely resemble those of the similar octahedral compound *trans*-bis(perchlorate)-tetrapyridine-nickel(II) which exhibits pyridyl  $\text{N-Ni}^{\text{II}}$  bond lengths ranging from  $2.085 \text{ \AA}$  to  $2.115 \text{ \AA}$ .<sup>44</sup> The  $\text{Ni1-N3}$  bond length is significantly shorter ( $2.009(3) \text{ \AA}$ ) than the others. This is presumably caused by the  $\text{N4/C17-C21}$  pyridine ring wrapping around to co-ordinate to the  $\text{Ni}^{\text{II}}$  ion, forcing N3 to adopt a closer position to the metal. The oxygen donor (O2) lies at a notably longer distance from the nickel centre ( $2.226(2) \text{ \AA}$ ) in comparison to the nitrogen donor atoms, which again leads to deviation away from a regular octahedron in which all bond lengths are identical. This bond length is, however, similar to other

### Chapter 3: The Co-ordination and Electrochemical Behaviour of Two Analogous Tetra- and Pentadentate Tripodal Ligand Frameworks

structures in which a nickel ion is co-ordinated by five nitrogen donors and an oxygen. The example given above contains a perchlorate O–Ni<sup>II</sup> bond length of 2.162 Å.

A second perchlorate counterion which balances the cationic character of the complex is located within the lattice and is involved in hydrogen bonding (Table 8) which supports the molecular packing.

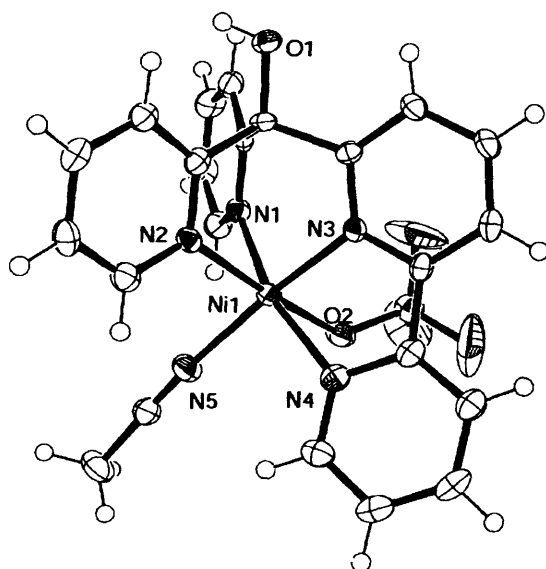


**Figure 22:** Perspective view of the asymmetric unit of 3.4 showing the atom numbering. Displacement ellipsoids are shown at the 50% probability level. H atoms are represented by circles of arbitrary size.

**Table 7:** Significant Bond lengths (Å) and Angles (°) for [Ni<sup>II</sup>(L<sup>4</sup>)(ClO<sub>4</sub>)(CH<sub>3</sub>CN)][ClO<sub>4</sub>]

Ni(1)-N(1)	2.057(3)		Ni(1)-N(4)	2.076(3)
Ni(1)-N(2)	2.068(3)		Ni(1)-N(5)	2.047(3)
Ni(1)-N(3)	2.009(3)		Ni(1)-O(2)	2.226(2)
N(3)-Ni(1)-N(5)	173.03(12)		N(1)-Ni(1)-N(4)	163.50(12)
N(3)-Ni(1)-N(1)	91.74(11)		N(2)-Ni(1)-N(4)	108.23(11)
N(5)-Ni(1)-N(1)	95.19(12)		N(3)-Ni(1)-O(2)	97.37(10)
N(3)-Ni(1)-N(2)	84.16(11)		N(5)-Ni(1)-O(2)	83.87(11)
N(5)-Ni(1)-N(2)	95.88(12)		N(1)-Ni(1)-O(2)	85.74(10)
N(1)-Ni(1)-N(2)	83.86(11)		N(2)-Ni(1)-O(2)	169.53(10)
N(3)-Ni(1)-N(4)	78.74(12)		N(4)-Ni(1)-O(2)	82.20(10)
N(5)-Ni(1)-N(4)	94.68(12)			



## Chapter 3: The Co-ordination and Electrochemical Behaviour of Two Analogous Tetra- and Pentadentate Tripodal Ligand Frameworks

**Table 8:** H-bonding geometry (Å, °) for **3.4**

D-H...A	d(D-H)	d(H...A)	d(D...A)	<(DHA)
O(1)-H(1)...O(7)#1	0.82	2.01	2.805(3)	165

Symmetry transformations used to generate equivalent atoms:

#1 = 1-x, -y, -z.

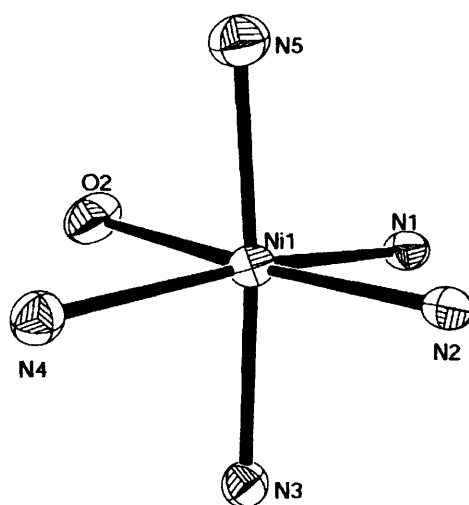


**Figure 23:** A view of the core geometry of **3.4** showing the atom numbering. Displacement ellipsoids are shown at the 50% probability level.

### 3.4.7.2 Crystal Structure of $[\text{Cu}^{\text{II}}(\text{L}^4)(\text{H}_2\text{O})][\text{ClO}_4]_2 \cdot (\text{CH}_3\text{OH})$ (**3.5**)

The  $\text{Cu}^{\text{II}}$  complex of  $\text{L}^4$  crystallises in the triclinic space group P-1 with one complex within the asymmetric unit (Fig. 24). The  $\text{Cu}^{\text{II}}$  cation lies at the centre of a distorted trigonal bipyramidal co-ordination geometry consisting of four pyridyl N-donors (N1–N4) and an oxygen donor (O2) located on a solvent water molecule. The continuous shape measures ( $S(\text{TBPY}) = 3.3524$  and  $S(\text{SPY}) = 3.38261$ ) indicate this structure has slightly more trigonal bipyramidal content than square pyramidal.

### Chapter 3: The Co-ordination and Electrochemical Behaviour of Two Analogous Tetra- and Pentadentate Tripodal Ligand Frameworks

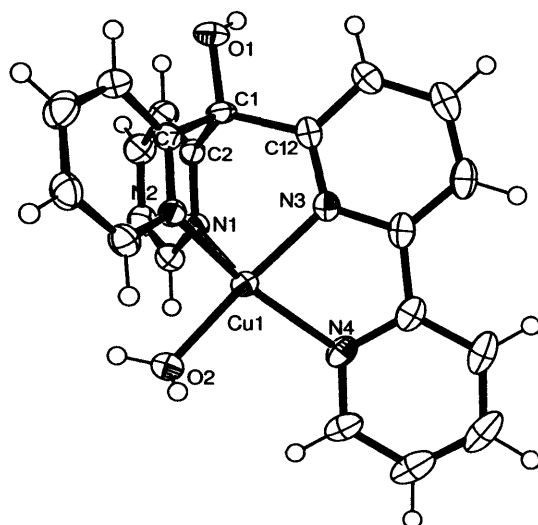


**Figure 24:** Perspective view of the asymmetric unit of 3.5 showing the atom numbering. Displacement ellipsoids are shown at the 50% probability level. H atoms are represented by circles of arbitrary size.

The trigonal plane is defined by the atoms N1, N2 and N4. The most significant distortions involve the angles surrounding this plane: the most acute angle is N1-Cu1-N2 ( $86.58(11)^\circ$ ), while the most obtuse is N2-Cu1-N4 ( $146.88(11)^\circ$ ). In order to generate a regular trigonal bipyramid *i.e.* in which these angles correspond to the theoretical  $120^\circ$ , it would be necessary for the pyridine rings N1/C2-C6 and N2/C7-C11 to lie closer to ring N4/C17-C21. Such movement is prevented by the rigid framework of the ligand; specifically, the bonds C2-C1 and C7-C1, *i.e.* the immediate bonds connecting both pyridines to the methine bridge, would be required to lengthen in order to satisfy this criteria. Furthermore, the bond angles surrounding C1 which indicate  $sp^3$  hybridisation would be required to distort significantly away from the idealised angles which are maintained in the present conformation. The angle between the two axial donors N3 and O2 ( $175.85(11)^\circ$ ) is only modestly less obtuse than the theoretical  $180^\circ$ . An example of a similar five co-ordinate structure which interestingly has been described as containing a ‘square-based pyramidal distorted trigonal bipyramidal (SBPDTB)  $CuN_4O$  chromophore’ is the compound aqua-bis(1,10-phenanthroline)-copper(II) diperchlorate.<sup>45</sup> Here, the pyridyl N-Cu<sup>II</sup> bond lengths range from  $1.980(4) \text{ \AA}$  to  $2.032(4) \text{ \AA}$  which compares well with

those found in compound **3.5**. Interestingly, the aqua O-Cu<sup>II</sup> bond lengths are 2.245(4) Å which are significantly longer than that found in **3.5** (1.948(2) Å).

There are two hydrogen bonds supporting the lattice framework which are described in Table 10. The co-ordinating water molecule (O2) is involved in H-bonding with both a molecule of solvent MeOH and an oxygen acceptor (O5) located on a symmetry generated perchlorate counterion. The oxygen acting as a H-bond acceptor on the solvent MeOH (O11) also acts as a H-bond donor to an oxygen atom located on the second perchlorate counterion. There is no evidence of any  $\pi$ - $\pi$  stacking interactions within the molecular packing. The presence of further peaks of electron density within the asymmetric unit indicated the presence of disordered solvent, consequently the structure was squeezed and a new set of reflection data was generated. The remaining solvent accessible void was 89.0 Å<sup>3</sup> which most likely corresponds to an additional MeOH.

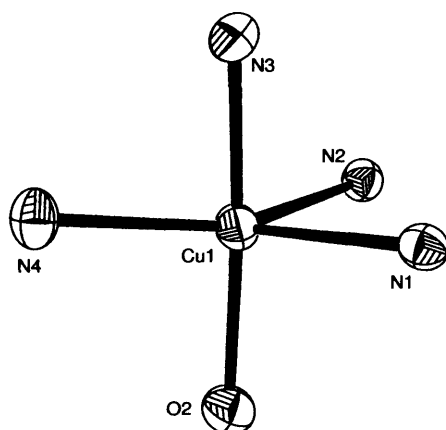


**Figure 25:** A view of the core geometry of **3.5** showing the atom numbering. Displacement ellipsoids are shown at the 50% probability level.

Chapter 3: The Co-ordination and Electrochemical Behaviour of Two Analogous Tetra- and Pentadentate Tripodal Ligand Frameworks

**Table 9:** Significant Bond lengths (Å) and Angles (°) for [Cu<sup>II</sup>(L<sup>4</sup>)(H<sub>2</sub>O)][ClO<sub>4</sub>]<sub>2</sub>·(CH<sub>3</sub>OH)

Cu(1)-N(1)	2.158(3)		O(2)-Cu(1)-N(3)	175.85(11)
Cu(1)-N(2)	2.063(3)		O(2)-Cu(1)-N(4)	94.95(11)
Cu(1)-N(3)	1.951(3)		N(3)-Cu(1)-N(4)	81.32(12)
Cu(1)-N(4)	2.017(3)		N(3)-Cu(1)-N(2)	88.75(11)
Cu(1)-O(2)	1.948(2)		N(4)-Cu(1)-N(2)	146.88(11)
			N(3)-Cu(1)-N(1)	86.17(11)
O(2)-Cu(1)-N(1)	94.45(10)		N(4)-Cu(1)-N(1)	123.80(11)
O(2)-Cu(1)-N(2)	95.38(11)		N(2)-Cu(1)-N(1)	86.58(11)

**Table 10:** H-bonding geometry (Å, °) for 3.5

D-H...A	d(D-H)	d(H...A)	d(D...A)	<(DHA)
O(2)-H(2A)...O(11)	0.86	1.828	2.683(3)	176
O(11)-H(11A)...O(10)#1	0.84	2.165	2.919(3)	149
O(2)-H(2B)...O(5)#2	0.86	1.991	2.794(3)	155

Symmetry transformations used to generate equivalent atoms:

#1 = 1-x, 1-y, 1-z. #2 = 1-x, 1-y, 2-z.

### 3.4.7.3 Crystal Structure of [Cd<sup>II</sup>(L<sup>4</sup>)(ClO<sub>4</sub>)(CH<sub>3</sub>CN)][ClO<sub>4</sub>] (3.7)

The Cd<sup>II</sup> complex of L<sup>4</sup> crystallises in the orthorhombic space group Pcab with one complex within the asymmetric unit (Fig. 26). The Cd<sup>II</sup> ion lies at the centre of a significantly distorted octahedral geometry ( $S(OC) = 3.95095$ ,  $S(TP) = 7.14619$ ) and is co-ordinated in an identical manner to the analogous Mn<sup>II</sup> compound, *i.e.* by four pyridyl N-donors (N1-N4), one solvent acetonitrile (N5) and one perchlorate counterion (O2). As the cadmium ion possesses no stereochemical preference, it can be reasonably assumed that in contrast to both L<sup>3</sup> and L<sup>5</sup>, ligand L<sup>4</sup> does not naturally adopt a trigonal prismatic conformation.

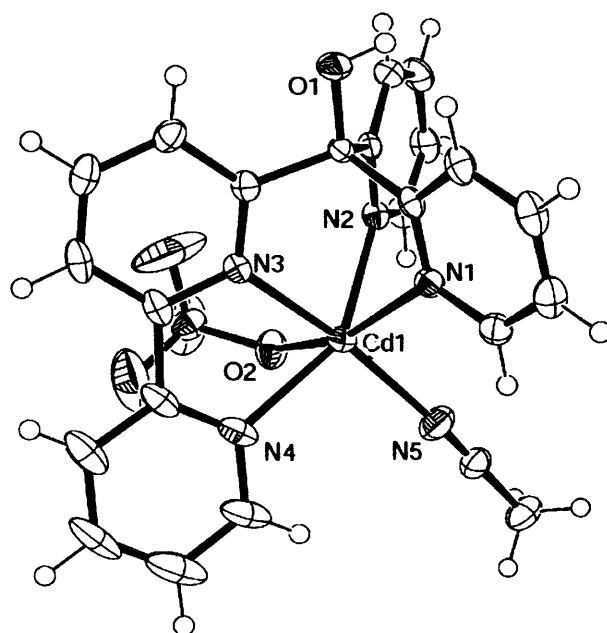


**Figure 26:** Perspective view of the asymmetric unit of **3.7** showing the atom numbering. Displacement ellipsoids are shown at the 50% probability level. H atoms are represented by circles of arbitrary size.

The three mutually trans sets of donor atoms all form significantly less obtuse bond angles than the expected  $180^\circ$ ; N1-Cd1-O2 ( $159.57(10)^\circ$ ), N2-Cd1-N4 ( $149.32(11)^\circ$ ), and N3-Cd1-N5 ( $169.20(12)^\circ$ ). The narrow bite angle of the bipy unit (N3-Cd1-N4 =  $72.36(11)^\circ$ ) is also another source of distortion from the regular octahedron. The co-ordinative bond angles between pyridyl N-donors on the three pyridine rings lying closest to the methine bridge are  $77.01(10)^\circ$ ,  $78.29(10)^\circ$  and  $84.71(10)^\circ$ , corresponding to the angles N1-Cd1-N2, N1-Cd1-N3 and N2-Cd1-N3 respectively. These angles are all clearly more acute than the equivalent angles in the analogous nickel and copper complexes of  $L^4$  (mean angles  $86.59(11)^\circ$  and  $87.17(11)^\circ$  respectively). The larger radius of the second row cation causes it to lie further out from the plane ( $1.54109(18)$  Å) as defined by N1, N2 and N3 (Fig. 27). The Ni and Cu cations have very similar radii and lie at an almost identical distance from this plane ( $1.2450(5)$  Å and  $1.2407(4)$  Å respectively).

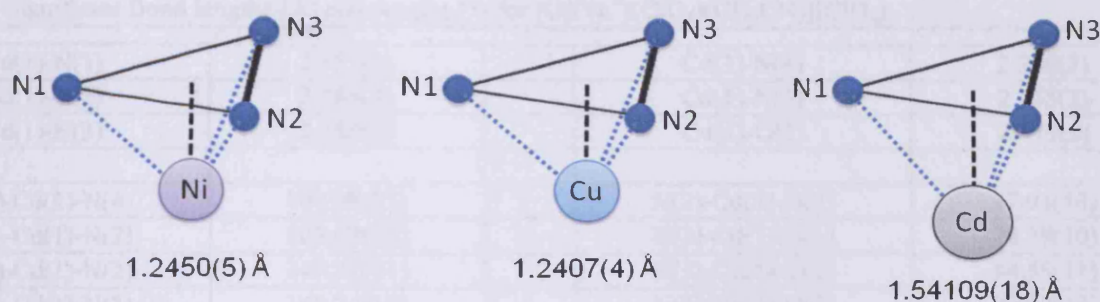


**Figure 27:** The co-ordinative bond angles (*i.e.*  $N \cdots M^{2+} \cdots N$ ) between the N-donors lying closest to the methine bridge are more acute for the cadmium complex (mean angle =  $80.00(10)^\circ$ ) than the nickel and copper complexes (mean angles  $86.59(11)^\circ$  and  $87.17(11)^\circ$  respectively).

The mean average angle between the three donor atoms lying furthest from the methine bridge is  $88.97(12)^\circ$ , leading to a slightly truncated geometry surrounding the  $Cd^{II}$  centre. An example of a similar six co-ordinate octahedral structure is the compound bis(perchlorate-O)-tetrapyridine-cadmium(II).<sup>46</sup> Here, the pyridyl N- $Cd^{II}$  bond lengths range from  $2.289(5) \text{ \AA}$  to  $2.347(4) \text{ \AA}$ , and the perchlorate O- $Cd^{II}$  bond length is  $2.381(6) \text{ \AA}$ . These values compare well with those in compound 3.7.

A single classical hydrogen bond is present between O1 and a non-coordinating perchlorate counterion located in the lattice (Table 12).

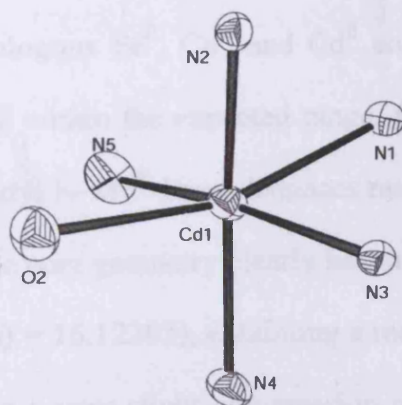


**Figure 28:** A view of the core geometry of 3.7 showing the atom numbering. Displacement ellipsoids are shown at the 50% probability level.

Chapter 3: The Co-ordination and Electrochemical Behaviour of Two Analogous  
Tetra- and Pentadentate Tripodal Ligand Frameworks

**Table 11:** Significant Bond lengths (Å) and Angles (°) for [Cd<sup>II</sup>(L<sup>4</sup>)(ClO<sub>4</sub>)(CH<sub>3</sub>CN)][ClO<sub>4</sub>]

Cd(1)-N(1)	2.351(3)		Cd(1)-N(4)	2.260(3)
Cd(1)-N(2)	2.285(3)		Cd(1)-N(5)	2.255(3)
Cd(1)-N(3)	2.285(3)		Cd(1)-O(2)	2.479(2)
N(5)-Cd(1)-N(4)	100.00(13)		N(2)-Cd(1)-N(1)	77.01(10)
N(5)-Cd(1)-N(2)	105.02(12)		N(3)-Cd(1)-N(1)	78.29(10)
N(4)-Cd(1)-N(2)	149.32(11)		N(5)-Cd(1)-O(2)	84.55(11)
N(5)-Cd(1)-N(3)	169.20(12)		N(4)-Cd(1)-O(2)	82.37(10)
N(4)-Cd(1)-N(3)	72.36(11)		N(2)-Cd(1)-O(2)	82.63(9)
N(2)-Cd(1)-N(3)	84.71(10)		N(3)-Cd(1)-O(2)	101.63(9)
N(5)-Cd(1)-N(1)	99.05(11)		N(1)-Cd(1)-O(2)	159.57(10)
N(4)-Cd(1)-N(1)	116.41(10)			

**Table 12:** H-bonding geometry (Å, °) for 3.7

D-H...A	d(D-H)	d(H...A)	d(D...A)	<(DHA)
O(2)-H(2A)...O(11)#1	0.84	2.04	2.843(4)	160

Symmetry transformations used to generate equivalent atoms:

#1 = 1/2-x, -1/2+y, 1-z.

#### 3.4.7.4 Crystal Structure of [Mn<sup>II</sup>(L<sup>5</sup>)(CH<sub>3</sub>CN)][ClO<sub>4</sub>]<sub>2</sub>·2(CH<sub>3</sub>CN) (3.8)

The Mn<sup>II</sup> complex of L<sup>5</sup> crystallises in the monoclinic space group P2<sub>1</sub>/n with one complex within the asymmetric unit (Fig. 29). The manganese is co-ordinated by all five pyridyl N-donors (N1-N5) and a further N donor atom (N6) located on a solvent molecule of acetonitrile. This donor set is identical to the analogous Fe<sup>II</sup>, Co<sup>II</sup> and Cd<sup>II</sup> complexes of L<sup>5</sup>. The co-ordinative bond lengths (Table 13) are well within the expected range, for example the similar compound [Mn<sup>II</sup>(bpy)<sub>3</sub>][ClO<sub>4</sub>]<sub>2</sub> reveals pyridyl N-Mn<sup>II</sup> bond distances ranging from 2.214(4) Å to 2.294(4) Å.<sup>47</sup> However, in this instance the core geometry clearly has more trigonal prismatic content than octahedral (*S*(TP) = 0.752, *S*(Oh) = 16.12203), exhibiting a mean Bailar twist angle of 2.0°. The mean *s/h* ratio is 1.08 indicating a very slight compression relative to an ideal trigonal prism, which is clearly due to the narrow bite angle of the two bipyridyl groups. The mean N...N distances between the three donor atoms closest to the methine bridge are significantly shorter

(2.915(3) Å) than those between the three distal N donors (3.170(3) Å), resulting in a truncated geometry around the metal centre.

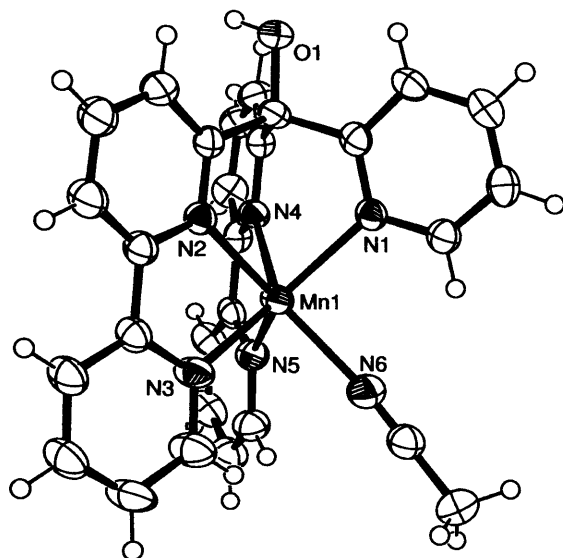


**Figure 29:** Perspective view of the asymmetric unit of **3.8** showing the atom numbering. Displacement ellipsoids are shown at the 50% probability level. H atoms are represented by circles of arbitrary size.

This generates a core geometry with pseudo- $C_{3v}$  symmetry, in contrast to the  $D_{3h}$  symmetry observed in regular trigonal prisms. This truncation most likely results from the methine bridge to which the three closest pyridine rings are directly attached which prevents these groups from adopting more distant positions. The extent of this effect is clearly reduced for the more distal donor groups which have no such restriction. The  $Mn^{II}$  cation does not have any stereochemical preference in its high-spin configuration, thus,  $L^5$  can be said to possess a natural trigonal prismatic conformation. In a similar manner to  $L^3$ , this most likely results from the  $sp^3$  hybridisation of the methine bridge to which the two rigid bipy units and pyridine are directly attached.

There is one classical hydrogen bond within the lattice framework between the oxygen atom O1 and another oxygen (O8) located on a symmetry generated perchlorate counterion (symmetry operator: 1-x, 1-y, -z). There are two disordered solvent molecules of acetonitrile



### Chapter 3: The Co-ordination and Electrochemical Behaviour of Two Analogous Tetra- and Pentadentate Tripodal Ligand Frameworks

within the molecular packing which have both been refined at half occupancy and without protons.

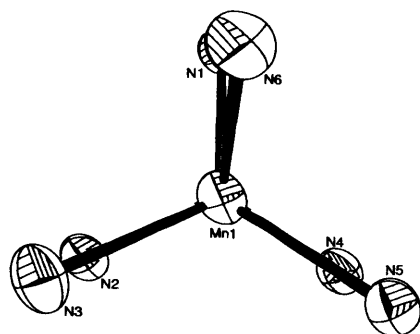


**Figure 30:** A view of the core geometry of **3.8** showing the atom numbering. Displacement ellipsoids are shown at the 50% probability level.

**Table 13:** Significant Bond lengths (Å) and Angles (°) for  $[\text{Mn}^{\text{II}}(\text{L}^5)(\text{CH}_3\text{CN})][\text{ClO}_4]_2 \cdot 2(\text{CH}_3\text{CN})$

Mn(1)-N(1)	2.293(3)		Mn(1)-N(4)	2.240(3)
Mn(1)-N(2)	2.240(3)		Mn(1)-N(5)	2.260(3)
Mn(1)-N(3)	2.262(3)		Mn(1)-N(6)	2.247(4)
N(2)-Mn(1)-N(4)	79.78(11)		N(6)-Mn(1)-N(3)	85.17(13)
N(2)-Mn(1)-N(6)	138.73(12)		N(5)-Mn(1)-N(3)	96.94(12)
N(4)-Mn(1)-N(6)	137.27(12)		N(2)-Mn(1)-N(1)	80.01(11)
N(2)-Mn(1)-N(5)	130.22(11)		N(4)-Mn(1)-N(1)	81.45(11)
N(4)-Mn(1)-N(5)	72.56(11)		N(6)-Mn(1)-N(1)	87.72(12)
N(6)-Mn(1)-N(5)	86.02(12)		N(5)-Mn(1)-N(1)	133.18(11)
N(2)-Mn(1)-N(3)	72.90(11)		N(3)-Mn(1)-N(1)	128.65(11)
N(4)-Mn(1)-N(3)	132.85(12)			

**Table 14:** H-bonding geometry (Å, °) for **3.8**

D-H...A	d(D-H)	d(H...A)	d(D...A)	<(DHA)
O(1)-H(1)...O(8)#1	0.82	2.01	2.807(5)	165

Symmetry transformations used to generate equivalent atoms:

#1 = 1-x, 1-y, -z.

#### 3.4.7.5 Crystal Structure of $[\text{Fe}^{\text{II}}(\text{L}^5)(\text{CH}_3\text{CN})][\text{ClO}_4]_2 \cdot (\text{C}_4\text{H}_{10}\text{O})$ (**3.9**)

The  $\text{Fe}^{\text{II}}$  complex of  $\text{L}^5$  crystallises in the triclinic space group P-1 with one complex within the asymmetric unit (Fig. 31). The donor set surrounding the  $\text{Fe}^{\text{II}}$  cation is identical to the analogous

### Chapter 3: The Co-ordination and Electrochemical Behaviour of Two Analogous Tetra- and Pentadentate Tripodal Ligand Frameworks

$\text{Mn}^{\text{II}}$  complex, however, the co-ordination geometry in this instance is predominantly octahedral ( $S(\text{Oh}) = 1.35202$ ,  $S(\text{TP}) = 10.29726$ ). This indicates that the strong stereochemical preference of the  $d^6$  ion (assuming low-spin) forces  $L^5$  to adopt an octahedral conformation. The Bailar twist angle in this instance is  $45.8^\circ$  which is the largest for this series of compounds. The co-ordinative bond lengths (Table 15) are virtually identical to those found in the similar compound  $[\text{Fe}^{\text{II}}(\text{bipy})_3][\text{ClO}_4]_2$  which range from  $1.953(3) \text{ \AA}$  to  $1.972(3) \text{ \AA}$ .<sup>48</sup> The bipyridine groups are considerably bent in order to satisfy the stereochemical requirements of the metal; the dihedral angle between  $\text{N2/C7-C11}$  and  $\text{N3/C12-C16}$  is  $28.2(3)^\circ$  and the dihedral angle between  $\text{N4/C17-C21}$  and  $\text{N5/C22-C26}$  is  $13.8(2)^\circ$ . The bond angles between the three sets of mutually trans donor atoms,  $\text{N1-Fe1-N3}$ ,  $\text{N2-Fe1-N5}$  and  $\text{N4-Fe1-N6}$  are  $168.95(14)^\circ$ ,  $163.44(15)^\circ$  and  $172.90(15)^\circ$  respectively, which all deviate significantly from the ideal  $180^\circ$ . Again, the sterical restrictions imposed by the methine bridge upon the immediately adjacent pyridines lead to truncation, *i.e.* the mean  $\text{N}\cdots\text{N}$  distance between the proximal  $\text{N1}$ ,  $\text{N2}$  and  $\text{N4}$  set of atoms ( $2.696(4) \text{ \AA}$ ) is significantly shorter than between the more distal  $\text{N3}$ ,  $\text{N5}$  and  $\text{N6}$  set of atoms ( $2.791(4) \text{ \AA}$ ).

There is one classical H-bond supporting the molecular packing between  $\text{O1}$  and another oxygen atom ( $\text{O4}$ ) located on a perchlorate counterion (Table 16). There is no evidence of any intermolecular  $\pi$ - $\pi$  stacking interactions. There are two perchlorate anions present in the asymmetric unit which balance the cationic character of the complex.

Chapter 3: The Co-ordination and Electrochemical Behaviour of Two Analogous Tetra- and Pentadentate Tripodal Ligand Frameworks

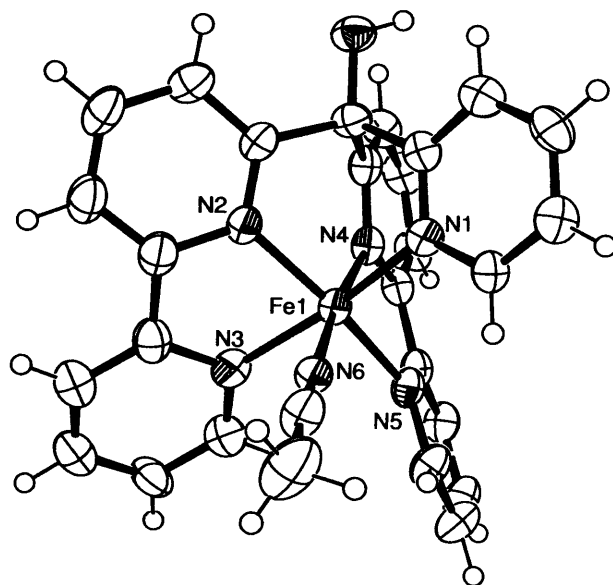


**Figure 31:** Perspective view of the asymmetric unit of **3.9** showing the atom numbering. Displacement ellipsoids are shown at the 50% probability level. H atoms are represented by circles of arbitrary size.

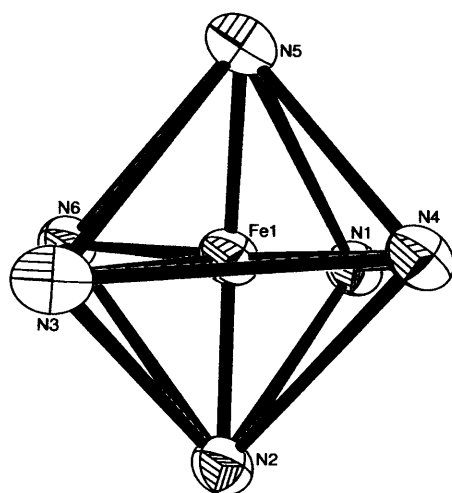


**Figure 32:** A view of the core geometry of **3.9** showing the atom numbering. Displacement ellipsoids are shown at the 50% probability level.

Chapter 3: The Co-ordination and Electrochemical Behaviour of Two Analogous Tetra- and Pentadentate Tripodal Ligand Frameworks

**Table 15:** Significant Bond lengths (Å) and Angles (°) for  $[\text{Fe}^{\text{II}}(\text{L}^5)(\text{CH}_3\text{CN})][\text{ClO}_4]_2 \cdot (\text{C}_4\text{H}_{10}\text{O})$

Fe(1)-N(1)	1.973(4)		Fe(1)-N(4)	1.907(3)
Fe(1)-N(2)	1.928(4)		Fe(1)-N(5)	1.976(4)
Fe(1)-N(3)	2.014(4)		Fe(1)-N(6)	1.954(4)
N(4)-Fe(1)-N(2)	89.24(15)		N(6)-Fe(1)-N(5)	96.29(15)
N(4)-Fe(1)-N(6)	172.90(15)		N(1)-Fe(1)-N(5)	100.85(15)
N(2)-Fe(1)-N(6)	95.07(14)		N(4)-Fe(1)-N(3)	102.47(15)
N(4)-Fe(1)-N(1)	84.41(15)		N(2)-Fe(1)-N(3)	80.38(16)
N(2)-Fe(1)-N(1)	91.18(16)		N(6)-Fe(1)-N(3)	83.85(15)
N(6)-Fe(1)-N(1)	89.85(15)		N(1)-Fe(1)-N(3)	168.95(14)
N(4)-Fe(1)-N(5)	80.74(15)		N(5)-Fe(1)-N(3)	88.89(15)
N(2)-Fe(1)-N(5)	163.44(15)			

**Table 16:** H-bonding geometry (Å, °) for **3.9**

D-H...A	d(D-H)	d(H...A)	d(D...A)	<(DHA)
O(1)-H(1)...O(4)	0.84	1.95	2.760(5)	163

### 3.4.7.6 Crystal Structure of $[\text{Co}^{\text{II}}(\text{L}^5)(\text{CH}_3\text{CN})][\text{ClO}_4]_2 \cdot 0.5(\text{H}_2\text{O})$ (**3.10**)

The  $\text{Co}^{\text{II}}$  complex of  $\text{L}^5$  crystallises in the monoclinic space group  $\text{P2}_1/\text{C}$  with two symmetrically unrelated complexes within the asymmetric unit (Fig. 33). The donor atom sets surrounding the metal centres are consistent with both the  $\text{Mn}^{\text{II}}$ ,  $\text{Fe}^{\text{II}}$  and  $\text{Cd}^{\text{II}}$  analogues and in both instances the geometry surrounding the metal centre has slightly more trigonal prismatic character than octahedral ( $S(\text{TP})$  for complexes 1 and 2 = 4.35867 and 3.95879,  $S(\text{Oct})$  for complexes 1 and 2 = 5.75956 and 5.95792). This indicates a higher degree of TP character in **3.10** than in the analogous  $\text{Fe}^{\text{II}}$  and  $\text{Ni}^{\text{II}}$  complexes of  $\text{L}^5$ , which is most likely a consequence of the smaller octahedral preference of the  $\text{Co}^{\text{II}}$  ion. The mean Bailar twist angles of complexes 1 and 2 are  $26.60^\circ$  and  $27.70^\circ$ , furthermore the mean  $s/h$  ratio in both instances is 1.12 indicating significant compression. These values serve to highlight the extent of the departure from an ideal trigonal prism. The co-ordinative bond lengths are similar to those within the complex  $[\text{Co}^{\text{II}}(\text{bpy})_3][\text{ClO}_4]_2$ , which range from 2.119(2) to 2.136(2) Å.<sup>49</sup> The mean  $\text{N}\cdots\text{N}$  distance

### Chapter 3: The Co-ordination and Electrochemical Behaviour of Two Analogous Tetra- and Pentadentate Tripodal Ligand Frameworks

between the three donor atoms closest to the methine bridge (2.820(4) Å) is significantly shorter than the mean distance between the three distal N donors (3.016(4) Å), resulting in a truncated geometry with pseudo- $C_{3v}$  symmetry.

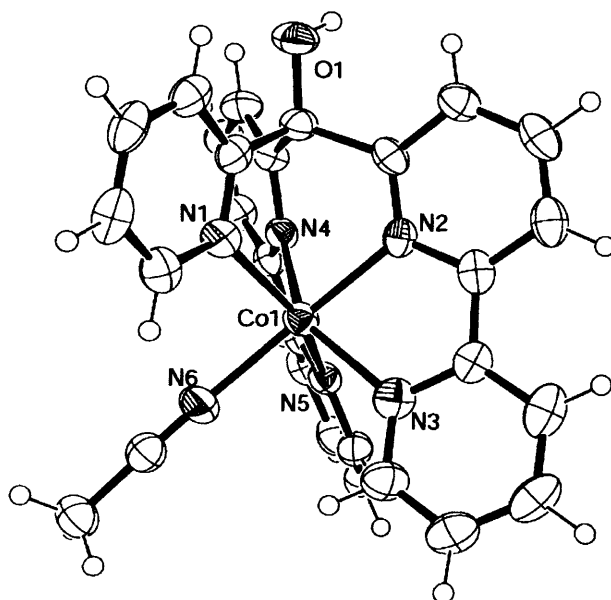


**Figure 33:** Perspective view of the asymmetric unit of **3.10** showing the atom numbering. Displacement ellipsoids are shown at the 50% probability level. H atoms are represented by circles of arbitrary size.

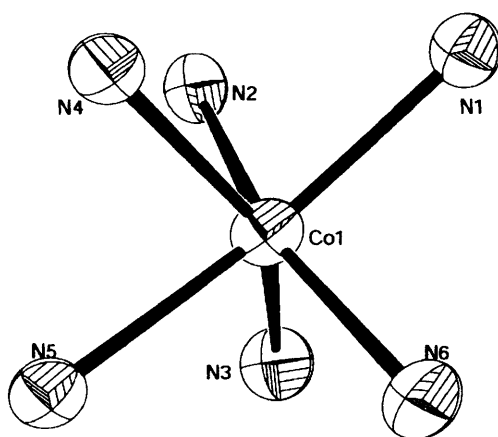


**Figure 34:** A view of the core geometry of **3.10** showing the atom numbering. Displacement ellipsoids are shown at the 50% probability level.

Chapter 3: The Co-ordination and Electrochemical Behaviour of Two Analogous  
Tetra- and Pentadentate Tripodal Ligand Frameworks

**Table 17:** Significant Bond lengths (Å) and Angles (°) for  $[\text{Co}^{\text{II}}(\text{L}^5)(\text{CH}_3\text{CN})][\text{ClO}_4]_2 \cdot 0.5(\text{H}_2\text{O})$

N(1)-Co(1)	2.170(3)		N(7)-Co(2)	2.131(3)
N(2)-Co(1)	2.097(4)		N(8)-Co(2)	2.105(4)
N(3)-Co(1)	2.136(4)		N(9)-Co(2)	2.229(4)
N(4)-Co(1)	2.096(4)		N(10)-Co(2)	2.114(3)
N(5)-Co(1)	2.215(3)		N(11)-Co(2)	2.112(3)
N(6)-Co(1)	2.097(4)		N(12)-Co(2)	2.118(4)
N(4)-Co(1)-N(2)	82.81(14)		N(8)-Co(2)-N(11)	146.72(14)
N(4)-Co(1)-N(6)	111.31(15)		N(8)-Co(2)-N(10)	84.00(14)
N(2)-Co(1)-N(6)	162.26(14)		N(11)-Co(2)-N(10)	76.30(14)
N(4)-Co(1)-N(3)	146.32(14)		N(8)-Co(2)-N(12)	108.39(14)
N(2)-Co(1)-N(3)	76.17(15)		N(11)-Co(2)-N(12)	97.27(14)
N(6)-Co(1)-N(3)	95.25(16)		N(10)-Co(2)-N(12)	162.88(15)
N(4)-Co(1)-N(1)	86.31(14)		N(8)-Co(2)-N(7)	87.45(14)
N(2)-Co(1)-N(1)	81.71(13)		N(11)-Co(2)-N(7)	114.33(14)
N(6)-Co(1)-N(1)	88.36(14)		N(10)-Co(2)-N(7)	79.36(13)
N(3)-Co(1)-N(1)	115.76(14)		N(12)-Co(2)-N(7)	89.22(13)
N(4)-Co(1)-N(5)	73.78(14)		N(8)-Co(2)-N(9)	73.95(13)
N(2)-Co(1)-N(5)	114.18(13)		N(11)-Co(2)-N(9)	90.83(14)
N(6)-Co(1)-N(5)	81.04(14)		N(10)-Co(2)-N(9)	116.05(13)
N(3)-Co(1)-N(5)	91.10(14)		N(12)-Co(2)-N(9)	79.48(13)
N(1)-Co(1)-N(5)	152.00(14)		N(7)-Co(2)-N(9)	153.65(13)

**Table 18:** H-bonding geometry (Å, °) for **3.10**

D-H...A	d(D-H)	d(H...A)	d(D...A)	<(DHA)
O(1)-H(1)...O(19)	0.84	1.88	2.720(5)	177
O(2)-H(2)...O(15)	0.84	2.03	2.856(5)	168

### 3.4.7.7 Crystal Structure of $[\text{Ni}^{\text{II}}(\text{L}^5)(\text{Br})][\text{ClO}_4]$ (3.11)

The  $\text{Ni}^{\text{II}}$  complex of  $\text{L}^5$  crystallises in the monoclinic space group  $\text{P}2_1/\text{n}$  and contains one complex within the asymmetric unit (Fig. 35). The donor set surrounding the metal centre is different compared to the analogous  $\text{Mn}^{\text{II}}$ ,  $\text{Fe}^{\text{II}}$  and  $\text{Co}^{\text{II}}$  complexes of  $\text{L}^5$ , in this instance the inner co-ordination sphere contains a bromine ion which could have arisen as a trace impurity from any of the synthetic steps involving bromine substitution. The remaining donor set is composed of five pyridyl N-donors. The co-ordination geometry surrounding the  $\text{Ni}^{\text{II}}$  ion is best

### Chapter 3: The Co-ordination and Electrochemical Behaviour of Two Analogous Tetra- and Pentadentate Tripodal Ligand Frameworks

described as a significantly distorted octahedron ( $S(\text{Oh}) = 3.74706$ ,  $S(\text{TP}) = 8.12666$ ). This compound exhibits pyridyl  $\text{N-Ni}^{\text{II}}$  bond distances ranging between 2.017(4) and 2.220(5) Å and has a  $\text{Ni1-Br1}$  bond length of 2.5457(9) Å. The three mutually trans pairs of donor atoms have bond angles of  $160.49(18)^\circ$ ,  $156.41(19)^\circ$  and  $166.78(15)^\circ$  indicating significant deviations away from an ideal octahedron. A search of the Cambridge Structural Database (CSD)<sup>50</sup> using Conquest<sup>51</sup> results in just four hits for such structures containing a nickel(II) centre co-ordinated by five N-donors and a bromine atom (Date: 12/2008). The co-ordinative bond lengths of **3.11** are in good agreement with the compound bis(bromo-bis(*n*-propylamine-*N*)-(1,3,5-tri-*n*-propyl-1,3,5-triazacyclohexane-*N,N',N''*)-nickel(II)), which exhibits  $\text{Ni}^{\text{II}}\text{-N}$  bond lengths ranging from 2.059(7) Å to 2.212(8) Å and a  $\text{Ni}^{\text{II}}\text{-Br}$  distance of 2.5036(14) Å.<sup>52</sup>

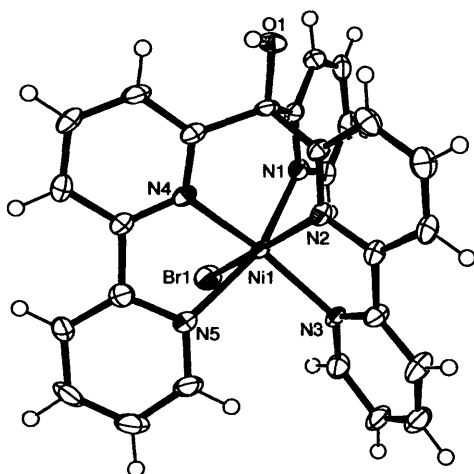


**Figure 34:** Perspective view of the asymmetric unit of **3.11** showing the atom numbering. Displacement ellipsoids are shown at the 50% probability level. H atoms are represented by circles of arbitrary size.

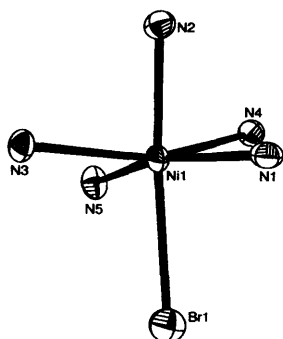


**Figure 35:** A view of the core geometry of **3.11** showing the atom numbering. Displacement ellipsoids are shown at the 50% probability level.

Chapter 3: The Co-ordination and Electrochemical Behaviour of Two Analogous Tetra- and Pentadentate Tripodal Ligand Frameworks

**Table 19:** Significant Bond lengths (Å) and Angles (°) for  $[\text{Ni}^{\text{II}}(\text{L}^5)(\text{Br})(\text{CH}_3\text{CN})][\text{ClO}_4]$

N(1)-Ni(1)	2.111(5)		N(4)-Ni(1)	2.017(4)
N(2)-Ni(1)	2.041(5)		N(5)-Ni(1)	2.220(5)
N(3)-Ni(1)	2.082(4)		Ni(1)-Br(1)	2.5457(9)
N(4)-Ni(1)-N(2)	87.09(19)		N(3)-Ni(1)-N(5)	91.64(19)
N(4)-Ni(1)-N(3)	156.41(19)		N(1)-Ni(1)-N(5)	160.49(18)
N(2)-Ni(1)-N(3)	79.11(18)		N(4)-Ni(1)-Br(1)	98.64(13)
N(4)-Ni(1)-N(1)	89.27(19)		N(2)-Ni(1)-Br(1)	166.78(15)
N(2)-Ni(1)-N(1)	79.14(18)		N(3)-Ni(1)-Br(1)	99.02(13)
N(3)-Ni(1)-N(1)	106.55(19)		N(1)-Ni(1)-Br(1)	88.97(12)
N(4)-Ni(1)-N(5)	75.80(19)		N(5)-Ni(1)-Br(1)	81.09(14)
N(2)-Ni(1)-N(5)	112.0(2)			

**3.4.7.8 Crystal Structure of  $[\text{Cd}^{\text{II}}(\text{L}^5)(\text{CH}_3\text{CN})][\text{ClO}_4]_2 \cdot (\text{CH}_3\text{CN})$  (3.14)**

The  $\text{Cd}^{\text{II}}$  complex of  $\text{L}^5$  crystallises in the monoclinic space group  $\text{P}2_1/\text{n}$  and contains one complex within the asymmetric unit (Fig. 37). The  $\text{Cd}^{\text{II}}$  ion is co-ordinated in an identical fashion to the analogous  $\text{Mn}^{\text{II}}$ ,  $\text{Fe}^{\text{II}}$  and  $\text{Co}^{\text{II}}$  complexes, *i.e.* by all five pyridyl N-donors (N1-N5) and an N donor (N6) located on a solvent acetonitrile molecule.

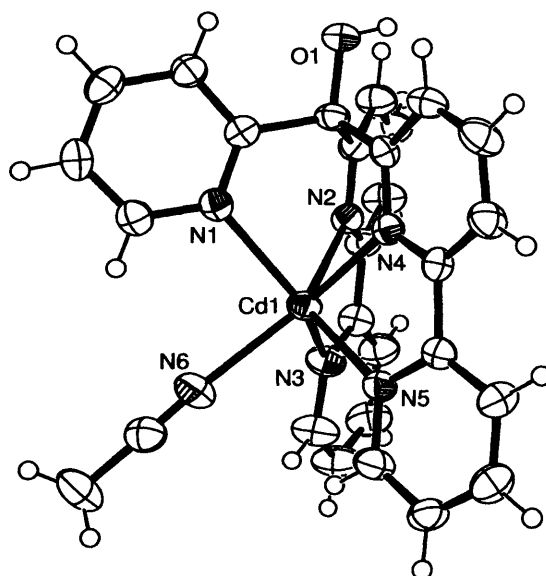


**Figure 37:** Perspective view of the asymmetric unit of 3.14 showing the atom numbering. Displacement ellipsoids are shown at the 50% probability level. H atoms are represented by circles of arbitrary size.



### Chapter 3: The Co-ordination and Electrochemical Behaviour of Two Analogous Tetra- and Pentadentate Tripodal Ligand Frameworks

The co-ordination geometry surrounding the metal is clearly trigonal prismatic which is confirmed by the shape mapping results ( $S(\text{TP}) = 1.08542$  and  $S(\text{Oh}) = 16.39691$ ). This is also reflected by the small Bailar twist angle ( $1.883^\circ$ ). There are, however, some minor distortions from an ideal TP environment. For example, the mean  $s/h$  ratio is 1.09 which indicates a slight compression along one axis. Furthermore, the mean  $\text{N}\cdots\text{N}$  distance between the N-donors lying closest to the methine bridge is  $2.964(4)$  Å, whilst the mean distance between three furthest lying N-donors ( $3.337(4)$  Å) is significantly larger, indicating truncation of the trigonal prism leading to pseudo- $\text{C}_{3v}$  symmetry. The co-ordinative bond lengths (Table 20) span a very similar range compared to those of the similar compound  $[\text{Cd}^{\text{II}}(\text{bpy})_3][\text{ClO}_4]_2$  which range between  $2.308(5)$  Å and  $2.355(5)$  Å in an unconstrained octahedral environment.<sup>53</sup>

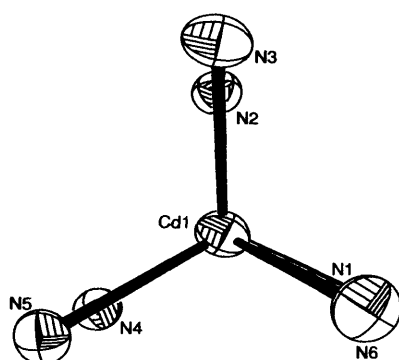


**Figure 38:** A view of the core geometry of **3.14** showing the atom numbering. Displacement ellipsoids are shown at the 50% probability level.

**Table 20:** Significant Bond lengths (Å) and Angles ( $^\circ$ ) for  $[\text{Cd}^{\text{II}}(\text{L}^5)(\text{CH}_3\text{CN})][\text{ClO}_4]_2 \cdot (\text{CH}_3\text{CN})$

N(1)-Cd(1)	2.346(3)		N(4)-Cd(1)	2.330(3)
N(2)-Cd(1)	2.327(3)		N(5)-Cd(1)	2.323(3)
N(3)-Cd(1)	2.314(4)		N(6)-Cd(1)	2.348(4)
N(3)-Cd(1)-N(5)	100.10(13)		N(2)-Cd(1)-N(1)	78.43(12)
N(3)-Cd(1)-N(2)	71.43(13)		N(4)-Cd(1)-N(1)	80.18(12)
N(5)-Cd(1)-N(2)	128.72(12)		N(3)-Cd(1)-N(6)	86.86(14)
N(3)-Cd(1)-N(4)	131.19(13)		N(5)-Cd(1)-N(6)	88.16(13)
N(5)-Cd(1)-N(4)	70.99(12)		N(2)-Cd(1)-N(6)	139.13(14)
N(2)-Cd(1)-N(4)	77.96(12)		N(4)-Cd(1)-N(6)	138.32(13)
N(3)-Cd(1)-N(1)	127.39(13)			
N(5)-Cd(1)-N(1)	132.16(12)			

## Chapter 3: The Co-ordination and Electrochemical Behaviour of Two Analogous Tetra- and Pentadentate Tripodal Ligand Frameworks

**Table 21:** H-bonding geometry (Å, °) for 3.14

D-H...A	d(D-H)	d(H...A)	d(D...A)	<(DHA)
O(1)-H(1)...O(4)#1	0.82	2.02	2.811(5)	161

Symmetry transformations used to generate equivalent atoms:

#1 = 1-x, 1-y,-z.

### 3.5 Conclusions

#### Structural Overview and Continuous Shape Mapping

Since ligands  $L^4$  and  $L^5$  have fewer bipyridyl arms than  $L^3$ , the steric strain involved in twisting the ligand to produce an octahedral geometry is decreased. Therefore, it was expected that these frameworks would have a reduced capacity for enforcing trigonal prismatic co-ordination modes, with  $L^4$  being the weakest in this respect. It was also anticipated, therefore, that the ligand field stabilisation energy would become the leading factor in establishing ligand conformation in complexes 3.1-3.14. Indeed, this is reflected in the crystallographic data; the cadmium complex of  $L^4$  has continuous shape measures of  $S(\text{TP}) = 7.14619$  and  $S(\text{Oct}) = 3.95095$ , confirming that in the presence of a metal with no stereoelectronic preference this framework adopts a predominantly octahedral co-ordination sphere. As might be expected, the  $\text{Ni}^{\text{II}}$  complex of  $L^4$  is clearly octahedral ( $S(\text{Oct}) = 1.44713$ ).

**Table 22:** Continuous Shape Mapping Results – Six Co-ordinate Structures

HP-6	$D_{6h}$	Hexagon
PPY-6	$C_{5v}$	Pentagonal pyramid
OC-6	$O_h$	Octahedron
TPR-6	$D_{3h}$	Trigonal prism
JPPY-6	$C_{5v}$	Johnson pentagonal pyramid J2

Chapter 3: The Co-ordination and Electrochemical Behaviour of Two Analogous Tetra- and Pentadentate Tripodal Ligand Frameworks

Structure	(HP-6)	(PPY-6)	(OC-6)	(TPR-6)	(JPPY-6)
L <sup>4</sup> _Ni (3.4)	27.69056	21.92348	1.44713	10.67394	25.48418
L <sup>4</sup> _Cd (3.7)	27.38178	18.76345	3.95095	7.14619	22.22338
L <sup>5</sup> _Mn (3.8)	31.20675	13.39159	16.12203	0.752	17.43315
L <sup>5</sup> _Fe (3.9)	30.74398	22.65617	1.35202	10.29726	26.05447
L <sup>5</sup> _Co (3.10)	32.01928	17.338	5.75956	4.35867	20.69159
L <sup>5</sup> _Co (3.10) <sup>a</sup>	33.10962	17.88985	5.95792	3.95879	21.42826
L <sup>5</sup> _Ni (3.11)	31.09594	19.32187	3.74706	8.12666	22.11117
L <sup>5</sup> _Cd (3.14)	31.0529	12.98358	16.39691	1.08542	16.80655

<sup>a</sup> Compounds 3.10 contains two crystallographically independent complexes present within the asymmetric unit.

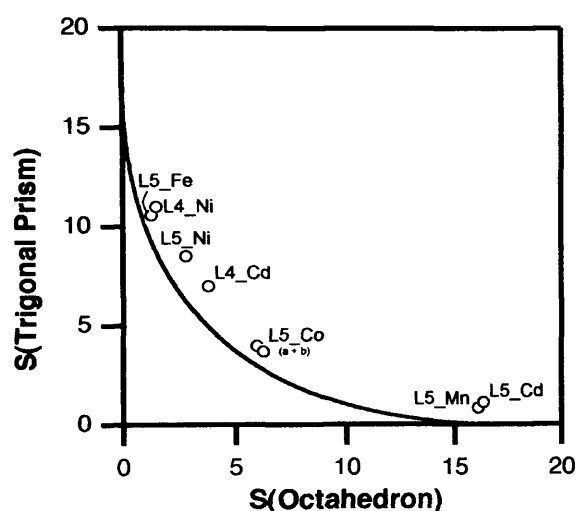


Figure 39: Octahedron – Trigonal Prism shape map showing the Bailar pathway (continuous line) and the experimental data for L<sup>4</sup> and L<sup>5</sup> (circles).

In contrast, ligand L<sup>5</sup> clearly maintains a preference for a trigonal prismatic conformation which is demonstrated in the crystal structures of the Mn<sup>II</sup> (d<sup>5</sup>) and Cd<sup>II</sup> (d<sup>10</sup>) complexes; the core geometries have *S*(TP) values of 0.752 and 1.08542, respectively. However, while L<sup>3</sup> maintains near-TP configurations in the presence of metal ions with strong octahedral preferences, L<sup>5</sup> distorts towards predominantly octahedral co-ordination spheres. The octahedral character in the complexes of L<sup>5</sup> increases in the order Co<sup>II</sup> < Ni<sup>II</sup> < Fe<sup>II</sup>. A representation of the calculated values in a shape map (Fig. 39; Table 22) illustrates that all structures are close to the Bailar path for the interconversion of the trigonal prism and the octahedron. It is likely that any minor deviations

Chapter 3: The Co-ordination and Electrochemical Behaviour of Two Analogous Tetra- and Pentadentate Tripodal Ligand Frameworks

from this path are due to the constrained geometry of the tetra- and pentadentate tripodal ligand frameworks.

**Table 23:** The mean average Bailar twist angles for complexes 3.4, 3.5, 3.7-3.11 and 3.14 amongst other pertinent data.

Compound	Bailar twist angle, $\phi$ , $^\circ$	$s/h$	Mean bond M...N length, $\text{\AA}$	Dihedral angle between trigonal faces, $^\circ$	Effective ionic radius of the metal ion (pm) <sup>b</sup>
L <sup>4</sup> _Ni (3.4)	33.23	1.13	2.081	5.58(16)	69
L <sup>4</sup> _Cd (3.7)	36.87	1.08	2.319	11.10(16)	95
L <sup>5</sup> _Mn (3.8)	2.00	1.08	2.714	11.00(17)	67
L <sup>5</sup> _Fe (3.9)	45.8	1.19	1.959	1.4(2)	61(ls), 78(hs)
L <sup>5</sup> _Co (3.10)	26.6	1.12	2.135	5.5(2)	65(ls), 74.5(hs)
L <sup>5</sup> _Co (3.10) <sup>a</sup>	27.7	1.12	2.135	3.85(19)	65(ls), 74.5(hs)
L <sup>5</sup> _Ni (3.11)	37.6	1.16	2.170	5.6(2)	69
L <sup>5</sup> _Cd (3.14)	1.87	1.09	2.331	12.99(19)	95

<sup>a</sup> Compounds 3.10 contains two crystallographically independent complexes present within the asymmetric unit. <sup>b</sup> Values taken from reference 54.

The copper compound of L<sup>4</sup>, 3.5, differs from the other compounds by adopting a five coordinate geometry which lies almost exactly halfway between trigonal bipyramidal and square pyramidal (Table 24;  $S(\text{TBPY}) = 3.3524$  and  $S(\text{SPY}) = 3.38261$ ). The shape map describing the interconversion between these two geometries is shown below (Fig. 40).

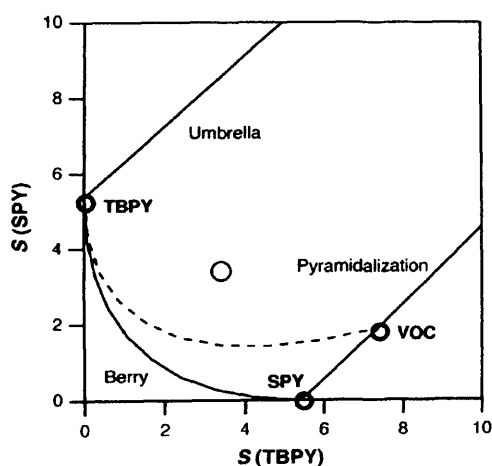


**Figure 40:** Shape map sourced directly from reference 55 which shows the interconversion pathway (Berry pseudorotation). The three bold circles represent the positions of the ideal geometries (TBPY: trigonal bipyramid, SPY: square pyramid, and VOC: vacant octahedron). The light circle indicates the position of 3.5.

## Chapter 3: The Co-ordination and Electrochemical Behaviour of Two Analogous Tetra- and Pentadentate Tripodal Ligand Frameworks

It is immediately apparent that there exists a significant departure from the conventional interconversion pathway, the Berry pseudo-rotation. A non-Berry pathway that converts these two polyhedra involves a *T* arrangement of the equatorial donors (Fig. 41) and is reportedly found in a number of Cu<sup>II</sup> species.<sup>55</sup>

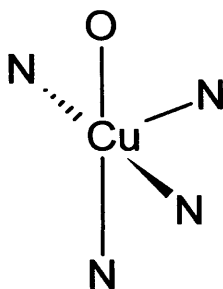


**Figure 41:** A non-Berry interconversion between a trigonal bipyramid and a square pyramid, involving a *T* arrangement of the equatorial donors.

**Table 24:** Continuous Shape Mapping Results – Five Co-ordinate Structures

PP-5	D <sub>5h</sub>	Pentagon
VOC-5	C <sub>4v</sub>	Vacant octahedron
TBPY-5	D <sub>3h</sub>	Trigonal bipyramid
SPY-5	C <sub>4v</sub>	Spherical square pyramid
JSPY-5	C <sub>4v</sub>	Johnson square pyramid J1
JTBP-5	D <sub>3h</sub>	Johnson trigonal bipyramid J12

Structure	(PP-5)	(VOC-5)	(TBPY-5)	(SPY-5)	(JSPY-5)	(JTBP-5)
L <sup>4</sup> _Cu (3.5)	27.49756,	3.91047	3.3524	3.38261	3.91047	6.64894

### 3.6 References

1. P. Tomasik, Z. Ratajewicz, *Heterocyclic Compounds*, 1985, 14, 6, 189, Wiley, New York, Eds. G. R. Newkome, L. Strekowski.
2. E. C. Constable, *Adv. Inorg. Chem.*, 1989, 34, 1-63.

Chapter 3: The Co-ordination and Electrochemical Behaviour of Two Analogous Tetra- and Pentadentate Tripodal Ligand Frameworks

3. V. Balzani, G. Bergamini, F. Marchioni, P. Ceroni, *Coord. Chem. Rev.*, 2006, 250, 1254-1266.
4. A. A. Vlcek, *Coord. Chem. Rev.*, 1982, 43, 39-62.
5. V. Balzani, A. Juris, M. Venturi, S. Campagna, S. Serroni, *Chem. Rev.*, 1996, 96, 759-833.
6. A. Juris, V. Balzani, F. Barigelletti, S. Campagna, P. Belser, A. von Zelewski, *Coord. Chem. Rev.*, 1988, 84, 85-277.
7. P. E. Rillema, G. Allen, T. J. Meyer, D. Conrad, *Inorg. Chem.*, 1983, 22, 1617-1622.
8. Based on the conversion of the reduction potential (*vs* SCE): W. P. Griffith, *The Chemistry of the Rarer Platinum Earth Metals, (Os, Ru, Ir, Rh)*, Interscience, New York, 1967, 215.
9. Y. Ohsawa, M.-H. Whangbo, K. W. Hanck, M. K. De Armond, *Inorg. Chem.*, 1984, 23, 3426-3428.
10. Y. Ohsawa, M. K. De Armond, K. W. Hanck, D. E. Morris, *J. Am. Chem. Soc.*, 1983, 105, 6522-6524.
11. B. Dietrich, J.-M. Lehn, J.-P. Sauvage, *Tetrahedron Lett.*, 1969, 2895.
12. B. Dietrich, J.-M. Lehn, J.-P. Sauvage, J. Blanzat, *Tetrahedron Lett.*, 1973, 1629.
13. L. Echegoyen, Q. Xie, E. Pérez-Cordero, *Pure and Appl. Chem.*, 1993, 65, 441-446.
14. J.-M. Lehn, A. Rigault, *Angew. Chem.*, 1988, 100, 1121-1122.
15. J.-M. Lehn, A. Rigault, *Angew. Chem. Int. Ed. Engl.*, 1988, 27, 1095-1097.
16. R. Krämer, J.-M. Lehn, A. Marquis-Rigault, *Proc. Natl. Acad. Sci. USA*, 1993, 90, 5394-5398.
17. E. C. Constable, M. J. Hannon, D. A. Tocher, *J. Chem. Soc. Dalton Trans.*, 1993, 1883-1890.

Chapter 3: The Co-ordination and Electrochemical Behaviour of Two Analogous  
Tetra- and Pentadentate Tripodal Ligand Frameworks

18. E. C. Constable, M. G. B. Drew, M. D. Ward, *J. Chem. Soc. Chem. Commun.*, 1987, 1600-1602.
19. M. Barley, E. C. Constable, S. A. Corr, M. G. B. Drew, C. S. McQueen, J. C. Nutkins, M. D. Ward, *J. Chem. Soc. Dalton Trans.*, 1988, 2655-2660.
20. K. T. Potts, M. Keshavarz, F. S. Tham, H. D. Abruña, C. R. Arana, *Inorg. Chem.*, 1993, 32, 4422-4435.
21. J.-P. Gisselbrecht, M. Gross, J.-M. Lehn, J.-P. Sauvage, R. Ziessel, C. Piccini-Leopardi, J. M. Arrieta, G. Germain, M. Van Meerssche, *Nouv. J. Chim.*, 1984, 8, 661-667.
22. Y. Yao, M. W. Perkovic, D. P. Rillema, C. Woods, *Inorg. Chem.*, 1992, 31, 3956.
23. P. Federlin, J.-M. Kern, A. Rastegar, C. Dietrich-Buchecker, P. A. Marnot, J.-P. Sauvage, *New J. Chem.*, 1990, 14, 9.
24. J. A. Wytko, C. Bourdon, J. Weiss, M. Gross, *Inorg. Chem.*, 1996, 35, 4469.
25. V. Amendola, L. Fabbrizzi, P. Pallavicini, *Coord. Chem. Rev.*, 2001, 216-217, 435.
26. O. Johansson, R. Lomoth, *Chem. Commun.*, 2005, 1578-1580.
27. N. Singh, Ph.D. Dissertation, Cardiff University, 2008.
28. D. E. Scaife, D. W. A. Sharp, R. H. Nuttall, N. S. Gill, *J. Inorg. Nucl. Chem.*, 1961, 18, 79-87.
29. M. T. Halfpenny, J. G. Hartley, L. M. Venanzi, *J. Chem. Soc., A*, 1967, 627.
30. A. B. P. Lever, *Coord. Chem. Rev.*, 1968, 3, 119.
31. B. F. Little, G. J. Long, *Inorg. Chem.*, 1978, 17, 3401.
32. G. M. Bancroft, K. D. Butler, *J. Chem. Soc., Dalton Trans.*, 1972, 1209.
33. R. D. Feltham, H. G. Metzger, W. Silverthorn, *Inorg. Chem.*, 1968, 10, 2003.
34. W. C. Jones, W. E. Ball, *J. Chem. Soc. (A)*, 1968, 1849.
35. W. O. Gillum, R. A. D. Wentworth, R. F. Childers, *Inorg. Chem.*, 1970, 9, 1825-1832.

Chapter 3: The Co-ordination and Electrochemical Behaviour of Two Analogous  
Tetra- and Pentadentate Tripodal Ligand Frameworks

36. B. J. Hathaway, D. E. Billing, *Coord. Chem. Rev.*, 1970, 5, 143.
37. W. Fitzgerald, B. Murphy, S. Tyagi, B. Walsh, B. J. Hathaway, *J. Chem. Soc., Dalton Trans.*, 1981, 2271.
38. M. M. Morrison, D. T. Sawyer, *Inorg. Chem.*, 1978, 17, 333-337.
39. S.-M. Chen, *Inorg. Chim. Acta*, 1996, 249, 143-150.
40. Y. G. Budnikova, D. G. Yakhvarov, V. I. Morozov, Y. M. Kargin, A. V. Il'yasov, Y. N. Vyakhireva, O. G. Sinyashin, *Russ. J. Gen. Chem.*, 2002, 72, 168-172.
41. P. N. Bartlett, V. Eastwick-Field, *Electrochimica Acta*, 1993, 38, 2515-2523.
42. B. Henne, D. Bartak, *Inorg. Chem.*, 1984, 23, 369.
43. R. R. Ruminski, *Inorg. Chim. Acta*, 1985, 103, 159-161.
44. D. V. Soldatov, J. A. Ripmeester, *Supramol. Chem.*, 1997, 9, 175.
45. G. Murphy, C. Murphy, B. Murphy, B. Hathaway, *J. Chem. Soc., Dalton Trans.*, 1997, 2653.
46. C.-F. Ding, M. Zhu, X.-M. Li, S.-S. Zhang, H. Xu, P.-K. Ouyang, *Asian J. Chem.*, 2006, 18, 1685. CCDC deposition no. 646794.
47. X.-M. Chen, R.-Q. Wang, Z.-T. Xu, *Acta Crystallogr.*, 1995, C51, 820.
48. S. R. Batten, K. S. Murray, N. J. Sinclair, *Acta Crystallogr.*, 2000, C56, e320.
49. J.-C. Yao, L.-F. Ma, F.-J. Yao, *Z. Kristallogr.-New Cryst. Struct.*, 2005, 220, 483. CCDC deposition no. 240261.
50. The Cambridge Structural Database: a quarter of a million structures and rising. F. H. Allen, *Acta Crystallogr.*, 2002, B58, 380-388.
51. New Software for searching the Cambridge Structural Database and visualising crystal structures. I. J. Bruno, J. C. Cole, P. R. Edgington, M. Kessler, C. F. McCabe, J. Pearson, R. Taylor, *Acta Crystallogr.*, 2002, B58, 389-397.



Chapter 3: The Co-ordination and Electrochemical Behaviour of Two Analogous  
Tetra- and Pentadentate Tripodal Ligand Frameworks

52. P. B. Hitchcock, T. H. Lee, G. J. Leigh, *Inorg. Chim. Acta*, 2003, 355, 168. CCDC deposition no. 201648.
53. M. Chaudhury, E. R. T. Tiekink, D. Mandal, N. Kundu, *Appl. Organomet. Chem.*, 2005, 19, 1268. CCDC deposition no. 275094.
54. R. D. Shannon, *Acta Crystallogr.*, 1976, A32, 751-767.
55. S. Alvarez, D. Avnir, P. Alemany, D. Casanova, M. Llunell, J. Cirera, *Coord. Chem. Rev.*, 2005, 249, 1693-1708.

# **Chapter 4: Determination of Stability Constants for a Series of Pyridine- Carboxylate Based Tripodal Ligand Frameworks\***

---

\*Some of the results and part of the discussion in this paper were described at the international conference CHEMTECH in Sri Lanka, 2007. A summary appeared in the Abstracts of the Conference.

## 4.1 Introduction

### General Background and Aims

Bio-medical imaging is an expanding and increasingly important field in modern diagnostic medicine.<sup>1</sup> The ability to obtain physiological data that may identify disease states and their extent by non-invasive means has clear importance. The value of non-invasive imaging has long been established with the application of X-ray imaging and the continual development of data handling and computational methods leading to enhanced techniques (*e.g.* Computed Tomography, CT) of greater clinical value. The advent of new technologies during the last 20-30 years has broadened the field of imaging enormously, principally with the introduction of radiochemical methods, magnetic resonance imaging (MRI), optical imaging and ultrasound methods. These technologies have introduced the opportunity to manipulate and ‘tune’ key limiting aspects of the various techniques such as sensitivity and resolution by appropriate use of chemical agents designed to enhance the underlying physical process of the imaging method. The design of suitable chemical agents also introduces the opportunity to manipulate biological specificity, a feature of great value which can not only enhance the accuracy of diagnosis at earlier stages of a disease process, but also broadens the scope of the technique making it relevant to a wider range of conditions that it can be of clinical value for. Thus, it is becoming increasingly clear that chemical design, synthesis and the understanding of chemical interactions within the biological system are of key importance in underpinning developments in bio-medical imaging.

Many of the imaging methods now used clinically require metal based agents either at the core of the technique (*e.g.* in a number of radiochemical applications)<sup>2,3</sup> or for image enhancement (as in MRI).<sup>4</sup> Most of these metal complexes require carefully designed ligands for

## Chapter 4: The Determination of Stability Constants for a Series of Pyridine-Carboxylate Based Tripodal Ligand Frameworks

them to exhibit the required biological properties of stability, specificity *etc.* and consequently it is very important to have an understanding of the underlying key physical properties.

In developing new lanthanide/ligand complexes for MRI contrast agent applications, several properties of the complexes are important.<sup>5</sup> One main concern is that lanthanide metals are toxic and a primary task of the ligand is to form complexes which are resistant to dissociation (and hence delivery of the free metal ion) under biological conditions. This feature may be quantified by measuring stability constants. Various strategies are available to enhance stability. Some systems rely upon the macrocyclic co-ordination effect whereas others maximise the potential of the chelate effect in order to simplify synthetic pathways to appropriate ligands. To address this issue of stability, the work presented in this chapter focuses on a tripodal ligand scaffold based upon a tris-pyridine core with peripheral carboxylate functionalities *ortho* to the pyridyl nitrogens. This chapter also investigates how modifying the denticity of the ligand from four to six by changing the number of peripheral binding functions affects overall complex stability and the nature of species in solution. The design focussed most heavily upon here is the hexadentate ligand, L<sup>8</sup> (Fig. 1; right).

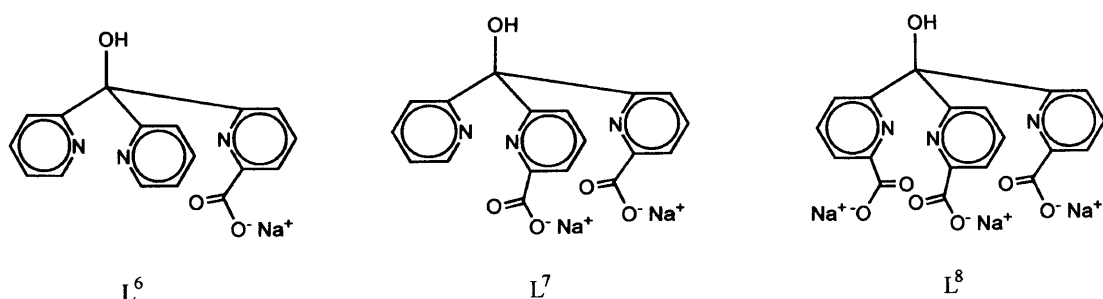


**Figure 1:** The tripodal ligand series under investigation.

## Protonation and Stability Constants

### 4.1.1 *Historical Developments*

The calculation of stability constants has long provided a way of measuring the affinity of a ligand towards a metal ion in solution. Initial interest in stability constants was provoked by von Euler<sup>6</sup> and Bodlander<sup>7</sup> but only went so far as to ascertain empirical formulas and overall stability constants. N. Bjerrum<sup>8</sup> and J. Bjerrum<sup>9</sup> later pioneered advances in this field which enabled a more detailed critical analysis of these systems, involving the calculation of stepwise hydrolysis constants and stepwise stability constants. The numerous reports of stability constants which have since been published all follow the same principles of accurately establishing equilibrium constants and mass balance equations using quite complex algebraic manipulation. The theoretical background to these early calculations was summarised by Rossotti and Rossotti.<sup>10</sup>

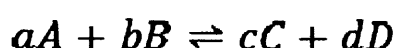
Important developments in the field of stability constant determination have recently had very advantageous implications. One of the most beneficial of these has been the advent of specific computer programs containing computational methods which have hastened the processing of equilibrium data and hence the determination of highly accurate stability constants. These computer programs have also extended their usefulness to multidentate ligands and to examples containing several ligands and metals ions which otherwise would have been too complex to calculate. One such computer program “HyperQuad” designed by Peter Gans<sup>11</sup> has been especially helpful in the context of this work.

The arrival of two stability constant databases<sup>12,13</sup> has been another useful addition to this field. These databases conveniently provide a comprehensive selection of stability constants from the literature and, crucially, this data is accompanied by detailed experimental information.

This information is essential for drawing conclusions from the reported values and also for comparing one set of data to another.

#### 4.1.2 *Stability Constants – What are they?*

Stability constants are a quotient of the activities of the reacting species in solution when at equilibrium. They can be defined mathematically as the product of the activities of the reaction products raised to the appropriate power which is decided by the relative stoichiometry of each species in the reaction at equilibrium, then divided by the product of the activities of the reacting species also raised to the appropriate power. It can be represented by equation 1:



$$K_{eq} = \frac{a_C^c \cdot a_D^d}{a_A^a \cdot a_B^b} \quad (1)$$

At equilibrium, the product and reactant species in their standard states have their own respective Gibbs free energies. This provides a quantitative description of the reactivities of all the species involved, and the stability constant acts as a direct measure of the difference in these Gibbs free energies.

An important factor to consider when determining stability constants is the ionic strength of the solution being investigated. It is quite impractical to measure the ionic activities of complex ionic species during the course of a reaction, and so to evade this problem a non-reacting electrolyte can be introduced far in excess of the reacting ionic species in question. This has the effect of controlling the ionic strength in the solution, making the concentrations equate to the activities of the ionic solutes. It is now standard procedure to determine stability constants

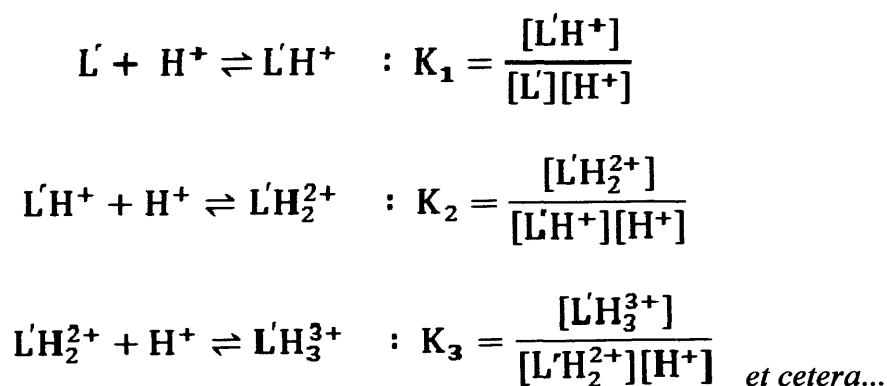
#### Chapter 4: The Determination of Stability Constants for a Series of Pyridine-Carboxylate Based Tripodal Ligand Frameworks

whilst at constant ionic strength sustained by the supporting electrolyte. The most obvious advantage of this approach is the practicality; the activities in the previous equation can now be substituted with the molar concentrations:

$$K_c = \frac{[C]^c \cdot [D]^d}{[A]^a \cdot [B]^b} \quad (2)$$

This also has further rewards in that any concentration values taken from the potentiometric studies can be directly linked to those obtained through other means, such as absorbance techniques. Also, conveniently, the results can be directly substituted into mass balance equations which are used for the calculation of stability constants and protonation constants.

As metal ions are in competition with protons for ligand sites, the determination of protonation constants is a necessary first step in the determination of metal complex stability constants. The protonation constants for ligands are defined as follows.<sup>14</sup>



The nature of the ligand and the number of sites available for protonation determines the number of protonation constants to be expected. As aliquots of base are added to the reaction

solution, the ligand under investigation will become increasingly deprotonated and the dynamic equilibrium will be reverted to the initial forms.

#### 4.1.3 *Why Are Stability Constant's Useful?*

For a system containing species comprising of weak bonding interactions, by varying concentration or pH it can be possible for a reactive species to exist in several different forms. Stability constant determination is vital to understanding such equilibria in solution. In addition to the aforementioned role in evaluating MRI contrast agents, there are many further practical applications, one example being in examining host-guest interactions. For instance, Liu *et al.*<sup>15</sup> used stability constants to assess the stability of anions (such as oxalate<sup>2-</sup>, sulfate<sup>2-</sup> and fumarate<sup>2-</sup> *etc.*) within polyammonium macrocycles. Another case<sup>16</sup> involves the polyaza macrocycle depicted in Figure 2 which contains two polydentate compartments, each capable of binding a Cu<sup>II</sup> cation. In basic media (pH>10) the amide groups are de-protonated and each Cu<sup>II</sup> ion lies within the square planar co-ordination environment of the bis-deprotonated diamide-diamine donor set (Fig. 2; left). Acidifying the solution (pH 3-6) re-protonated the amide groups and led to an intramolecular dislocation of the Cu<sup>II</sup> ions (Fig. 2; right). These become co-ordinated *via* the tridentate pyridine-diamine donor set and the remaining co-ordination sites are filled with solvent water molecules. Using the results from the stability constant analysis, it was possible to plot the relative proportion of each of the species in solution as the pH was modified. This speciation diagram enabled useful conclusions based upon the composition of the solution throughout specific pH range.



## Chapter 4: The Determination of Stability Constants for a Series of Pyridine-Carboxylate Based Tripodal Ligand Frameworks

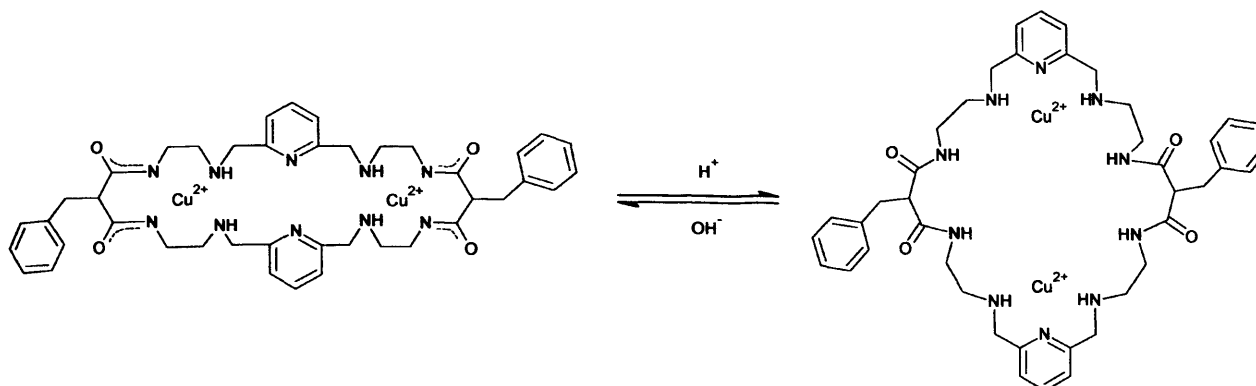


**Figure 2:** The host-guest interaction is an example of where stability constant determination is useful.

The determination of stability constants is clearly very important for many areas of modern research, with numerous other applications in, for example, catalysis,<sup>17</sup> cation-selective complexation<sup>18</sup> and bio-inorganic chemistry.<sup>19</sup>

### 4.1.4 *The Chelate Effect*

A molecule or ion comprising two or more donor atoms can be termed a chelate. The linking of two or more donor atoms leads to greatly enhanced stability constants with metal ions as compared to the separate donor groups. Several causes of this effect have been explored in depth.<sup>20-23</sup> The conventional thermodynamic explanation for the chelate effect points out the increase in entropy associated with chelate binding relative to the binding of separate monodentate donors. This is due to an increase in the total number of particles generated upon displacement.

In addition to the entropic contribution, a further explanation lies in the abnormally fast formation of the second M-X bond (where X = any donor atom) relative to an unlinked second donor. Donor atoms in a flexible chelate are known to dissociate as rapidly as analogous monodentate ligands. Therefore, to prevent the chelate dissociating at a rate similar, the

## Chapter 4: The Determination of Stability Constants for a Series of Pyridine-Carboxylate Based Tripodal Ligand Frameworks

enhanced stability of chelates must also be attributed to unusually rapid re-binding. Thus, the kinetic effect can be described as an associative one.

### 4.1.5 *Hard-Soft Acid-Base Classification (HSAB)*

In 1941, Sidgwick<sup>24</sup> published a paper entitled 'Complex Formation' within which he recognised the pattern of affinities of some common ligands for various acceptor ion and molecules. This theory was expanded upon in 1958 by Ahrland *et al.* who classed acceptor ions and molecules into two well-defined types: class (a), which form their most stable complexes with the first ligand atom in each group, and class (b), which form their most stable complexes with the second or subsequent ligand atom of each group.<sup>25</sup> Although the terms 'hard' and 'soft' were not used until some years after this, it was clearly understood that small, highly charged metal ions (hard acids) form the strongest complexes with small, electronegative donor atoms (hard bases), whilst larger, polarisable metal ions (soft acids) form the strongest complexes with larger, less electronegative donors (soft bases). Table 1 comprises a selection of categorised metal ions and ligands according to their classification.

**Table 1:** A selection of metal ions and ligands grouped into hard and soft categories

	<b>Hard</b>	<b>Intermediate</b>	<b>Soft</b>
<b>Metal Ions</b>	$Mn^{2+}$ , $Sc^{3+}$ , $Cr^{3+}$ , $Fe^{3+}$	$Fe^{2+}$ , $Co^{2+}$ , $Ni^{2+}$ , $Cu^{2+}$	$Ag^+$ , $Pd^{2+}$ , $Pt^{2+}$ , $Rh^+$
<b>Ligands</b>	$R_2O$ , $ROH$ , $OH^-$ , $SO_4^{2-}$ , $Cl^-$	$Br^-$ , $py$	$R_2S$ , $R_3P$ , $CO$ , $CN^-$ , $I^-$

### 4.1.6 *The Irving-Williams Order*

In 1948, H. Irving and R. J. P. Williams reported a series of bivalent metal ions based upon the relative stabilities of the complexes they form.<sup>26</sup> It was found that the order  $Mn < Fe < Co < Ni < Cu > Zn$  holds for the stability of nearly all such complexes irrespective of the

## Chapter 4: The Determination of Stability Constants for a Series of Pyridine-Carboxylate Based Tripodal Ligand Frameworks

nature of the co-ordinated ligand or the number of ligands involved. This communication was expanded upon in 1953<sup>27</sup> when it was suggested that this ordering is a consequence of two parameters, namely the reciprocal of the ionic radius of the metal ion, and the second ionisation potential. Both of these increase monotonically throughout the series from manganese to copper. Therefore, if water is replaced by a ligand of greater electron-donating power, the gain in stability will increase with the second ionisation potential of the metal concerned. Secondly, if water is replaced by a ligand with a formal negative charge, the stability increment through purely electrostatic forces will increase as the radius of the cation decreases, *i.e.*, in the same order. The stabilities of copper complexes are often surprisingly high, due largely to the stabilisation incurred by Jahn-Teller distortions.

### 4.1.7 *Electrode Calibration Theory*

In acid/base equilibria in aqueous solution the concentration of hydrogen ions may be measured by means of a glass electrode. The requirement, therefore, to calibrate the electrode response in terms of hydrogen ion concentration is evident. Ideally the potential,  $E$ , of a glass electrode follows the Nernst equation:

$$E = E^0 + \frac{RT}{nF} \log_e \{H\} \quad (3)$$

where  $E^0$  is the standard electrode potential,  $R$  is the gas constant,  $T$  is the temperature in Kelvin,  $F$  is the Faraday constant, and  $n = 1$  in the case of the glass electrode.

This equation shows that the electrode response is linear in hydrogen ion activity as indicated by  $\{ \}$ . As stated previously, the ionic strength is kept high and stable by a supporting electrolyte and prevents difficulties associated with the variation of activity coefficients as under

#### Chapter 4: The Determination of Stability Constants for a Series of Pyridine-Carboxylate Based Tripodal Ligand Frameworks

such conditions it can be assumed that they remain constant. The following equation can be derived:

$$E = E^0 + s \log_e [H] \quad (4)$$

where the slope,  $s$ , ideally should have a value of around  $T/5.0399$  mV.

It is possible therefore, where the concentration of hydrogen ions is known for a series of data points, to establish  $E^0$  and the slope factor.

The titration is carried out using strong acid and strong base of known concentrations in a supporting electrolyte of high ionic strength. The titration vessel is filled with 2 mL of acid ( $\text{HNO}_3$ , 0.10 M) and 50 mL of the supporting electrolyte solution ( $\text{NaNO}_3$ , 0.1 M). After addition of 0.05 mL of base ( $\text{NaOH}$ , 0.1021 M), the mineral acid concentration,  $T_H$ , is given by the following equation:

$$T_H = \frac{a_H \cdot v_0 + \gamma \cdot b_H \cdot v}{v_0 + v_1 + v_2} \quad (5)$$

where  $a_H$  is the concentration ( $\text{mol dm}^{-3}$ ) of acid of which  $v_0$  mL were added to the titration vessel,  $b_H$  is the concentration ( $\text{mol dm}^{-3}$ ) of base in the burette (by convention given a negative sign),  $v_1$  is the volume (mL) of background electrolyte solution added to the titration vessel, and  $v$  (mL) is the volume of base added from the burette.

Due to any uncertainty in the base concentration, a coefficient gamma,  $\gamma$ , has been introduced. As the base concentration is conventionally given a negative sign,  $T_H$  is positive at low pH, zero at the equivalence point and negative at high pH. Therefore,  $T_H$  can be determined knowing all the quantities in equation 5 and knowing this makes the calculation of hydrogen ion concentration relatively simple.

## Chapter 4: The Determination of Stability Constants for a Series of Pyridine-Carboxylate Based Tripodal Ligand Frameworks

The hydrogen ion concentration can be determined from the mineral acid concentration,  $T_H$ , whilst remembering the self-dissociation of water,  $K_w$ .

$$[H_2O] = K_w \cdot [H] \cdot [OH]; \quad pK_w = -\ln(K_w) \quad (6)$$

$$T_H = [H] - K_w \cdot [H]^{-1} \quad (7)$$

- (i) At pH values lower than 5, the second term in equation 7 is minute compared to the initial term and hence can be regarded as negligible;  $[H] = T_H$ .
- (ii) At pH values higher than 9, the initial term in equation 7 is minute compared to the second and can be regarded as negligible;  $[H] = K_w / (-T_H)$ .

One inevitable concern is that the base solution may be contaminated with a slight amount of carbonate. This impurity level, determined as a percentage, is calculated *via* a Gran's plot<sup>28</sup> and is then used to amend the alkali concentration. The parameters  $E^0$ ,  $s$ ,  $\gamma$  and  $pK_w$  are determined by least-squares fitting of the observed electrode potentials to the values calculated by equation 5.

### 4.1.8 Errors and their minimisation

Considering the finely tuned nature of the practical aspects of this technique, any errors have the potential for a large impact on the quality of results obtained. Therefore, it is essential to eliminate any scope for error during the course of the entire experiment.

Errors are most likely to arise from inaccurate standardisation of the reagents. For instance, any inconsistency in initial protonated ligand concentration would produce a marked error in the concentration of the available hydrogen ion. Conveniently, within the program HyperQuad is a means of accurately establishing the true initial concentrations of both the ligand

and hydrogen ions in solution by means of a lengthy refinement process. This has the effect of minimising any errors from inaccurate standardisation.

Another major source of error can be the glass electrode itself, and every care must be taken to ensure the electrode is stored properly according to the manufacturer's specifications. When the electrode is not in use, it should be immersed in the supporting electrolyte containing roughly 0.001M H<sup>+</sup>. The electrode may show unpredictable behaviour if in the presence of heavy metal. For instance, touching the metal temperature probe may give rise to considerable leaps in pH, which can be restored by immersing the electrode in 0.1M HCl.

Before any data point can be recorded, adequate time must be allowed for the system to reach equilibrium. There are two factors to consider here; firstly, time must be allowed for the system to physically adjust itself to the new conditions, and secondly, depending on the reaction being studied, time must also be allowed for the varying reaction rates of different species undergoing dissociation. On addition of the first aliquot of base, equilibrium can be assumed to have reached completion when the pH has remained constant for 30 seconds. On nearing the end-point of a titration where the pH value jumps considerably into the basic region, it can be necessary to wait for periods of ten minutes or more for the system to reach complete equilibrium.

## 4.2 Experimental

### General

The synthesis of ligands L<sup>6</sup>, L<sup>7</sup> and L<sup>8</sup> has been reported by Dr. Neha Singh<sup>29</sup> and is summarised in Figure 3. Reagents were obtained from commercial sources and used as received. Solvents

## Chapter 4: The Determination of Stability Constants for a Series of Pyridine-Carboxylate Based Tripodal Ligand Frameworks

were dried and purified under  $N_2$  by using standard methods<sup>30</sup> and were distilled immediately before use. All compounds were prepared under  $N_2$ .

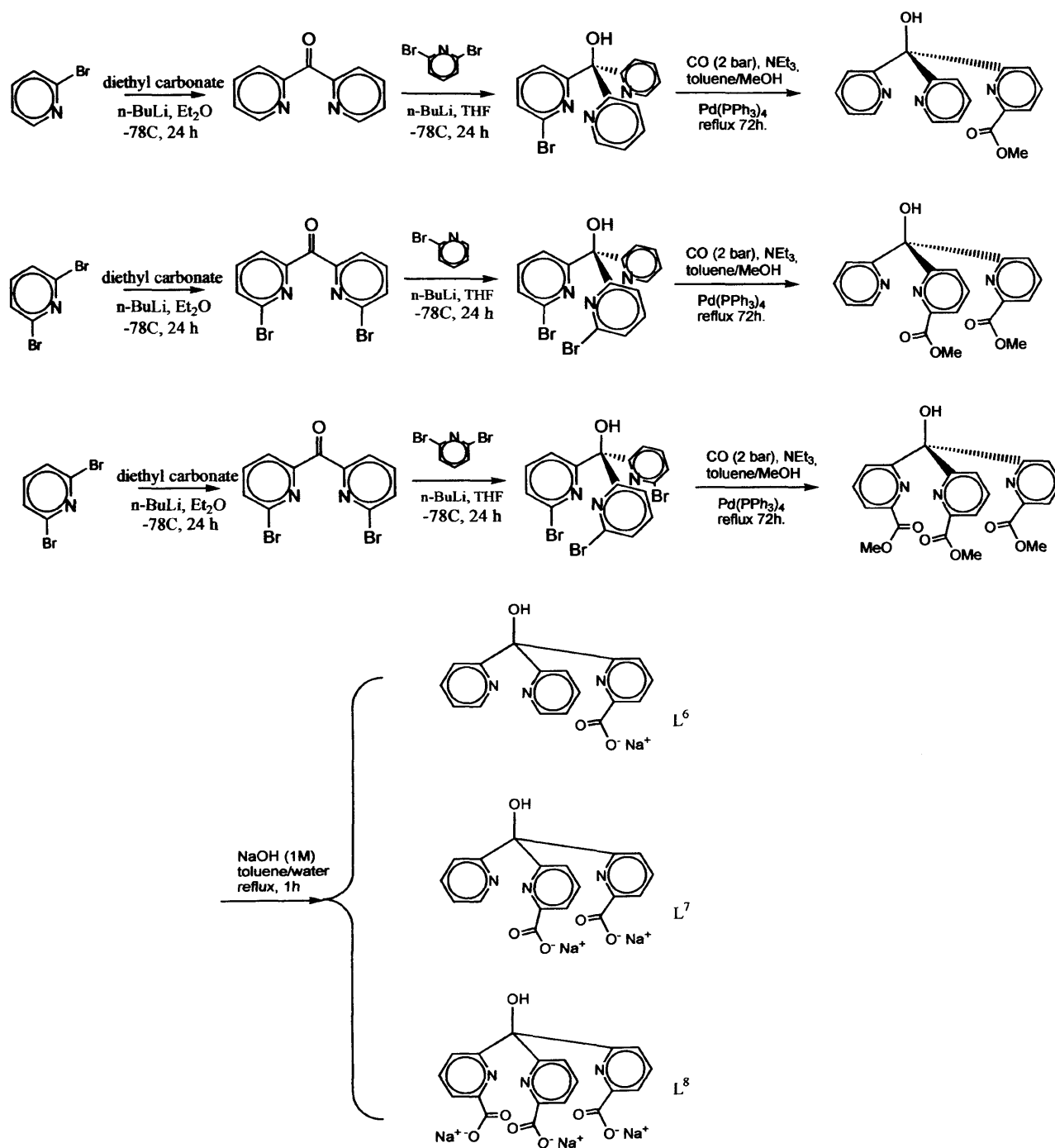


**Figure 3:** Synthetic route to ligands  $L^6$ - $L^8$

## Potentiometric Titrations

The potentiometric studies were conducted with a TIM840 autotitrator (Radiometer Analytical). A Metrohm combined pH glass electrode (Ag/AgCl) with 3M KCl internal filling solution was used. Solutions were prepared using doubly deionised freshly distilled water and kept under a stream of N<sub>2(g)</sub>. The electrode was calibrated with dilute standard acid and alkali solutions (*cf.* Section 4.1.7), thus defining  $\text{pH} = -\log [\text{H}^+]$  ( $\text{pK}_w = -13.78$ ). The electrolyte, NaNO<sub>3</sub> (0.1 M), was prepared in the form of a stock solution from analytically pure grade NaNO<sub>3</sub> obtained from commercial sources (Aldrich). The standard acid (HNO<sub>3</sub>) and standard base (NaOH) were also prepared to the same concentration as the electrolyte and were again obtained from commercial sources (Acros and Aldrich respectively) free from any carbonate contamination which would have had the adverse effect of buffering the reaction mixture. The reaction vessel was kept under an inert atmosphere *via* a constant flow of nitrogen gas. The temperature of the reaction mixture was controlled by a thermostat which maintained a flow of water in a water-tight layer encapsulating the reaction cell at a constant 25°C (298K). The standard base was delivered in 0.05 mL aliquots using an autoburette, which was a useful means of measuring identical amounts quickly with negligible deviation from the desired volume. The solution was constantly mixed by a magnetic stirrer bar at an appropriate speed (typically 200 rpm), fast enough to thoroughly mix the solution but not so quickly as to disturb the electrode.

In a typical experiment, an aqueous solution (50 mL) was prepared containing the ligand (1 mM), metal nitrate salt (1 mM) and a known quantity of HNO<sub>3</sub> (0.1M). The ionic strength (*I*) of this solution was adjusted to 0.1 with NaNO<sub>3</sub>. The temperature of solutions (25°C) in the covered, water-jacketed cell was kept constant by a Fischer Scientific BC10 circulating bath. Upon reaching equilibrium, this solution was titrated with NaOH (0.1021 N). Each titration



## Chapter 4: The Determination of Stability Constants for a Series of Pyridine-Carboxylate Based Tripodal Ligand Frameworks

consisted of more than 80 data points spanning a pH range of 2 – 11. The protonation constants of the ligands and overall stability constants of the metal complexes were calculated using the HyperQuad suite of programs, the mathematical basis of which has been reviewed in the literature.<sup>11</sup> The reported equilibrium constants are the mean average of two separate measurements. Immediately prior to this investigation, a trial experiment involving the known ligand tris(2-aminoethyl)amine (TREN, Fig. 4) was used as a control. The data matched, within statistical error, the comprehensive set of data from the literature.<sup>31</sup>

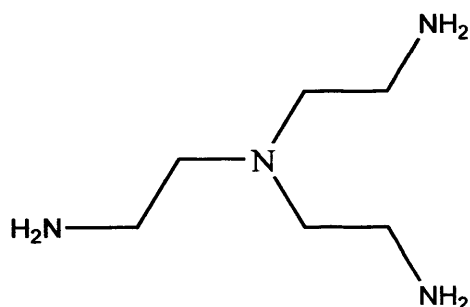


**Figure 4:** TREN. Literature protonation constants: 10.14, 9.43, 8.45. This work: 10.12(4), 9.46(2), 8.46(3).

### 4.3 Results and Discussion

The protonation constants for  $L^6$ - $L^8$  are shown in Table 2. Shown here are 4, 5 and 6 stepwise protonation constants respectively, which correspond to the number of donor atoms present on each ligand. A detailed search of the literature using the stability constant database<sup>12</sup> reveals many examples of protonation constants for both pyridine and carboxylate functionalities (Table 3) from which meaningful comparisons can be drawn.

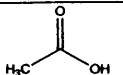
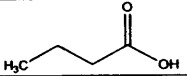
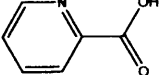
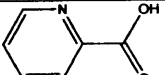
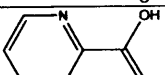
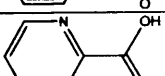
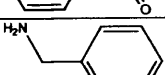
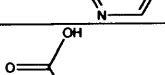
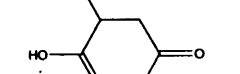
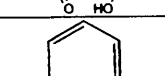
## Chapter 4: The Determination of Stability Constants for a Series of Pyridine-Carboxylate Based Tripodal Ligand Frameworks

**Table 2:** Thermodynamic Properties for the Ligands L<sup>6</sup> – L<sup>8</sup>

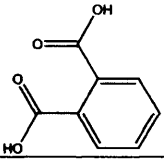
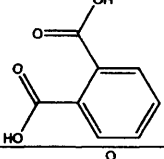
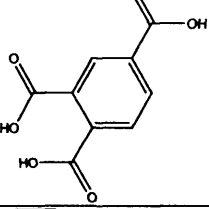
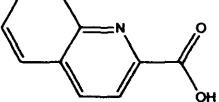
Quotient	Constant	L <sup>6</sup>	L <sup>7</sup>	L <sup>8</sup>
[LH]/[L][H]	log K <sub>LH</sub>	5.97(3)	5.97(4)	5.49(4)
[LH <sub>2</sub> ]/[LH][H]	log K <sub>LH2</sub>	5.52(4)	4.43(1)	4.27(3)
[LH <sub>3</sub> ]/[LH <sub>2</sub> ][H]	log K <sub>LH3</sub>	3.73(2)	3.73(3)	3.98(3)
[LH <sub>4</sub> ]/[LH <sub>3</sub> ][H]	log K <sub>LH4</sub>	3.43(4)	3.34(4)	3.76(3)
[LH <sub>5</sub> ]/[LH <sub>4</sub> ][H]	log K <sub>LH5</sub>	-	2.65(3)	3.56(4)
[LH <sub>6</sub> ]/[LH <sub>5</sub> ][H]	log K <sub>LH6</sub>	-	-	2.17(2)
ΣpK <sub>a</sub>		18.65	20.12	23.23

All constants were determined at 25°C and 0.1 M NaNO<sub>3</sub>.

**Table 3:** A selection of related chemical moieties extracted from literature.

Moiety	Method	Medium (Ionic concentration)	Temp/°C	Log K Value(s)	Ref
	glass electrode	No electrolyte	25	4.756	32
	glass electrode (calorimetry)	KCl (0.1 M)	25	5.01	33
	glass electrode	KNO <sub>3</sub> (0.15 M)	25	5.184, 0.88	34
	glass electrode	NaClO <sub>4</sub> (3 M)	25	5.93, 1.99	35
	glass electrode	NaNO <sub>3</sub> (2 M)	25	6.00	36
	glass electrode	NaClO <sub>4</sub> (0.1 M)	25	5.12	37
	calorimetry	NaCl (0.15 M)	25	8.649, 2.08	38
	glass electrode	NaClO <sub>4</sub> (0.5 M)	25	5.71, 4.21, 2.40	39
	glass electrode	NaClO <sub>4</sub> (0.5 M)	25	4.87, 3.45	40
	glass electrode	NaCl (concentration not reported)	25	4.7	41

Chapter 4: The Determination of Stability Constants for a Series of Pyridine-Carboxylate Based Tripodal Ligand Frameworks

	glass electrode	NaCl (0.1 M)	25	4.95, 2.733	42
	glass electrode	KCl (0.001 M)	25	5.41, 2.95	43
	glass electrode	No electrolyte	25	5.54, 4.00, 2.48	44
	glass electrode	KCl (0.1 M)	25	5.90, 4.50	45

From these literature values, it is evident that the pyridinium cation is typically less acidic than a carboxylic acid functional group. This is due in part to the resonance stabilisation of a carboxylate group, in contrast to a pyridine-N atom in which the lone pair of electrons is not a part of the aromatic  $\pi$ -system. Therefore, it is a reasonable assumption that the highest protonation constants in each case are attributable to the three basic pyridine groups. The sequence of  $K_n$  values is  $K_1 > K_2 > K_3$  which relates to the build up of positive charge as the pyridines are successively protonated, also there is a statistical contribution to  $K_n$  which is most favourable for the initial protonation, *i.e.* the statistical contribution for a reaction  $LH_1 + H \rightarrow LH$  is reliant on the relative number of sites at which a new proton may attach. The first three protonation constants therefore range from 5.97 to 3.73 (log units) which is expected considering the pyridine-N atom of picolinic acid has a protonation constant of 6.00 to 5.12, depending on the experimental conditions.<sup>34-37</sup> This value is also very sensitive to the nature of substituents around the pyridine, for instance the compound 2-(aminomethyl)pyridine displays a protonation constant of 2.08 for the pyridine group.<sup>38</sup>

## Chapter 4: The Determination of Stability Constants for a Series of Pyridine-Carboxylate Based Tripodal Ligand Frameworks

The remaining protonation constants for this ligand series are attributable to the carboxylic acid groups which range from 3.76 to 2.17. This is interesting as picolinic acid typically presents values in the range 1.99 to 0.88 for this group, depending on the conditions. On broadening the search to encompass several structurally related compounds it becomes evident that this too is very sensitive to substituents on the adjoining pyridine. For instance, one such compound, quinoline-2-carboxylic acid, has a pKa of 4.50 for the carboxylate group.<sup>45</sup>

The summation of each ligands pKa values ( $\Sigma pK_a$ ) conveys the overall basicity which is an insightful parameter. While basicity is not the only factor to take into consideration when designing stable complexes (electrostatic hard-soft interactions for example also have a large bearing), some groups<sup>46</sup> have had success in optimising the basicity of similar ligands in order to enhance stability. Table 4 shows the stability constants for the Eu<sup>III</sup> complexes and it can be seen here that the most basic ligand L<sup>8</sup> correspondingly has the highest overall stability upon complexation,  $\log K_{EuL} = 10.27(2)$ . This value is several orders of magnitude lower than commercially available octadentate contrast agents Gd-DTPA (Magnevist®) and Gd-DOTA (Dotarem®), which have stability constants of 22.1 and 25.8 respectively. This is a consequence of the hexadentate ligand exhibiting a reduced chelate effect leading to a thermodynamically less favourable interaction, and consequently the pentadentate ligand L<sup>7</sup> is an order of magnitude lower still. Mazzanti *et al.* reported the heptadentate compound H<sub>3</sub>tpaa (Fig. 5), which is structurally similar to L<sup>8</sup>, having an overall stability constant,  $\log K_{GdL}$ , of 10.2(2).<sup>47</sup> This is approximately the same as L<sup>8</sup> despite having an additional tertiary amine donor atom, this could be a consequence of the superior structural rigidity of L<sup>8</sup> which is often reported as a significant factor in complex stability.

## Chapter 4: The Determination of Stability Constants for a Series of Pyridine-Carboxylate Based Tripodal Ligand Frameworks

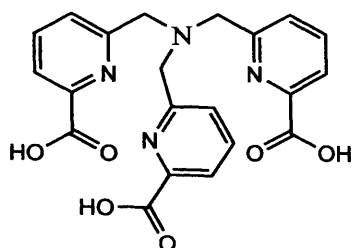


**Figure 5:** H<sub>3</sub>tpaa (α,α',α''-nitrilotri(6-methyl-2-pyridinecarboxylic acid))

**Table 4:** Stability constants of ligands L<sup>6</sup>-L<sup>8</sup> with Eu<sup>III</sup>

Quotient	Constant	L <sup>6</sup>	L <sup>7</sup>	L <sup>8</sup>
[EuL]/[Eu][L]	log KEuL	8.40(3)	9.27(3)	10.27(2)
[EuLH]/[EuL][H]	log KEuLH	-	5.50(2)	4.98(3)
[EuL <sub>2</sub> ]/[EuL][L]	log KEuL <sub>2</sub>	7.04(4)	-	-
[EuH <sub>1</sub> ]/[Eu][H <sub>1</sub> ]	log KEuH <sub>1</sub>	-8.37	-8.37	-8.37
	pEu (pH = 7.4)	11.2	10.2	11.2

The case of L<sup>6</sup> is quite different on comparison to both L<sup>7</sup> and L<sup>8</sup>. Analysis of the potentiometric data with the program HyperQuad indicates the formation of a species with a metal to ligand ratio of 1:2. Attempts at modelling a 1:1 ratio led to unstable refinement and large  $\chi^2$ -squared values indicating a poor correlation between the calculated and experimental titration curves. This indicates that in sufficiently basic media the Eu<sup>III</sup> is co-ordinated by two tetradentate ligands with successive stability constants of 8.40(3) and 7.04(4) respectively. The decrease in stability constant for the co-ordination of the second ligand is again largely due to statistical factors relating to the diminished number of co-ordination sites on the metal.

The speciation diagrams of each ligand have been presented below in Figures 6 - 8. These diagrams are in a form which represents the percentage of species in solution relative to Eu<sup>III</sup> across the entire experimental pH range. The speciation plot of L<sup>6</sup> (Fig. 6) reveals that the species EuL begins to be formed at approximately pH 3 which is also observed for both L<sup>7</sup> and

$L^8$ . However, in contrast, this species reaches a maximum around pH 4 and gradually decreases until *ca.* pH 8.5 at which stage it sharply declines. The species  $EuL_2$  is formed at *ca.* pH 3.5 and gradually increases, in precise contrast to the species  $EuL$ , this is again until pH 8.5 whereupon it undergoes a sharp increase. At roughly pH 10,  $EuL_2$  surpasses  $EuL$  as the major species in solution. Also observed is the presence of the hydrolysis product of europium which increases in a similarly sharp fashion, mirroring  $EuL_2$ . This is commonly observed for trivalent lanthanides in aqueous solution, which can be hydrolysed in media as low as pH 6.<sup>48</sup> The presence of free  $Eu^{III}$  declines rapidly as  $EuL$  and  $EuL_2$  are formed, but does not begin to diminish completely until *ca.* pH 8.5 where it quickly reaches negligible quantities in the now basic solution.

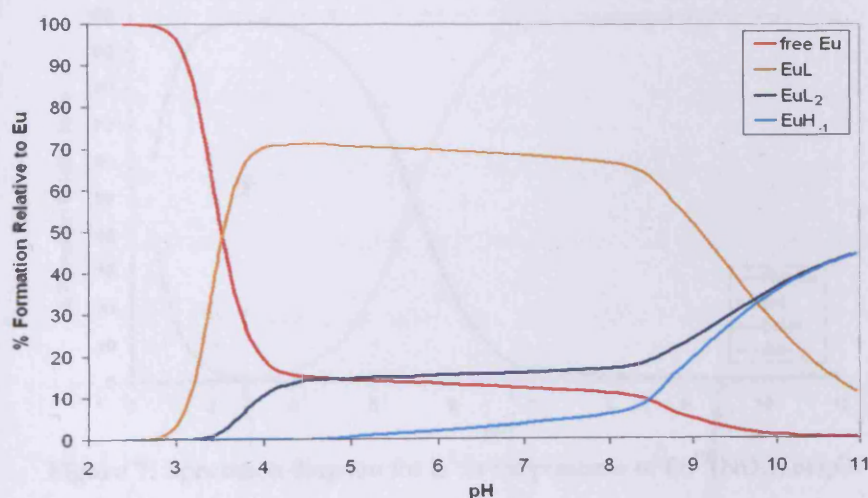
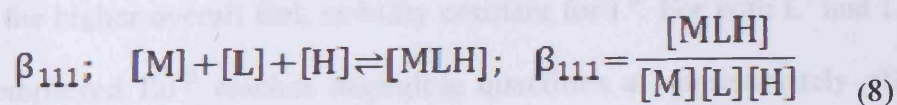


Figure 6: Speciation diagram for  $L^6$  in the presence of  $Eu^{III}(NO_3)_3 \cdot 6H_2O$

In the case of  $L^7$  (Fig. 7) and  $L^8$  (Fig. 8), there are two major species formed during the course of the titration tending towards higher pH. These are successively MLH and ML, which correspond to equations 8 and 9;



$$\beta_{110}; [M] + [L] \rightleftharpoons [ML]; \quad \beta_{110} = \frac{[ML]}{[M][L]} \quad (9)$$

These equations are cumulative, for clarity to represent the individual stepwise constant for  $\log K_{111}$ , the value is simply:  $\log K_{111} = \beta_{111} - \beta_{110}$ , corresponding to the equilibrium:



which occurs at a pH below that at which complete complex formation as expected.

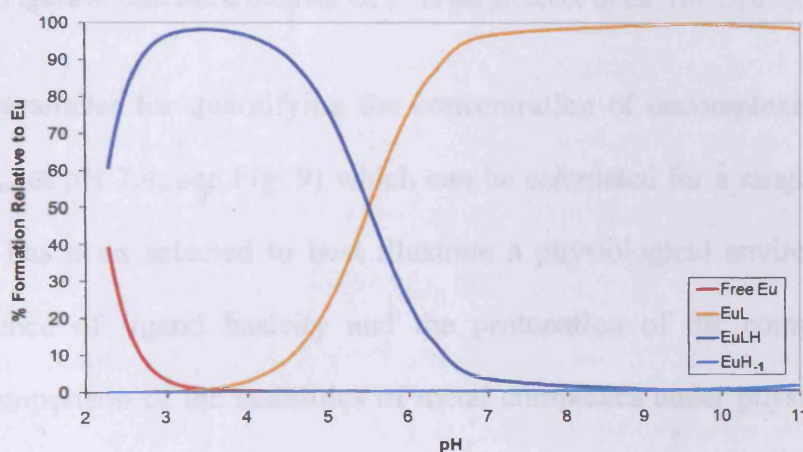


Figure 7: Speciation diagram for  $L^7$  in the presence of  $\text{Eu}^{\text{III}}(\text{NO}_3)_3 \cdot 6\text{H}_2\text{O}$

It can be seen that both  $L^7$  and  $L^8$  present very similar species distribution across the entire pH range. The most significant difference is the crossover point at which EuL surpasses EuLH as the major species. In the case of  $L^8$ , this occurs at approximately pH 5, which is in a slightly more acidic environment on comparison to  $L^7$  which occurs at *ca.* pH 5.5, this is a direct consequence of the higher overall EuL stability constant for  $L^8$ . For both  $L^7$  and  $L^8$ , the relative amount of uncomplexed  $\text{Eu}^{\text{III}}$  reaches negligible quantities at approximately pH 3.5. This is

crucially important as the toxicity of free  $Gd^{III}$ , resulting from dissociation or transmetallation, has been widely documented.<sup>49</sup>

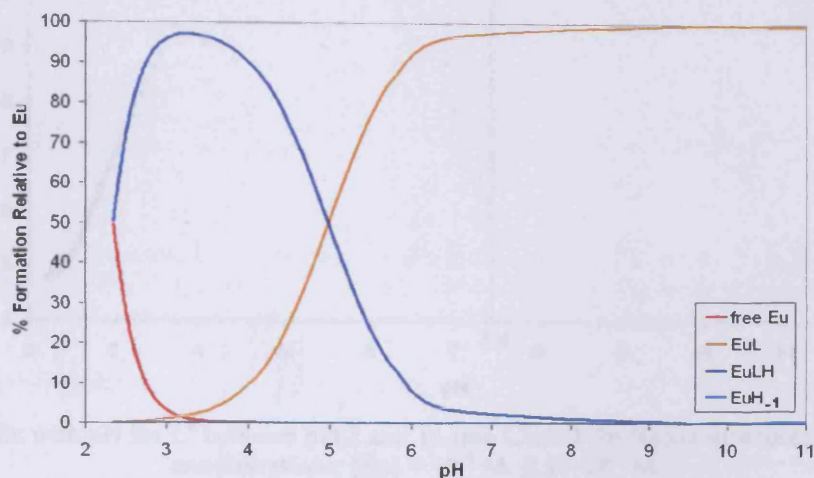


Figure 8: Speciation diagram for  $L^8$  in the presence of  $Eu^{III}(NO_3)_3 \cdot 6H_2O$

A useful parameter for quantifying the concentration of uncomplexed metal is the pM value ( $-\log_{10}[M]_{free}$  at pH 7.4; see Fig. 9) which can be calculated for a range of conditions, but here a pH of 7.4 has been selected to best illustrate a physiological environment. This value reflects the influence of ligand basicity and the protonation of the complex and allows a straightforward comparison of the stabilities of metal complexes under physiologically relevant conditions. The larger the pM value, the higher the affinity of the ligand for the metal ion under the stated conditions. It is worth noting that the lowest theoretically possible value of pM, assuming all the stated conditions have been adhered to is 6,  $pM = -\log_{10}[1 \times 10^{-6}]$  indicating complete dissociation of the complex.



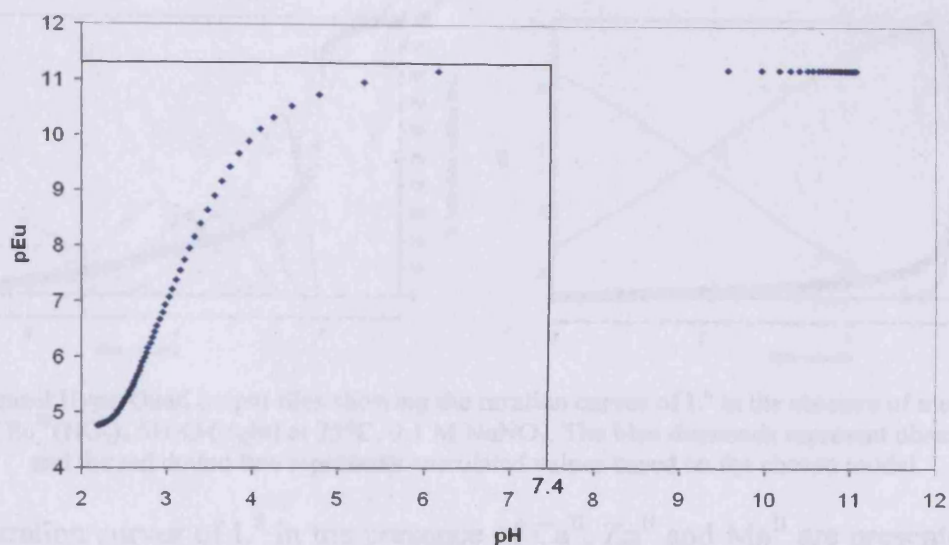
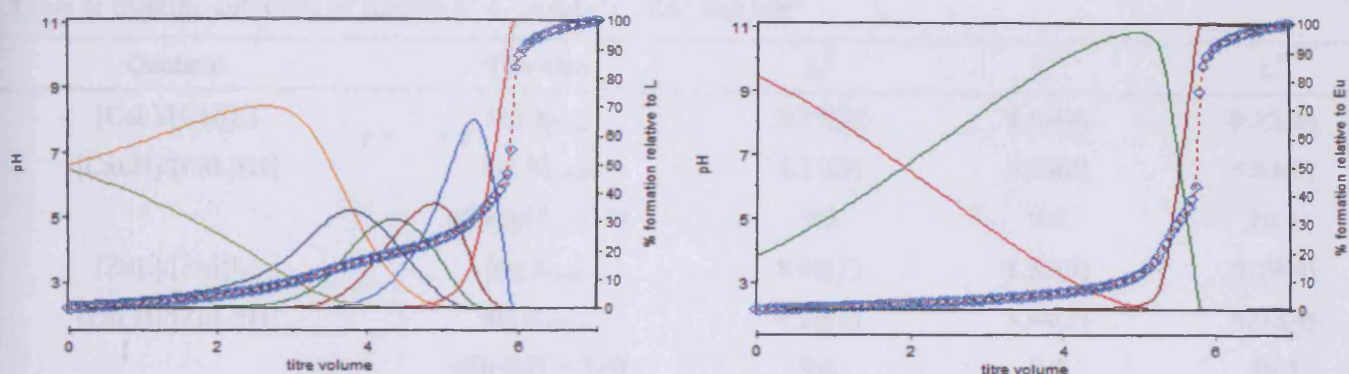


Figure 9: Plot of pEu with pH for  $L^8$  between pH 2 and 11 (see Chart 1 for ligand structures). Calculated for total concentrations;  $[Eu] = 10^{-6}$  M,  $[L] = 10^{-5}$  M.

The titration curves of  $L^8$  which compare both europium complex formation and ligand deprotonation are shown below (Fig. 10). The ligand deprotonation curve (Fig. 10; left) in the absence of any metal shows a long buffer region corresponding to the loss of all six protons which is followed by a sharp inflexion point after the addition of 6 mL of base when the sixth and final proton is neutralised completely. The titration curve of the ligand in the presence of  $Eu^{III}(NO_3)_3 \cdot 6H_2O$  (Fig. 10; right) reveals a clear inflexion point upon the addition of 5.8 mL of base, which in this instance indicates the completion of neutralisation of the monoprotinated complex,  $EuLH$ . This occurs concomitantly with the deprotonated species,  $EuL$ , reaching a plateau as the most dominant species in solution. On closer inspection, this inflexion point is immediately preceded by another which starts at approximately pH 3. This corresponds to the completion of deprotonation of the acidified free ligand which occurs simultaneously with the  $EuLH$  species reaching its maximum concentration (*cf.* Fig. 8).



**Figure 10:** Typical HyperQuad output files showing the titration curves of L<sup>8</sup> in the absence of metal (left) and in the presence of Eu<sup>III</sup>(NO<sub>3</sub>)<sub>3</sub>·6H<sub>2</sub>O (right) at 25°C, 0.1 M NaNO<sub>3</sub>. The blue diamonds represent observed data points and the red dotted line represents calculated values based on the chosen model.

The titration curves of L<sup>8</sup> in the presence of Ca<sup>II</sup>, Zn<sup>II</sup> and Mn<sup>II</sup> are presented together in Figure 11. Each of these curves are very similar in shape and, in a similar manner to that seen in the analogous Eu<sup>III</sup> complex of L<sup>8</sup>, each possesses two clear inflexion points. The first occurs upon the addition of *ca.* 5.5 mL of base and corresponds to the completion of neutralisation of the acidified free ligand, whilst the second inflexion point after *ca.* 6 mL of base is a consequence of the completion of neutralisation of the monoprotonated complex, MLH.

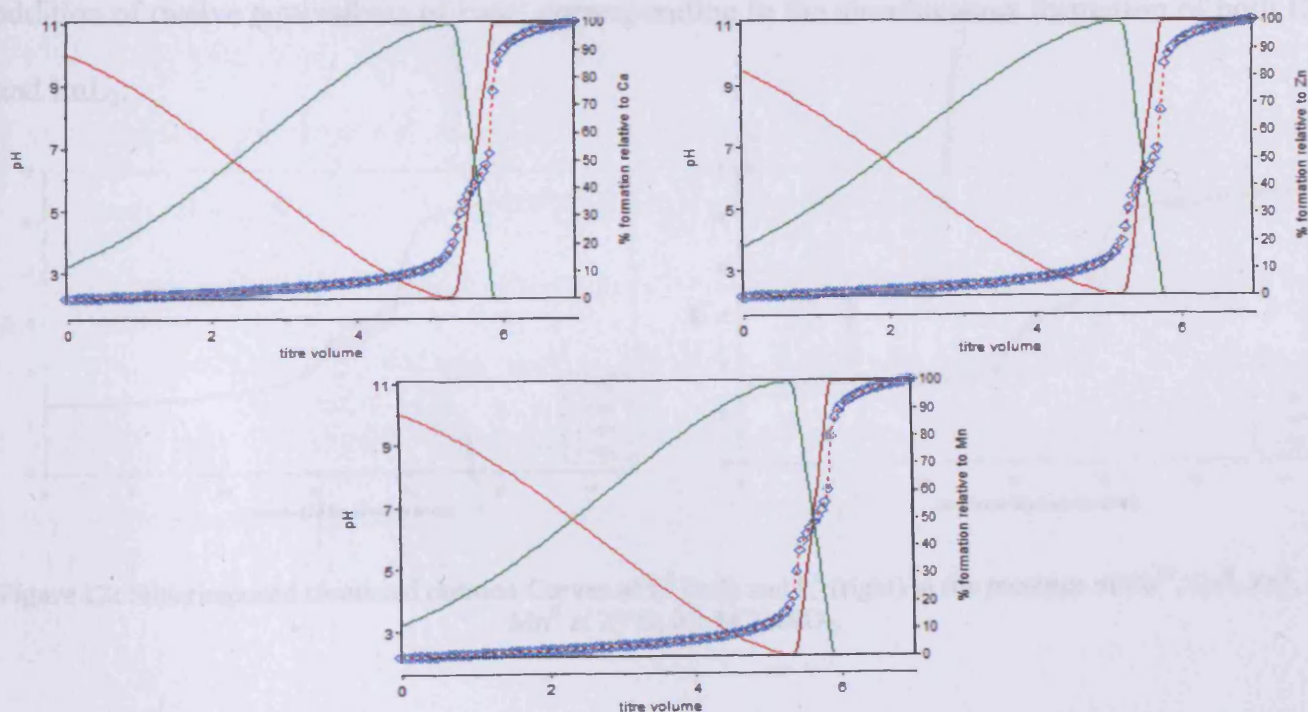


**Figure 11:** Titration Curves of L<sup>8</sup> in the presence of Ca<sup>II</sup> (top left), Zn<sup>II</sup> (top right) and Mn<sup>II</sup> (bottom middle) at 25°C, 0.1 M NaNO<sub>3</sub>.

## Chapter 4: The Determination of Stability Constants for a Series of Pyridine-Carboxylate Based Tripodal Ligand Frameworks

**Table 5:** Stability constants of ligands L<sup>6</sup>-L<sup>8</sup> with Ca<sup>II</sup>, Zn<sup>II</sup> and Mn<sup>II</sup>

Quotient	Constant	L <sup>6</sup>	L <sup>7</sup>	L <sup>8</sup>
[CaL]/[Ca][L]	log K <sub>CaL</sub>	8.39(3)	8.64(4)	9.12(4)
[CaLH]/[CaL][H]	log K <sub>CaLH</sub>	6.11(3)	5.23(2)	5.84(3)
	pCa (pH = 7.4)	9.3	9.6	10.1
[ZnL]/[Zn][L]	log K <sub>ZnL</sub>	8.08(2)	8.55(3)	9.19(4)
[ZnLH]/[ZnL][H]	log K <sub>ZnLH</sub>	6.22(3)	5.94(3)	6.02(4)
	pZn (pH = 7.4)	9.0	9.5	10.1
[MnL]/[Mn][L]	log K <sub>MnL</sub>	7.86(4)	8.27(3)	8.52(3)
[MnLH]/[MnL][H]	log K <sub>MnLH</sub>	6.35(1)	5.98(4)	6.43(3)
	pMn (pH = 7.4)	8.8	9.1	9.2

The simulated titration curves of L<sup>6</sup> and L<sup>7</sup> in the presence of Eu<sup>III</sup>, Ca<sup>II</sup>, Zn<sup>II</sup> and Mn<sup>II</sup> have been superimposed in Figure 12 in order to highlight the similarities which are observed across this series of compounds. In most instances, both of these ligands contain features analogous to those described in the preceding example. However, the titration curve of L<sup>6</sup> in the presence of Eu<sup>III</sup> is clearly different and reveals just a single sharp inflexion point upon the addition of twelve equivalents of base, corresponding to the simultaneous formation of both EuL and EuL<sub>2</sub>.

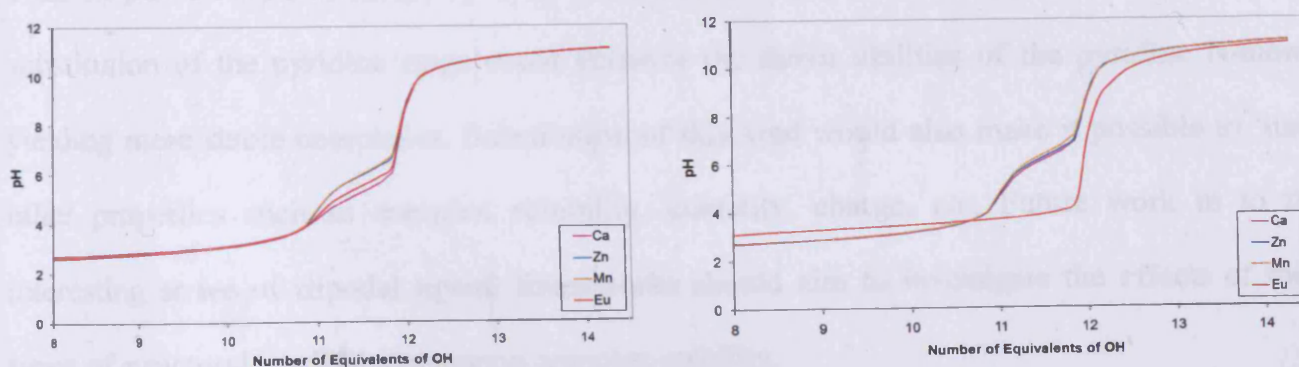


**Figure 12:** Superimposed simulated titration Curves of L<sup>7</sup> (left) and L<sup>6</sup> (right) in the presence of Eu<sup>III</sup>, Ca<sup>II</sup>, Zn<sup>II</sup>, and Mn<sup>II</sup> at 25°C, 0.1 M NaNO<sub>3</sub>.

## 4.4 Conclusions

A critical factor in the development of a successful MRI contrast agent is the lanthanide sequestering ability of the ligand. With this purpose in mind, the protonation constants of the ligand series L<sup>6</sup>-L<sup>8</sup> and the stability constants of the corresponding europium complexes have been determined *via* potentiometric methods in conjunction with the HyperQuad suite of programs. The stability constants of the complexes formed between this ligand series and some physiologically relevant metals (Ca<sup>II</sup>, Zn<sup>II</sup> and Mn<sup>II</sup>) have also been established. Furthermore, the computational program HySS has been used to produce simulated species distribution plots which provide an insightful and convenient means of visualising the relative distributions of each species throughout the course of each titration. Using this data it was possible to extract other useful information such as the pM values which highlight the extent of dissociation of these complexes in conditions similar to those in biological media.

Ligands L<sup>6</sup>-L<sup>8</sup> can each be seen to bind preferentially with Eu<sup>III</sup> over Ca<sup>II</sup>, Zn<sup>II</sup> and Mn<sup>II</sup> (Fig. 13), however, while the stability of this series of ligands does not compare favourably with even the poorest commercially available contrast agents.\* It is anticipated, however, that suitable substitution of the pyridine rings could enhance the donor abilities of the pyridine N-atoms, yielding more stable complexes. Substitution of this kind would also make it possible to ‘tune’ other properties such as complex solubility, denticity, charge, *etc.* Future work in to this interesting series of tripodal ligand frameworks should aim to investigate the effects of these types of structural modifications upon complex stability.

---

\* DTPA-BMA has the lowest, where pGd = 16.8. The highest is DOTA, where pGd = 25.6.

## Chapter 4: The Determination of Stability Constants for a Series of Pyridine-Carboxylate Based Tripodal Ligand Frameworks

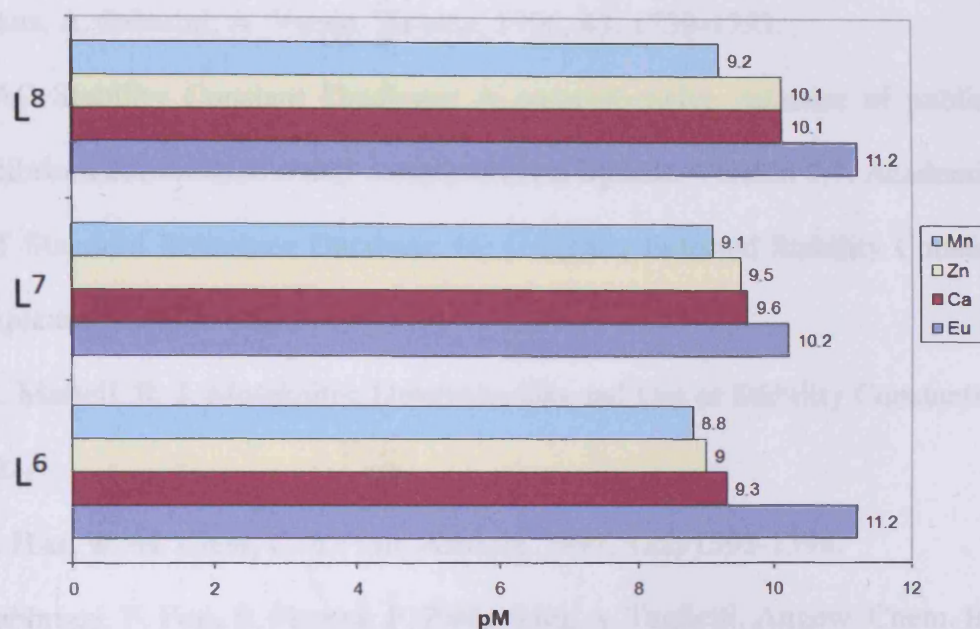


Figure 13: Selectivity of Ligands L<sup>6</sup>-L<sup>8</sup> for Eu<sup>3+</sup> over Ca<sup>2+</sup>, Zn<sup>2+</sup> and Mn<sup>2+</sup>. 25°C, pH 7.4, 0.1 M NaNO<sub>3</sub>, [L]<sub>total</sub> = 10 μM, [M]<sub>total</sub> = 1 μM.

### 4.5 References

1. M. K. Thomas, *British Medical Journal*, 2007, 334.
2. M. J. Adam, D. S. Wilbur, *Chem. Soc. Rev.*, 2005, 34, 153.
3. S. H. Britz-Cunningham, S. J. Adelstein, *J. Nucl. Med.*, 2003, 44, 1945.
4. P. Caravan, J. J. Ellison, T. J. McMurry, R. B. Lauffer, *Chem. Rev.*, 1999, 99, 2293.
5. S. Aime, M. Botta, Terreno, *Adv. Inorg. Chem.*, 2005, 57, 173.
6. H. Von Euler, *Ber.*, 1903, 1854.
7. G. Bodlander, O. Z. Storbeck, *Anorg. Chem.*, 1902, 31.
8. N. Bjerrum, Ph.D. Dissertation, Copenhagen, 1908.
9. J. Bjerrum, Thesis, Copenhagen, 1941; reprinted 1957, P. Haase and Son, Copenhagen.
10. F. J. C. Rossotti, H. Rossotti, *The Determination of Stability Constants*, McGraw-Hill: New York, 1961.

#### Chapter 4: The Determination of Stability Constants for a Series of Pyridine-Carboxylate Based Tripodal Ligand Frameworks

11. P. Gans, A. Sabatini, A. Vacca, *Talanta*, 1996, 43, 1739-1753.
12. IUPAC Stability Constant Database: A comprehensive database of published data on equilibrium constants of metal complexes and ligands. Version 5.7. Academic Software.
13. NIST Standard Reference Database 46. Critically Selected Stability Constants of Metal Complexes. Version 8.0.
14. A. E. Martell, R. J. Motekaitis, *Determination and Use of Stability Constants*, 2<sup>nd</sup> Edition, 1992.
15. J.-C. Hsu, W.-H. Chen, C.-Y. Liu, *Analyst*, 1997, 122, 1393-1398.
16. L. Fabbrizzi, F. Foti, S. Patroni, P. Pallavicini, A. Taglietti, *Angew. Chem. Int. Ed.*, 2004, 43, 5073-5077.
17. M. R. Yashiro, *Biol. Inorg. Chem.*, 2004, 9, 914-921.
18. G. Arena, A. Contino, E. Longo, D. Sciotto, G. Spoto, *J. Chem. Soc.-Perkin Trans.*, 2001, 2, 2287-2291.
19. Y. Hara, M. Akiyama, *J. Am. Chem. Soc.*, 2001, 123, 7247-7256.
20. H. Uchimura, A. Tajiri, M. Hatano, *Bull. Chem. Soc. Jpn.*, 1984, 57, 341.
21. K. Nakamoto, *J. Phys. Chem.*, 1960, 64, 1420.
22. O. Borgen, B. Mestvedt, I. Skauvik, *Acta Chem. Scand. A*, 1976, 30, 43.
23. M. Eigen, R. G. Wilkins, *Adv. Chem. Ser.*, 1965, 49, 55.
24. N. V. Sidgwick, *J. Chem. Soc.*, 1941, 433-443.
25. S. Ahrland, J. Chatt, N. Davies, *Chem. Soc. Rev.*, 1958, 12, 265.
26. H. Irving, R. J. P. Williams, *Nature*, 1948, 162, 746-747.
27. H. Irving, R. J. P. Williams, *J. Chem. Soc.*, 1953, 3192.
28. P. Gans, B. O'Sullivan, *Talanta*, 2000, 51, 33-37.
29. N. Singh, Ph.D. Dissertation, Cardiff University, 2008.

#### Chapter 4: The Determination of Stability Constants for a Series of Pyridine-Carboxylate Based Tripodal Ligand Frameworks

30. W. L. F Armarego, D. D. Perrin, *Purification of Laboratory Chemicals*, 4<sup>th</sup> Ed., Oxford: Butterworth-Heinemann, 1997.
31. P. Amico, R. Bonomo, R. Cali, *Inorg. Chem.*, 1989, 28, 3555.
32. R. Goldberg, N. Kishore, R. Lennen, *J. Phys. Chem.*, 2002, 31, 231.
33. V. Panyushkin, T. Storozhenko, I. Sukhno, *Zh. Obshch. Khim.*, 2002, 72, 1250.
34. O. Jons, E. Johansen, *Inorg. Chim. Acta*, 1988, 151, 129.
35. H. Matsui, H. Ohtaki, *Bull. Chem. Soc. Jpn.*, 1982, 55, 2131.
36. R. Kulshreshtha, M. Singh, *J. Indian Chem. Soc.*, 1984, 61, 132.
37. F. Gaizer, P. Buxbaum, E. Papp-Molnar, *J. Inorg. Nucl. Chem.*, 1974, 36, 859.
38. E. G-Espana, F. Nuzzi, A. Sabatini, A. Vacca, *Gazz. Chim. Ital.*, 1987, 117, 275; 115, 607.
39. Bogdan, G. Peczely, F. Gaizer, *Polyhedron*, 2001, 20, 1809.
40. L. Campanella, G. D'Angelis, A. Napoli, *Bull. Soc. Chim. Belges*, 1972, 81, 489.
41. M. Emara, N. Farid, A. Wasfi, *Electrochim. Acta*, 1982, 27, 647.
42. C. Rey-Castro, R. Castro-Varela, R. Herrero, *Talanta*, 2003, 60, 93.
43. D. Barron, S. Buti, J. Barbosa, *Phys. Chem. Chem. Phys.*, 1999, 1, 295.
44. F. Crea, G. D'Ascenzo, A. De Robertis, *Talanta*, 2003, 61, 611.
45. M. Zaky, M. Moawad, S. Stefan, *Oriental J. Chem.*, 1988, 4, 247.
46. Y.-M. Wang, T. H. C. Stude, G. C. Liu, R. S. Sheu, T. S. Jaw, *Proc. Intl. Soc. Mag. Reson. Med.*, 2001, 9.
47. Y. Bretonnière, M. Mazzanti, F. A. Dunand, A. E. Merbach and J. P'ecaut, *Inorg. Chem.*, 2001, 40, 6737.
48. M. A. Khan, E. Bentouhami, G. M. Bouet, J. Meullemeestre, F. Vierling, *Comptes Rendus Chimie*, 2004, 7, 5, 537-545.

**Chapter 4: The Determination of Stability Constants for a Series of  
Pyridine-Carboxylate Based Tripodal Ligand Frameworks**

49. J. G. Penfield, R. F. Reilly Jr., *Nature Clinical Practice Nephrology*, 2007, 3, 654-668.

50. W. Cacheris, S. Quay, S. Rocklage, *MRI*, 1990, 8, 467-481.



# **Chapter 5: Determination of Stability Constants for a 2,2'- Bipyridine-Derivatised Tripodal Ligand Series**

## 5.1 Introduction

In chapters two and three, the transition metal complexes of ligands L<sup>3</sup>-L<sup>5</sup> were examined closely in a crystallographic context, as well as in terms of their electrochemical behaviour in solution. This chapter focuses on the determination of stability constants of this ligand series in the presence of Eu<sup>III</sup>, Ca<sup>II</sup>, Zn<sup>II</sup> and Mn<sup>II</sup> metal ions, using the same potentiometric techniques as described in chapter four. This part of the investigation aims to evaluate the efficiency with which this ligand series selectively binds Eu<sup>III</sup> over physiologically relevant metals, and to assess how well this ligand series compares with the analogous carboxylate-functionalised ligand series, L<sup>6</sup>-L<sup>8</sup>. This study considers how modifying the peripheral functions *ortho* to the pyridyl nitrogen of the tris-pyridine core affects overall complex stability and the nature of species formed in solution.

### Solution Structure and Properties of 2,2'-Bipyridine:

The free ligand 2,2'-bipyridine assumes a near-planar *transoid* arrangement in the solid state (Fig. 1a), although in solution there is the possibility of free rotation around the interannular C-C bond. In contrast, the chelate bonding mode requires a *cisoid* arrangement about the interannular bond (Fig. 1b). Likewise, the first protonation of bipyridine changes the conformation from *transoid* to *cisoid*, with the proton being shared between both nitrogens *via* hydrogen bonding.<sup>1-3</sup> The C-C distance, *a*, is relatively independent of metal ion, whereas the M-L bond distance, *r*, and the N-M-N angle,  $\phi$ , depend on the cation used. The formation and decomposition of [M(bpy)<sub>3</sub>]<sup>n+</sup> complexes exhibits a marked pH dependence which fits for a simple Eigen-Wilkins type of mechanism involving monodentate bipy intermediates.<sup>4</sup>

## Chapter 5: Determination of Stability Constants for a 2,2'-Bipyridine-Derivatised Tripodal Ligand Series

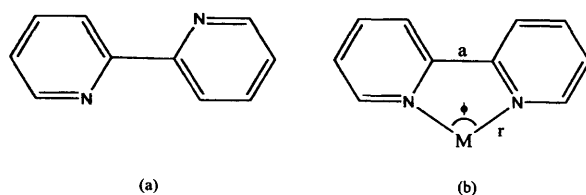


Figure 1: Transoid (a) and cisoid (b) arrangements about the interannular C-C bond.

### 5.1.1 Protonation Constants of 2,2'-Bipyridine and its Derivatives

To date, there have been no fewer than 85 reports of the protonation constants of bipy using a staggering variety of techniques, conditions and media. Collected in Table 2 is a selection of protonation constants determined in methods most similar to those used in this work for comparison. The most noticeable feature of this Table is the relatively small variation that occurs despite changes in temperature, ionic media and strength. The first protonation constant is evidently in the region  $\log K_1 = 4.4 \pm 0.3$ , which is significantly lower than free pyridine ( $\log pK_1 = 5.26^*$ ).<sup>5</sup> This is largely due to the extended conjugation attributable to the presence of a further pyridine ring, offering further stabilisation to the deprotonated form. The second protonation constant is heavily dependent on ionic strength of the supporting medium, however, it is significantly lower in the region  $1.95 \pm 0.8$ . This is due to a combination of factors; firstly, as mentioned previously, the monoprotonated form exists in a *cisoid* conformation with the proton being shared *via* H-bonding between both nitrogen atoms. This requires forcing conditions, *i.e.* lowering pH, in order to protonate both sites. Secondly, the build up of positive charge following the initial protonation will lead to a less favourable electrostatic interaction upon the addition of the second. Thirdly, there is also a statistical contribution to  $K_n$  which is most favourable for the initial protonation as the second proton will have only half the number of sites which are available to the first.

\* Measured at 25°C in aqueous solution, using NaNO<sub>3</sub> (0.1M) supporting electrolyte.

## Chapter 5: Determination of Stability Constants for a 2,2'-Bipyridine-Derivatized Tripodal Ligand Series

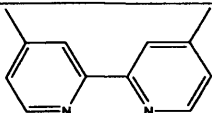
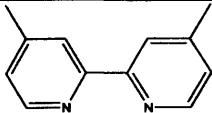
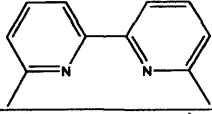
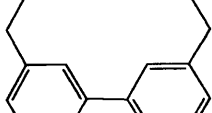
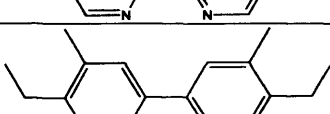
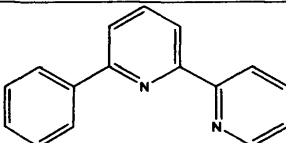
**Table 2:** A Selection of protonation constants for 2,2'-bipyridine from the literature.

Method	Medium	Temp/°C	Conc./M	Log K <sub>1</sub>	Log K <sub>2</sub>	Ref
glass	KNO <sub>3</sub>	25	0.1	4.42	1.5	6
glass	KCl	25	0.2	4.52	1.55	7
glass	NaNO <sub>3</sub>	25	0.1	4.23	1.32	7
glass	NaNO <sub>3</sub>	37	0.1	4.23	1.32	8
glass	KNO <sub>3</sub>	35	0.5	4.4	2.8	8
glass	KNO <sub>3</sub>	30	0.1	4.48	1.51	9
glass	NaClO <sub>4</sub>	35	0.1	4.65	1.52	10
glass	KNO <sub>3</sub>	25	0.1	4.41	1.09	11
glass	KNO <sub>3</sub>	25	0.1	4.11	1.1	12

A search of the SC-Database<sup>13</sup> reveals only a limited selection of protonation constant data (Table 3) involving 2,2'-bipy derivatives. For comparative purposes, the sets of data that have been chosen are reasonably consistent internally so far as salt effects, temperature, and intrinsic accuracy are concerned. However, the low solubility of some ligands has prevented the use of water as a solvent, and a number of protonation constants have been measured in aqueous mixtures with dioxan. It should be noted that with increasing dioxan content there are significant increases in the measured formation constants due to the high dielectric constant of the solvent.<sup>14,15</sup> It can be seen that substitution at any position will alter the protonation constants significantly, for instance the addition of electron-releasing methyl groups, particularly in positions *para* to the N-donor, will decrease the acidity of the initial protonation site by an order of magnitude.

## Chapter 5: Determination of Stability Constants for a 2,2'-Bipyridine-Derivatised Tripodal Ligand Series

**Table 3:** A Selection of protonation constants for 2,2'-bipyridine derivatives extracted from the literature.

Compound	Method	Medium	Temp/°C	Conc.	Log K <sub>1</sub>	Log K <sub>2</sub>	Ref
	emf	KCl	23	0.1M	5.35	-	16
	glass	KNO <sub>3</sub>	25	0.1M	5.32	-	17
	glass	Dioxan mixed solvents	25	50%	4.23	-	18
	glass	Dioxan mixed solvents	25	50%	4.38	-	18
	glass	Dioxan mixed solvents	25	50%	4.59	-	18
	glass	unknown	25	2M	4.18	1.0	19

### 5.1.2 The Stability Constants for a Series of Tris 2,2'-Bipy Complexes

A collection of stability constants relating to the tris 2,2'-bipyridine complexes of Eu<sup>III</sup>, Ca<sup>II</sup>, Zn<sup>II</sup> and Mn<sup>II</sup> in a range of conditions have been compiled in Table 4. In most cases, a series of stepwise stability constants (log K<sub>1</sub>, log K<sub>2</sub> and log K<sub>3</sub>) have been reported, corresponding to the consecutive species [M(bipy)]<sup>n+</sup>, [M(bipy)<sub>2</sub>]<sup>n+</sup> and [M(bipy)<sub>3</sub>]<sup>n+</sup>. These constants all proceed in the order log K<sub>1</sub> > log K<sub>2</sub> > log K<sub>3</sub>, largely due to the statistical contribution to K<sub>n</sub> which is most favourable for the co-ordination of the first bipyridine to the metal centre. The co-ordination of the second bipyridine will have only two-thirds the number of sites which are available to the first, and similarly, the third bipyridine group only has one-third of the sites available to the first.

## Chapter 5: Determination of Stability Constants for a 2,2'-Bipyridine-Derivatised Tripodal Ligand Series

**Table 4:** A selection of stability constants for tris 2,2'-bipyridine complexes extracted from the literature.

Metal	Method <sup>a</sup>	Medium	Temp/°C	Conc.	Log K <sub>1</sub>	Log K <sub>2</sub>	Log K <sub>3</sub>	Comment	Ref
Eu <sup>3+</sup>	sp	non-aq	25	100%	2.75			Ethylacetate	20
Ca <sup>2+</sup>	sp	non-aq	25	100%	2.71	2.1	1.0	Acetonitrile	21
Ca <sup>2+</sup>	sp	non-aq	25	100%	2	0.66		Acetone	21
Ca <sup>2+</sup>	sp	non-aq	25	100%	1.66	0.9		Methanol	21
Zn <sup>2+</sup>	gl	KNO <sub>3</sub>	25	0.10M	5.04	4.56	3.6		11
Zn <sup>2+</sup>	gl	KNO <sub>3</sub>	30	1.0M	5.26	4.55	3.96		22
Zn <sup>2+</sup>	gl	KNO <sub>3</sub>	25	0.10M	5.4	4.4	3.5		23
Zn <sup>2+</sup>	gl	NaNO <sub>3</sub>	20	0.10M	5.3	4.53	3.8		24
Zn <sup>2+</sup>	gl	NaClO <sub>4</sub>	25	1.0M	4.89	4.58	4.27		25
Mn <sup>2+</sup>	sp	NaClO <sub>4</sub>	25	0.20M	2.97				26
Mn <sup>2+</sup>	sp	NaClO <sub>4</sub>	25	0.30M	2.57				27
Mn <sup>2+</sup>	dis	KNO <sub>3</sub>	30	1.0M	2.54	1.85	1.51		28
Mn <sup>2+</sup>	gl	NaClO <sub>4</sub>	25	1.0M	4.06	3.78	3.63		29
Mn <sup>2+</sup>	dis	KCl	25	0.10M	2.62	2	1.1		30

<sup>a</sup>Abbreviations: sp = spectrophotometry; gl = glass electrode; dis = distribution.

Comparing stability constants which have been determined in different media and/or using different experimental parameters (*e.g.* ionic strength, temperature *etc.*) is inadvisable, therefore the europium and calcium complexes will not be discussed in relation to the other complexes, however it is evident that in both instances the metal ions exhibit a strong affinity for bipyridyl co-ordination. This is not surprising and is clearly due to the entropy increase associated with the displacement of monodentate solvent molecules with a bidentate chelate (*cf.* Section 4.1.4). It is also evident that Zn<sup>II</sup> forms more stable complexes than Mn<sup>II</sup> in identical conditions.<sup>25,29</sup> This is in agreement with the Irving-Williams order (*cf.* Section 4.1.6) and is a largely the result of the larger ionic potential, *i.e.*, the charge to radius ratio of the zinc cation.

## 5.2 Experimental

The experimental procedures for potentiometric titrations are consistent with those described in chapter four.

### 5.3 Results and Discussion

The models yielding the best fits between the measured and calculated titration data, together with the refined stability constants, are reported in Tables 4-6. Selection of the equilibrium models was based on a critical evaluation of the least-squares fitting results, namely analysis of the weighted residuals and statistical parameters ( $\chi^2$  and  $\sigma$ ).<sup>31</sup> The tetra-, penta- and hexadentate ligands have four, five and six protonation constants respectively. In accordance with related literature compounds (Tables 2 and 3), it is clear the three least acidic constants in each case, ranging from 4.08 to 4.75, are attributable to either the initial protonation of a bipyridyl arm or the protonation of a pyridine which is not part of a bipyridyl group. The remaining constants, ranging from 1.80 to 2.15, are attributable to the second protonation of a bipyridyl group. The overall sum of the basicities increases in accordance with the number of donors atoms, however, these are much lower than those observed for the related pyridine-carboxylate based ligands examined in the previous chapter. It can reasonably be expected that considering the reduced basicities and electrostatic contributions, these ligands will form more unstable metal complexes.

**Table 4.** Thermodynamic Properties for the Ligands L<sup>3</sup> – L<sup>5</sup>

Quotient	Constant	L <sup>4</sup>	L <sup>5</sup>	L <sup>3</sup>
[LH]/[L][H]	log K <sub>LH</sub>	4.75(3)	4.63(3)	4.71(2)
[LH <sub>2</sub> ]/[LH][H]	log K <sub>LH2</sub>	4.21(2)	4.55(2)	4.36(4)
[LH <sub>3</sub> ]/[LH <sub>2</sub> ][H]	log K <sub>LH3</sub>	4.08(3)	4.12(3)	4.24(3)
[LH <sub>4</sub> ]/[LH <sub>3</sub> ][H]	log K <sub>LH4</sub>	1.89(1)	2.12(3)	2.15(3)
[LH <sub>5</sub> ]/[LH <sub>4</sub> ][H]	log K <sub>LH5</sub>	-	1.99(4)	2.05(1)
[LH <sub>6</sub> ]/[LH <sub>5</sub> ][H]	log K <sub>LH6</sub>	-	-	1.8(4)
ΣpKa		14.93	17.41	19.31

<sup>a</sup> All constants were determined at 25°C and 0.1 M NaNO<sub>3</sub>.

Chapter 5: Determination of Stability Constants for a  
2,2'-Bipyridine-Derivatised Tripodal Ligand Series

Indeed, the stability constants for the  $\text{Eu}^{\text{III}}$  complexes are approximately an order of magnitude less stable than the pyridine-carboxylate based frameworks. This is reflected most significantly by the pM values which indicate a considerable degree of uncomplexed europium at pH 7.4. As expected, the overall stability increases significantly in accordance with the donor capacity of each ligand, however it is worth noting this seemingly has little effect on the formation constant of the monoprotonated complex ( $\text{EuLH}$ ) which ranges between 5.24 and 5.65. Comparison between the logarithmic formation constants of the monoprotonated complexes of the three ligands is difficult because they differ slightly in proton dependence. There are no relevant bipyridine-containing  $\text{Eu}^{\text{III}}$  complexes for which stability constant data is available for a reliable comparison. However, the  $\text{Eu}^{\text{III}}$  complex of a similar tetradentate compound *N,N'*-dimethyl-1,10-phenanthroline-2,9-dimethanamine<sup>32</sup> (Fig. 2) has an overall stability constant,  $\log K_1 = 7.47$  (where  $K_1 = [\text{ML}]/[\text{M}][\text{L}]$ ) and a monoprotonated form ( $\text{EuLH}$ ) with an formation constant,  $\log K_{111}$ , of 7.06.

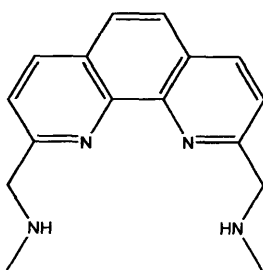


Figure 2: *N,N'*-dimethyl-1,10-phenanthroline-2,9-dimethanamine

Table 5: Stability constants of ligands  $\text{L}^5$ - $\text{L}^7$  with  $\text{Eu}^{\text{III}}$

Quotient	Constant	$\text{L}^4$	$\text{L}^5$	$\text{L}^3$
$[\text{EuL}]/[\text{Eu}][\text{L}]$	$\log K_{\text{EuL}}$	7.97(4)	8.43(4)	9.12(3)
$[\text{EuLH}]/[\text{EuL}][\text{H}]$	$\log K_{\text{EuLH}}$	5.24(3)	5.65(2)	5.63(3)
$[\text{EuH}_{-1}]/[\text{Eu}][\text{H}_{-1}]$	$\log K_{\text{EuH}_{-1}}$	-8.37	-8.37	-8.37
	pEu (pH = 7.4)	8.9	9.4	10.1



All three  $\text{Eu}^{\text{III}}$  complexes present very similar species distribution plots, the most notable difference is the relative proportion of the monoprotonated complex at low pH. Ligand  $\text{L}^4$  has the smallest  $\text{EuLH}$  formation constant and consequently is deprotonated more readily upon the addition of base. This leads to a slightly narrower region across which  $\text{EuLH}$  is present and the formation of  $\text{EuL}$  at a comparatively lower pH. Conversely, ligands  $\text{L}^5$  and  $\text{L}^3$ , which have the same  $\text{EuLH}$  formation constants within statistical error, are  $0.40 \pm 0.01$  pKa units larger than  $\text{L}^4$  and consequently the speciation plots reveal the concentration of  $\text{EuLH}$  'peaking' across a wider pH range.

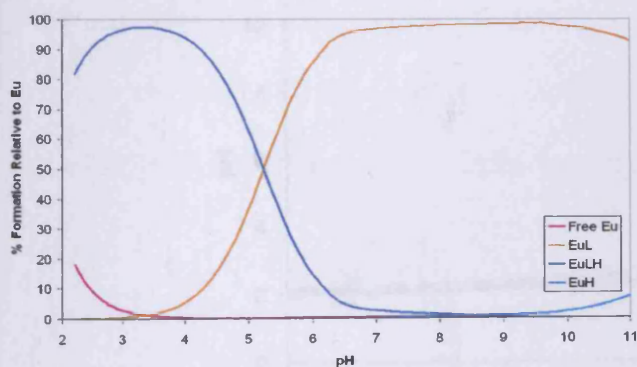


Figure 3: Speciation diagram for  $\text{L}^4$  in the presence of  $\text{Eu}^{\text{III}}(\text{NO}_3)_3 \cdot 6\text{H}_2\text{O}$

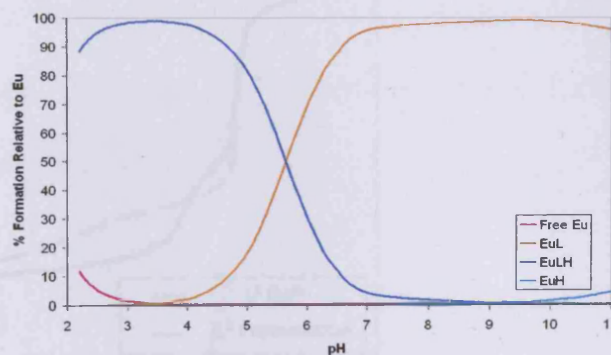


Figure 4: Speciation diagram for  $\text{L}^5$  in the presence of  $\text{Eu}^{\text{III}}(\text{NO}_3)_3 \cdot 6\text{H}_2\text{O}$

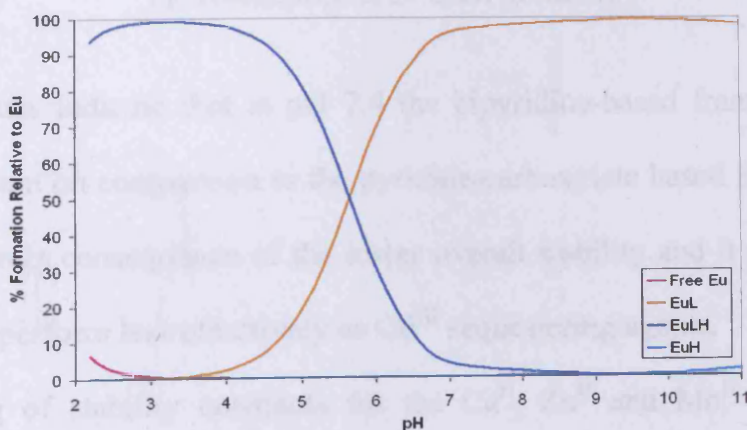
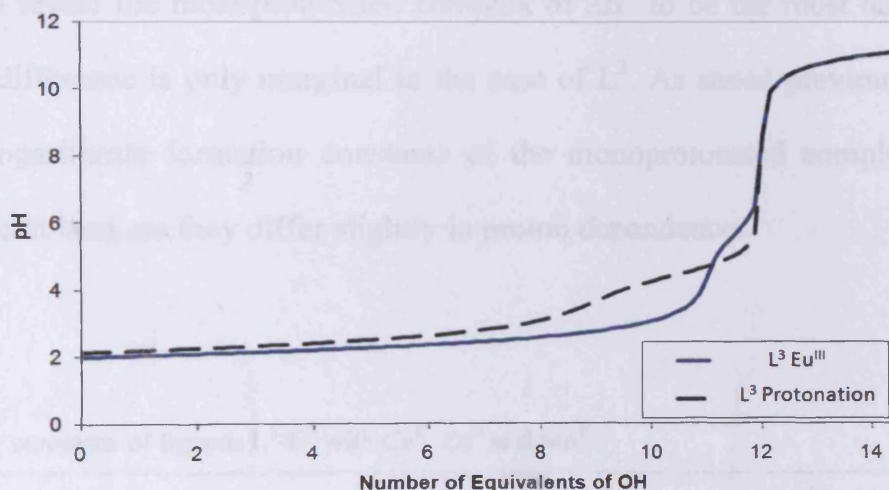


Figure 5: Speciation diagram for  $\text{L}^3$  in the presence of  $\text{Eu}^{\text{III}}(\text{NO}_3)_3 \cdot 6\text{H}_2\text{O}$

The titration curve of  $L^3$  in the presence of  $Eu^{III}$  is presented in Figure 6, together with the protonation titration curve for comparative purposes. Upon close inspection, it is clear the ligand is fully deprotonated after twelve molar equivalents of base, the completion of this neutralisation is reflected by a well-defined inflexion point. The slight 'hump' is an indication of the considerable difference between the three least acidic protonation sites and the three most acidic. The formation of the  $EuL$  species occurs concurrently with complete ligand deprotonation as expected. The preceding inflexion point is an indication of the completion of formation of the  $EuLH$  species.



**Figure 6:** Titration Curve of  $L^3$  + 8 molar equivalents of  $HNO_3$  in the presence of  $Eu^{III}(NO_3)_3 \cdot 6H_2O$  at  $25^\circ C$ ,  $0.1 M NaNO_3$ .

The  $pEu$  values indicate that at  $pH 7.4$  the bipyridine-based frameworks lead to more uncomplexed europium on comparison to the pyridine-carboxylate based ligands of the previous chapter. This is a direct consequence of the lower overall stability and it can be concluded that these ligands would perform less effectively as  $Gd^{III}$  sequestering agents.

The ordering of stability constants for the  $Ca^{II}$ ,  $Zn^{II}$  and  $Mn^{II}$  complexes (Table 6) increases in order of effective nuclear charge ( $Ca^{II} < Mn^{II} < Zn^{II}$ ) in agreement with the Irving-

Chapter 5: Determination of Stability Constants for a  
2,2'-Bipyridine-Derivatized Tripodal Ligand Series

Williams order. As expected, analysis of the titration data reveals 1:1 metal to ligand ratios for each set of metal complexes. The titration curves are presented in Figures 7 – 9.

Ligand L<sup>4</sup> reveals an initial inflexion point in the presence of Eu<sup>II</sup>, Ca<sup>II</sup> and Mn<sup>II</sup> after the addition of approximately eleven equivalents of base, indicating the formation of species [MLH]. The second inflexion point after the addition of approximately twelve equivalents of base indicates the completion of deprotonation of [MLH] and the consequent formation of [ML]. The Zn<sup>II</sup> complex also undergoes this progression, however it is not apparent in the titration curve as log K<sub>111</sub> is comparatively much smaller than log K<sub>110</sub>, and thus the two appear combined. Both L<sup>5</sup> and L<sup>3</sup> also reveal the monoprotonated complex of Zn<sup>II</sup> to be the most acidic, however the extent of this difference is only marginal in the case of L<sup>3</sup>. As stated previously, a comparison between the logarithmic formation constants of the monoprotonated complexes of the three ligands is difficult because they differ slightly in proton dependence.

**Table 6:** Stability constants of ligands L<sup>3</sup>-L<sup>5</sup> with Ca<sup>II</sup>, Zn<sup>II</sup> and Mn<sup>II</sup>

Quotient	Constant	L <sup>4</sup>	L <sup>5</sup>	L <sup>3</sup>
[CaL]/[Ca][L]	log K <sub>CaL</sub>	5.72(7)	6.01(3)	6.90(6)
[CaLH]/[CaL][H]	log K <sub>CaLH</sub>	5.55(2)	5.23(4)	5.72(3)
	pCa (pH = 7.4)	6.8	7.0	7.9
[ZnL]/[Zn][L]	log K <sub>ZnL</sub>	7.59(6)	8.39(5)	8.71(5)
[ZnLH]/[ZnL][H]	log K <sub>ZnLH</sub>	3.64(2)	4.07(3)	5.42(3)
	pZn (pH = 7.4)	8.5	9.3	9.6
[MnL]/[Mn][L]	log K <sub>MnL</sub>	6.14(2)	6.53(5)	6.89(4)
[MnLH]/[MnL][H]	log K <sub>MnLH</sub>	4.68(1)	6.08(5)	6.65(2)
	pMn (pH = 7.4)	7.1	7.5	7.9

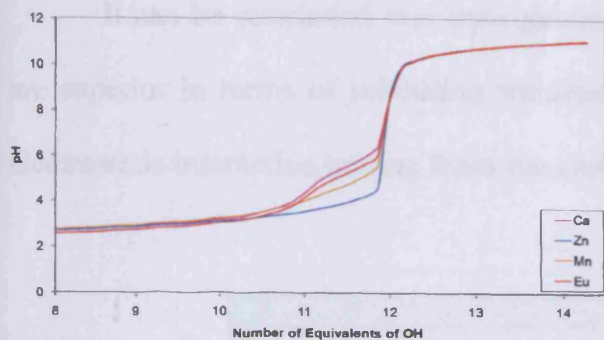


Figure 7: Titration Curve of  $L^4$  in the presence of  $Eu^{III}$ ,  $Ca^{II}$ ,  $Zn^{II}$  and  $Mn^{II}$  at  $25^\circ C$ ,  $0.1 M NaNO_3$ .

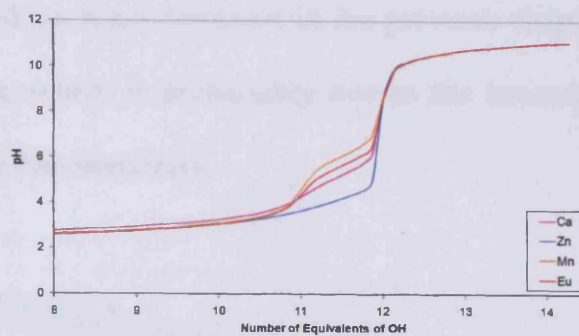


Figure 8: Titration Curve of  $L^5$  in the presence of  $Eu^{III}$ ,  $Ca^{II}$ ,  $Zn^{II}$  and  $Mn^{II}$  at  $25^\circ C$ ,  $0.1 M NaNO_3$ .

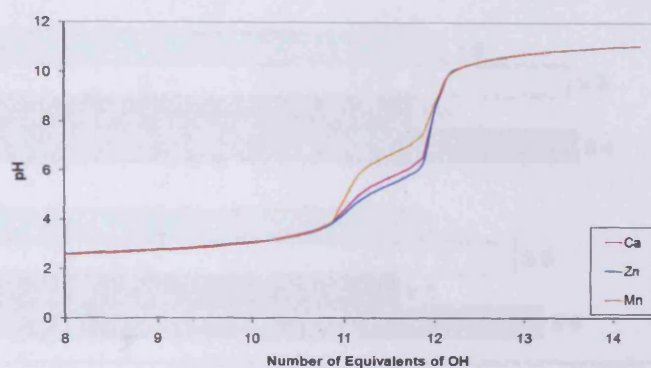


Figure 9: Titration Curve of  $L^3$  in the presence of  $Ca^{II}$ ,  $Zn^{II}$  and  $Mn^{II}$  at  $25^\circ C$ ,  $0.1 M NaNO_3$ .

## 5.4 Conclusions

This chapter has examined the protonation constants of the ligand series  $L^3 - L^5$  and the stability constants of the corresponding  $Eu^{III}$ ,  $Ca^{II}$ ,  $Zn^{II}$  and  $Mn^{II}$  complexes. It is imperative for ligands which are used to sequester gadolinium for medical imaging purposes to show selectivity for  $Gd^{III}$  over  $Ca^{II}$ . This is largely due to the potential development of hypocalcemia resulting from transmetallation.<sup>33</sup> A comparison of the pM values at pH 7.4 (Fig. 10) reveals that ligands  $L^3 - L^5$  each show modest selectivity for  $Eu^{III}$  over  $Ca^{II}$ . Whilst the hexadentate ligand,  $L^3$ , clearly has a higher overall pEu value (10.1), it is the pentadentate ligand,  $L^5$ , which exhibits the greatest selectivity for  $Eu^{III}$  over  $Ca^{II}$ .

It can be concluded that the ligands L<sup>6</sup>-L<sup>8</sup> which were discussed in the previous chapter are superior in terms of inhibiting transmetallation, which is presumably due to the increased electrostatic interaction arising from the carboxylate functionalities.

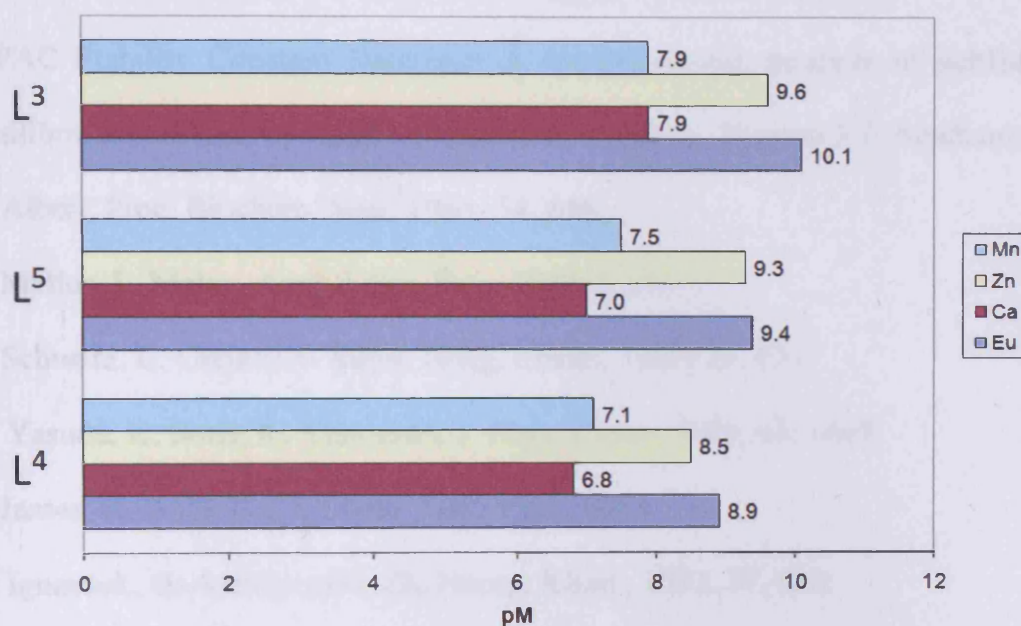


Figure 10: Selectivity of Ligands L<sup>3</sup>-L<sup>5</sup> for Eu<sup>3+</sup> over Ca<sup>2+</sup>, Zn<sup>2+</sup> and Mn<sup>2+</sup>. 25°C, pH 7.4, 0.1 M NaNO<sub>3</sub>, [L]<sub>total</sub> = 10 μM, [M]<sub>total</sub> = 1 μM

## 5.5 References

1. H. Uchimura, A. Tajiri, M. Hatano, Bull. Chem. Soc. Jpn., 1984, 57, 341.
2. K. Nakamoto, J. Phys. Chem., 1960, 64, 1420.
3. O. Borgen, B. Mestvedt, I. Skauvik, Acta. Chem. Scand. A, 1976, 30, 43.
4. M. Eigen, R. G. Wilkins, Adv. Chem. Ser., 1965, 49, 55.
5. D. Banerjea, T. Kaden, H. Sigel, Inorg. Chem., 1981, 20, 2586.
6. G. Condike, A. Martell, J. Inorg. Nucl. Chem., 1969, 31, 2455.
7. T. Jakusch, P. Buglyo, J. Pessoa, T. Kiss, Inorg. Chim. Acta, 2002, 339, 119.
8. G. Mukherjee, A. Das, Proc. Indian Acad. Sci., 2002, 114, 163.

Chapter 5: Determination of Stability Constants for a  
2,2'-Bipyridine-Derivatised Tripodal Ligand Series

9. C. Reddy, Shivaraj, M. Reddy, *J. Indian Chem. Soc.*, 1994, 71, 59.
10. S. Abbasi, *Pol. J. Chem.*, 1983, 57, 727.
11. P. Daniele, G. Ostacoli, P. Amico, *Talanta*, 1978, 25, 177.
12. G. Ostacoli, P. Daniele, A. Vanni, *Ann. Chim. (Rome)*, 1975, 65, 197.
13. IUPAC Stability Constant Database: A comprehensive database of published data on equilibrium constants of metal complexes and ligands. Version 5.7. Academic Software.
14. A. Albert, *Proc. Biochem. Soc.*, 1953, 54, 646.
15. D. Mellor, L. Maley, *Aust. J. Sci. Res.*, 1949, 2, 92.
16. H. Schwarz, C. Creutz, N. Sutin, *Inorg. Chem.*, 1985, 24, 433.
17. M. Yasuda, K. Sone, K. Yamasaki, *J. Phys. Chem.*, 1956, 60, 1667.
18. B. James, R. Williams, *J. Chem. Soc.*, 1961, 2007.
19. M. Ignaczak, G. Andrijewski, *Zh. Neorg. Khim.*, 1992, 37, 833.
20. V. Smagina, E. Yudina, *Zh. Neorg. Khim.*, 2005, 50, 213.
21. J. Ghasemi, M. Shamsipur, *J. Coord. Chem.*, 1992, 26, 337.
22. R. Davies, K. Dunning, *J. Chem. Soc.*, 1965, 4168.
23. M. Yasuda, K. Sone, K. Yamasaki, *J. Phys. Chem.*, 1956, 60, 1667.
24. G. Anderegg, *Helv. Chim. Acta*, 1963, 46, 2397.
25. G. Atkinson, J. Bauman, *Inorg. Chem.*, 1962, 1, 900.
26. M. Emara, M. Bahr, *Bull. Soc. Chim. Fr.*, 1983, 1, 25.
27. D. Hague, S. Martin, *J. Chem. Soc., Dalton Trans.*, 1974, 254.
28. R. Davies, K. Dunning, *J. Chem. Soc.*, 1965, 4168.
29. G. Atkinson, J. Bauman, *Inorg. Chem.*, 1962, 1, 900.
30. H. Irving, D. Mellor, *J. Chem. Soc.*, 1962, 5222-5237.
31. A. Sabatini, A. Vaca, P. Gans, *Talanta*, 1974, 21, 53.

Chapter 5: Determination of Stability Constants for a  
2,2'-Bipyridine-Derivatised Tripodal Ligand Series

32. Z.-M. Wang, Z.-F. Zhou, H.-K Lin, *Acta Chimica Sinica*, 2001, 59, 701.
33. J.-M. Idée, M. Port, I. Raynal, M. Schaefer, S. Le Greneur, C. Corot, *Fund. Clin. Pharmacol.*, 2006, 20, 6, 563-576. *Erratum*: *Fund. Clin. Pharmacol.*, 2007, 21, 3, 335.

# **Chapter 6: Novel Gd(III) Complexes as MRI Contrast Agents: Measuring Efficiency *via* Relaxometry**



## 6.1 Introduction

Magnetic resonance imaging (MRI) over the last three decades has cemented itself as an indispensable medical imaging technique among the various diagnostic modalities. The procedure has emerged as a valuable tool due to its exceptional capacity for differentiating types of soft tissue, coupled with its non-invasive nature and lack of harmful ionising radiation. Its excellent spatial resolution has proved useful in the location of tumours, assessing organ perfusion, occurrence of abnormalities in kidney clearance, and circulation problems.<sup>1,2</sup> Its applications are also useful in biomedical research enabling the acquisition of high resolution, three-dimensional images of the distribution of water *in vivo*.<sup>3,4</sup>

### Underlying Principles of Magnetic Resonance Imaging<sup>5-8</sup>

Spin is a fundamental property of nature possessed by protons, electrons, and neutrons. Each one of these individually comprises a spin of a half and can be positive or negative. Any arrangement of these subatomic particles in an atom will lead to a combined value of zero, 1/2, 1, 3/2 and so on in multiples of 1/2. Within a magnetic field of strength  $B$ , a particle with a net spin can absorb a photon, of frequency  $\nu$ . The frequency,  $\nu$ , depends on the gyromagnetic ratio,  $\gamma$ , of the particle.

$$\nu = \gamma B \quad (1)$$

For hydrogen,  $\gamma = 42.58 \text{ MHz / T}$ .

A proton has a magnetic moment vector, and when the proton is placed in an externally applied magnetic field, the spin vector of the particle aligns itself with this field. There is a low energy configuration in which the proton lies parallel to the direction of the magnetic field, and also a high energy configuration where the proton lies in an anti-parallel fashion. The exposure

Chapter 6: Novel Gd(III) Complexes as MRI Contrast Agents:  
Measuring Efficiency *via* Relaxometry

of this system to radio-frequency (RF) radiation can lead to a low energy proton transitioning to the higher energy state. This occurrence is dependent on the condition that the absorbed photon is of equal energy to the separation between these two states. The energy of a photon required to induce such a transition is referred to as the resonance (or Larmor) frequency, and is related to its frequency,  $\nu$ , by Planck's constant ( $h = 6.626 \times 10^{-34}$  J s).

$$E = h\nu \quad (2)$$

Combining equations (1) and (2) leads to the expression:

$$E = h\gamma B \quad (3)$$

The slight excess of spins in the lower energy level,  $N^+$ , compared to the higher energy level,  $N^-$ , is reflected in expression (4):

$$N^-/N^+ = e^{-E/kT} \quad (4)$$

where  $E$  is the difference in energy difference of the high and low energy spin states;  $k$  is Boltzmann's constant ( $1.3805 \times 10^{-23}$  J/Kelvin); and  $T$  is the temperature in Kelvin. The ratio  $N^-/N^+$  will decrease as the temperature decreases. As the temperature increases, the difference in population between energy states will eventually become zero.

The signal intensity observed in MRI is a result of the difference between the energy absorbed by nuclei which undergo a transition to a higher energy spin state, and the energy released by nuclei which simultaneously transition back to the lower energy state. Therefore it is proportional to the population difference between the states. The sensitivity of MRI is very beneficial and is a direct consequence of the exchange of energy at a specific frequency between the spins and the spectrometer. There are other factors which influence the MRI signal; these include the natural abundance of the isotope and biological abundance of the nuclei of interest.

The advantage of ‘targeting’  $^1\text{H}$  is that the natural abundance is very high (99.985%), the remaining percent accountable to deuterium and tritium.

### 6.1.1 $T_1$ ‘Longitudinal/Spin-Lattice’ Relaxation

The net magnetisation vector upon equilibrium lies parallel to the direction of the externally applied magnetic field  $B_0$ ,\* and is termed the equilibrium magnetisation  $M_0$ . There are no transverse ( $M_x$  or  $M_y$ ) components, and thus the net magnetisation is composed entirely of the longitudinal magnetisation vector,  $M_z$ .

The exposure of the nuclear spin system to RF radiation of a frequency equal to the energy difference between the spin states will alter the net magnetisation vector and will acquire a transverse component. The nuclei will naturally rotate about the Z axis at a frequency equal to the frequency of the photon which induces a transition between the two energy states. This is termed the Larmor frequency. If the RF radiation is of sufficient intensity, the spin system will become saturated and the net magnetisation vector will become entirely composed of transverse components, thus  $M_z$  becomes zero.

Upon ceasing the exposure to radiation, the spin system will relax back to the initial equilibrium state. The longitudinal magnetisation vector then returns to its initial equilibrium value by a factor of  $e$ . The time constant which describes this process is called the spin lattice relaxation time,  $T_1$ . Equation (5) describes the behaviour of  $M_z$  as a function of the time  $t$  after its initial displacement.

$$M_z = M_0 ( 1 - e^{-t/T_1} ) \quad (5)$$

---

\* The magnetic field during a clinical MRI scan is typically between 15 and 80 MHz for hydrogen imaging.

Thus, after time  $T_1$  the longitudinal magnetisation will have returned to 63% of its initial value (see below).

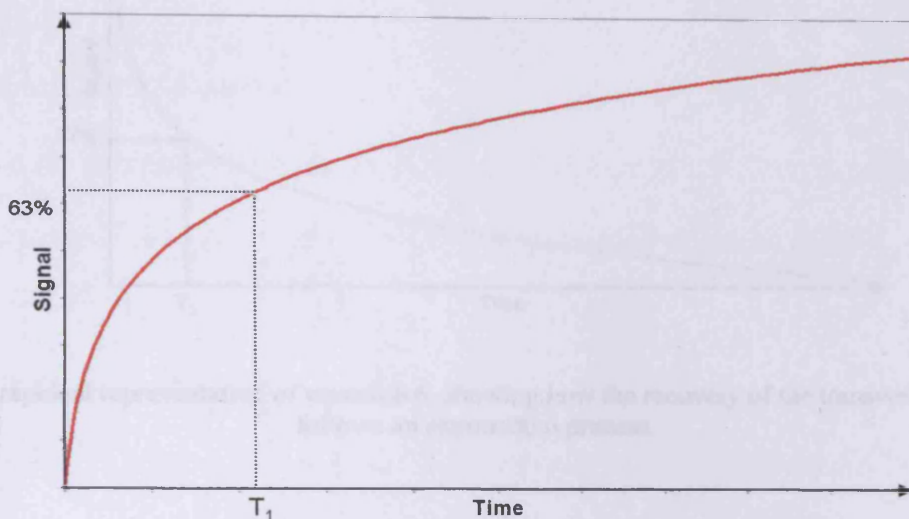


**Figure 1:** A graphical representation of equation 5, showing how the recovery of the longitudinal magnetisation follows an exponential process.

### 6.1.2 $T_2$ 'Transverse/Spin-Spin' Relaxation

The transverse magnetisation vector is designated as  $M_{xy}$  and is perpendicular to  $B_0$ . Decoherence of the initial phasing of this transverse nuclear spin magnetisation is a complex phenomenon. As the nuclei rotate together around  $B_0$ , the local magnetic fields generated by the spinning protons will each interact and thus slightly modify and randomise the rates of precession, thus causing the cumulative loss in phase. The time constant describing the return to equilibrium of the transverse magnetisation is known as  $T_2$ . The phase difference increases as the time elapses, this is reflected in the following equation:

$$M_{XY}(t) = M_{XY}(0) e^{-t/T_2} \quad (6)$$

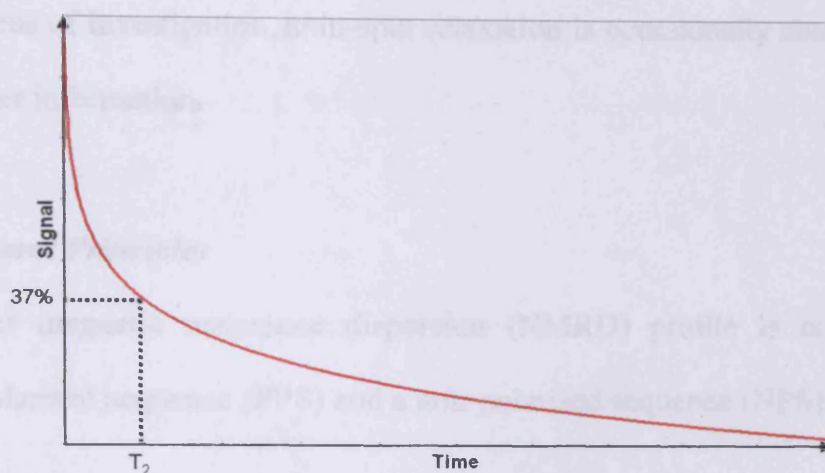


**Figure 2:** A graphical representation of equation 6, showing how the recovery of the transverse magnetisation follows an exponential process.

The magnetic field inhomogeneity experienced by nuclei *in vivo* also contributes to the dephasing of the transverse nuclear spin magnetisation. It is the variety of chemical environments in which protons are located *in vivo* which leads to a range of marginally different resonance frequencies rotating around  $B_0$ . As time elapses the coherence of the initial phasing of the magnetisation vector diminishes. The overall decay of the transverse magnetisation is therefore described as a combination of these factors and is represented by the time constant  $T_2^*$ . The relationship between the 'pure' spin-spin decay,  $T_2$ , and the decay resulting from magnetic field inhomogeneity,  $T_{2\text{inhomo}}$  is described in equation 7.

$$1/T_2^* = 1/T_2 + 1/T_{2\text{inhomo}} \quad (7)$$

### Fast Field-Cycling Relaxometry<sup>9-11</sup>

The objective of a fast field-cycling (FFC) relaxometry experiment is to measure, in most instances, the spin-lattice relaxation times of a sample as the external magnetic field is cycled through a range of discrete field strengths. While spin-lattice relaxation times are most

commonly the focus of investigation, spin-spin relaxation is occasionally considered as a means of acquiring further information.

### 6.1.3 *General Principles*

A typical nuclear magnetic resonance dispersion (NMRD) profile is compiled using two methods; a pre-polarised sequence (PPS) and a non-polarised sequence (NPS).

### 6.1.4 *PPS: When $B_r \ll B_p$*

In the PPS phase of collecting a complete NMRD profile, a strong magnetic field is established,  $B_p$ , which polarises the nuclear spin system in a similar fashion to a typical NMR experiment. The instrument then switches the magnetic field to a lower flux density,  $B_r$ , which is maintained for a known period of time,  $\tau$ . This switch is accomplished, in the case of the Stellar Spinmaster FFC-2000 relaxometer, by modifying the current in the magnetic coil. The magnetisation at this stage lies along the external magnetic field direction and is initially equal to the equilibrium magnetisation in the polarisation field:

$$M(0) = M_z(0) = M_0(B_p) \quad (8)$$

The nuclear spin system then relaxes towards the new magnetisation vector  $M_0(B_r)$  and consequently the magnetisation evolves according to the solution of equation (9):

$$M_z(\tau) = M_0(B_r) + [M_0(B_p) - M_0(B_r)]\exp\{-\tau/T_1(B_r)\} \quad (9)$$

The remaining signal following this relaxation process is determined by switching to a higher magnetic field of known flux density,  $B_d$ , followed by exposure of the sample to RF radiation tuned to a preset frequency irrespective of the relaxation field. Following the 90° RF pulse, the

signal is detected *via* free induction decay (FID)\*. To re-establish the net magnetisation vector to that prior to the initial relaxation, the field is returned to flux density,  $B_p$ , for an extended time period after which the process is repeated.

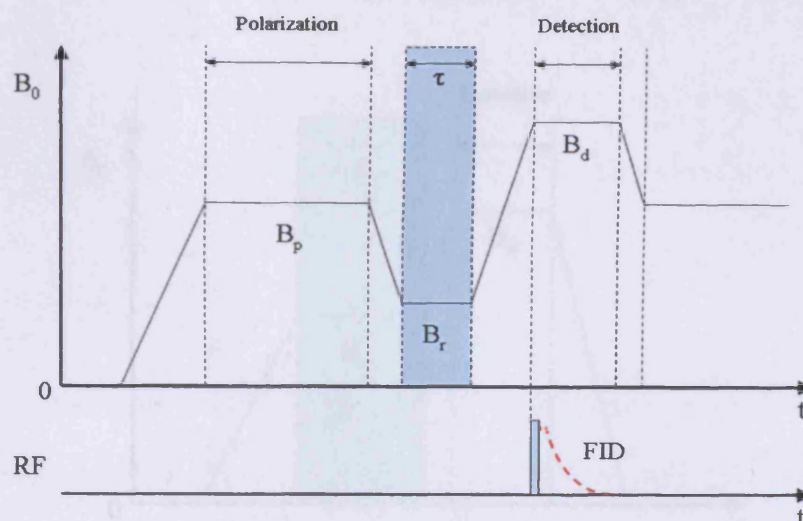


Figure 3: A graphical representation of the magnetic field strength during a pre-polarised sequence.

### 6.1.5 NPS: where $B_r \rightarrow B_d$

A pre-polarised sequence is appropriate in situations where the relaxation flux density,  $B_r$ , is significantly lower than the polarisation field,  $B_p$ , however the accuracy of the data is compromised when the difference in magnetisation vector,  $\Delta M_z^{\text{eff}}$ , between the two flux densities becomes sufficiently small. Therefore, a non-polarised sequence (NPS) is essential when  $B_r$  becomes so high that it approaches  $B_p$ .

An NPS cycle is initiated without any initial polarisation phase of the nuclear spin system, the relaxation curve in this instance is generated *via* a typical inversion recovery method. A  $180^\circ$  pulse rotates the net magnetisation vector down to the  $-Z$  axis, the magnetisation then undergoes spin-lattice relaxation which returns the net magnetisation to its equilibrium position along the  $+Z$  axis. Before it reaches equilibrium, a  $90^\circ$  pulse rotates the longitudinal

\* The precessing magnetisation will induce a corresponding oscillating voltage in a detection coil surrounding the sample. The signal is then recorded electronically.

magnetisation into the XY plane. Once magnetisation is present in the XY plane it rotates about the Z axis and dephases giving an FID. The relaxation curve is then of the type:

$$M_z^{\text{detected}}(\tau) = M_z^{\infty} - \Delta M_z^{\text{eff}} \cdot e^{-\tau/T1} \quad (10)$$

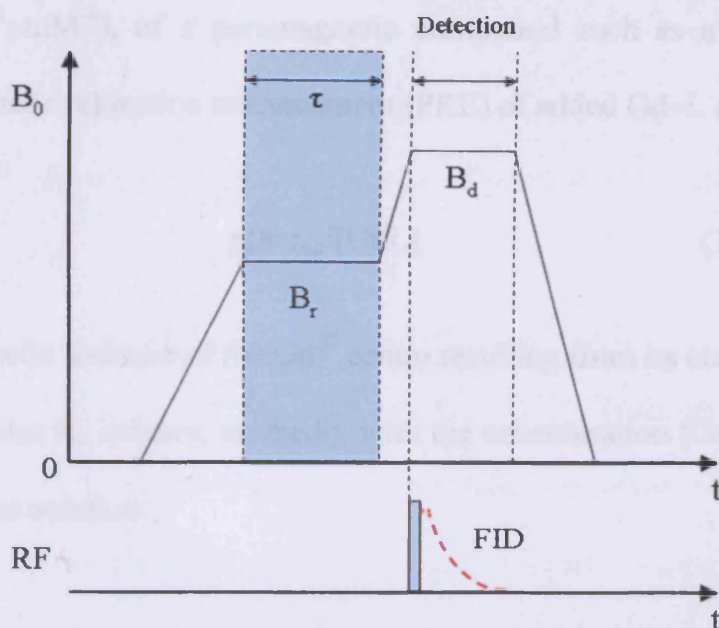


Figure 4: A graphical representation of a non-polarised sequence.

The major advantage of FFC relaxometry is the ability to cycle incrementally through a range of relaxation flux densities,  $B_r$ , as specified by the user\*, leading to a NMRD profile from which very important information can be extracted.

An important consideration when analysing relaxivity data is the contribution of the diamagnetic component arising from the medium the sample is within (pure water).

$$r_{\text{ap}} \equiv r_{\text{a}} - r_{\text{ad}} \text{ per mM} \quad (11)$$

where p = paramagnetic, d = diamagnetic.

\* In most cases, the range 10 kHz to 30 MHz was used as it typically reflected the maximum range which could be safely explored without the risk of the magnet overheating. A safeguard would activate if the temperature peaked at any stage above 40°C, halting the collection immediately.



## Chapter 6: Novel Gd(III) Complexes as MRI Contrast Agents: Measuring Efficiency *via* Relaxometry

The reference rate in a diamagnetic solution corresponds to the absence of a paramagnetic Gd–L complex and is denoted by:

$$r_{\text{ad}} \equiv 1/T_{\text{ad}} \quad (\alpha = 1, 2) \quad (12)$$

The relaxivity,  $r_a$  ( $\text{s}^{-1} \text{mM}^{-1}$ ), of a paramagnetic compound such as a contrast agent is thus defined as a paramagnetic relaxation enhancement (PRE) of added Gd–L complex:

$$r_a \equiv r_{\text{op}}/[\text{GdL}] \quad (13)$$

Due to the large magnetic moment of the  $\text{Gd}^{\text{III}}$  centre resulting from its electronic spin  $S=7/2$ , the observed relaxation rates  $R_a$  increase markedly with the concentration  $[\text{GdL}]$  (mM) of the Gd–L complexes added to the solution.

### **Efficacy of $T_1$ Weighted Contrast agents:**

The efficacy of a contrast agent is measured by the ability of its 1 mM solution to increase the longitudinal relaxation rate  $r_1$  ( $1/T_1$ ) of water protons. The Solomon–Bloembergen–Morgan (SBM) theory associates several physico-chemical parameters with effects on overall relaxivity. Parameters which can be chemically tuned are of particular focus in attempts to design superior ligands.<sup>12</sup>

Such parameters include:

- (i) The number of inner-sphere water molecules directly bound to the  $\text{Gd}^{\text{III}}$  ion,  $q$ .
- (ii) The mean residence time of co-ordinated water molecules,  $\tau_M$ .

## Chapter 6: Novel Gd(III) Complexes as MRI Contrast Agents: Measuring Efficiency *via* Relaxometry

- (iii) The rotational correlation time representing the molecular tumbling time of a complex,  $\tau_R$ .
- (iv) The number of second-sphere and outer-sphere water molecules (hydration number  $q_{ss}$  and mean residence time  $\tau_{Mss}$ ).
- (v) Electronic parameters.

Many of these physico-chemical parameters are typically assessed *via* the interpretation NMRD experiments, this procedure is commonly used for the characterisation of all compounds considered as potential contrast agents. According to the SBM theory, the efficiency of commercially available contrast agents such as Gd-DTPA (Magnevist®) and Gd-DOTA (Dotarem®) is only a small fraction of what is theoretically possible, therefore by designing a ligand which optimises each of these parameters it is possible to provide greatly enhanced imaging potential. A beneficial consequence of this will be the decrease application dose as currently patients are being administered these agents in gram quantities.

Other parameters which contribute to the overall relaxivity, such as electronic relaxation of the Gd<sup>III</sup> ion ( $T_{1e,2e}$ ), the trace of zero-field splitting (ZFS) tensor ( $\Delta^2$ ) and electronic modulation time ( $\tau_v$ ) are not as well explored. However, the recently developed Rast-Borel theory has contributed much to the understanding of electron spin relaxation of Gd<sup>III</sup> complexes.<sup>13,14</sup> Current theories concerning electronic relaxation have been published quite recently in the form of two useful reviews.<sup>15,16</sup>

## Using Luminescence Decay Lifetimes to Determine the Number of Inner Sphere Water Molecules

For most metal ions and their complexes in solution, determining the number of metal-coordinated water molecules,  $q$ , is difficult or impossible. However, for luminescent trivalent lanthanide ions, most notably  $\text{Eu}^{\text{III}}$  and  $\text{Tb}^{\text{III}}$ , a convenient method proposed by Horrocks *et al.* is available.<sup>17,18</sup>

Several factors contribute to the de-excitation of an excited state ion. The rate of the overall exponential decrease of luminescence intensity,  $\tau_{\text{obsd}}^{-1}$ , following an excitation is represented in equation 14:

$$\tau_{\text{obsd}}^{-1} = \tau_{\text{nat}}^{-1} + \tau_{\text{nonrad}}^{-1} + \tau_{\text{OH}}^{-1} \quad (14)$$

Where  $\tau_{\text{nat}}^{-1}$  is the natural rate constant for the emission of photons,  $\tau_{\text{nonrad}}^{-1}$  reflects the rate constant of nonradiative deexcitation, and  $\tau_{\text{OH}}^{-1}$  represents the nonradiative energy transfer to the OH vibrational manifold of OH oscillators in the inner sphere e.g. co-ordinated water molecules. For  $\text{Eu}^{\text{III}}$  complexes,  $\tau_{\text{OH}}^{-1}$  is the most significant contribution. The efficiency of the de-excitation pathway increases as the energy difference between the emissive state,  $^5\text{D}_0$ , and the highest energy level of the ground state manifold decreases.<sup>19</sup> There is a very significant isotope effect on this energy transfer, and if the protons within the inner sphere are replaced by deuterium this de-excitation pathway becomes remarkably less efficient.<sup>20</sup> Therefore, it becomes possible to determine the contribution of  $\tau_{\text{OH}}^{-1}$  by performing experiments independently in both  $\text{H}_2\text{O}$  and  $\text{D}_2\text{O}$ . In a  $\text{D}_2\text{O}$  solution, the contribution to the deexcitation *via* OH oscillators is removed:

$$\tau_{\text{obsd}}^{-1} = \tau_{\text{nat}}^{-1} + \tau_{\text{nonrad}}^{-1} \quad (15)$$

Chapter 6: Novel Gd(III) Complexes as MRI Contrast Agents:  
Measuring Efficiency via Relaxometry

In this instance, any negligible contribution of OD oscillators to the overall deexcitation is included in the latter term, and simple subtraction yields  $\tau_{OH}^{-1}$  which is proportional to the number of metal-bound water molecules. By performing several solid-state experiments on compounds which had been characterised crystallographically, Horrocks formulated the following equation:

$$q_{Ln} = A_{Ln}(\tau_{H_2O}^{-1} - \tau_{D_2O}^{-1}) \quad (16)$$

where  $A_{Ln}$  is a constant ( $Eu^{III} = 1.05$ ). Here, the estimated uncertainty in  $q$  is approximately  $\pm 0.5$  water molecules.

A collection of known ligands (Table 1; Fig. 5) has been included to provide a useful comparison to the ligands investigated herein.

**Table 1:** A selection of known ligands with accompanying relaxivities and  $q$  values of their Gd<sup>III</sup> complexes.

Ligand	Temp (°C)	<sup>1</sup> H freq (MHz)	$r_1$ (s <sup>-1</sup> mM <sup>-1</sup> )	$q$	ref
DTPA	25	20	4.3	1.2	21,22
DTPA-BMA	25	20	4.39	1	23
DTPA-BPDA	25	20	4.432	1	24
TPAA	25	60	13.3	2	25
DOTA	37	20	4.2	1.2	21,26
DO3A	40	20	4.8	1.9	27,28
TREN-1,2-HOPO	25	20	9.5	2	29
PCTP-[13]	25	20	7.7	1	30
N <sub>6</sub> -L1	25	20	12.8	3	31
BOPTA	39	20	4.39	1.2	28,32

Chapter 6: Novel Gd(III) Complexes as MRI Contrast Agents:  
Measuring Efficiency *via* Relaxometry

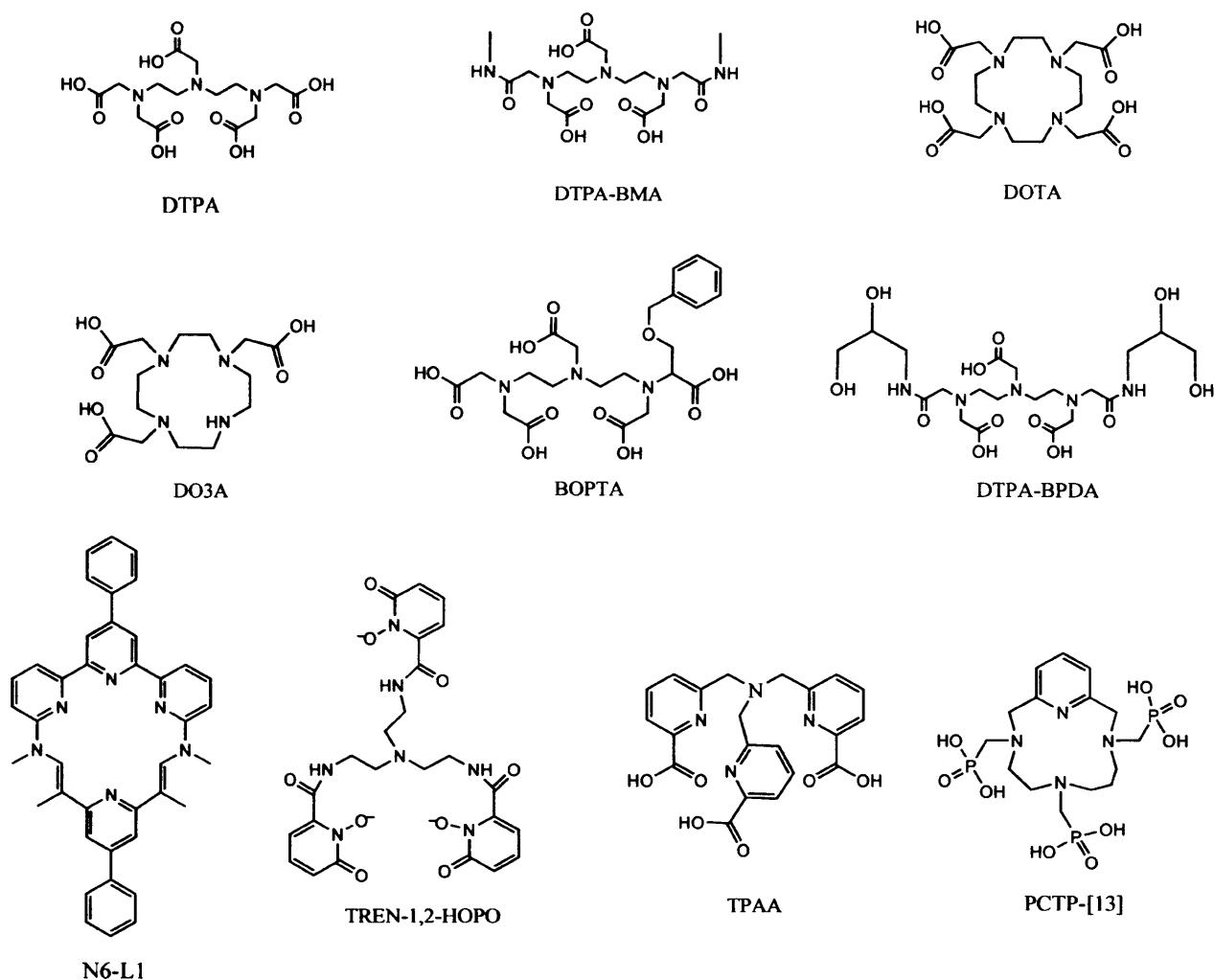


**Figure 5:** A chart showing examples of ligands used as Gd<sup>III</sup> sequestering agents. Accompanying data are presented in Table 1.

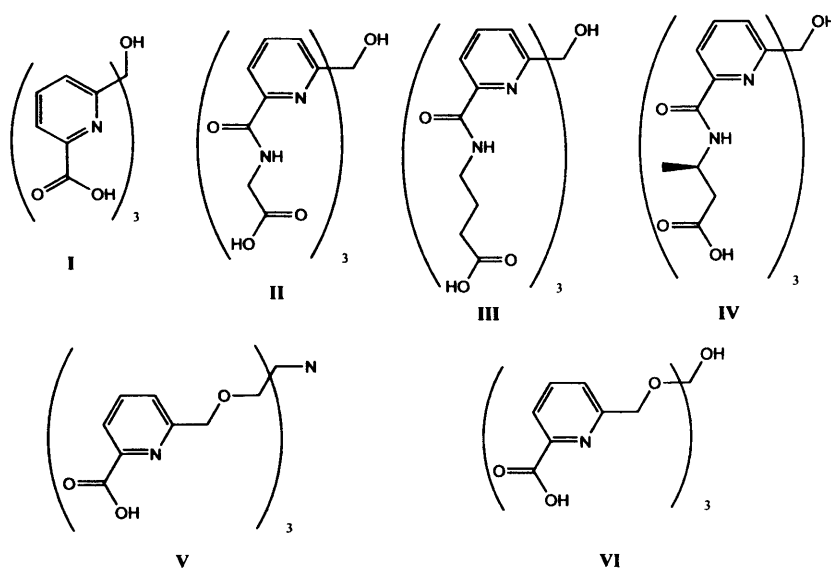


**Figure 6:** The ligands series under investigation as potential Gd<sup>III</sup>-based contrast agents.

## 6.2 Experimental

### 6.2.1 <sup>1</sup>H NMRD acquisition:

The  $1/T_1$  NMRD profiles were obtained on a Stelar Spinmaster FFC-2000 relaxometer, typically covering a continuum of magnetic fields from  $2.4 \times 10^{-4}$  to 0.72 T (corresponding to a proton Larmor frequency range 0.01 - 30 MHz). Technical details are available in the reference manual available upon request from Stelar\*. A Spinmaster Variable Temperature Controller (VCT) allowed the setting and monitoring of the sample temperature ranging in these experiments between 15 - 37°C with a resolution up to 0.01°C. The temperature gradient over the sample region was dependent on the air (nitrogen) flow and the installed temperature. The temperature in the probehead was measured with a Fluke 52 k/j digital thermometer with an uncertainty of 0.5 K. The temperature inside the probe was controlled by circulation of perfluoroalkanes. Each sample was allowed to acclimatise to the desired temperature for 15 minutes prior to data collection. The reproducibility in  $T_1$  measurements was within less than 1%.

### 6.2.2 Luminescence

Having prepared the complexes, the luminescent properties were established using a Perkin-Elmer LS55 fluorimeter. The complexes gave characteristic emission spectra (Fig. 12), indicating incorporation of the europium(III) ions within the metal binding sites. Luminescent lifetime measurements (collected in Tables 2 and 3) were obtained by iterative reconvolution of the detector response (obtained by using a scatterer) with exponential components for growth and decay of the metal centred luminescence, using a spreadsheet running in Microsoft Excel. The details of this approach have been discussed elsewhere.<sup>33</sup>

---

\*Stelar s.r.l., Via E. Fermi, 4, I-27035, Mede (PV), Italy. Telephone: +39 0384 820096 Fax: +39 0384 805056  
Email: info@stelar.it Website: www.stelar.it

### 6.2.3 Ligand Synthesis

The synthetic procedure for compound **I** is summarised in chapter four, all other ligands under investigation were prepared by members of the Amoroso research group.

### 6.2.4 Sample Preparation

The Gd<sup>III</sup> complexes were prepared in a sample tube by mixing equimolar amounts of either Gd(NO<sub>3</sub>)<sub>3</sub>.6H<sub>2</sub>O (99.99%; Aldrich) or Gd<sub>2</sub>O<sub>3</sub>.6H<sub>2</sub>O (99.99%; Aldrich) and the ligand in doubly distilled water to the required concentration. A slight excess (5%) of ligand was used and the pH was adjusted by adding HNO<sub>3</sub> or NaOH (each 0.1 M). The solution was allowed to react at room temperature for 12 h. The absence of free (uncomplexed) metal was checked in each sample with the complexometric dye Xylenol orange.<sup>34</sup>

## 6.3 Results and Conclusions

### 6.3.1 Compound Gd-I: Overview

The <sup>1</sup>H NMRD profile of compound Gd-I at a range of temperatures is illustrated in Figure 7. Lowering the temperature of the sample induces a relaxivity enhancement, this is typical as relaxation rates are inversely proportional to the diffusion coefficient.<sup>35</sup> At 30 MHz, the relaxivity of Gd-I (pH 7.4, 25°C) is 4.39 mM<sup>-1</sup>s<sup>-1</sup>, which is comparable to the performance of commercially available contrast agents Magnevist® and Dotarem® (see Table 1). Figure 8 reveals how the relaxivity varies as a function of pH across the same temperature range. For solutions in excess of pH 9.89, the relaxivity remains constant within statistical error. This supports the potentiometric data which reveals complete complex formation in this region. As

the solution is made increasingly acidic, the relaxivity is enhanced due to progressive complex dissociation. The relaxivity of free Gd<sup>III</sup> ions is *ca.* 9 mM<sup>-1</sup>s<sup>-1</sup> which is observed at *ca.* pH 2, this is again consistent with speciation plots. After data acquisition, each of the samples was tested with the complexometric dye Xylenol orange. The results again support the potentiometric data, revealing no free Gd<sup>III</sup> in basic media and, conversely, a strong positive result in lower pH solutions. The dependency of relaxivity on pH is consistent despite changes in temperature.

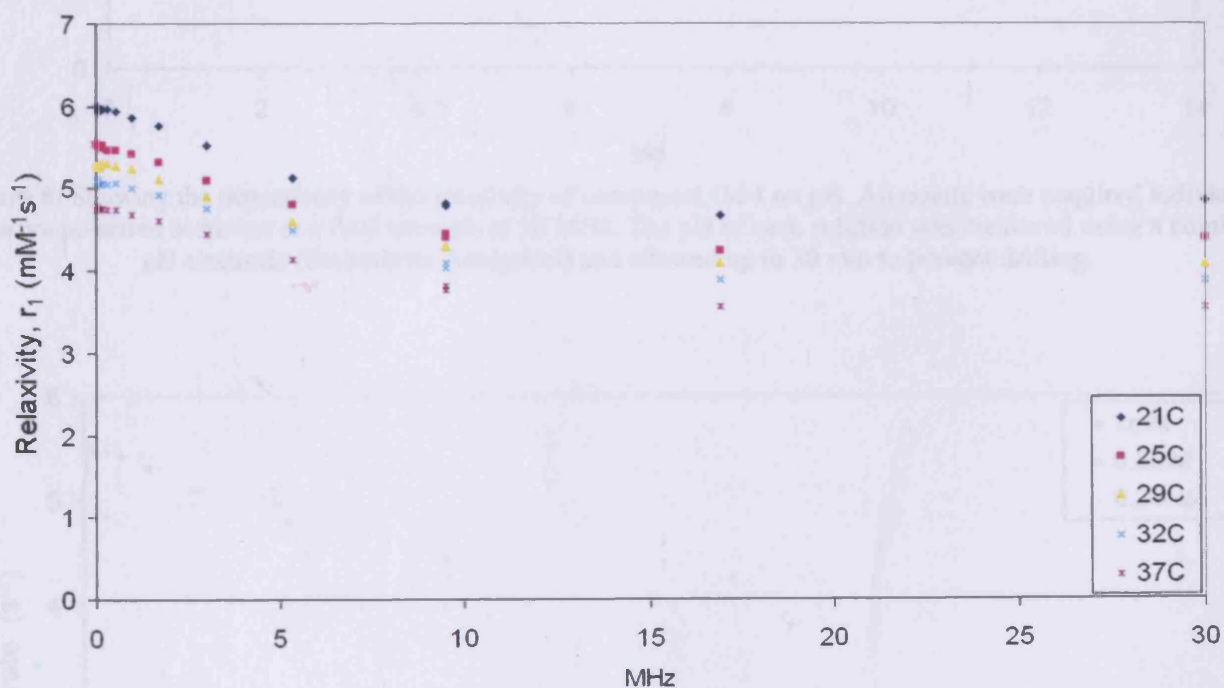


**Figure 7:** The <sup>1</sup>H NMRD profile of compound Gd-I, revealing the effects of changes in temperature. The samples were adjusted to pH 7.4 to represent physiologically relevant conditions.



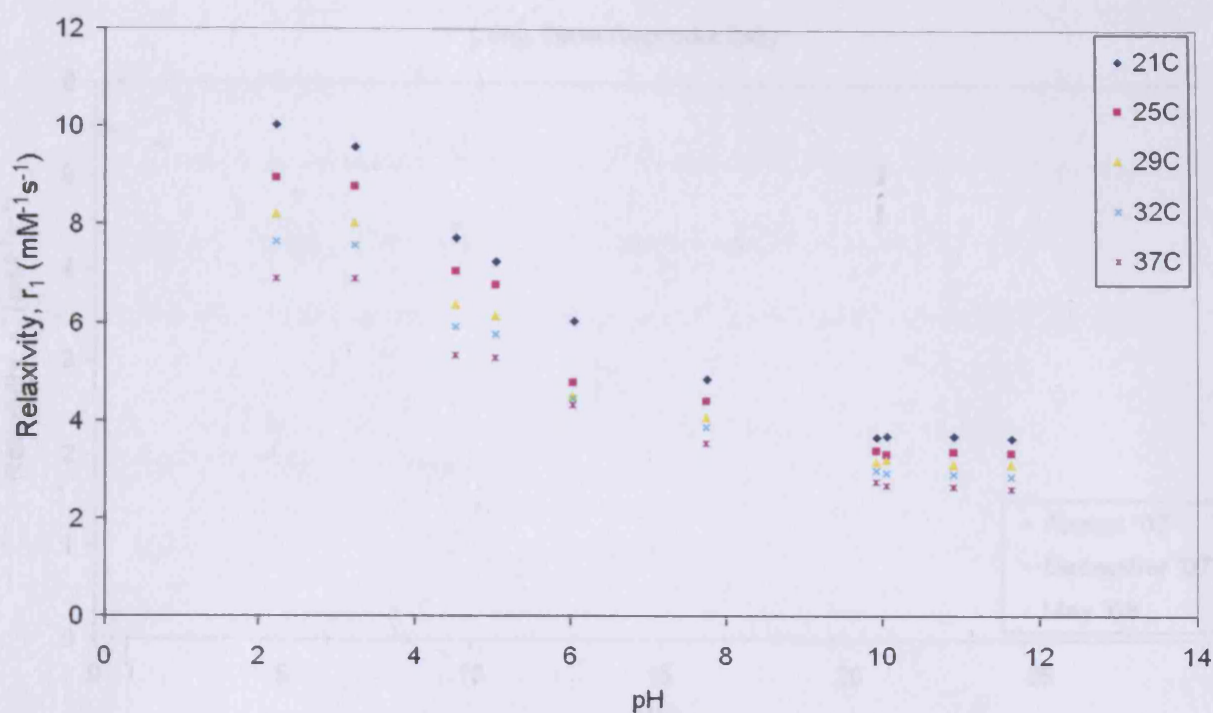


**Figure 8:** Showing the dependency of the relaxivity of compound Gd-I on pH. All points were acquired individually *via* a nonpolarised sequence at a field strength of 30 MHz. The pH of each solution was measured using a combined pH electrode (Radiometer Analytical) and allowed up to 30 min to prevent drifting.

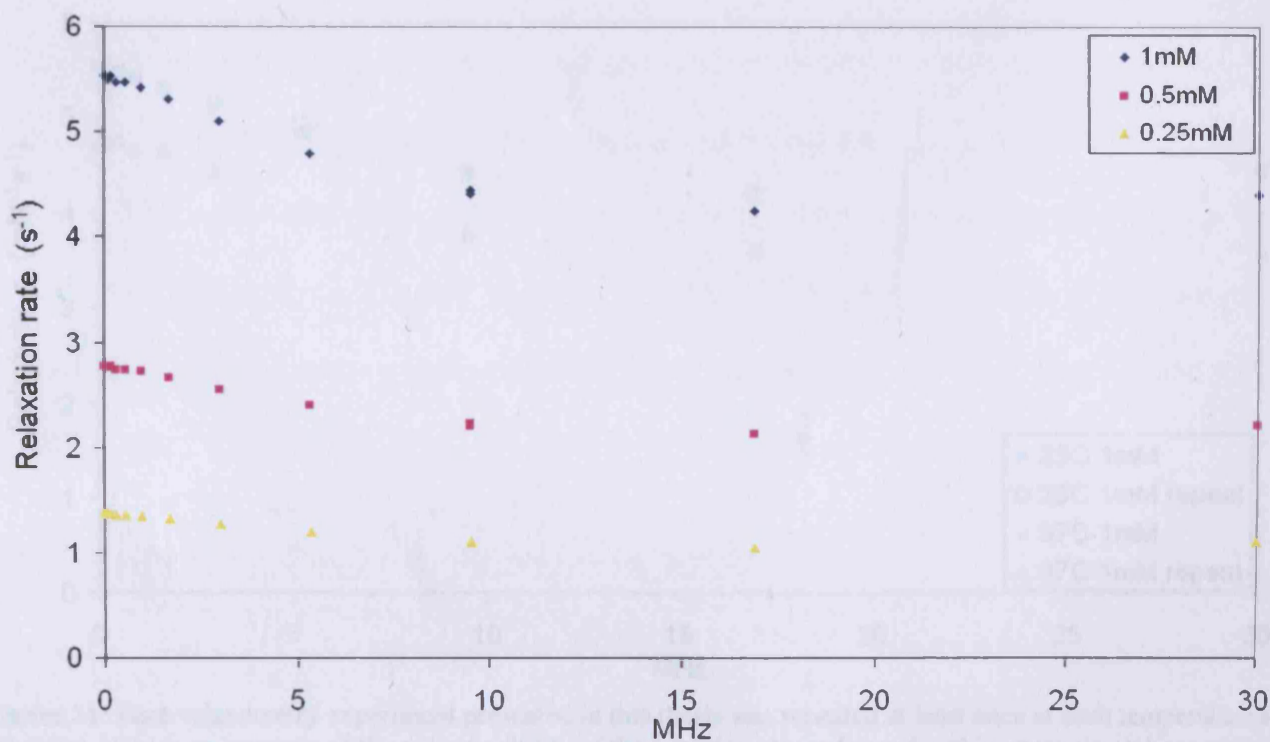


**Figure 9:** Showing the variation of relaxation rate with concentration. Each profile was recorded at pH 7.4 and at 25°C. Conversion into the standard units of relaxivity ( $\text{mM}^{-1}\text{s}^{-1}$ ) reveals the relaxivity remains constant.

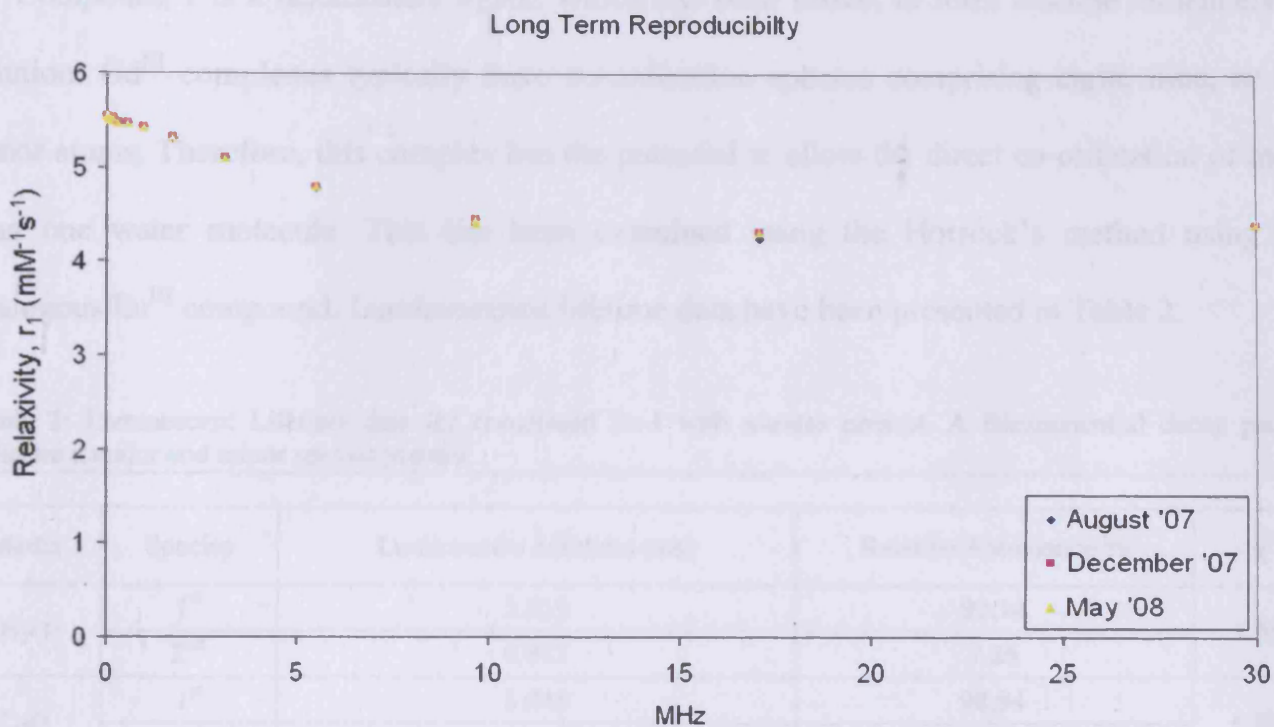


Figure 10: Reproducing identical experimental conditions with the same sample over an extended time period confirmed the high stability of the complex.

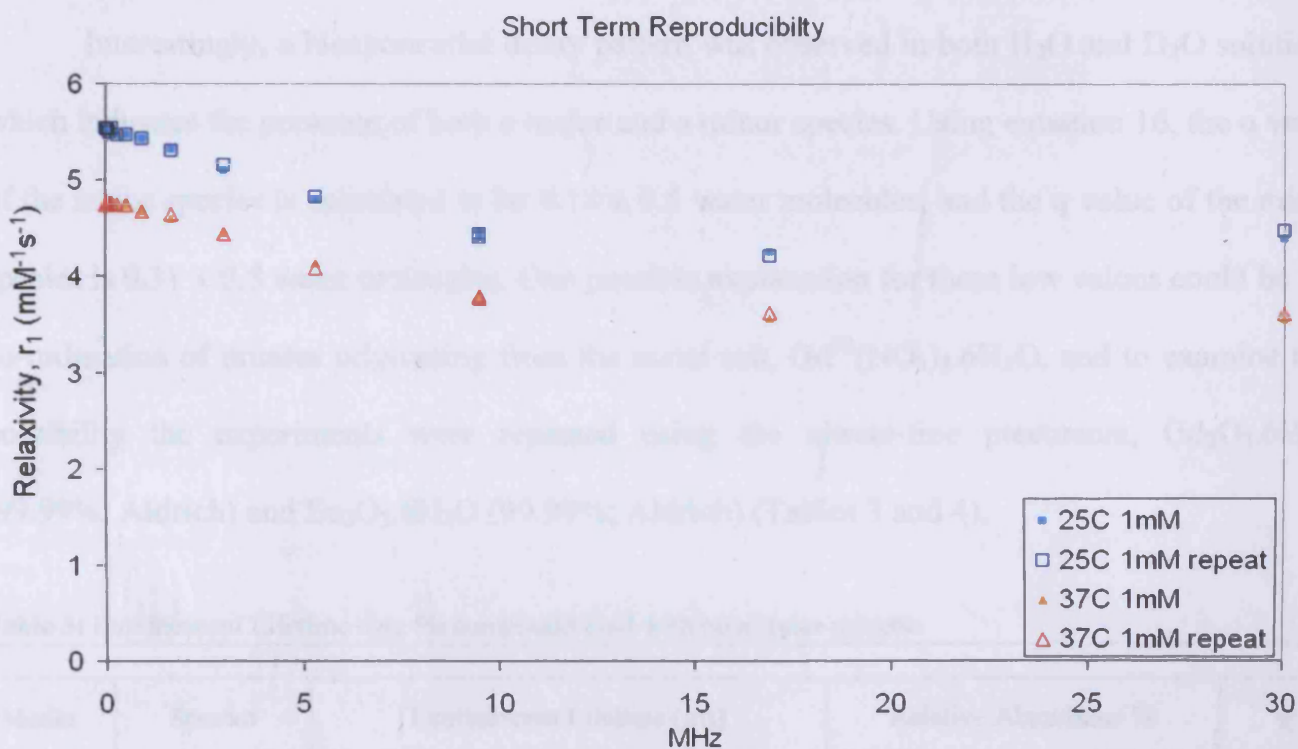


Figure 11: Each relaxometry experiment presented in this thesis was repeated at least once at each temperature and pH value. Here is an example of the reproducibility of the experiments performed within approximately one hour of each other.

Chapter 6: Novel Gd(III) Complexes as MRI Contrast Agents:  
Measuring Efficiency *via* Relaxometry

Compound I is a hexadentate ligand which has been shown to form discrete monomers in solution. Gd<sup>III</sup> complexes typically have co-ordination spheres comprising eight, nine, or ten donor atoms. Therefore, this complex has the potential to allow the direct co-ordination of more than one water molecule. This has been examined using the Horrock's method using the analogous Eu<sup>III</sup> compound. Luminescence lifetime data have been presented in Table 2.

**Table 2:** Luminescent Lifetime data for compound Eu-I with nitrates present. A Biexponential decay pattern indicates a major and minor species present.

Media	Species	Luminescent Lifetime (ms)	Relative Abundance %	$\chi^2$
H <sub>2</sub> O	1 <sup>st</sup>	2.019	92.14	1.057
	2 <sup>nd</sup>	0.817	7.86	
D <sub>2</sub> O	1 <sup>st</sup>	3.048	98.94	0.976
	2 <sup>nd</sup>	1.075	1.06	

Interestingly, a biexponential decay pattern was observed in both H<sub>2</sub>O and D<sub>2</sub>O solutions which indicates the presence of both a major and a minor species. Using equation 16, the q value of the major species is calculated to be  $0.18 \pm 0.5$  water molecules, and the q value of the minor species is  $0.31 \pm 0.5$  water molecules. One possible explanation for these low values could be the co-ordination of nitrates originating from the metal salt, Gd<sup>III</sup>(NO<sub>3</sub>)<sub>3</sub>.6H<sub>2</sub>O, and to examine this possibility the experiments were repeated using the nitrate-free precursors, Gd<sub>2</sub>O<sub>3</sub>.6H<sub>2</sub>O (99.99%; Aldrich) and Eu<sub>2</sub>O<sub>3</sub>.6H<sub>2</sub>O (99.99%; Aldrich) (Tables 3 and 4).

**Table 3:** Luminescent Lifetime data for compound Eu-I with no nitrates present.

Media	Species	Luminescent Lifetime (ms)	Relative Abundance %	$\chi^2$
H <sub>2</sub> O	1 <sup>st</sup>	0.740	62.68	1.962
	2 <sup>nd</sup>	0.197	37.32	
D <sub>2</sub> O	One species	2.021	100	1.975

## Chapter 6: Novel Gd(III) Complexes as MRI Contrast Agents: Measuring Efficiency *via* Relaxometry

While the experiment performed in H<sub>2</sub>O similarly resulted in a biexponential decay pattern indicating the presence of two species in solution, the same experiment performed in D<sub>2</sub>O yielded a monoexponential decay pattern indicative of only one species. It is impossible therefore to draw any firm conclusions regarding the number of inner-sphere water molecules based on this data, however assuming the one species present in the D<sub>2</sub>O experiment is identical to the major species of the H<sub>2</sub>O experiment this would lead to a  $q$  value of  $0.90 \pm 0.5$  water molecules. Similarly, assuming this species is identical to the minor species of the H<sub>2</sub>O experiment, this would lead to a much larger  $q$  value of  $4.81 \pm 0.5$  water molecules. Both of these values suggest an increase in the number of water molecules directly co-ordinating to the europium following the removal of nitrates from solution, however these values must be treated with suspicion.

The <sup>1</sup>H NMRD profile of compound Gd-I, recorded in the absence of nitrates, is presented in Figure 13. There are several features of note; firstly at 30 MHz the relaxivity is  $4.36 \text{ mM}^{-1}\text{s}^{-1}$  (pH 7.4, 25°C), which is unchanged from the initial experiment within statistical error. Secondly, the shape of the profile itself is quite different, in this instance there is a clear enhancement starting at *ca.* 10 MHz which increases towards higher fields, this is a very common feature of typical low-molecular-weight chelates. Rapid molecular reorientations are a dominant factor in the observed relaxivity and as molecular reorientations are slowed, the relaxivity increases leading to a characteristic high-field “hump” which is present in the <sup>1</sup>H NMRD profiles of many similar compounds.<sup>36,37</sup> A third observation is the reduced significance of temperature change on relaxivity. As stated previously, relaxation rates are inversely proportional to the diffusion coefficient and while this is clearly still a feature of the <sup>1</sup>H NMRD profile of the nitrate-free compound, the reduced temperature effect could be a consequence of enhanced water exchange rates. Each experiment was repeated at concentrations of 0.5 mM and

0.25 mM, the relationship between relaxation rates ( $s^{-1}$ ) and concentration is clearly proportional and resulted in perfectly consistent relaxivities ( $mM^{-1}s^{-1}$ ) in each case. An example of this is provided in Figure 9 (p. 262).

**Table 4:**  $^1H$  NMRD Relaxivity profile output data<sup>a</sup> for compound Gd-I in the presence and absence of nitrates

Compound	$T_1$ Relaxation time <sup>b</sup> /s	$r_1$ Relaxation rate <sup>b</sup> / $s^{-1}$	% Error	$\pm$ Error (R1)
Gd-I (with nitrates)	0.228	4.392	1.6270E-01	7.7516E-03
Gd-I (no nitrates)	0.229	4.362	1.2821E-01	6.0698E-03

<sup>a</sup>Performed at 30MHz, 1mM, pH 7.4, 25°C. <sup>b</sup>Values after subtraction of the diamagnetic water contribution.

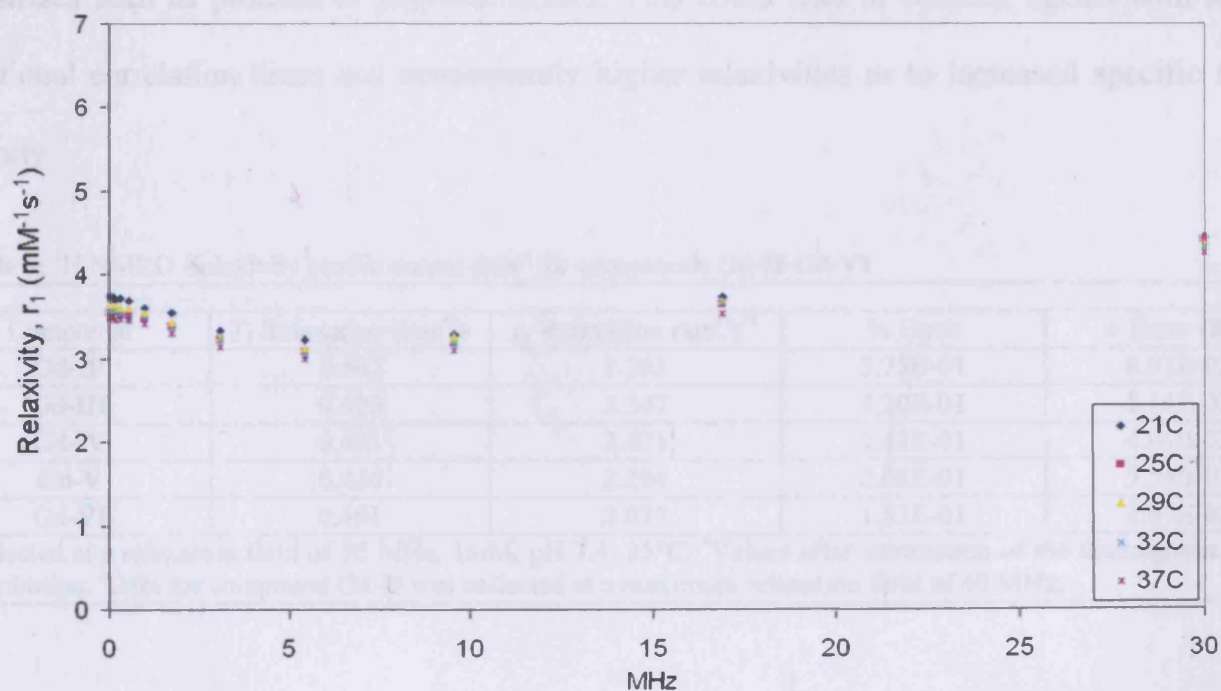


**Figure 13:** The  $^1H$  NMRD profile of Gd-I repeated using the nitrate-free precursor  $Gd_2O_3 \cdot 6H_2O$ . The experiment was repeated across a range a temperatures.

### 6.3.2 Compounds Gd-II – Gd-VI: Overview

The  $^1H$  NMRD profiles in the case of each  $Gd^{III}$  complex are strikingly similar (see Figures 14 – 18). This is likely a result of the structural similarities across the series, for instance the molecular weight only spans a narrow range from 727.76  $gmol^{-1}$  (Gd-II) to 811.92  $gmol^{-1}$  (Gd-

Chapter 6: Novel Gd(III) Complexes as MRI Contrast Agents:  
Measuring Efficiency *via* Relaxometry

III and Gd-IV). The rotational correlation time is directly related to the size of a complex, and for typical low molecular-weight chelates such as these, rapid molecular reorientation would largely determine the overall relaxivity.<sup>38</sup> The similarities in co-ordination modes for this ligand series would also inevitably lead to other aspects such as the mean water residence time,  $\tau_M$ , and the number of metal-bound water molecules,  $q$ , being highly comparable.

While the comparative relaxivities of compounds Gd-II – Gd-VI are quite low (*cf.* Table 1; p. 257), the introduction of substituents on the pyridine rings allows us to envisage ligands with functional groups capable of noncovalent or covalent interactions with slowly moving substrates such as proteins or polysaccharides. This could lead to contrast agents with longer rotational correlation times and consequently higher relaxivities or to increased specific tissue affinity.

**Table 5:** <sup>1</sup>H NMRD Relaxivity profile output data<sup>a</sup> for compounds Gd-II-Gd-VI

Compound	$T_1$ Relaxation time <sup>b</sup> /s	$r_1$ Relaxation rate <sup>b</sup> /s <sup>-1</sup>	% Error	± Error (R1)
Gd-II <sup>c</sup>	0.567	1.763	3.75E-01	8.01E-03
Gd-III	0.426	2.347	4.20E-01	1.14E-02
Gd-IV	0.413	2.421	1.43E-01	4.01E-03
Gd-V	0.436	2.294	2.08E-01	5.55E-03
Gd-VI	0.491	2.037	1.52E-01	3.67E-03

<sup>a</sup>Collected at a relaxation field of 30 MHz, 1mM, pH 7.4, 25°C. <sup>b</sup>Values after subtraction of the diamagnetic water contribution. <sup>c</sup>Data for compound Gd-II was collected at a maximum relaxation field of 40 MHz.

### 6.3.3 Compound Gd-II

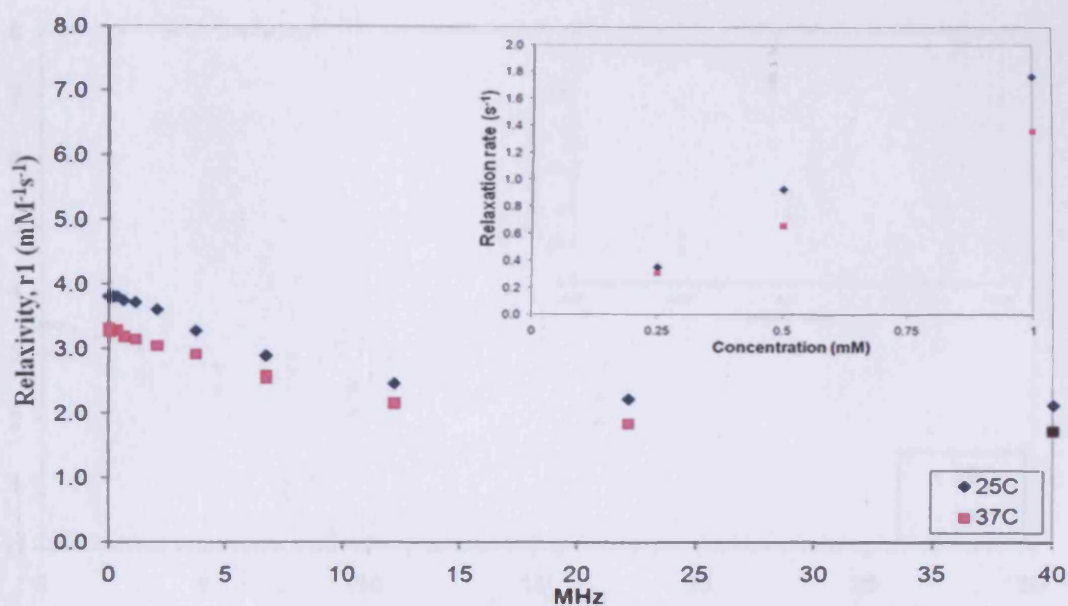


Figure 14: The  $^1\text{H}$  NMRD profile of compound Gd-II, performed at both 25°C and 37°C. Further experiments collecting single points at 40 MHz and pH 7.4 (inset: top right corner) confirmed a linear proportional relationship between relaxation rate ( $\text{s}^{-1}$ ) and concentration (mM).

### 6.3.4 Compound Gd-III

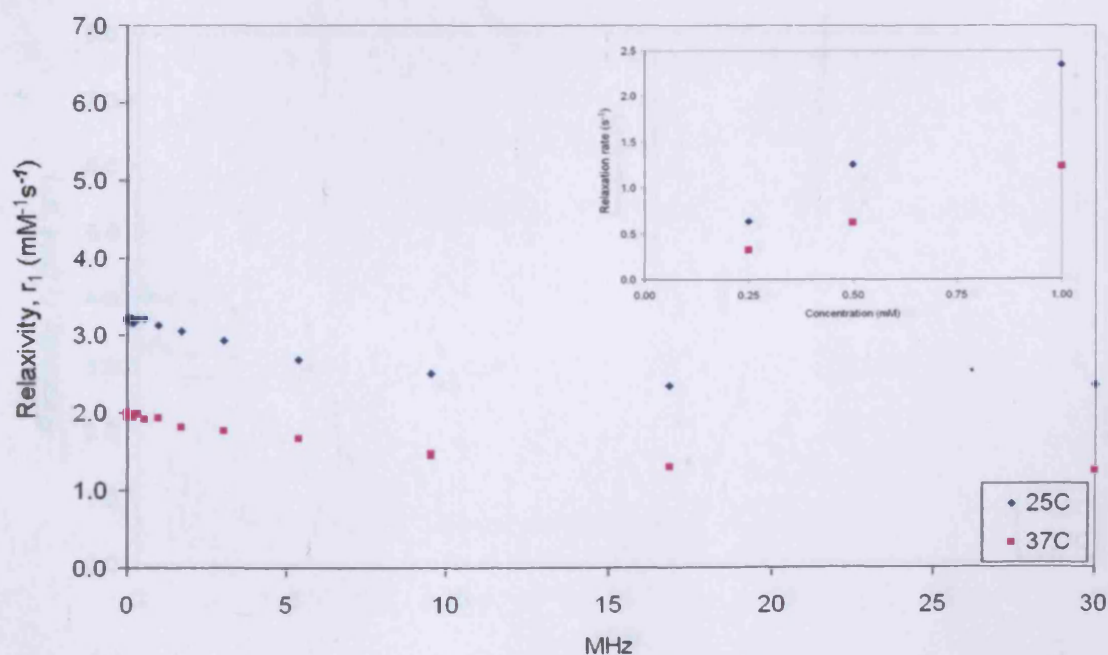
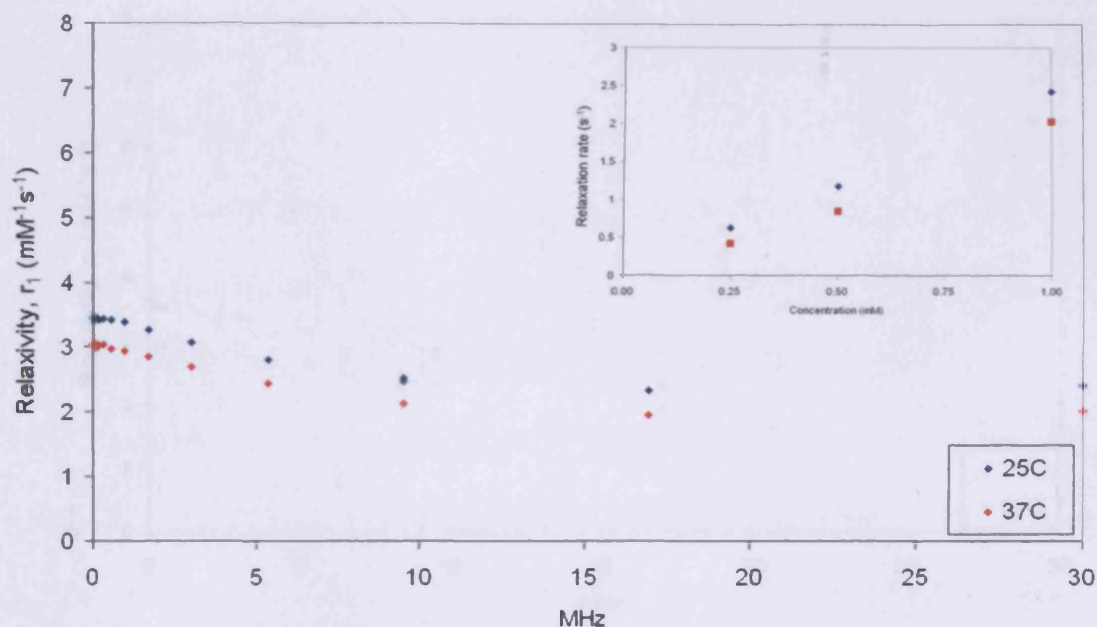


Figure 15: The  $^1\text{H}$  NMRD profile of compound Gd-III, performed at both 25°C and 37°C. Further experiments collecting single points at 30 MHz and pH 7.4 (inset: top right corner) confirmed a linear proportional relationship between relaxation rate ( $\text{s}^{-1}$ ) and concentration (mM).

### 6.3.5 Compound Gd-IV



**Figure 16:** The <sup>1</sup>H NMRD profile of compound Gd-IV, performed at both 25°C and 37°C. Further experiments collecting single points at 30 MHz and pH 7.4 (inset: top right corner) confirmed a linear proportional relationship between relaxation rate (s<sup>-1</sup>) and concentration (mM).

### 6.3.6 Compound Gd-V

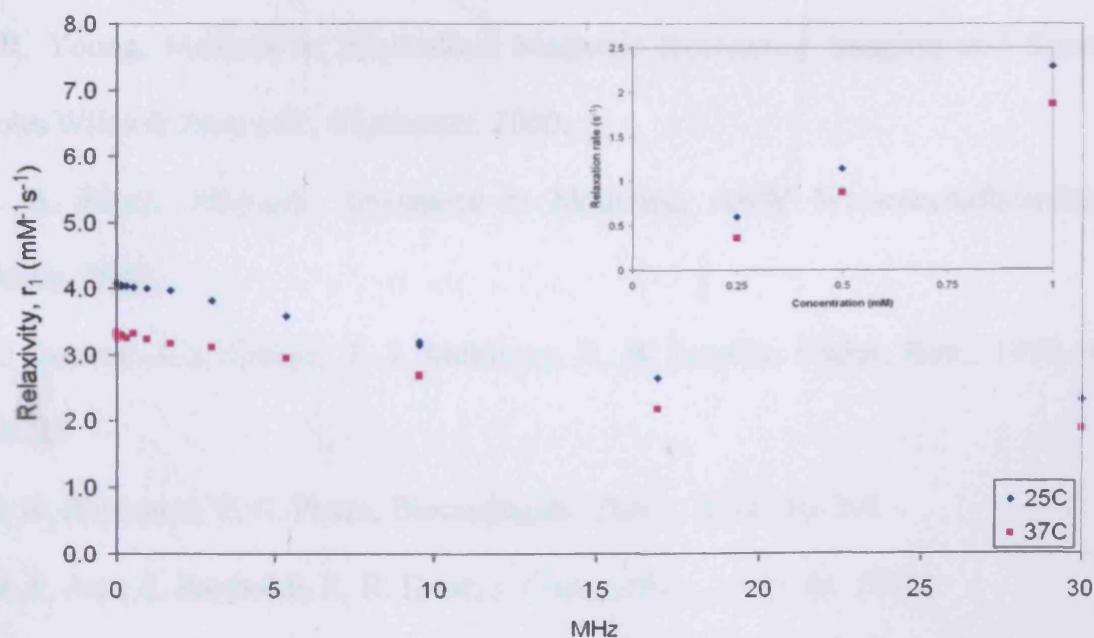


**Figure 17:** The <sup>1</sup>H NMRD profile of compound Gd-V, performed at both 25°C and 37°C. Further experiments collecting single points at 30 MHz and pH 7.4 (inset: top right corner) confirmed a linear proportional relationship between relaxation rate (s<sup>-1</sup>) and concentration (mM).



### 6.3.7 Compound Gd-VI

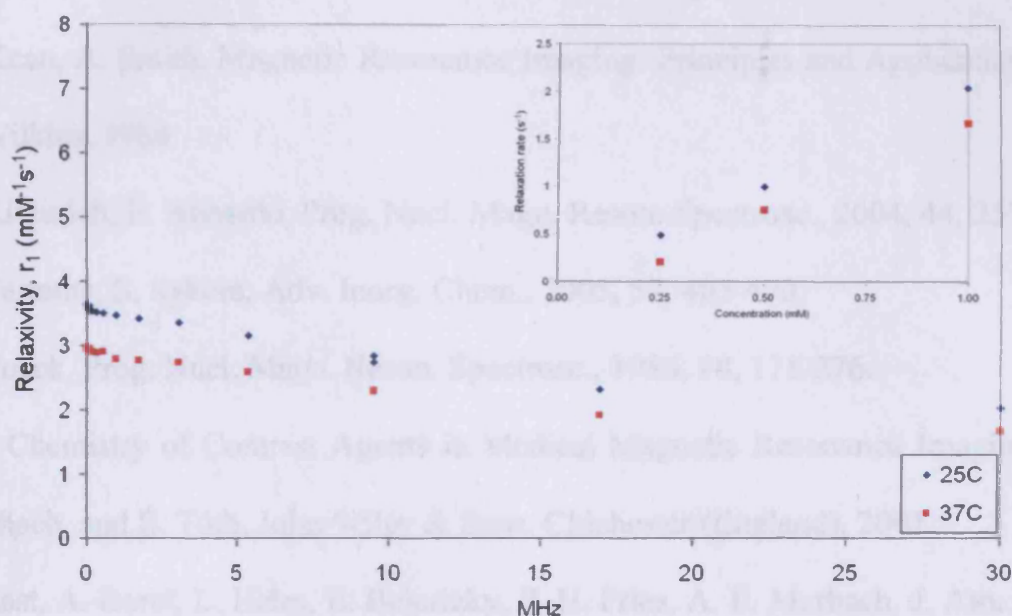


**Figure 18:** The <sup>1</sup>H NMRD profile of compound Gd-VI, performed at both 25°C and 37°C. Further experiments collecting single points at 30 MHz and pH 7.4 (inset: top right corner) confirmed a linear proportional relationship between relaxation rate (s<sup>-1</sup>) and concentration (mM).

## 6.4 References

1. I.R. Young, *Methods in Biomedical Magnetic Resonance Imaging and Spectroscopy*, John Wiley & Sons Ltd., Chichester, 2000.
2. P. A. Rinck, *Magnetic Resonance in Medicine*, ABW Wissenschaftsverlag GmbH, Berlin, 2003.
3. P. Caravan, J. J. Ellison, T. J. McMurry, R. B. Lauffer, *Chem. Rev.*, 1999, 99, 2293-2352.
4. K. N. Raymond, V. C. Pierre, *Bioconjugate Chem.*, 2005, 16, 3-8.
5. W. P. Aue, E. Bartholdi, R. R. Ernst, *J. Chem. Phys.*, 1976, 64, 2229.
6. M. A. Brown, R. C. Semelka, *MRI: Basic Principles and Applications*, 3<sup>rd</sup> edition, Wiley-Liss, 2003.

Chapter 6: Novel Gd(III) Complexes as MRI Contrast Agents:  
Measuring Efficiency *via* Relaxometry

7. V. Kuperman, *Magnetic Resonance Imaging: Physical Principles and Applications*, Academic Press, 2000.
8. D. Kean, A. Smith, *Magnetic Resonance Imaging: Principles and Applications*, Williams & Wilkins, 1986.
9. R. Kimmich, E. Ansaldo, *Prog. Nucl. Magn. Reson. Spectrosc.*, 2004, 44, 257-320.
10. G. Ferrante, S. Sykora, *Adv. Inorg. Chem.*, 2005, 57, 405-470.
11. F. Noack, *Prog. Nucl. Magn. Reson. Spectrosc.*, 1986, 18, 171-276.
12. *The Chemistry of Contrast Agents in Medical Magnetic Resonance Imaging*, ed. A. E. Merbach, and É. Tóth, John Wiley & Sons, Chichester (England), 2001.
13. S. Rast, A. Borel, L. Helm, E. Belorizky, P. H. Fries, A. E. Merbach, *J. Am. Chem. Soc.*, 2001, 123, 2637.
14. S. Rast, P. H. Fries, E. Belorizky, A. Borel, L. Helm, A. E. Merbach, *J. Chem. Phys.*, 2001, 115, 7554.
15. L. Helm, *Prog. Nucl. Magn. Reson. Spectrosc.*, 2006, 49, 45–64.
16. J. Kowalewski, D. Kruk and G. Parigi, *Adv. Inorg. Chem.*, 2005, 57, 41–104.
17. W. D. Horrocks Jr, D. R. Sudnick, *J. Am. Chem. Soc.*, 101, 1979, 334.
18. W. D. Horrocks Jr, D. R. Sudnick, *Acc. Chem. Res.*, 14, 1981, 384.
19. J. L. Kropp, M. W. Windsor, *J. Chem. Phys.*, 1965, 42, 1599-1608.
20. G. Stein, E. Würzberg, *J. Chem. Phys.*, 1975, 62, 208-213.
21. S. Aime, M. Botta, M. Panero, M. Grandi, F. Uggeri, *Magn. Reson. Chem.*, 1991, 29, 923-927.
22. C. C. Bryden, C. N. Reilley, *Anal. Chem.*, 1982, 54, 610-615.
23. D. H. Powell, O. M. Ni Dhubhghaill, D. Pubanz, L. Helm, Y. S. Lebedev, W. Schlaepfer, A. E. Merbach, *J. Am. Chem. Soc.*, 1996, 118, 9333-9346.

Chapter 6: Novel Gd(III) Complexes as MRI Contrast Agents:  
Measuring Efficiency *via* Relaxometry

24. H. Lammers, F. Maton, D. Pubanz, M. W. Van Laren, H. Van Bekkum, A. E. Merbach, R. N. Muller, J. A. Peters, *Inorg. Chem.*, 1997, 36, 2527-2538.
25. Y. Bretonnière, M. Mazzanti, J. Pécaut, F. A. Dunand, A. E. Merbach, *Chem. Commun.*, 2001, 621–622.
26. M. Murru, D. Parker, G. Williams, A. Beeby, *J. Chem. Soc., Chem. Commun.*, 1993, 1116-1118.
27. S. I. Kang, R. S. Ranganathan, J. E. Emswiler, K. Kumar, J. Z. Gougoutas, M. F. Malley, M. F. Tweedle, *Inorg. Chem.*, 1993, 32, 2912-2918.
28. P. L. Anelli, V. Balzani, L. Prodi, F. Uggeri, *Gazz. Chim. Ital.*, 1991, 121, 359-364.
29. C. J. Jocher, E. G. Moore, J. Xu, S. Avedano, M. Botta, S. Aime, K. N. Raymond, *Inorg. Chem.*, 2007, 46, 9182-9191.
30. S. Aime, M. Botta, S. G. Crich, G. B. Giovenzana, R. Pagliarin, M. Piccinini, M. Sisti, E. J. Terreno, *Biol. Inorg. Chem.*, 1997, 2, 470-479.
31. J. Hall, R. Haner, S. Aime, M. Botta, S. Faulkner, D. Parker, A. S. de Sousa, *New J. Chem.*, 1998, 22, 627-631.
32. F. Uggeri, S. Aime, P. L. Anelli, M. Botta, M. Brocchetta, C. de Haën, G. Ermondi, M. Grandi, P. Paoli, *Inorg. Chem.*, 1995, 34, 633-642.
33. A. Beeby, S. Faulkner, *Chem. Phys. Lett.*, 1997, 266, 116.
34. G. Brunisholz, M. Randin, *Helv. Chim. Acta*, 1959, 42, 1927-1938.
35. P. Vallet, Y. Van Haverbeke, P. A. Bonnet, G. Subra, J.-P. Chapat, R. N. Muller, *Magn. Reson. Med.*, 2005, 32, 1, 11-15.
36. S. Aime, M. Fasano, E. Terreno, *Chem. Soc. Rev.*, 1998, 27, 19.

Chapter 6: Novel Gd(III) Complexes as MRI Contrast Agents:  
Measuring Efficiency *via* Relaxometry

37. P. Caravan, N. J. Cloutier, M. T. Greenfield, S. A. McDermid, S. U. Dunham, J. W. M. Bulte, J. C. Amedio Jr., R. J. Looby, R. M. Supkowski, W. D. Horrocks, Jr., T. J. McMurry, R. B. Lauffer, *J. Am. Chem. Soc.*, 2002, 124, 3152.
38. F. K. Kálmán, M. Woods, P. Caravan, P. Jurek, M. Spiller, G. Tircsó, R. Király, E. Brulcher, A. D. Sherry, *Inorg. Chem.*, 2007, 46, 13.

# Appendix

## PEER-REVIEWED PUBLICATIONS (\*denotes the corresponding author)

- 1 The Synthesis and Coordination Chemistry of a Novel Tris-8-aminoquinoline Tripod, Angelo J. Amoroso,\* Peter G. Edwards, James C. Knight, Sian Howard, Lisa Stratford, K. M. Abdul Malik, A.-R. H. Al-Sudani, Li-Ling Ooi, *submitted to Dalton Transactions*
- 2 *rac-N*-{6-[Bromo(hydroxy)methyl]-2-pyridyl}pivalamide, *Acta Crystallographica Sect. E*, 2009, E65, o647, James C. Knight,\* Fawaz A. Saad, Angelo J. Amoroso, Benson M. Kariuki, Simon J. Coles
- 3 Novel Expanded Ring N-heterocyclic Carbenes: Free Carbenes, Silver Complexes and Structures; *Organometallics*, 2008, 27 (13), pp 3279-3289, Athanasia Dervisi,\* James C. Knight, Manuel Iglesias, Dirk J. Beestra, Ian A. Fallis,\* Kingsley J. Cavell,\* Louise Male, Andreas Stasch, Simon J. Coles, Li-Ling Ooi
- 4 Bis{N-[bis(6-bromopyridin-2-yl)methylene-κN]ethane-1,2-diamine-κ<sup>2</sup>N,N'}nickel(II) bis(perchlorate); *Acta Crystallographica Sect. E*, 2007, E63, m1046-m1047, James C. Knight,\* Angelo J. Amoroso, Peter G. Edwards, Ravi Prabakaran
- 5 2-(Cyclohexylamino)-1,4-naphthoquinone; *Acta Crystallographica Sect. E*, 2007, E63, o1226-o1227, James C. Knight,\* Thomas Tatchell, Ian A. Fallis
- 6 catena-Poly[[[diaquacadmium(II)]-μ-2,2'-bipyridine-6,6'-dicarboxylato] dihydrate]; *Acta Crystallographica Sect. E*, 2006, E62, m3306-m3308, James C. Knight,\* Angelo J. Amoroso, Peter G. Edwards, Li-Ling Ooi

